SUPERCONDUCTIVE THIN FILMS FOR RF APPLICATIONS

Thesis submitted in accordance with the requirements of
the University of Liverpool for the degree of Doctor in Philosophy by

Paolo Pizzol

October 2018

Abstract

A particle accelerator is a complex machine, made of different parts constantly evolving in step with the technology advancements. One part of the accelerator, the LINAC, has nearly reached its maximum potential.
This structure provides the acceleration through resonating cavities that under RF excitation transduce power into accelerating gradient. Superconductive structures are necessary to reduce the energy drain that these LINACs require. Niobium is the material of choice thanks to its high T_c and high field of first penetration H_{c1}, but the research now has pushed the material to its limits. In addition, the infrastructure required to cool and operate a superconducting LINAC is very energy intensive and costly. New research avenues are opening aimed at reducing the costs of operating a superconducting LINAC. One of them is to create thin layers of niobium and niobium alloys on a high thermal conductive material, copper. If successful, the cost reduction in creating a functional Nb on Cu cavity versus a full Nb cavity will be substantial: a lower quantity of Nb will be required and better cooling will be achieved thanks to the higher thermal conductivity of Cu.
This work aims at depositing Nb and Nb alloys on Cu substrates by using Chemical vapour deposition methods (CVD, PECVD, ALD) to verify if the obtained films are superconductive and can be employed in SRF applications.

A series of different CVD chambers have been designed, built and evaluated to deposit the niobium-based superconducting films. Gas flow simulations were made by using Ansys Fluent® to aid the understanding of the deposition results. The importance of a properly designed system has been highlighted, influencing factors like growth rate, uniformity and quality of the films. The deposition results were studied by electron microscopy (SEM, TEM, FIB), X-Ray diffraction (XRD) and X-ray photoelectron spectroscopy (XPS) to investigate their structural properties while the superconductivity was assessed by residual resistivity ratio (RRR) measurements, SQUID and localized magnetometry. The use of the chlorine-based precursors was anticipated to be detrimental to the stainless steel reactors used, due to the repeated cycles of hot HCl gas exposure followed by air / moisture. However, the heightened corrosion speed of the chamber resulted in the inclusion of iron precipitates in the niobium films. This issue was addressed by redesigning the deposition chamber.

One of the thesis objectives was to evaluate the feasibility of using chemical vapour deposition to coat copper for SRF cavities. CVD processes based on the chlorinated precursors ($NbCl_5$ and $TiCl_4$) have been evaluated and successful depositions of Nb, NbN, and NbTiN on copper substrates has been demonstrated.
Further, it has been demonstrated that Nb-based films can be deposited by CVD on copper with superconductive properties for the first time. It has been shown that CVD

can be used to produce niobium coatings, with T_c matching the bulk material although with lower field of first penetration. The temperature influenced greatly the films: above 500 °C no chlorine residue was present in the films, and no oxygen contamination thanks to the UHV deposition chambers. The best results were obtained by depositing at 700 °C, with an RRR of ≈ 30 and large crystallites (≤ 500 nm across). The results suggest that the films would have more bulk Nb like properties if deposited at higher temperatures, but going above 700 °C would compromise the Cu substrate by softening it or melting it. The NbN and NbTiN films possess structural properties matching the literature reference materials, however it was not possible to separate these films from the copper structures by dissolution. Consequently, their superconductive properties could not be measured, however the availability of new local magnetometry techniques will make this feasible in the future.

Contents

Illustrations

List of Figures

List of Tables

Notations

Arabic

c	**C**onstant for the speed of light
ΔG_f	**G**ibbs free energy of the components
ΔG_r	**G**ibbs free energy of the reaction
e	**C**harge of the electron
E	**E**lectric field
$E_{binding}$	**B**inding energy
$E_{kinetic}$	**K**inetic energy
E_{photon}	**P**hoton incident energy
f	**F**requency of a cavity
G	**G**eometry factor
$\hbar$	Planck's constant
H	Magnetic Field
H_c	**C**ritical field
H_{ext}	**Ext**ernal field
H_{sh}	**S**uper **H**eating field
I	**C**urrent
I_0	**C**urrent at time zero
j_s	**C**urrent density
k	Ginzburg Landau parameter
k_B	**B**oltzmann's constant
K	Equilibrium constant
Kn	Knudsen number
L	**L**ength of a cavity
m	**M**ass of the electron
n_s	**N**umber density of superconducting carriers
N_a	Avogadro's number

P_{diss}	**P**ower dissipated
P_{diss}	**P**ower dissipated
Q_0	**Q**uality factor
Q_r	**R**eaction quotient
R	**R**esistance
R_a	**S**hunt impedance
R_{BCS}	**BCS** resistance
R_e	**R**eynolds number
R_g	**G**as constant
$R_{Resistance}$	**R**esidual resistance
R_s	**S**urface resistance
T	**T**emperature
T_c	**C**ritical temperature
v	**V**elocity
v_F	**F**ermi's velocity
V_b	**A**cceleranting voltage
z_i	**S**tochiometric coefficient for the "i" species

Greek

Δ_b	**B**oundary layer
Δ_{ph}	**P**hase difference
ϵ	**S**train
ϵ_0	**C**oherence length
ϵ_c	**S**ize of the vortex core
θ	**A**ngle
λ	**W**avelength
λ_L	**L**ondon penetration depth
μ	**D**ynamic viscosity of gas
μo	**M**agnetic permeability
ρ	**D**ensity of gas
ρ_0	**R**esistivity
ρ_m	**R**esistivity in a magnetic field
$\rho_{ph}(T)$	**T**emperature dependant phonon scattering contribution
ρ_{res}	**R**esistivity depending on the defects and impurity
ρ_{tot}	**T**otal resistivity
ϕ	**W**ork function
Φ_a	**A**mplitude ratio
φ_0	**RF** cycle
Φ_0	**R**esistivity

Acronyms

ALD	**A**tomic **L**ayer **D**eposition
BCS	**B**arden **C**ooper **S**chrieffer
CERN	**C**onseil **E**uropeenne pour la **R**echerche **N**uclaire
CTE	**C**oefficient of **T**hermal **E**xpansion
CVD	**C**hemical **V**apour **D**eposition
CW	**C**ontinuous **W**ave
DC	**D**irect **C**urrent
ECR	**E**lectron **C**yclotron **R**esonance
EDX	**E**nergy **D**ispersive **X**eam
FIB	**F**ocussed **I**on **B**eam
GIXRD	**G**lancing **I**ncidence **X** **R**ay **D**iffraction
HZB	**H**elmholtz **Z**entrum **B**erlin
LINAC	**LIN**ear **AC**celerator
LHC	**L**arge **H**adron **C**ollider
MOCVD	**M**etal **O**rganic **C**hemical **V**apour **D**eposition
PEALD	**P**lasma **E**nhanced **A**tomic **L**ayer **D**eposition
PECVD	**P**lasma **E**nhanced **C**hemical **V**apour **D**eposition
PVD	**P**ysical **V**apour **D**eposition
RF	**R**adio **F**requency
RPECVD	**R**emote **P**lasma **E**nhanced **C**hemical **V**apour **D**eposition
SIC	**S**urface **I**mpedance **C**haracterization
RRR	**R**esidual **R**esistivity **R**atio
SEM	**S**canning **E**lectron **M**icroscope
SLAC	**S**tanford **L**inear **A**ccelerator **C**enter
SQUID	**S**uperconducting **QU**antum **I**nterference **D**evice
SRF	**S**uperconducting **R**adio **F**requency
TEM	**T**ransmission **E**lectron **M**icroscope
TBTDEN	**T**ert **B**utylimido **T**ris **D**i **E**thylamido **N**iobium
UHV	**U**ltra **H**igh **V**acuum
XRD	**X** **R**ay **D**iffraction
XPS	**X**ray **P**hotoelectron **S**pectroscopy

List of publications

Pizzol, P., Chalker, P., Hannah, A., Heil, T., Malyshev, O., Pattalwar, S., Stenning, G., Valizadeh, R., Superconducting Coatings Synthetized by CVD/PECVD for SRF Cavities, *Proceedings, 17th International Conference on RF Superconductivity (SRF2015), Whistler, Canada, September 13-18, 2015*, 2015, TUPB038

Pizzol, P., Chalker, P., Hannah, A., Heil, T., Malyshev, O., Pattalwar, S., Stenning, G., Valizadeh, R., Superconducting Coatings Synthesized by CVD/PECVD for SRF Cavities, *Proceedings, 6th International Particle Accelerator Conference (IPAC 2015): Richmond, Virginia, USA, May 3-8, 2015*, 2015, WEPHA058

Pizzol, P., Chalker, P., Heil, T., Malyshev, O., Pattalwar, S., Stenning, G. , Valizadeh, R., CVD Deposition of Nb Based Materials for SRF Cavities, *Proceedings, 7th International Particle Accelerator Conference (IPAC 2016): Busan, Korea, May 8-13, 2016*, 2016, WEPMB056

Pizzol, P., Chalker, P., Malyshev, O., Roberts, J., Valizadeh, R., Wrench, J., Atomic Layer Deposition of Niobium Nitride from Different Precursors, *8th Int. Particle Accelerator Conf.(IPAC'17), Copenhagen, Denmark, 14 - 19 May, 2017*, 2017, 1094-1097

Acknowledgements

And in a blink of an eye, 4 years have gone. Years filled with joy, frustration, anger, delight, surprise, tears, sweat and blood.
I will start by thanking my university supervisor, Prof. Paul Chalker, for being there for me every step of the way, for the inestimable support and care he's shown me along these four years.
I would like to thank my ASTeC supervisors, Doctor Reza Valizadeh and Doctor Oleg Malyshev, for having given me the possibility to work with them, to put together this book and not giving up on me. Sure, the drive at times hasn't been smooth, but we are here now, which is all that matters.
I can't thank enough Joe Herbert, Adrian Hannah and James Conlon: Joe, thank you for everything you've done for me and the other students. Adrian, thank you for not having stabbed me (yet) in the eye with a screwdriver for all the stupid questions I've asked you, or the stuff I broke. It's been fun. James, thank you because your weekend stories make Mondays less bad. Sshhht, I won't tell. I swear.
A special word goes to all the people at Daresbury Labs that helped me along the way: Debbie Clucas and Theresa Hillon (sorry for that fire alarm), Diane, Graham, Gary and Steve from the mechanical workshop (I have a quick job that needs doing, no, no, for real this time...), Nigel up the tower and I'm sure I'm forgetting someone. If I have, I owe you one.
An enormous thank you goes to Tobias and Karl at the UoL Nanoinvestigation centre, for all the time they wasted trying to teach me how to use the instrumentation and for all the "Could you do it by yesterday" samples I've merciless unloaded on them.
As they say, there's strength in numbers: Tom, Alisa, Andrew, Billy, Taylor, Pavel, Bianca, Alex, Roland, Kay, Joe, Sam, without all of you it wouldn't have been as much fun as it has. Kinda. No, it has, seriously.
Shout out for all the vacuum lab peeoooopleee: Ruta, Taaj, Sihui, Sonal, Stuart and Kareem. I've been blessed with you lot, and yes, it's been a journey and some of us are not out of it yet, but keep your eyes on the prize and you'll manage.
A massive thank you goes to my new work partners: Mark, Phil, Greg, Louis, Stuart (again, we're stuck! At least now separate bedrooms), Paul, Jane and Mike. Thank you

for having taken me on with the ESS HB Cavity project, I'm sure we'll be fine.

Of course, a special thank you goes to all the Warrington Board Game Club members, too many to name them all, but surely I'll name a few: Dan and Sara, Tom and Jenny, Dave and Terry, Andre and Becky, Paul, Dave, Craig, Craig, Adam, Colin, Mike, Nigel, Jon, Jules. It's been a blast. Thanks for the countless laughs, the "Yeah, I know the rules" and I'd forgotten a few, the political arguments, the 12 hours of Twilight Imperium, and, really, for all of you. I couldn't have asked for more.

And now for the ones left behind: a massive thank you goes to all my friends back home, because every time I go back they strive to make me feel like I've never left. Marta, Stefano, Nicola, Carla, Giuseppe, Marco, Elena, Marco, Erica, Francesco, Silvia, Max, Anna, Checo, Maria, Dennis, Chiara, Don Samuele, Samuele, Camilla, Sara, Enrico, Sara, Luca and all the little ones.

Words are not enough to express what I feel for my family: Laura, papa' Luciano and mamma Catia. I know it must be hard to see me once a year on a good year, and still you're there for me. I love you all.

And now, last but not least, my partner in crime, the one that is always there for me, even when I don't know I need her. Monia, who's been with me for so long, and has been by my side during these four rollercoaster years. Who has seen my best and my worst, and is still here with me.

I'm not going to thank you. That wouldn't be enough. What do you say, would you marry me?

Part I

Background

Chapter 1

Introduction

Superconductivity, as presented in chapter 2, has been discovered more than a hundred years ago. Enormous progress has been made in understanding the physics underpinning this phenomenon, to the point that now superconductors are used in a vast range of applications, from satellites to research instrumentation. One field where superconductor materials have become irreplaceable is particle accelerators. These machines, even if not well known by the general public, are at the roots of most technological progress of the last century. Without particle accelerators we would not have televisions, mobile phones or the internet. One of the crucial parts of an accelerator, the LINAC, is manufactured out of niobium metal, a superconductor that has been used in this field since the 60s. To perform, RF power is fed to the Nb that is cooled to 1.8 °K, presenting a high cost in energy and infrastructure. After more than 50 years of constant improvements, though, the material has been pushed to its accelerating gradients theoretical limits, so the research is now focusing on how to reduce its operational cost by either reducing the quantity of material used or by coupling with materials with better thermal conductivity. This work aims at both targets at the same time: depositing a thin layer of Nb, maintaining its superconducting properties, on copper substrates, having a better thermal conductivity. This will be done by using Chemical Vapour Deposition (presented in chapter 3), a coating technique that allows to create layers on complex surfaces, like cavities in a LINAC.

Particle accelerators are hereby presented, to familiarize the reader with the field of application. The material, Nb, is introduced, with some considerations on potential alternatives. Thin films are then introduced, as a promising way to replace the bulk material.

1.1 Particle accelerators - a brief history

A particle accelerator is, as the name suggests, a machine that accelerates charged particles to nearly the speed of light by the use of electromagnetic fields [1]. The driving force behind the development of the first particle accelerator came from Ernest Rutheford

theorization of the atomic nucleus in 1909 [2]: his experiment suggested that the atom possessed a core, later called the nucleus, that could itself be "split" and therefore studied. To do so, a new type of instrument was required: machines that could produce highly energetic beams capable of "slicing" through the nucleus of atoms.

1.1.1 Cyclotrons

The first particle accelerator, called the Betatron, was theorized in 1927 by Rolf Widere [3] but the technology at the time was not yet ready to allow one to be built. In 1932 Ernest Lawrence, inspired by Wildere work, developed and patented the first circular accelerator, called the Cyclotron, at the University of California, Berkeley [4, 5].

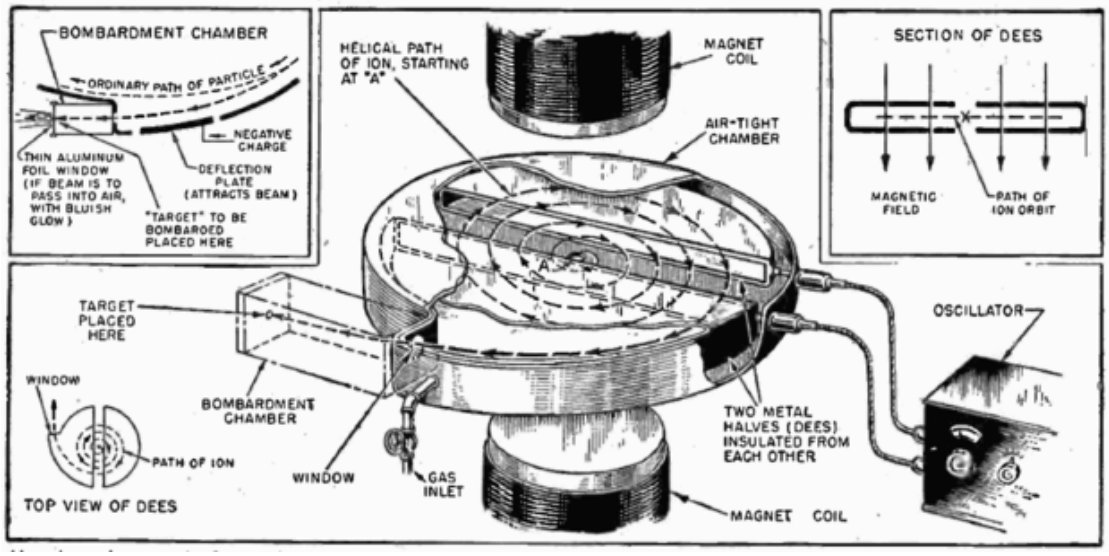

FIGURE 1.1: Diagram of a cyclotron

A cyclotron is a circular machine where the particles are emitted in the centre, held on a spiral trajectory by a static magnetic field and and accelerated towards the outside by a switching radio frequency (RF) field. Figure 1.1 [6] shows the diagram of how a cyclotron operates. Lawrence's cyclotron was 69 cm in diameter and capable of accelerating ions up to 4.8 MeV (Mega electron volt, equivalent to 1.6×10^{-13} Joules). To compare it with a more recent machine, one beam of the Large Hadron Collider at CERN is capable of reaching 6.5 TeV (Tera electron volt), 10^6 times more energetic [7].

1.1.2 Synchrotrons

For many years cyclotrons were the most powerful machines available to physicists to perform high energy experiments. This changed in 1944, when Vladimir Veksler invented the principles for the Synchrotron [8], which was independently built by Edwin McMillan in 1945 to accelerate electrons [9]. The proton synchrotron came a few years later, in 1952, by Sir Marcus Oliphant. A synchrotron is an evolution of the cyclotron concept, where the magnetic field is not static any more, but instead it changes according to

the speed of the particles [10]. This improves on many aspects of a synchrotron: first of all, the path that the particles travel on can now be kept constant since the field is not changing in space any more but in time. As a consequence, the vacuum chamber required now can be a pipe, instead of a disk, allowing a more efficient use of the magnets compared to the cyclotrons.

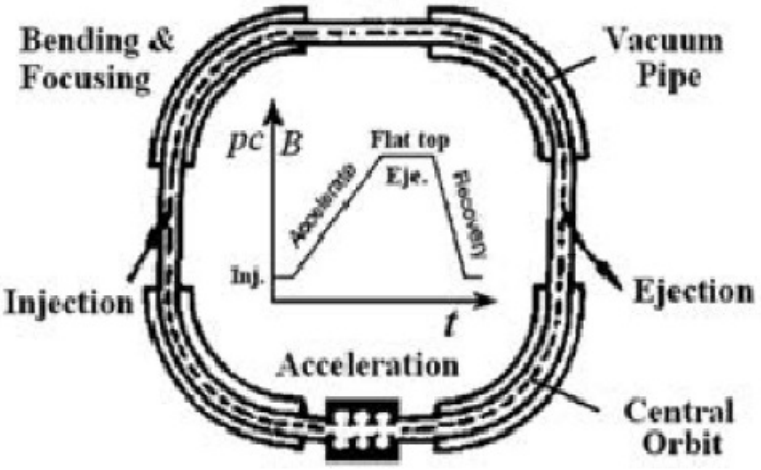

FIGURE 1.2: Diagram of a synchrotron

Figure 1.2 [10] shows the diagram of a synchrotron. This new concept of accelerator lead to a steep increase in achievable beam energy: as a comparison the "Cosmotron", one of the first proton synchrotrons ever built, reached 3.3 GeV (Giga electron volt) in 1953, a bit less than 10^3 times more energetic than the first cyclotron. Over the years many designs inspired by these early accelerators came in operation, reaching higher energies over longer paths. As previously mentioned, the Large Hadron Collider (LHC) is nowadays capable of producing two beams that travel through the machine at up to 6.5 TeV per beam, for a total of 13 TeV of energy.

1.1.3 What makes a particle accelerator?

A modern particle accelerator is a collection of complex parts that have to operate together very precisely to provide the results that are expected. Even so, an accelerator can be broken down into a few main sections:

- A beam pipe: the essential part of a particle accelerator is a space in which the particles can travel. This is generally a vacuum vessel made up of steel piping; vacuum is required to allow the particles to travel through the machine without interactions with other particles normally present in the atmosphere.

- A particle source: this part provides the particles that will be accelerated. Different sources will produce the appropriate type of particles for a specific accelerator, such as electrons, ions, protons or other charged particles.

- A linear accelerator: once produced, the particles will be then accelerated in a linear accelerator, otherwise known as LINAC. A LINAC is a resonating structure where the particles are subjected to alternating electric fields that, if synchronized with the speed and the position of the particles, provide the acceleration. There are mostly two types of LINACS: normal conducting, operating at room temperature, and superconducting, operating at cryogenic temperatures.

- A synchrotron: once the particles leave the LINAC they enter a circular accelerator, a synchrotron as previously mentioned. Every revolution around the length of the ring will add more energy - and therefore speed- to the particles. There can be more than one synchrotron in one accelerator: a smaller one commonly called a Booster, right after the LINAC, and a bigger one, commonly called the Main ring. Having more than one synchrotron is needed to reach higher energies while still being able to control the direction of the beam.

- Beam stations or targets: once the particles have reached the desired energy, they are deviated from the main ring into either targets or beam stations. Targets can be materials under study onto which the particles are directed, to then analyse the outcomes of the collisions. Beam stations can be locations where users can set up more complex experiments that may require more space than what is available inside the beam pipe.

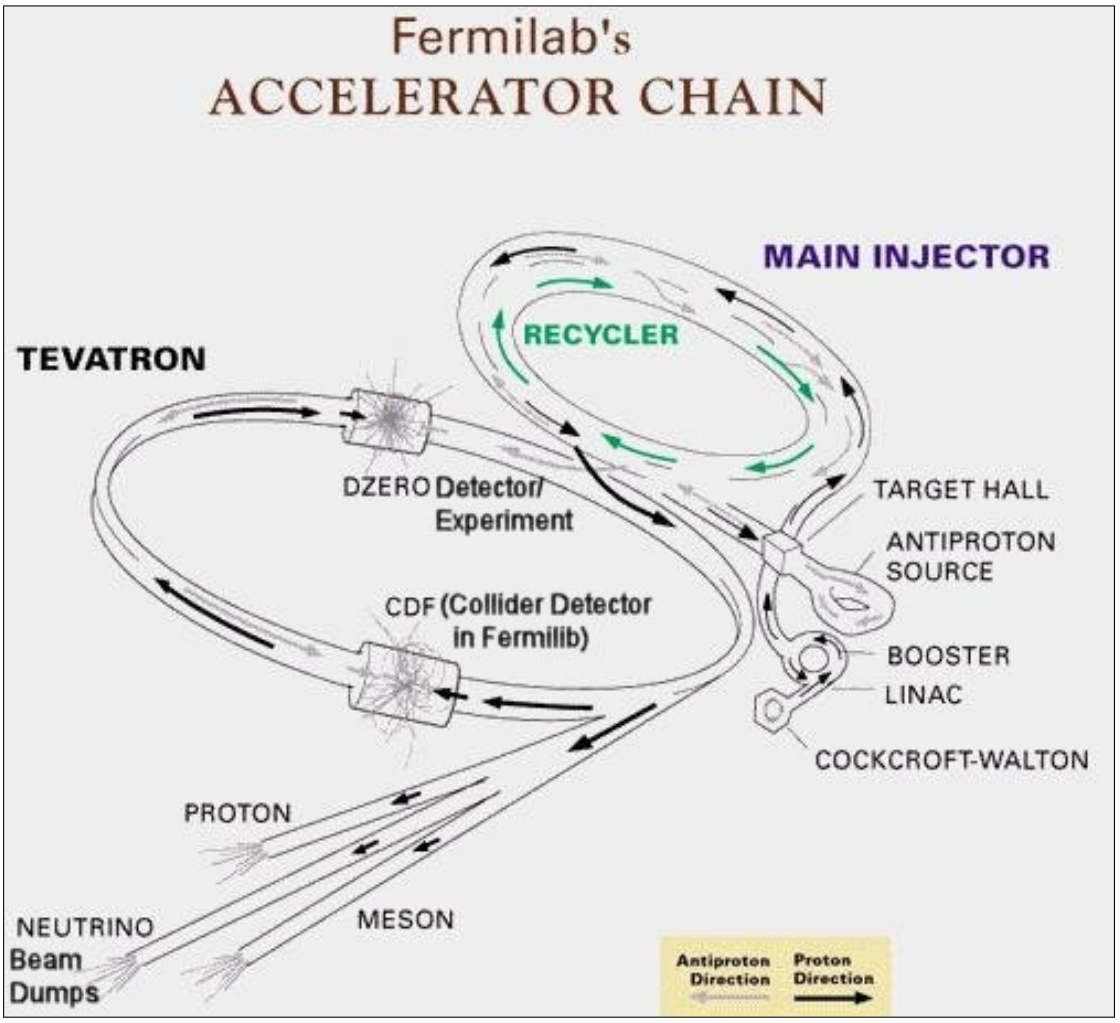

FIGURE 1.3: Schematic of the Fermilab's "Tevatron" accelerator

Figure 1.3 [11] shows how the aforementioned components come together in a real machine. This one in particular is Fermilab's "Tevatron", the second highest energy particle collider in the world after the LHC, capable of reaching energies of up to 1 TeV (Tera electron volt) [11], hence the name.

Discussing every component of an accelerator in great detail is beyond the scope of this work. The focus will be instead one subpart of the LINAC, the radio frequency cavities.

1.1.4 What is a LINAC?

As mentioned before, LINAC stands for Linear Accelerator, and as the name suggest is a straight section of the infrastructure that provides the initial acceleration force to the particles.

The LINAC structure was proposed in 1924 [12], while the first operating LINAC was build 4 years later [3]. LINACs are used in a vast range of applications, spawning from the medical field (x-ray generation[13]) to power plants [14].

To accelerate the particles down the beam line, the LINAC is excited by radio frequency power, oscillating at a particular frequency dictated by the size of the LINAC and by the acceleration energy required. Inside the LINAC, resonating structures have the task to transduce this power into accelerating force, the discussion of which is outside the scope of this work, falling into the beam dynamics branch of accelerator physics.

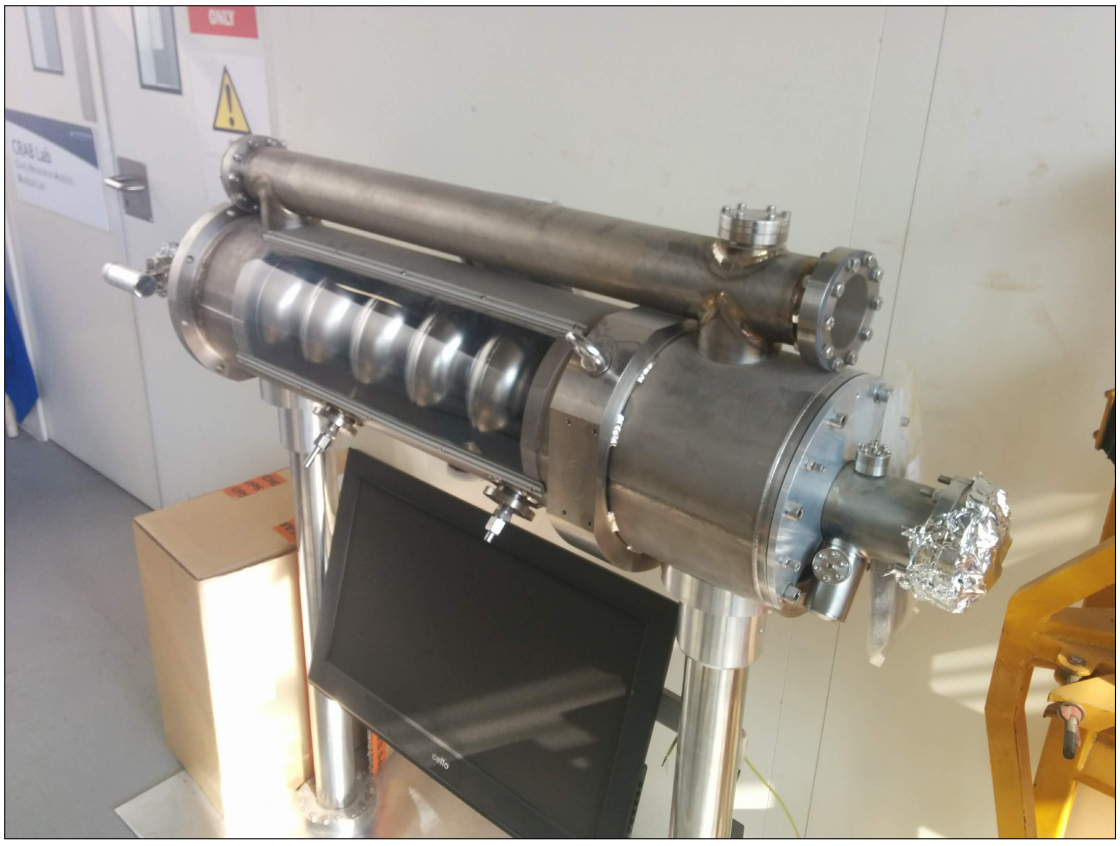

FIGURE 1.4: Niobium 9-cell cavity

These resonating structures are called cavities. As per definition, cavities are hollow structures where the excited waves exist. Figure 1.4 shows an SRF cavity with its titanium jacket cut out to expose the internal cells.

FIGURE 1.5: Example of SRF cavity cells: the different size relates to their operating frequency

Cavities are composed by many sub structures, called cells, welded together in a number dictated by design and acceleration requirements. Figure 1.5 shows three different types of cells; as mentioned, the size of a cavity (and its cells) is connected to its wavelength through the equation 1.1:

$$L = \frac{c}{2f} \tag{1.1}$$

where L is its length of a cell in meters, c is the speed of light and f the frequency. For an SRF particle accelerator, the most used frequency is 1.3 GHz, returning a cell length of 11.5 cm. It is not difficult to understand that, for an average SRF LINAC made of tens and tens of 9-cell cavities, size becomes an important factor, and a massive cost.

1.2 Niobium

Niobium is a metal that belongs to the transition elements in the periodic table, chemically and physically very similar to tantalum. It has a body centred cubic structure, belonging to the lm-3m space group. It was formerly known as Columbium, as named by the English chemist Charles Hatchett in 1801 [15], when he discovered it and its similarities to Tantalum. From 1809 it was thought that the two metals were actually

the same element, wrongly. It was so until 1846 when a German chemist, Heinrich Rose, found traces of a second element in Tantalum ore, naming the discovery *Niobium*. This became the official name in 1949 [16].

1.2.1 Why Niobium in SRF?

For many years now SRF cavities have been manufactured out of Niobium. There are very valid reasons for this choice:

- Highest T_c of all the pure metals, at 9.26 K,
- Lowest H_{c1} of all pure metals
- Relative ease of fabricating structures out of it

Even if many other superconductors have been discovered that possess higher T_c([17]), they are either not capable of sustaining high RF fields or are too difficult to manufacture in complex shapes. The research so far has been focusing on trying to improve Niobium performances for SRF cavities, to the point that currently the SRF technology for Niobium is very close to its physical limits of $H_c = 180$ milliTesla [18–20].

For these reasons, the wide majority of SRF accelerating structures are, up to this day, being manufactured out of Niobium. More recent developments have highlighted the progress of Nb_3Sn cavities [21, 22], where tin is evaporated inside a niobium cavity following the work of [17, 23] to create a thin alloyed layer of Nb_3Sn. This material has a T_c of 18 K, twice Niobium, which would considerably reduce the cost of cooling. Promising research has been conducted on *nitrogen doping* of Nb cavities [24, 25]: by introducing nitrogen gas in a warm (150 °C) Nb cavity, a NbN phase seems to form between the grains of the material, increasing the quality factor by an order of magnitude. Amongst the research on pure niobium, other niobium based candidate materials are being investigated as a potential replacement.

1.3 Niobium based materials

As previously mentioned, current SRF technology is approaching the physical limits of niobium. Once those limits are reached, the amount of accelerating gradient produced by the electric field will not increase any further, being impossible to increase the magnetic field without compromising the superconductivity. This makes a very strong case for the exploration of RF applications for other superconductors: the possibility of operating at higher T_c and potentially higher H_c values will lead to a significant cost reduction in the cryogenic infrastructure. The criteria for a superconductor to be elegible as a good SRF candidate are:

- high T_c
- low resistivity ρ_0

- high H_c or H_{sh} and a small Ginzburg Landau parameter

Even though many superconducting materials exist, only a few have a T_c higher than niobium and can therefore be considered for SRF applications. Figure 1.6 [26] shows a plot where the resistivity of some superconducing materials is plotted against their T_c. The dotted lines represent materials that with different T_c and ρ_n have the same R_{BCS}.

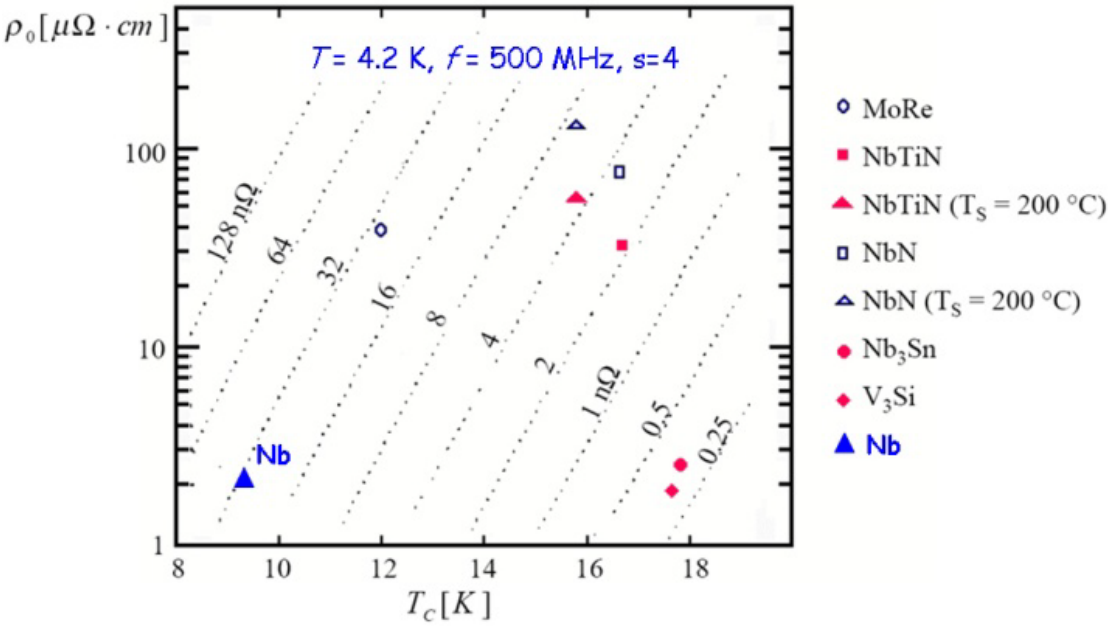

FIGURE 1.6: Resistivity Vs Critical temperature calculated for different materials at T=4.2K, f=500 MHz, s=4

TABLE 1.1: Parameters for some of the materials that can be used in SRF applications

Material	T_c**[K]**	$\rho_n[\mu\Omega cm]$	$H_c(0)$**[T]**	$H_{c1}(0)$**[T]**	$H_{c2}(0)$**[T]**	λ**[nm]**
Nb	9.2	2	0.2	0.17	0.4	40
NbN	16.2	70	0.23	0.02	15	200
NbTiN	17.5	35		0.03		151
Nb_3Sn	18.3	20	0.52	0.04	30	135

The niobium compounds, with some of their parameters reported in table 1.1, were chosen for this work since their possible use in SRF applications.

1.3.1 Niobium Nitride

Niobium nitride is a binary compound of niobium, being characterized by a B1 NaCl-like crystalline structure where the metallic atoms form a face centered cubic (Fm-3m) structure and the non metallic atoms sits in the interstices, as shown in figure 1.7

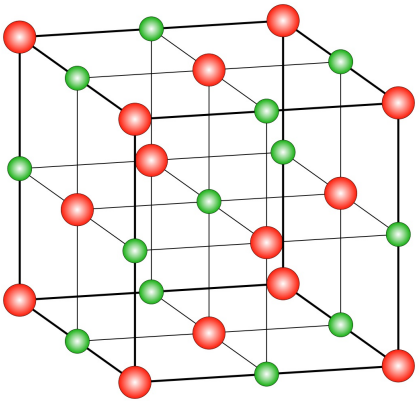

FIGURE 1.7: NaCl like structure where the red dots represent Niobium atoms and the green ones represent Nitrogen

B1 compounds are also known for having a certain number of randomly distributed vacancies in their structure, that affect the stochiometry and the superconductive properties.

Of all the phases that NbN can assume, it has been found that the most useful for SRF applications is the δ-NbN, characterized by a lattice parameter of 4.24 angstrom [27]. Niobium nitride has been studied extensively [28, 29] over the last 50 years, and even if its properties are well known, the applications in SRF are still limited: the main reason seems to be that the preferred deposition path is physical vapour deposition (PVD), where a NbN target is sputtered on the substrate. This is a line of sight technique, not capable of coating closed or round shapes like cavity cells easily. Progress are being made by the use of High-power impulse magnetron sputtering(Hi-pims, [30, 31]), which is a slower sputtering technique that has a higher degree of control on the coating, but there are still is regarding the thickness uniformity of the layers.

1.3.2 Niobium Titanium nitride

Niobium titanium nitride is a ternary compound of niobium, which is also a B1 compound. It presents the same advantages of NbN (higher T_c than Nb), with better electrical conduction properties the higher the atomic % of Ti in the material [32]. The compound is a mixture of NbN and TiN, since the two are perfectly miscible. The stoichiometry is therefore fundamental and trying to achieve the right concentration of each molecular species is challenging, due to the wide parameter space [33, 34].

1.4 Niobium thin film

For all the reasons listed up to now, niobium is the material of choice for SRF applications. This, though, comes with two trade offs:

- *Cost of material*: niobium is an expensive metal, currently placed at over 40000 £ per metric ton [35]. This does not include the cost of machining a cavity, which

sends up the price to an average of 250000 £ for a 9-cell Nb cavity. This is a high cost, which becomes less relevant only if the accelerator is placed underground: at that point, the cost of the tunnelling is vastly greater than the cost of the cavities.

- *Cost of cooling*: to perform at its maximum, niobium is supercooled to 1.8 K. Leaving aside for now the poor thermal conductivity of Nb, liquid helium is not cold enough to reach these very low temperatures, and a special type of plant has to be provided. This adds to the costs of an already expensive infrastructure: an SRF accelerator is certainly cheaper to run than a normal conducting one, but if the cooling power cost is factored in, the financial gain is still there, but reduced [36].

If any progress could be made to improve any of these points, the room for savings could be very large. This is where this work tries to step in. Reducing the amount of material needed (superconductor) and improve the thermal conductivity of it (substrate).

1.4.1 What is a thin film

A thin film is, as the name suggests, is a layer of material with a thickness between a few nanometers to a few micrometers. Thanks to technological achievements and research, the techniques that have been developed over the years are now capable of creating thin deposits of different types of materials, ranging from pure metals to ceramic multicomponent insulators. If deposited in the right conditions, a thin film can have similar properties of a thick layer of the same material [37]: as an example, copper thin layers are used vastly by the semiconductor industry to fill our digital devices, as their electrical performance is, for the voltages and currents required, still very good. For the same reason, though, power lines are still made of thick wiring, since the power would burn a thin film to dust!

1.4.2 Scope of this work - Thin films of niobium for SRF on copper

This field of research has been explored for more than 50 years, with the majority of studies done by depositing Nb or Nb based materials with PVD techniques[38]. PVD guarantees a high quality film, but coating geometrically complex substrates can be challenging[39].

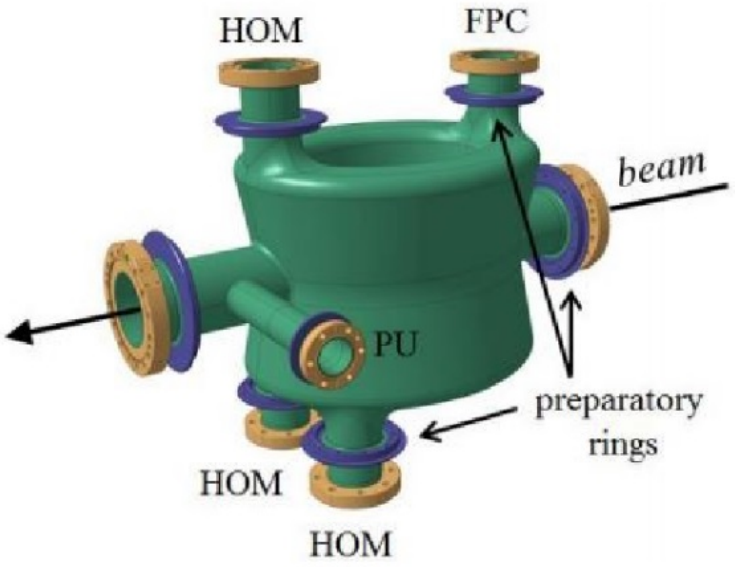

FIGURE 1.8: Crab cavity design

PVD, being a line of sight deposition technique, can produce high quality coatings but is limited to flat or relatively simple 3D surfaces, since the deposition can not reach areas that are in the shadow relative to the source. As a new complex design of cavities is being developed, called *Crab cavities* shown in figure 1.8 [40] due to their effect on the beam, PVD limitations prevent its use to provide the required coating.

This is the reason of choosing CVD: the gases enter the chamber and, if in the right conditions, coat every surface available. The complexity of the deposition shape is, for the coatings required, not a hindrance.

In comparison with PVD, research on chemical vapour depositions of Nb has been very limited, even more so for SRF applications: a work from Audisio et al [41] describes the reduction of $NbCl_5$ on iron, and depositing on copper with Zn added to the reaction area, suggesting that relative low deposition temperatures can be achieved by sacrificing the purity of the Nb layer, now contaminated with Zn. The only group active in CVD for SRF is, except the writer of this work, from Cornell University, USA. In collaboration with a private company called Ultramet, they have deposited and tested one niobium cavity made entirely with CVD: first, they created an anti cavity mandrel made of graphite, which was inserted in a vacuum furnace and heated up via RF induction heating. Then, once the deposition was over, they etched away the graphite and were left with a few millimetres thick structure, which performed reasonably well [42–44]. Only recently, as they presented at the International Particle Accelerator Conference (IPAC) in 2017, they started to deposit on copper substrates [45], including in their plenary talk some results from the writer's work.

More efforts have been focussed on Atomic layer deposition (ALD) of niobium and other superconductors, in the work or Claire Antoine and Thomas Proslier [46–49].

This is the rationale of this work: deposit niobium and niobium alloys on copper substrates, and test the superconductive properties of the materials grown. This is at this moment in time an important research question that need answering, to benefit the SRF community as a whole.

1.5 Overview of this work structure

This work is divided into three main parts.

Part I includes this introduction, then describes the theory of superconductivity (Chapter 2), followed by the mechanisms of chemical vapour deposition and atomic layer deposition (Chapter 3).

Part II is dedicated to the instrumentation and techniques used to characterize the samples obtained (Chapter 4).

Part III contains the results of this work, starting from the chemical used (Chapter 5), followed by the deposition facilities assembled (Chapter 6) to terminate with the depositions results with chemical vapour deposition with and without plasma (Chapter 7).

The work is concluded with a summary and outlook for future experiments (Chapter 8).

An appendix on atomic layer deposition work conducted is presented after the conclusions (Appendix A), followed by the study of the development of a PECVD system (Appendix B).

Chapter 2

Theory of Superconductivity

Chapter 2 introduces the concept of particle acceleration. An overview of superconductivity theory is presented, followed by a brief description of what is a cavity and its operation.

2.1 Superconductivity

Superconductivity is when a material, once it reaches a certain critical temperature, exhibits zero electrical resistance and expels all the magnetic flux fields.

2.1.1 A brief history

This phenomenon was discovered in 1911 by Dutch physicist H. Kamerlingh-Onnes while studying mercury, lead and tin. His discovery was made possible by another previous achievement of his in 1909, the liquefaction of helium, which happens at 4.2 kelvin at atmospheric pressure [50]. Following the theoretical studies of James Dewar, H. Kamerlingh-Onnes started working on the behaviour of the electrical resistance of platinum and gold at first, followed by mercury, as a function of temperature. Once he reached about 4 kelvin, his instruments could not read any electrical resistance. He called this new phenomenon **superconductivity**, and the temperature at which this it appears the **critical temperature** T_c. The materials that exhibit this property are called **superconductors**.

This means that when a superconductive material ring is exposed to a changing magnetic field (for example, by introducing a permanent magnet through the hole of the ring before T_c and by then removing it once T_c has been reached), the induced voltage generates a "permanent current" that will flow without dissipation through the material, as shown in figure 2.1 [50].

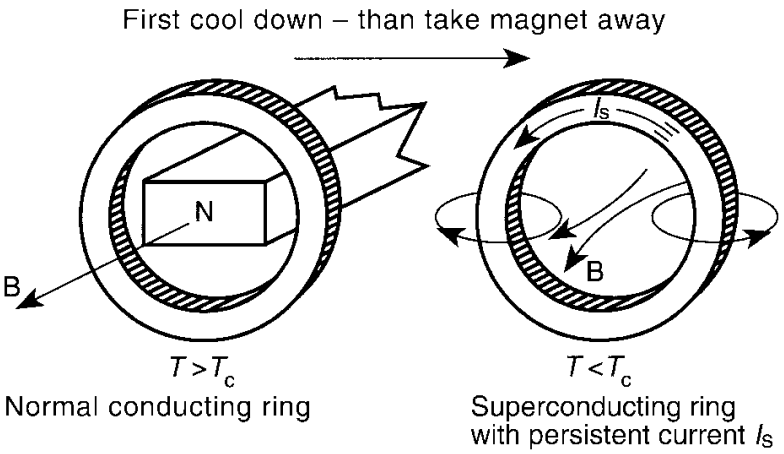

FIGURE 2.1: Effect of the magnetic field in a superconductive ring

This current will dissipate if the material is not in its superconductive state anymore, for example by warming up above its T_c. Then, for a finite resistance value of R, the current will decrease with time according to equation 2.1

$$I(t) = I_0 e^{-\frac{R}{L}t} \tag{2.1}$$

Here L is the self induction coefficient, that depends on the geometry of the ring, I_0 is the current at a time chosen as time zero, t is time. The measurement of I(t) can be done accurately: Kamerlingh-Onnes and later Tuyn developed this method, in which two superconductor concentric rings have a current induced.

This current keeps the rings parallel. One of the two rings (the inner one) is suspended on a torsion thread and then slightly turned away from the parallel position. The torsion thread and the current will both exert a force and an angular momentum, reaching an equilibrium.

This equilibrium is measured via a light beam hitting a mirror on the torsion thread. Any decay in the current would lead to a change in the equilibrium position, therefore of the mirror and of the reflected beam position. During these experiments, no chance has ever been measured, proving that if the materials remain in their superconductive state, there is no decay in the permanent current. A diagram of the experimental setup is shown in figure 2.2 [51].

A practical application of this phenomenon is seen in superconducting magnets, that once magnetized can be operated with virtually no current losses for long periods of time.

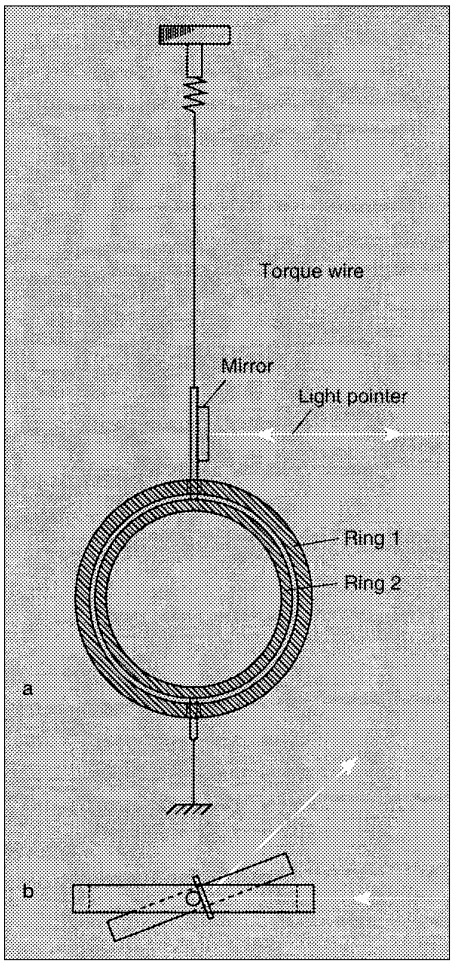

FIGURE 2.2: Experimental setup to test permanent current decay

2.1.2 The Meissner Effect

Infinite conductivity is one of the aspects that define superconductivity. The other one, as discovered in 1933 by Walther Meissner and Robert Ochsenfeld [52], is the perfect magnetic flux exclusion. When a superconductor is cooled past its T_c in the presence of a magnetic field H_{ext}, this is abruptly expelled from the material. This phenomenon is called Meissner effect, and it's schematically shown in Figure 2.3.

This is true if, as shown in equation 2.2,

$$H_{ext} < H_c \tag{2.2}$$

where H_c is called **Critical Field**, defined as the highest magnetic field under which a material remains superconducting. This is a function of temperature and is different for different materials.

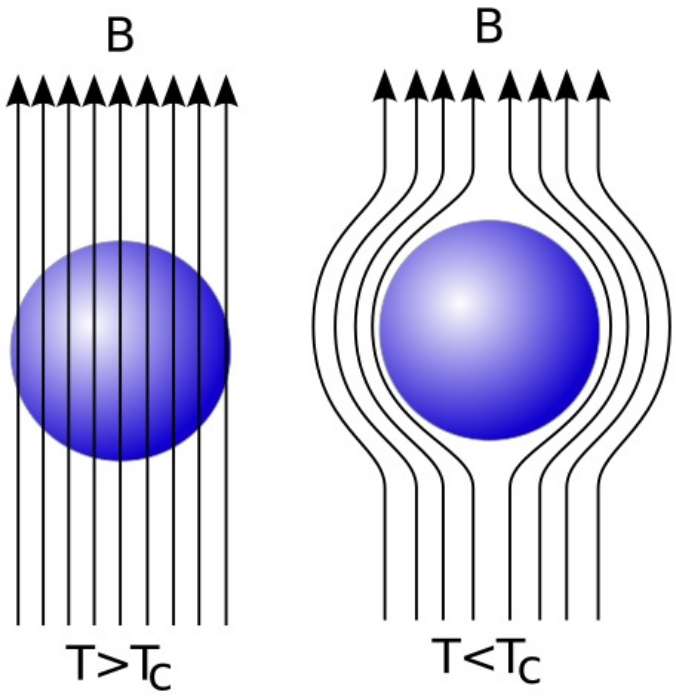

FIGURE 2.3: Meissner effect on a spherical superconductor, Wikimedia Commons, CC

2.1.3 London equations and Penetration Depth (λ_L)

In 1935, following Meissner discovery, Fritz and Heinz London conducted a quantitative analysis of the Meissner effect [53]. In the presence of an electric field E, the superconducting electrons will be accelerated freely without dissipation so that, as shown in equation 2.3,

$$m\frac{\partial v}{\partial t} = -eE \tag{2.3}$$

where v is the mean velocity of the electrons, t is time, e the charge of the electron and m the electron mass. Equation 2.3 represents the equation for infinite conductivity. By substituting equation 2.4

$$j_s = -n_s e v \tag{2.4}$$

equation 2.3 can be written as

$$\frac{\partial j_s}{\partial t} = \frac{n_s e^2}{m} E \tag{2.5}$$

Equation 2.5 is known as the first London equation. By substituting equation 2.5 in Faraday's law of induction (equation 2.6)

$$\nabla \times E = -\frac{1}{c}\frac{\partial H}{\partial t} \tag{2.6}$$

magnetic field and current density can be related as equation 2.7

$$\frac{\partial}{\partial t}\left(\nabla \times j + \frac{n_s e^2}{mc} H\right) = 0 \tag{2.7}$$

Together with the Maxwell equation, shown in equation 2.8

$$\nabla \times H = \frac{4\pi}{c} j \tag{2.8}$$

connects the magnetic field and the current density that can exist within a perfect conductor. According to equation 2.8, a static current density j can be determined by any static field H. Since equation 2.7 allows time indipendent solutions for H and j, this is not compatible with what happens in a superconductor, which is the expulsion of magnetic field. By restricting the solutions allowed by equation 2.7 by these conditions (shown in equation 2.9)

$$\nabla \times H = \frac{n_s e^2}{mc} H \tag{2.9}$$

the London brothers discovered that they could describe the behaviour of superconductors. For the Meissner effect to happen, the quantity (equation 2.10)

$$\nabla \times j + \frac{n_s e^2}{mc} H \tag{2.10}$$

has to be equal to 0. Therefore

$$\nabla^2 H = \frac{4\pi n_s e^2}{mc^2} H \tag{2.11}$$

and

$$\nabla^2 j = \frac{4\pi n_s e^2}{mc^2} j \tag{2.12}$$

From equation 2.11 and equation 2.12, it emerges that magnetic fields and currents can only exists if the superconductive material has a certain thickness, called London penetration depth, λ_L. This value is given by equation 2.13

$$\lambda_L = \sqrt{\frac{mc^2}{4\pi n_s e^2}} \tag{2.13}$$

and is temperature dependant, showing that the external field H penetrates deeper into the material, as its temperature approaches T_c.

Typical values for λ_L range between 50 and 500 nm. Table 2.1 shows the values for the London penetration depth for different materials [54].

Material	Coherence Length (nm)
Tin	34
Aluminium	16
Lead	37
Cadmium	110
Niobium	39

TABLE 2.1: Values of London penetration depth for different materials

2.1.4 BCS theory and Coherence Length (ε_0)

A full theoretical understanding of superconductivity was not achieved until the 1950s with the work of Bardeen, Cooper and Schrieffer, from whom the BCS theory takes its name [55]. At very low temperatures the vibrations of a material's crystal lattice (phonons) are minimal: the lack of vibrations leaves the electrons, when travelling through the lattice, free to interact with the positive charged ions at the lattice nodes, distorting the structure ever so slightly. This creates areas of locally strong positive charge that can shield the electrostatic repulsion between two electrons of similar energies, leading to them combining in a Boson-like entity called a *Cooper pair* [56]. The electrons in the pairs can be separated by a relative large distance, called *Coherence Length* (ε_0). An approximate calculation of this length can be extracted from 2.14

$$\varepsilon_0 = \frac{\hbar v_F}{k_B T_c} \tag{2.14}$$

where $\hbar$ is Planck's constant, k_B is Boltzmann's Constant and v_F is Fermi's velocity. This approximation does not take in consideration eventual impurities in the material, In table 2.2 are reported some ε_0 values for different materials [54].

Material	Coherence Length (nm)
Tin	230
Aluminium	1600
Lead	83
Cadmium	760
Niobium	38

TABLE 2.2: Values of Coherence Length for different materials

Since the Cooper pair electrons are a boson condensate, the Pauli Exclusion Principle does not apply, therefore two superconducting electrons can occupy the same electronic quantum state which has a significantly lower energy than electrons in the normal conducting state (δ per electron, so 2δ). In such state, the pair of electrons can travel through the material with virtually no electrical resistance R, because R is a consequence and measure of the collisions of conductive electrons with imperfections and disorder in the lattice. Since the energy that the Cooper pair would gain from scattering is less than 2δ that would be needed to break the pair, the material remains in its DC

superconductive state. This changes if the superconductor is exposed to AC currents: in a oscillating field, the Cooper pairs possess a finite inertia that generates a R, unable to then screen the remaining normal conducting electrons. These oscillate with the field, creating a resistance measurable in nΩs, called *Surface Resistance* (R_s). This is defined by two separate contributions, shown in equation 2.15

$$R_s = R_{BCS}(T, H) + R_{Residual}H \tag{2.15}$$

The first term is predicted by the BCS theory, R_{BCS}, and is approximated by equation 2.16

$$R_{BCS} = A\frac{f^2}{T}exp\Big[-\frac{\Delta}{k_BT}\Big] \tag{2.16}$$

where f is the frequency, T the temperature and A a constant that depends on the material. It is worth noticing that if the superconductor is at a temperature lower than T_c, according to 2.16 the contribution to the total surface resistance R_s by R_{BCS} becomes smaller exponentially. R_s reaches then a steady state, due to $R_{Residual}$: this can be due to many factors such as trapped magnetic field, localized heating and moving flux lines.

2.1.5 Type I and II superconductors

Superconducting materials can be divided in two types, I and II. The difference between the two types is dictated by which one between the penetration depth λ_L and the coherence length ε_0 has a bigger contribution [57]. A type I superconductor is characterized by a dominant ε_0 ($\varepsilon_0 > \sqrt{2}\lambda_L$), while if $\varepsilon_0 < \sqrt{2}\lambda_L$ then the superconductor is of type II. When an external magnetic field is applied to a superconductor, its energy is increased because induced screening currents expel the magnetic flux. If the flux in a small volume of radius ε_0 were to become normal conducting, the free energy would decrease in a region at a distance λ_L. On the other hand, the energy in the normal conducting volume would also increase because of the condensation energy of the previously paired Cooper pairs. Type I superconductors have an energetic disadvantage in creating normal conducting pockets, so it doesn't happen. This is not true for Type II superconductors, where the creation of small normal conducting volumes is energetically favoured. These regions are called vortices, and are characterized by a normal conducting core filled with magnetic flux surrounded by current loops, with the magnetic fields dissipating in the surrounding superconducting volume. This magnetic flux is quantized, and corresponds to the value shown in equation 2.17

$$\Phi_0 \approx 2.1 \times 10^{-15} \text{ Wb} \tag{2.17}$$

2.1.6 The Ginzburg Landau parameter

This difference between Type I and Type II superconductors leads to a different behaviour once in a magnetic field: a type I superconductor will remain in a perfect Meissner state up to an applied field H_c, to then become normal conducting. A type II would instead remain in a perfect Meissner state up to a value of magnetic field H_{c1}; then, it would enter a *mixed state*, where the magnetic field is stored in vortices. The material would become normally conducting once reaching a higher magnetic field value, H_{c2} (Figure 2.4). The *Ginzburg - Landau* parameter was introduced to determine superconductor types [58]. This parameter, k, is defined by equation 2.18

$$K = \frac{\lambda_L}{\varepsilon_0} \tag{2.18}$$

and it so applies (equation 2.19 and equation 2.20)

$$K < \frac{1}{\sqrt{2}} \rightarrow TypeI \tag{2.19}$$

$$K > \frac{1}{\sqrt{2}} \rightarrow TypeII \tag{2.20}$$

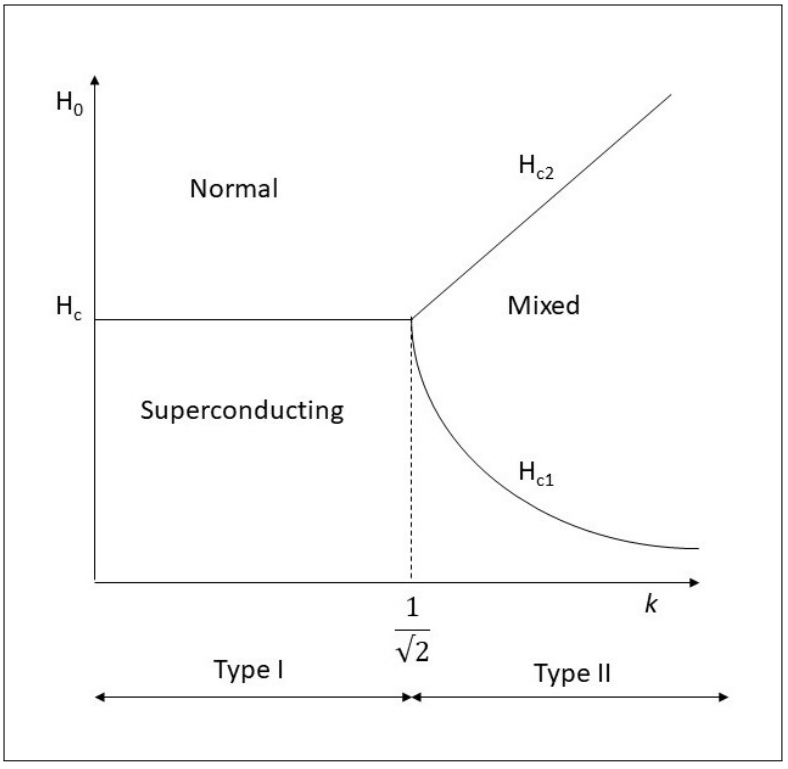

FIGURE 2.4: The response of a superconductor as a function of the applied magnetic field and the Ginzburg-Landau parameter

2.1.7 Critical fields

According to the BCS theory, the electrons in the Cooper pairs exist in a lower energy state than normal conduction, so in a state of higher order[59]. In a type II superconductor the value of H_{c1}, which is the smallest amount of applied magnetic field required for the vortices to be inside the superconductor and not on the surface any more, can be approximated by equation 2.21 [60]:

$$\mu_0 H_{c1} = \frac{\phi_0}{4\pi\lambda^2}(\ln k + 0.5) \tag{2.21}$$

if $k >> 1$. H_{c1} can be numerically calculated for smaller values of k [61].

At this value of field, the flux does not penetrate the superconductor, even if more energetically favourable. This metastable state is granted by an energy barrier, and is maintained until the external field reaches H_{sh}, called the *superheating field* [62]. For perfect (defect free) type II superconductors, this value can be calculated by using equation 2.22 [63]:

$$H_{sh} = H_c\left(\frac{\sqrt{20}}{6} + \frac{0.5548}{\sqrt{k}}\right) \tag{2.22}$$

where H_c is the thermodynamic field calculated in equation 2.23 [64]:

$$H_c = \frac{\phi_0}{2\sqrt{2}\pi\mu_0\lambda\varepsilon} \tag{2.23}$$

Once the field reaches the value of H_{sh}, the magnetic flux will penetrate the superconductor. Figure 2.5 shows the diagram for the superconductive heating field.

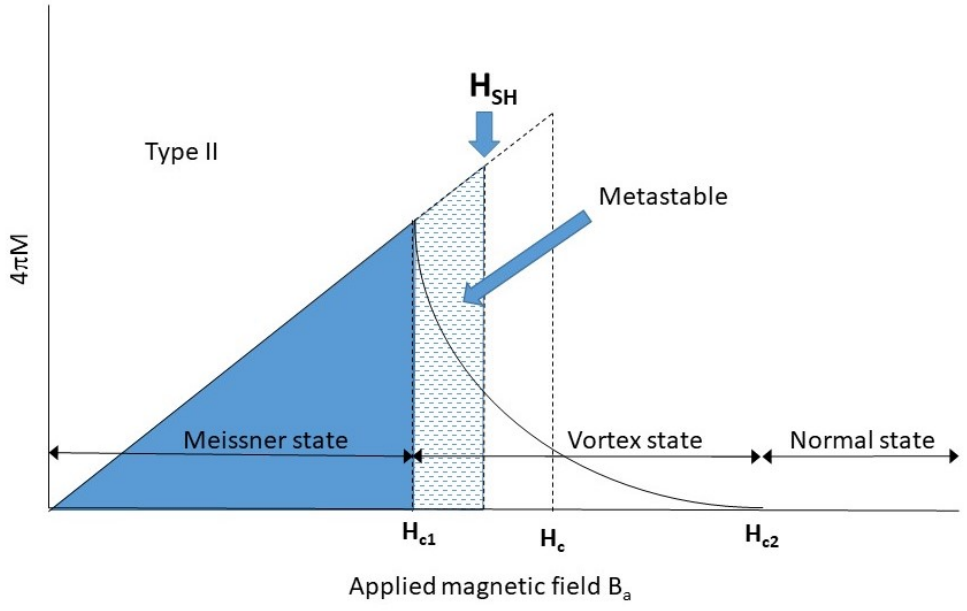

FIGURE 2.5: Superconducting heating field

Flux penetration is extremely detrimental in radio frequency (RF) applications: at 1 GHz, the magnetic field switches one billion times per second, and if the magnetic flux would penetrate the superconductor this would lead to large quantities of resistive heat due to the vortices being "dragged" around the material. The material would then *quench*, meaning that it would stop superconducting. Consequently H_{sh} is the higher field limit for superconductors for RF applications.

In the interval between H_{sh} and H_{c2} the material is still superconductive, but more and more volume becomes normal conducting with the increase of H. Once H_{c2} is reached, all the material is normally conducting. The value of H_{c2} can be calculated using the following 2.24:

$$\mu_0 H_{c2} = \frac{\phi_0}{2\pi\varepsilon^2} \tag{2.24}$$

where ϕ_0 is the flux quantum 2.17.

2.1.8 Contribution of impurities and defects

Any sort of irregularity in a superconductor lattice can hinder its properties. Impurities and defects can create small areas where it is more energetically convenient for the flux to enter the superconductor at lower fields than H_c [65]. Since the vortexes cores have a size of approximately ε_C, this means that any defects of such size can interact with the flux penetration energy. This, as previously mentioned, can be a problem for RF applications, but may be a desired feature for direct current (DC) uses. The impurities can "lock" the vortexes in place around them, preventing them from moving through the superconductor. For an electromagnet, this translates in a higher maximum current at zero resistance, and therefore a stronger magnetic field.

The imperfections also affect ε and λ: materials that are pure will have λ equal to the theoretical λ_L, and ε equal to ε_0. The density of impurities in a "dirty" superconductor can be extrapolated by the mean free path l, and at T = 0 λ and ε can be calculated:

$$\lambda(T=0) = \lambda_L \sqrt{1 + \frac{\varepsilon_0}{l}} \tag{2.25}$$

$$\varepsilon(T=0) = 0.739 \left(\varepsilon_0^{-2} + \frac{0.882}{\varepsilon_0 l} \right)^{-\frac{1}{2}} \tag{2.26}$$

From equation 2.25 and equation 2.25 we can deduce that k will increase with the impurity content, widening the interval between H_{c1} and H_{c2}.

2.2 RF Cavities

2.2.1 What is a cavity?

Cavities are electromagnetic resonators designed to produce large electromagnetic fields if provided with a small RF input. Cavities are characterized by *resonant modes*, and each one possesses its own particular *resonant frequency*. If RF energy is coupled with the cavity to excite a resonant mode, the energy will be stored in the cavity in the form of an electric or magnetic fields. There is one mode that is most commonly used to accelerate particles, the TM_{010} mode [65].

2.2.2 Pillbox cavity

An example commonly used to described the workings of a cavity is the pillbox structure. This is a crude simplified idealization that can be compared to a resonant circuit, as shown in figure 2.6, or LRC where L is the inductor, R the resistor and C the capacitor. If the excited mode is the TM_{010}, Once the RF is applied to it, the cavity undergoes

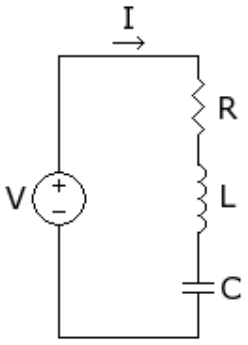

FIGURE 2.6: Schematic of an LRC circuit

charging and discharging cycles, corresponding to different phase advances of the RF cycle φ. Even though these stages form a continuum, for the sake of explaining four stages can be identified:

- $\Phi = 0°$: the charge is concentrated at one end of the cavity while the other end is discharged. There is no magnetic field, and the electric field is oriented along the longitudinal axis of the cavity (z). The energy is stored in the capacitor part of the circuit.
- $\Phi = 90°$: the charge is migrating from the charged end to the other, creating a current along the z axis. This induces a large magnetic field radial to the cavity, which at this stage is at its maximum when the electric field is 0. The energy is stored in the inductor part of the circuit, and some energy is dissipated through the walls of the cavity (the resistor).

- $\Phi = 180°$: the charge now is concentrated at the opposite end of the cavity, the electric field is maximum along z once again, but with opposite direction. There is no magnetic field.
- $\Phi = 270°$: the charge is again travelling from the charged end to the other, but this time in the -z direction. This creates a radial magnetic field of inverse direction to $\Phi = 90°$. There is no electric field.
- $\Phi = 360° = \Phi = 0°$

Cavities then are used to accelerate particles by carefully synchronizing the arriving particles (that travel in the z direction) with the phase of the RF cycle, therefore exposing them to the electric field in the desired direction.

2.2.3 Why the TM_{010} mode?

As previously mentioned, the most common mode chosen to accelerate particles with cavities is the TM_{010} mode. This is because it has a longitudinal electric field in the centre of the cavity which is exploited to accelerate the particles. The equations that describe this are the following (equations 2.28 – 2.32 [66]), where E and H are respectively the electric and magnetic field, and the indexes are the directions in cylindrical coordinates:

$$E_z = E_0 J_0\left(\frac{2.405r}{R}\right)e^{-i\omega t} \tag{2.27}$$

$$H_z = 0 \tag{2.28}$$

$$E_r = 0 \tag{2.29}$$

$$H_r = 0 \tag{2.30}$$

$$E_\varphi = 0 \tag{2.31}$$

$$H_\varphi = -\frac{1}{Z_0}E_0 J_1\left(\frac{2.405r}{R}\right)e^{-i\omega t} \tag{2.32}$$

In most of the directions, the E and H fields are equal to 0, apart from E_z and H_φ, which correspond to the longitudinal direction and the surface of the cavity, as shown in figure 2.7:

2.2.4 Acceleration gradient

When a particle travels through an RF cavity, it is subjected to the varying electric field depending on when it enters. The difference in voltage provides the *acceleration gradient*,

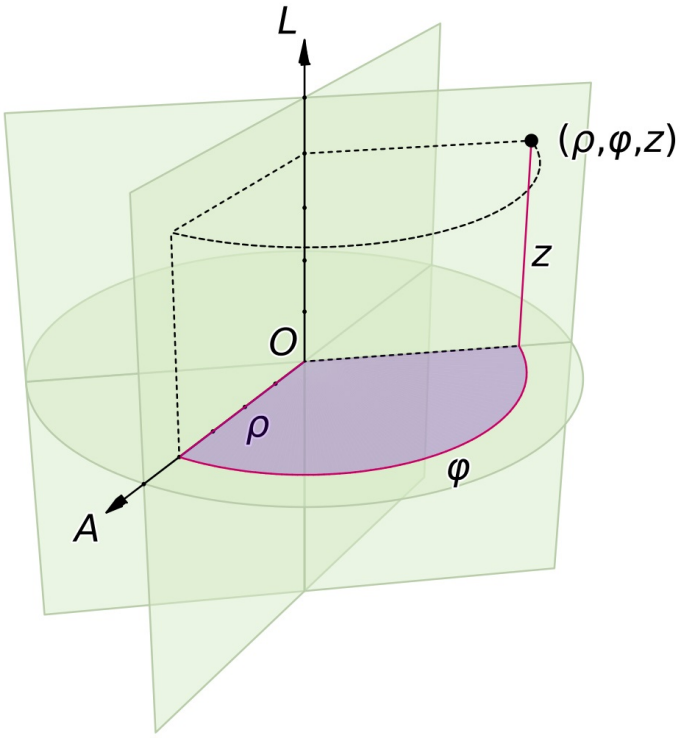

FIGURE 2.7: Cylindrical coordinates system, used to describe the pillbox cavity

which is the amount of acceleration that the particle receives, normally expressed in Megavolts per meter (MV/m). This increase in energy ΔE for the case of an electron can be expressed as equation 2.33 [66]:

$$\Delta E = eV_b \tag{2.33}$$

where V_b comes from equation 2.34

$$V_b = \int_{-\frac{L}{2}}^{\frac{L}{2}} E_z(z,t)e^{i\omega z f c}dz \tag{2.34}$$

Knowing that f is the frequency, c the speed of light and that the particle, to receive the maximum acceleration, it has to traverse the cavity in half the RF period (equation 2.35):

$$L = \frac{c}{2f} \tag{2.35}$$

the equation 2.34 and equation 2.35 can be combined in equation 2.36:

$$V_b = \int_{-\frac{L}{2}}^{\frac{L}{2}} E_z(z,t)e^{i\omega z f c}dz = E_{z0}LT\cos(\omega t) \tag{2.36}$$

Equation 2.36 shows the accelerating voltage, there T is the transit time factor and E_{z0} is the peak electric field along the z axis.

2.2.5 RF and SRF

RF Cavities can be manufactured out of any conductive material, but most commonly they are made out of copper [65]. Copper is the best thermal conductor and this eases the cooling of the cavities, due to the resistance being finite every RF cycle dissipates some energy in form of heat. By contrast, SRF cavities are manufactured out of superconducting materials [67]. The surface resistance in a superconductor is much smaller than in a normal conducting material, leading to less power dissipation and therefore less heat being generated. This allows SRF cavities to be operated in CW – continuous wave – mode, where the cavity is operated for long periods of time and that would be impossible for a normal copper cavity due to overheating and potentially melting of the structure.

2.2.6 Quality Factor of a cavity

Another parameter that distinguishes RF from SRF cavities is the *quality factor* Q_0. This parameter is given by equation 2.37 [66]:

$$Q_0 = \frac{G}{R_s} \tag{2.37}$$

where R_s is the surface resistance, assumed constant over the surface of the cavity, and G is called *geometry factor*, a constant that depends on the geometry of the cavity. The power dissipated by the cavity is given by 2.38:

$$P_{diss} = \frac{V^2}{Q_0 \frac{R_a}{Q_0}} \tag{2.38}$$

where R_a is known as *shunt impedance* and

$$\frac{R_a}{Q_0} \tag{2.39}$$

is a constant and depends on the geometry of the cavity.

SRF cavities require cryogenic temperatures to be operated below their critical temperature, and the heat generated by the dissipated power still has to be removed. Even though removing heat at very low temperatures is not a very efficient process, the power consumed to do so is still 10^2 - 10^3 times smaller [68] than the power required to operate a normal conducting cavity in CW mode.

The quality factor is therefore one of the most important parameters for an SRF cavity, since it contributes greatly in reducing the cooling energy requirements.

The previous discussion indicates that enhanced RF cavity design would be made from a superconducting material combined with a high thermal conductivity. In practice, this combination might be achieved with a copper cavity body, coated with a film of sufficient thickness to remain superconducting at the magnetic fluxes and electric fields in a typical LINAC geometry.

Chapter 3

Chemical vapour deposition process

Chapter 3 introduces the chemical vapour deposition process, with an overview of the mechanisms that regulate the processes. Plasma enhanced chemical vapor deposition (PECVD)is briefly introduced as a technique also used in this work. The books by Pierson "Handbook of Chemical Vapor Deposition: Principles, Technology and Applications" [69] and Jones and Hitchman "Chemical vapour deposition: precursors, processes and applications" [70] were used to source some of the background information presented in this chapter, as they provide a much more in-depth analysis of CVD techniques.

3.1 Introduction

Chemical vapour deposition (CVD) is a versatile technique that allows the deposition of a vast array of materials and coatings. Most metals can be deposited with this technique, and some non metals like silicon and carbon and their compounds, like carbides[71], silicides [72], nitrides[73] and so on. Many applications rely on this technique, from the automotive [74] to the biomedical industry [75], thanks to its versatility. The semiconductor industry has also made use of CVD for a long time, although these days in some cases due to the shrinking of semiconductors Atomic Layer deposition is becoming more prevalent. This chapter will present an overview of what CVD is and how it works.

3.2 What is CVD?

Chemical vapour deposition takes its name from the process, where a material deposits over a hot surface from chemical reactions in the vapour phase. In layman terms, two or more chemicals (called *precursors*) react in a vacuum chamber above a hot substrate, leading to a deposit and some byproducts. It belongs to the family of atomistic deposition techniques, where atoms or molecules or a combination of the two are deposited at the same time. In the same group we can count the Physical Vapour deposition (PVD) processes like evaporation and sputtering.

3.3 Advantages and disadvantages of CVD

The use of CVD offers many advantages:

- coverage: CVD is not a line of site process, where the source of the material to be deposited has to be directly exposed to the substrate to be coated. This is common to PVD processes, such as sputtering. This allows a CVD coating to reach areas that other processes may struggle to coat properly, such as trenches, holes and complex 3d shapes. In the semiconductor industry, this allows the coating of structures with aspect ratio of 10:1 [76, 77].

- growth rate: if the right conditions are met, CVD can produce coatings of μm per minute, leading to faster growth rates than PVD processes [78, 79].

- equipment cost: for the majority of coatings CVD does not require ultra high vacuum (UHV) set ups, which makes it cheaper than PVD processes, where UHV is needed [80, 81].

Of course, CVD is not the perfect technique. Disadvantages are also present, and some of them can be listed:

- reaction chemistry: for CVD to be effective, the deposition needs a chemical path to happen. Therefore certain materials may not be possible to deposit because of the lack of chemical precursors or the lack or a viable chemical reaction [82, 83].

- temperature: most CVD reactions require very high temperatures to proceed in a satisfactory way. These temperatures can be modified by changing the chemistry – introducing more unstable precursors leads normally to a lower deposition temperature – but frequently hundreds of degrees are always needed. Some types of substrate may be then unsuitable for certain deposited materials, if the deposition temperature is too close to their melting temperature [84–86].

- precursor nature: precursors with a high vapour pressure are preferable, since this facilitates their delivery to the deposition area. Often they are also highly reactive chemicals, to reduce the amount of thermal energy required for their interaction and deposition. These chemicals can release toxic gases if placed in contact with moisture or oxygen, making their handling a hazard. Often the byproducts of a CVD reaction are toxic too, and need to be managed and disposed with care [87, 88].

3.4 Theory of CVD

3.4.1 Thermodynamics

Chemical vapour deposition is, in essence, a chemical process, hence governed by *thermodynamics* and *kinetics*. Thermodynamics determine if the reaction is going to happen,

in which direction and at what energy cost, while kinetics determine how the chemicals reach the surface, how they move on it and how fast the reaction will happen. In chemistry, thermodynamics affect the energy transfers between the species involved in the reaction, the products of the reaction and the environment in which the reaction takes place, which in CVD means mostly between the gasses introduced in the vacuum chamber and the substrate. The following discussion uses equations taken from the "Atkins Physical Chemistry" by Atkins et al. [89], where a more thorough description of free energies is presented.

3.4.1.1 ΔG and chemical balance

Before proceeding with a CVD process, it is wise to know if the chemical reaction chosen will proceed the desired way. If the ΔG_r, the free energy change of the reaction / chemical system, is negative then the reaction will favour the products, leading to a successful outcome. This value can be calculated by knowing the free energy of formation ΔG_f, known as *Gibbs free energy*, of the components of the reaction. ΔG_r and ΔG_f are related by the following equation 3.1:

$$\Delta G_r^\circ = \Sigma \Delta G_f^\circ \text{ products} - \Delta G_f^\circ \text{ reactants} \tag{3.1}$$

ΔG_r is not a fixed value, it changes according to a multitude of factors like type of chemicals involved, their molar ratio, the temperature and pressure of the system, as shown in the following equation 3.2:

$$\Delta G_r^\circ = \Delta G_f^\circ + R_g T \ln Q \tag{3.2}$$

where, as seen in equation 3.3:

$$\Delta G_f^\circ = \Sigma z_i^i \Delta G_{f,i}^\circ \tag{3.3}$$

with

- z_i being the stochiometric coefficient of the i species taking part in the reaction. This value is negative for precursors and positive for the products.
- $\Delta G_{f,i}^\circ$ being the free energy of formation of the i species at temperature T and 1 atm.
- R_g = gas constant and T = temperature in kelvin.

Q_r, the reaction quotient at the moment of the reaction, is defined by equation 3.4:

$$Q_r = \Pi_i a_i^{zi} \tag{3.4}$$

where a_i is the *activity* of the species i which is equal to 1 for pure solids and liquids, but equal to p_i for gases, the *partial pressure*, where, as seen in equation 3.5:

$$p_i = x_i P_t \tag{3.5}$$

with x_i being the mole fraction of the species i and P_t being the total pressure of the system. By definition, the change of free energy is to zero when the reaction is in equilibrium, therefore, as seen in equation equation 3.6:

$$\Delta G = -R_g T \ln K \tag{3.6}$$

with K being the equilibrium constant. By calculating the composition and activities (if gases, their partial pressure) equilibrium it is possible to measure the yield of the reaction being studied.

3.4.2 Kinetics

Having described briefly the thermodynamics that affect a CVD process, a list of the main factors that affect the kinetics of the process is presented. A much in depth discussion of the following one may refer to Kee et al [90].

3.4.2.1 Deposition process

The thermodynamic calculations can tell us if the reaction happens once the gases reach the substrate, and with what yield. This though does not mean that the gases will reach the substrate, or how. This can be found out studying the *mass transport*, which dictates the reaction rate and the design of the reactor and its optimization. First of all, a CVD process is particularly challenging to model completely. The reactions are heterogeneous (from gases to solids), and the gases themselves have to travel through pipes, bellows and valves to reach the reaction chamber. If the conditions are right, the deposition may happen before the substrate, causing issues that will be later discussed. Any ever so small change in temperature or pressure in the gas lines may lead to drastic changes in the what happens on the surface. Figure 3.1 shows how the CVD deposition sequence happens.

The process can be roughly summarized in:

1. The gases enter the chamber
2. The gases reach the substrate crossing the boundary layer
3. The deposition happens at the surface of the substrate
4. The byproducts of the reaction leave the region through the boundary layer, pumped / carried away

The sequence determines the rate of the reaction, since the slowest step will slow down all the following steps.

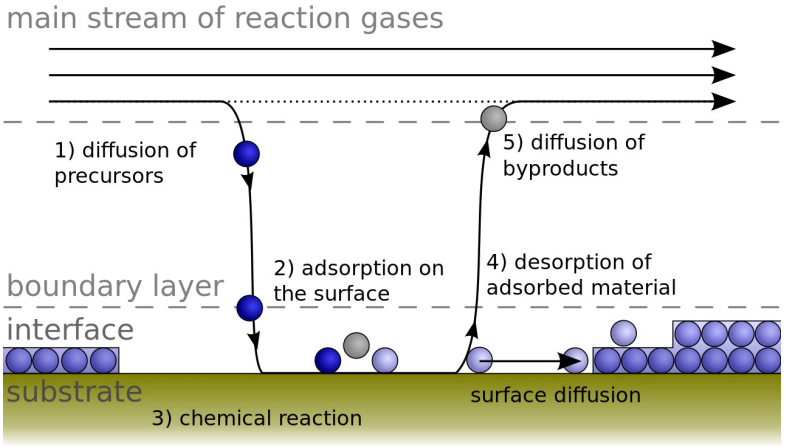

FIGURE 3.1: CVD deposition process sequence, Wikimedia Commons, CC

3.4.2.2 Boundary layer

The *boundary layer* identifies that area of a CVD chamber where the flow speed of the gas varies from 0 to the speed of the bulk of the gas. The concept of boundary layer can be discussed only if the gases in the chamber are in laminar flow, and the Reynolds number is small.

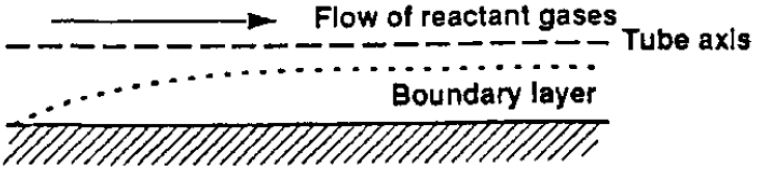

FIGURE 3.2: Boundary layer

As seen in figure 3.2 [69], the boundary layer begins at the gases outlet and increases until the flow becomes stable. The thickness of the boundary layer, Δ_b, can be calculated by using the following equation 3.7:

$$\Delta_b = \sqrt{\frac{x}{R_e}} \tag{3.7}$$

where x is the distance from the inlet in the flow direction, and R_e is the Reynolds number (equation 3.8):

$$R_e = \frac{\rho u x}{\mu} \tag{3.8}$$

where ρ is the density, u is the velocity of the gas, x a characteristic dimension, and μ is the dynamic viscosity.

From equations 3.7 and 3.8 it is possible to see that the thickness of the boundary layer increases with the increasing in distance from the outlet and with the lowering of the gas flow speed.

Gas velocity, walls temperature and precursor availability contribute in the shape of the deposition boundary layer, exhibiting their own boundary layers that, if the conditions are right, may overlap. In reality, even in the most simple geometry (a tube) the kinetic parameters are far from easy to model.

3.4.3 Rate limiting steps

After discussing thermodynamics and kinetics, it is time to have a look at what can limit the deposition rate of a CVD system. Generally the deposition is limited by either the surface reaction kinetics or the mass transport.

3.4.3.1 Surface - Reaction kinetics

If a process is surface-reaction limited, the amount of precursors available on the surface of the substrate is the limiting factor in the deposition. As an example, let us consider a CVD system with low pressure and low temperature.The low pressure leads to a thin boundary layer, and so the precursors have no difficulty reaching the surface of the substrate (figure 3.3 [69]).

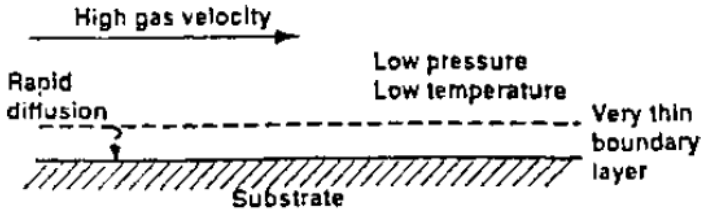

FIGURE 3.3: Surface reaction kinetics example

3.4.3.2 Mass transport

When the process is mass transport limited, the limiting factors are the diffusion rate of the precursors through the boundary layer and the removal of the byproducts after the reaction. As an opposite example, let us consider a CVD reactor at high pressure and high temperature, as shown in figure 3.4 [69].

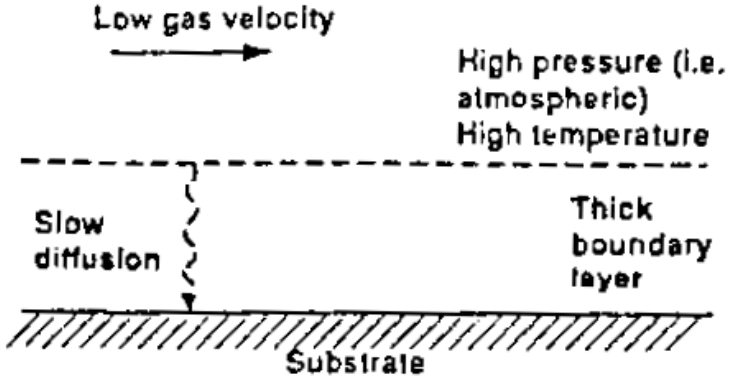

FIGURE 3.4: Mass transport example

The temperature will not limit the reaction speed because once the precursors reach the substrate they would react immediately. The boundary layer thickness though will be high, making it difficult for the precursors to reach the surface of the substrate.

3.4.3.3 Surface reaction kinetics versus Mass transport

To oversimplify, the surface reaction kinetics are the bottle neck at low temperatures while the mass transport is limiting at high temperatures. Knowing this for a chemical system, it is possible to transition from one limiting step to another by acting on the temperature. Figure 3.5 [69] shows the Arrhenius plot of the silicon growth process from different precursors in a hydrogen atmosphere, where the inverse of the deposition temperature is plotted against the growth rate.

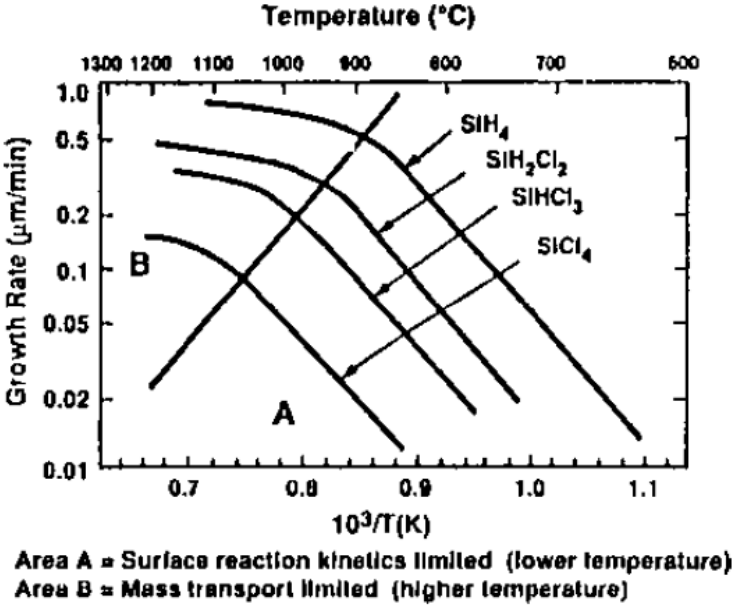

FIGURE 3.5: Example of an Arrhenius plot

The graph is split by a diagonal line: to the right of it, labelled A , the growth is controlled by surface reaction kinetics. To the left, labelled B, the growth is mass transport controlled and is linear with the partial pressure of the precursors. In a real case, the transition from one area to the other is not sharp, so both phenomena can coexist.The presence of a maximum value in the top left of the graph may mean that other reactions (such as precipitation of silicon in the gas phase) may limit the growth rate.

3.4.3.4 Pressure

The pressure at which the process happen can also limit the reactions, since the diffusivity of a gas is inversely proportional to its pressure. At low pressures the mobility of the precursors and the byproducts is high, making mass transport less of a critical factor. If the low pressure is achieved by lowering the partial pressure of one of the precursors, the process will be negatively affected since the partial pressure is directly proportional to the kinetic rate of the reactions. One way instead of lowering the pressure is by reducing the partial pressure of the carrier gas (an inert gas or mixture that facilitates the transport of reactive precursors into the reaction zone / chamber), which does not hinder the reactions.

3.5 Deposition mechanism

3.5.1 Growth of the deposit

The way in which a CVD deposit grows on a surface has been and still is source of discussions, even after many years of studies. Several theories have been put forward: one, based on thermodynamics, suggests that a solid nucleus forms in the supersaturated gas phase because of the difference between its surface free energy and its bulk free energy. Another one is based on atomistic nucleation and marries statistical mechanics with surface chemistry [91]. Regardless of this, there are three factors that control the nature and properties of the deposit:

- Epitaxy or nucleation
- Gas phase precipitation
- Thermal expansion

3.5.1.1 Epitaxy or nucleation

Once the deposition starts, one of the factors that will affect it is the nature of the substrate. *Epitaxy* is one example, where the substrate acts like a template. Epitaxy can be defined as a crystalline growth over a crystalline substrate, with the deposit seeding off the surface of the substrate. There are two types of epitaxy. It is homoepitaxy when the substrate and the deposited film are made of the same material, therefore having the

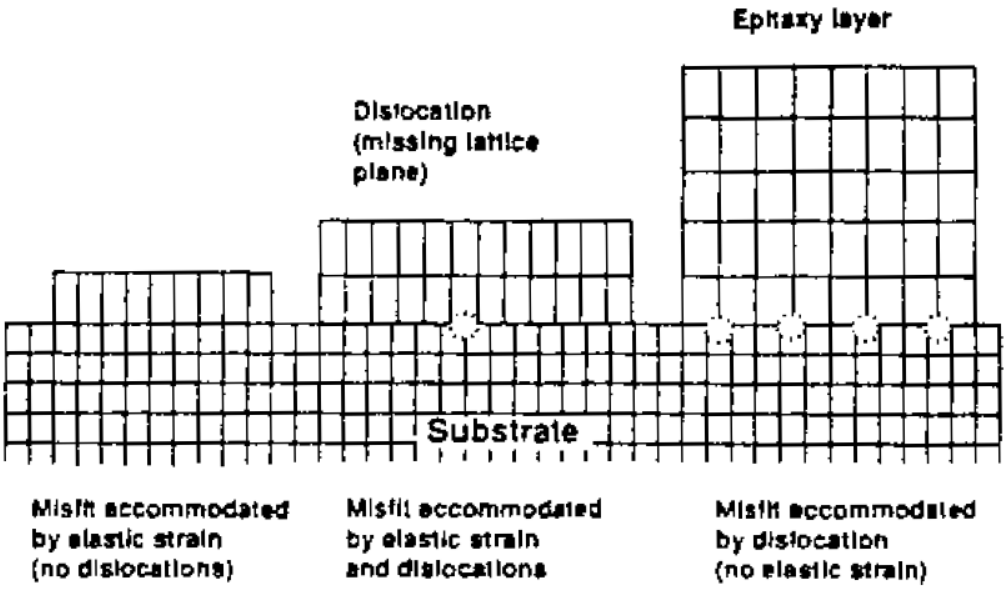

FIGURE 3.6: How epitaxy works on an atomic level

same lattice parameters or crystalline structure. If the deposited material is different from the material of the substrate then it is heteroepitaxy. If the two materials are too different in their crystalline structure, epitaxy can not happen.

Figure 3.6 [69] shows how epitaxial growth can develop on different substrates with slightly different lattice parameters. This limitation can sometimes be worked around by depositing a buffer layer of a material with a lattice parameter between the two desired ones. Epitaxial growth is the ideal mechanism: films deposited this way have generally better properties, or more similar to their respective bulk form. Hence, where possible, this mechanism should pursued. Frequently the mismatch between the substrate and film structure does not facilitate epitaxy. In which case, non-epitaxial (amorphous or polycristalline) coatings may be formed, as discussed in paragraph 3.5.2.1.

3.5.1.2 Gas phase precipitation

CVD reactions may happen in the gas phase, if the conditions allow it (a high concentration of reactants in the gas phase and a temperature high enough to trigger the reactions). This can be a problem since the precipitates can land on the substrate and be incorporate in the growing deposit, leading to unwanted inclusions that microscopically lead to dislocations, uneven chemistry, stresses in the film and macroscopically to poor adhesion and irregular properties. Some deposition processes may take advantage of this phenomenon, especially in the production of powders. In the thin film industry, though, the gas phase precipitation has to be avoided.

3.5.1.3 Thermal expansion

If the substrate and the deposited film have very different coefficients of thermal expansion (CTE), high loads of stress can be introduced in the deposit as the substrate cools down. These stresses can resolve in cracks or complete delamination of the deposit. As for the epitaxial growth, if two materials have too different CTEs, a buffer layer with an intermediate CTE can be deposited to minimize this problem. Otherwise, other types of CVD can be considered such as MOCVD – Metal-organic chemical vapour deposition, where the precursors are metallorganic complexes or molecules – or PECVD – plasma enhanced CVD, where the chemistry is enabled by plasma – where high temperatures are not necessarily required.

3.5.2 Structure of a CVD grown film

The deposition conditions of a CVD process determine the properties and structure of the resulting material.

3.5.2.1 Types of structures

The structure of a CVD deposited film can be classified in three major types, shown in figure 3.7 [92].

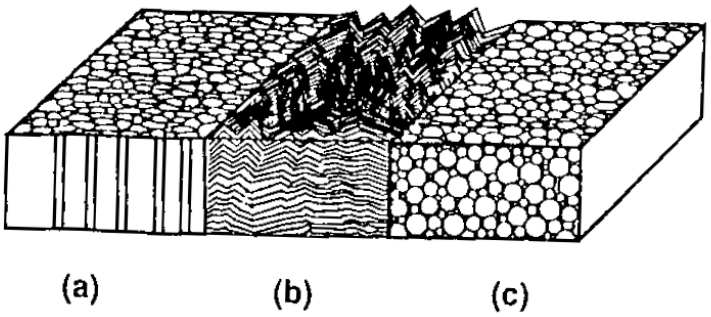

FIGURE 3.7: Types of structures obtained by CVD: *(a)* columnar grains with domed tops, *(b)* faceted columnar grains, *c* equiaxed fine grains

In zone *(a)*, the growth is characterized by columnar grains with domed top. Zone *(b)* is still made by columnar grains but with more faceted and angular shapes. Zone *(c)* is identified by fine grains. This figure is the CVD equivalent to the Movchan - Demshishin diagram for PVD processes. Different materials are more likely to grow in different types of structures. Ceramics, like SiO_2 and Al_2O_3, tend to grow in very small grains (type *c*) or be amorphous. Metals instead tend to crystallize and grow in structures more like *a* or *b*. The size of the grains is normally a function of the deposition temperature. Columnar structures may be unwanted in some applications (like in SRF, for example), since impurities can diffuse very quickly along the grain boundaries through the entirety of the material, compromising its properties.

3.5.3 Structure control

All the factors described up to here can help in controlling the microstructure of the deposited material. The amount of precursors transported affects the saturation of the chamber, which may lead to mass transport phenomena limiting the deposition to gas phase precipitation. The boundary layer can be controlled by the pressure of the reactants, allowing more or less transport of reactants to the surface of the sample. For example at low pressures the boundary layer thickens, limiting the amount of precursors reaching the surface of the substrate, making surface kinetics the dominant factor in the deposition. Depositing at high temperatures tend to produce larger grains arranged in columnar structures: this may also happen though in supersaturation conditions, since the film will grow in the direction of the precursor rich areas (the gas). Depositing at lower temperatures can instead lead to smaller grains or amorphous structures. Pressure, temperature and chemistry of a CVD deposition need to be chosen carefully because of their importance and influence on the final result.

3.6 Plasma enhanced CVD

Plasma enhanced chemical vapour deposition (PECVD) is used when the temperature required to activate a deposition path is too high for a chosen substrate. The energy required for the molecules to react is partially provided by a plasma, reducing the thermal energy budget required and allowing to lower the temperature of the deposition substrate.

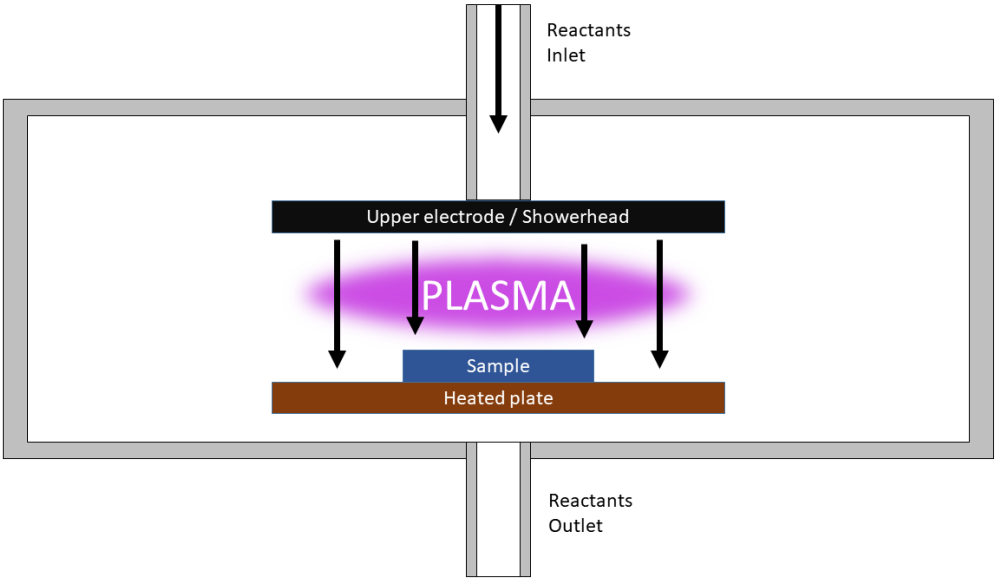

FIGURE 3.8: Schematic of a PECVD reactor

Compared to a traditional CVD reactor, a PECVD reactor, as shown in figure 3.8 requires a way to ignite and sustain a plasma. This is commonly achieved by connecting

the shower head (or a plate close to the gas inlet if there is no shower head) to an RF power supply capable of producing a voltage potential. The sample holder can then be either connected to ground or electrically biased with another power supply. By using this configuration, the substrate is immersed in the glow discharge, which has advantages and disadvantages. As mentioned, by using this technique the deposition temperature can be lowered and more thermally sensitive substrates can be used (as for example polymers [93]). The species created in the plasma, though, can negatively effect the deposited film: the surface of the substrate could be bombarded during the deposition, increasing its roughness or damaging it, and the gases in the plasma could react and create complex products that would then be included in the film, making its composition and properties difficult to control. These factors can be controlled by operating on the process parameters (RF power, pressure, temperature, gas concentration), but not easily.

To limit these drawbacks different chamber reactors and configurations have been developed over the years, but their full discussion would be beyond the scope of this work. One of the approaches, though, that has largely been explored and is worth to mention is the Remote Plasma Enhanced CVD (RPECVD).

3.6.1 Remote Plasma Enhanced CVD (RPECVD)

RPECVD reactors are characterized by having the plasma ignition area segregated from the main reaction area. Some chamber designs include a small quartz bell, placed 10 to 20 cm above the reaction area where the sample is positioned, wrapped in a copper coil that, once connected to the RF source, produces an inductive plasma [94, 95]. Some other chambers have the plasma ignition completely separated from the reaction area, with the reactive species being created remotely and carried to the chamber. Not all the reaction gases are introduced through the plasma: part of them (quite likely the less reactive ones) flow through the plasma discharge, while the more reactive ones are introduced downstream, close to the substrate.

One of the advantages of using this technique is that, by confining the plasma away from the sample, the bombardment of the substrate surface by energetic particles is minimized, which is a very important requirement for the semiconductor industry.

Another advantage is the better temperature control of the reaction zone on the substrate: during a PECVD process the sample is heated by the heater plate and by the energetic particles hitting it [96]. Variations in the absorption of RF power in the gas mixture can cause oscillations in the overall reaction temperature at the surface that could lead to irregular growth. This is not the case with RPECVD, since the plasma is contributing less to the heating of the sample due to its remote position, but still providing the activated species to the reaction area.

Unwanted reaction pathways can also be minimized by using this approach: in traditional PECVD all the precursors are introduced in the same plasma discharge, where the electrons can have energies ranging between 0 to 15 eV [97]. These can hit the

precursor molecules, creating numerous active species, sometimes hundreds [98], all process specific. The use of RPECVD limits this phenomenon: by applying magnetic or electric fields to the area downstream of the plasma discharge it is possible to prevent any charged particle to leave the plasma, leaving only the neutral species to mix with the other precursors and reach the surface of the substrate.

There are, of course, disadvantages, which are shared with the PECVD reactors: more costly, more difficult to operate due to the more parameters involved in carrying a deposition and more difficult to maintain, due to the electronics that a traditional CVD reactor does not need.

Nevertheless PECVD and RPECVD have been used widely and successfully for the last 30 years.

Part II

Instrumental part

Chapter 4

Methods of characterization

In this chapter the instruments and techniques utilised to characterize the deposited samples are described.

4.1 Superconductive properties characterization

Cryogenic temperatures are necessary to investigate the samples superconducting properties. The instruments need to be cooled down to temperatures below the T_c of the samples, which for niobium means below 9.3 kelvin.

4.1.1 Residual resistivity ratio

The residual resistivity ratio (RRR) of a material is the ratio between the resistivity (ρ) at room temperature and at 0 K. This temperature can not be reached, so there are different ways to extrapolate this value. In this work, the measurement for the low temperature is taken at 10 K.

$$RRR = \frac{R_{(300K)}}{R_{10K}} \tag{4.1}$$

The obtained RRR value is used to gauge the quality of the material being studied: for metals, according to Matthiessen rule, the total resistivity ρ is given by:

$$\rho_{tot} = \rho_{res} + \rho_{ph}(T) + \rho_m \tag{4.2}$$

where ρ_{res} is dependant on the defects and impurities of the material, $\rho_{ph}(T)$ is the phonon scattering contribution and it depends on the temperature, and the last ρ_m is the resistivity in a magnetic field. Since at very low temperatures the contribution of $\rho_{ph}(T)$ goes to 0, the importance of ρ_{res} becomes greater. If the material is contaminated by other atomic elements or is disseminated with defects, this value will increase due to the scattering between them and the conductive electrons, reducing the value of the RRR.

4.1.1.1 Four point probe measurement

The RRR can be measured in a variety of ways; in our work the measurement is taken in DC regime by using a four point probe, as shown in figure 4.1.

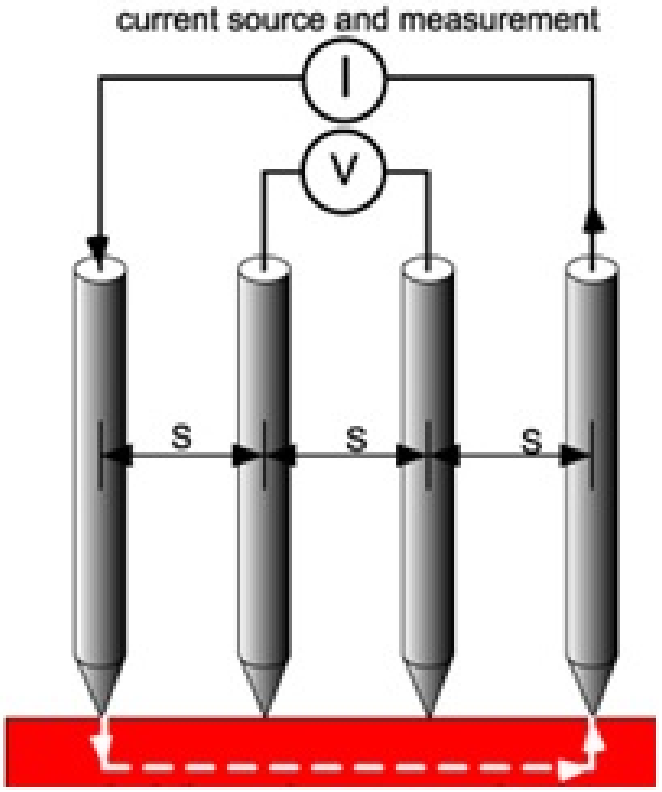

FIGURE 4.1: Four point probe used to measure RRR, Wikimedia Commons, CC

The sample is placed on a sample holder and held in place by four needles, placed equidistant in a line. The outermost needles are connected to a current generator, while the innermost needles are connected to a voltage reader. The current applied is kept constant and the voltage drop between the two inner needles is measured. The sample is then cooled down from room temperature down a temperature as low as achievable, and the changes in voltage are measured. If the sample is superconducting, once past its T_c and in the Meissner state, the current applied will travel between the needles without any resistance, therefore showing a voltage drop of 0.

A little care is needed when using this instrument: the amount of current applied to the sample may influence the measure by locally increasing the temperature via resistive heating. It is best so to minimize the amount of current applied (normally a few milliamperes are sufficient). The thermal state of the sample may also influence the measurement, since if the sample is large some areas may be colder than others. This is avoided by using small samples (10 mm x 5 mm) held in 300 mbar of helium gas, to allow a better thermalization between the sample and the cold head. The system used for this work was developed in house: the four pins were set at 3 mm apart from each other, so the total length from the first to the fourth pin was 9 mm. The

sample holder was made of PCB perforated board, to limit the thermal conductivity between the sample and the sample stick. During the test the sample was surrounded by 30 mbar of 99.999% purity helium gas, provided by BOC®. The cryostat was cooled by a Sumitomo® F-70 compressor and cryohead set, operating at 20 bar of He pressure. The current was produced by a Keithley® 6220 Precision Current Source and set at 10 mA for the experiments conducted; the voltage drop was measured with an HP® 34401A multimeter. Edge effects were taken into consideration but no mention of them was found after a literature survey [99, 100], therefore they were no further explored in this study.

4.1.2 Superconducting quantum interference device magnetometry

SQUID stands for Superconducting quantum interference device, and it describes an instrument used to measure magnetic fields, by relying on the superconductive Josephson effect, as shown in figure 4.2.

This effect can be seen when an electrical insulating material is sandwiched between two superconductor materials: in this configuration (and below the T_c of the superconductors) the Cooper pairs can tunnel through the insulator, creating a so called *supercurrent*.

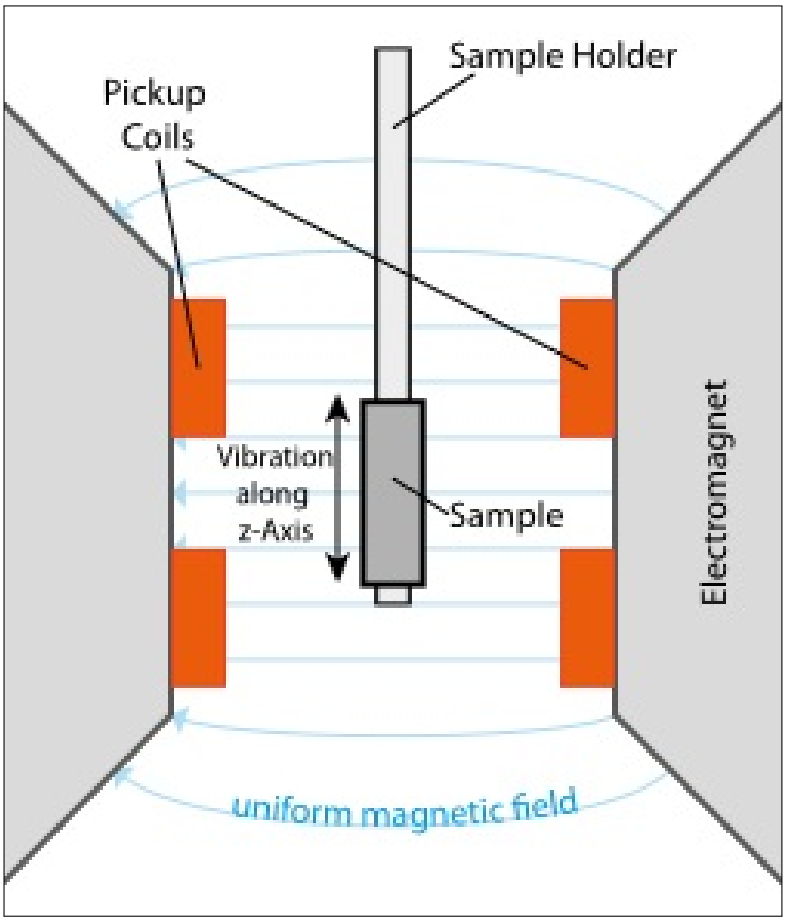

FIGURE 4.2: SQUID magnetometer sampling area schematic, Wikimedia Commons, CC

The samples are inserted into the instrument and an external magnetic field is applied. If the sample is superconductive the expulsion of external magnetic field creates a surface current (Meissner current), which in turn create an opposing magnetic field. As the sample is moved up and down through the instrument, this resistance is measured. As the external magnetic field is increased, it is so possible to measure the sample:

- H_{c1}: when the field starts entering the sample due to the surface of the sample being saturated with supercurrent.
- H_{c2}: when the field saturates the sample, which stops being superconductive.

The value of H_{c1} is considered critical for particle accelerator applications, since it's the value at which the magnetic field enters the superconductor. This causes localised heating and subsequent thermal breakdowns, effectively setting a limit for the maximum accelerating gradient achievable. A value of H_{c1} as close as possible to the bulk material is therefore highly desirable. A Quantum Design® MPMS XL-7 SQUID was used for this work: the samples were inserted in a plastic drink straw, to keep them from moving once inside the instrument, and introduced in the loading chamber. The measurements were conducted at 4.2 °K under varying magnetic field.

4.1.2.1 Sample preparation for RRR and SQUID studies

The aim of this work is to deposit niobium based materials on copper substrates. Measuring the RRR of these samples is not immediate, because the contribution of the copper substrate is too massive to allow a measurement. A way to isolate the substrate from the film has been developed: the samples are covered with a film of Kapton tape, and then immersed in a solution 50:50 of de-ionized water and nitric acid.

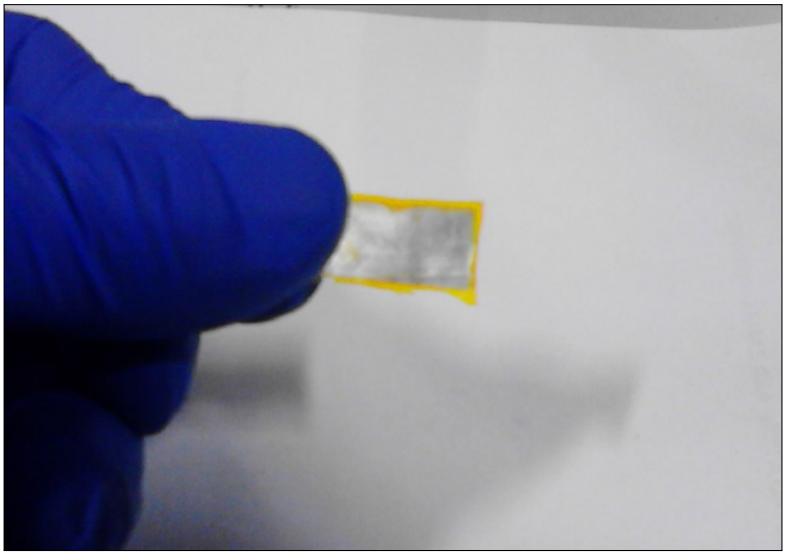

FIGURE 4.3: Thin film on kapton after the removal from substrate

This allows the complete dissolution of the copper substrate, as shown in figure 4.3, allowing the measurement of the RRR of the deposited film.

4.1.3 Local magnetometry measurement

Classical magnetometry (SQUID magnetometry) where the sample is immersed inside a uniform field is difficult to interpret for thin films. Indeed if the magnetic barycentre of the sample was perfectly centred on the detection coils symmetry axis, there would be no SQUID response [101, 102]. Most of the time when a parallel signal is observed it means the alignment is not perfect, and that the sample undergoes some perpendicular component. Since the demagnetization factor of thin films is usually huge it induce a strong transverse moment that tend to dominate the signal (if the system has two set of perpendicular detector coils crosstalk can be seen [103]). To overcome the issue the team from CEA Saclay, Paris, has developed a specific local magnetometer for the measurement of H_{c1} based on Alternate Current (AC) third harmonic analysis as described in [104, 105]. This technique is based on the hysteretic behavior of the magnetization in the critical state, that gives rise to non zero odd harmonics in the spectrum of the electrodynamic response of superconductors exposed to an ac magnetic field. The specificity of the Saclay set-up is that it is designed to reach the RF cavities operating condition, namely between 2 and 4.5 K, and a field between 150 and 180 mT, which requires a specific thermal design [106].

4.1.3.1 Principle of the measurement

A small coil is placed a fixed distance from the sample. The field attenuates quickly away from the coil so if the sample is large enough it can be approximated to an infinite plane and there is no edge or demagnetization effects anymore. The experiment is placed in a vacuum enclosure to prevent thermal contact between the sample and the coil (see figure 4.4).

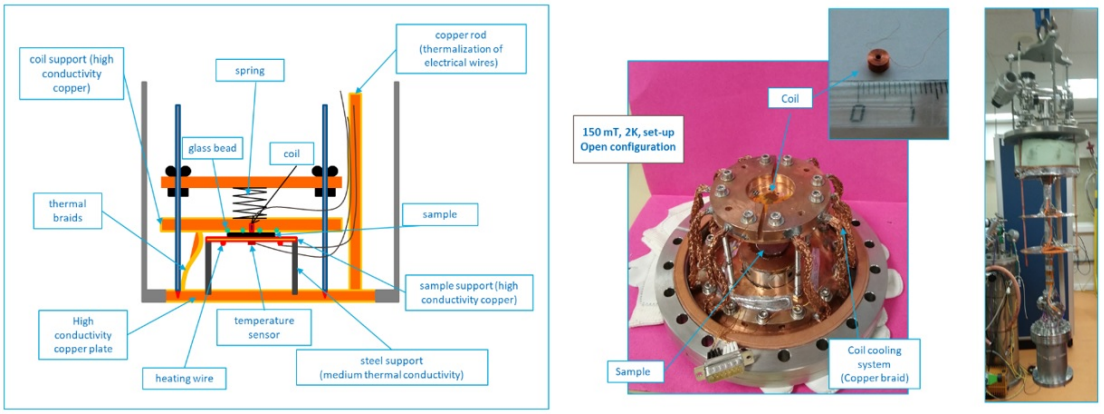

FIGURE 4.4: Schematic description and picture of the local magnetometry set-up at CEA, courtesy of Dr. Claire Antoine, CEA-Saclay

The experiment involves the cooling of the sample into its Meissner State without any applied fields. If an AC reference current is sent in the coil, it results in a field H cosωt on the sample. Screening supercurrent will generate an exact opposite moment, so that the sample behaves like a perfect magnetic mirror and the current in the coil keeps unaltered (linear behaviour). If the temperature is slowly raised, the sample will eventually cross the transition between Meissner state and mixed state. If the frequency is low enough ($\sim$ kHz), those vortices will be readily trapped on the materials defects and will produce a return force on the electron circulating in the coil, producing non-linearity in the current/tension. If one monitors the signal of the third harmonic, a Bell shaped signal appears upon the transition and disappears once the vortices become mobile in the SC (at so-called irreversibility or melting field). This experiment provide H_{c1} (or H_p in presence of surface defects) as well as some information on the pinning behaviour.

4.1.3.2 Other non destructive SRF measurement techniques

Measuring the SRF properties of deposited thin film is not trivial: most R&D depositions are performed on flat samples, since it simplifies the deposition system geometries. This has a limiting effect on the performance of the film, since a flat surface is not designed and engineered to accept RF fields with a high quality factor, and the results may be worse than what the film would achieve if deposited on an RF resonant structure. One of the alternatives is to deposit directly on cavity (or similar) shaped substrates, to then test the assembly in a standard cavity testing setup, but this is extremely costly.

To resolve this issue, a few systems have been developed around the world to allow the testing of flat samples (to the best knowledge of the author). Each one of them has advantages and disadvantages, showing that the perfect standardized system has not been developed yet.

One system has been designed and built at Cornell University, USA, in the CLASSE research group [107, 108] in 2013: the assembly is made of half a Nb cavity that mates with a specially designed holder that can accept round flat samples. The pro is that this system allows to gather data as close as possible to the real final application (i.e. a real cavity in an RF field at 1.8 K), but the con is that it requires samples 10 cm in diameter, which may not be easy to satisfy. A similar system exists at SLAC [109], which works on the same functioning principles of the Cornell instrument, but at a much higher frequency (11 GHz), and with much smaller samples (round samples 5 cm in diameter).

CERN built in 1997 a quadrupole resonator instrument [110]: this system allows the study of flat round samples of 7.5 cm in diameter and it exposes the film to both the magnetic and the electric field that a cavity surface would see in real operating condition. The limitations though are that the field applied can not reach above 70 mT and that, due to its functioning principle, it does not work well with substrates with high thermal conductivity, like copper.

An upgraded version of this setup exists at HZB [111], in Germany, where the instrument based on the CERN old design is capable of reaching fields of 120 mT at 1.3 GHz, which is the frequency that most SRF accelerators use. Even if this is remarkably better than the CERN one, it has a major drawback, since the samples have to be welded on a section of the chamber. This can be avoided by removing part of the instrument and coating it, but it increases the risk of contamination of the instrument itself and prevents the use of it with some deposition techniques like CVD.

Jefferson Lab in Virginia hosts another instrument called SIC [112], where round samples of 5 cm in diameter can be studied at very high frequencies (7.5 GHz). This does not simulate a real cavity, since the frequency is too high, and it is used mostly to measure the value of R_s for a given thin film. Even though it does not replicate a real application, it can accept the smallest sample size together with the SLAC system.

Each one of these system is a one of a kind, meaning that they all have very long sample backlogs and accessing them can be very difficult, since the entire SRF thin film community relies on their services. It is likely that in the coming years some more systems will be built improving on the existing ones, making the testing of SRF thin films easier and cheaper.

4.2 Morphological characterization

The microstructure and morphology of the samples has been studied, since different deposition conditions lead to different results.

4.2.1 Scanning electron microscopy

The scanning electron microscope (SEM) is a very versatile instrument that allows the imaging of the surface of a sample, with a resolution down to a few hundreds of nanometers. Electrons are generated at the top of a columnar vacuum chamber, and then accelerated, focussed and collimated through a series of magnets and projected onto the sample to be studied. A schematic of an SEM is shown in Figure 4.5

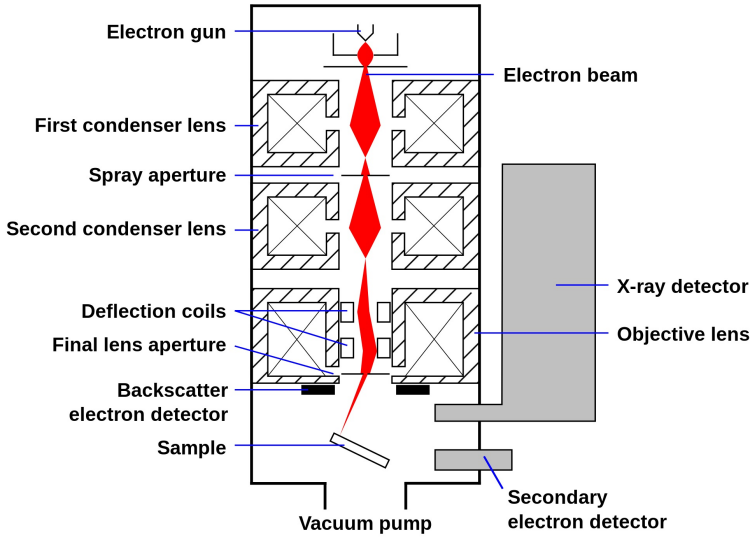

FIGURE 4.5: Schematic of a scanning electron microscope, Wikimedia Commons, CC

The collision between the electron beam and the sample generates a series of signals [113] (Figure 4.7):

- Secondary electrons: the electrons are emitted very close to the surface of the samples, leading to a very high resolution.
- Backscattered electrons: produced by the elastic interaction between the beam and the deeper atoms of the sample, they produce a lower resolution image.
- Characteristic X-rays: X-rays are produced by the removal of an inner orbital electron and the release of energy by another higher energy electron filling the gap. These depend on the atomic elements present in the sample, and used together with the backscattered electrons they can be used to identify the chemical composition of a sample.

Figure 4.6 shows that interaction between the beam and the sample does not strictly stop at the surface, but samples a small volume under the interaction point. The size

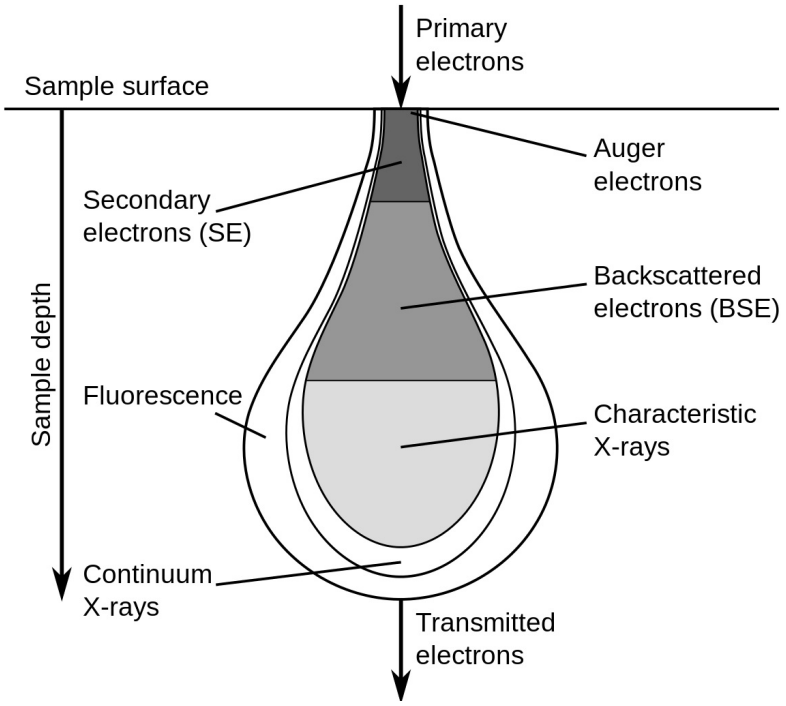

FIGURE 4.6: Volume of interaction under the SEM electron beam, Wikimedia Commons, CC

of this volume depends on the energy of the incident beam, which is determined by the acceleration voltage. The most common range of energies that an SEM beam can have is between 5 KeV and 20 KeV, with an increase in sampling volume with increasing energy.

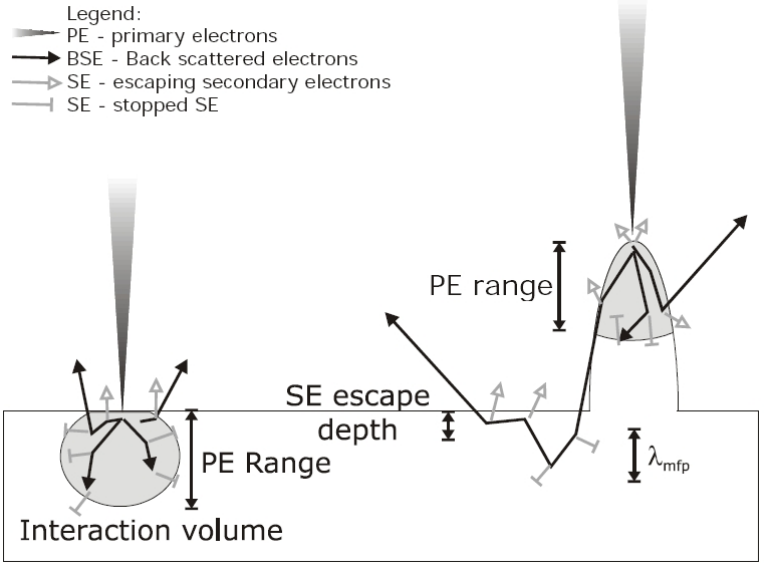

FIGURE 4.7: Types of beam - sample interactions, Wikimedia Commons, CC

Probing a large volume using a high energy beam produces strong signals and a clear image, but as shown in figure 4.7 the topography of the sample may produce artifacts,

as secondary electrons may be emitted from areas far from the investigation point due to chain collisions in the material. Probing a small volume limits this phenomenon, though greatly reducing the amount of signal produced and reducing the resolution of the image.

The sample preparation for SEM analysis is easy and straightforward, since the only requirement is for the sample to be electrically conductive. If not, the electron beam would charge the sample electrostatically and as a results saturate the detectors, rendering the imaging very difficult. This is commonly achieve by sputtering a thin layer of gold on the non conductive sample, then attached on a carbon sticky tape. In this work, all the samples were metallic therefore conductive, so no particular preparation technique was undertaken before the analyses. The SEM instrument used was a JEOL® 6610: the working height of the samples was adjusted between 10 mm and 6 mm, according to the desired image resolution. The magnification was adjusted as per need, as the energy of the incident beam (set at values between 20 KeV and 5 KeV).

4.2.2 EDX

EDAX stands for Energy-dispersive X-ray spectroscopy, an investigation technique that takes advantage of the X-rays generated by the SEM electron beam - sample interactions, as shown in figure 4.8. The X-rays are then collected by a detector and analysed via software.

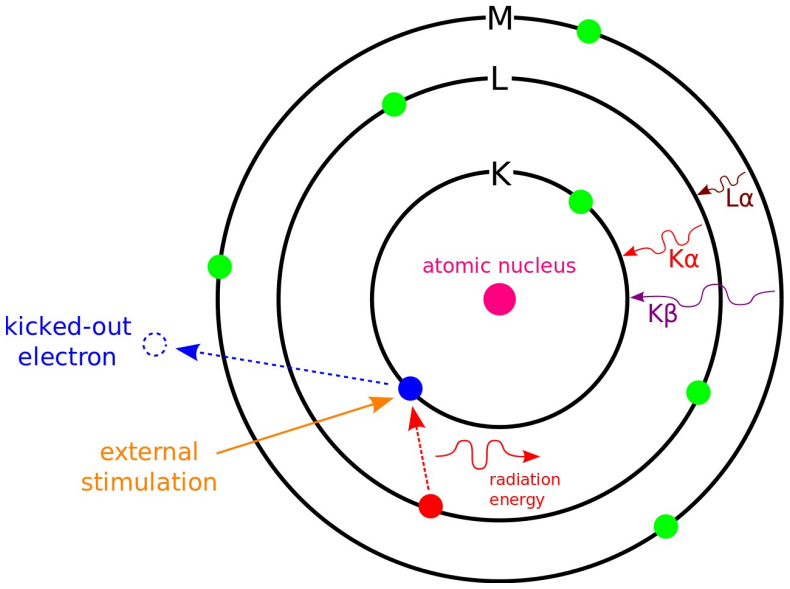

FIGURE 4.8: Principle of EDAX, Wikimedia Commons, CC

The energy of the X-rays generated depends on the atomic composition of the sample; this allow the compositional and quantitative analysis of a sample chemical composition. Many elements, though, may have overlapping energies – or very close – especially true for the lower atomic number Z atoms: this means that corrective factors are applied to the data, and that the errors in the quantitative estimates may increase with the

decreasing of the atomic mass. Qualitative analysis can be done by comparing the sample spectrum with a vast database since each element has a very specific X-ray emission pattern. Quantitative analysis relies on measuring the intensity of the X-rays emitted from the sample for a given element and compare them with the emission of a calibrated standard of known concentration. The results obtained are accurate to ± 2%, therefore for small concentrations they may not be sufficient to be used as single method of investigation. The detector used for this work was an Oxford Instruments® EDS (different acronym for EDAX meaning Energy Dispersion Spectroscopy), working in conjunction with the SEM JEOL® 6610. The system was calibrated against one standard element, used by the software to estimate the signals for the other elements. This is good enough to achieve a ±2 % accuracy, but no more since that would require to calibrate the system against standards of the materials being studied, which for the scope of this work was not necessary. To perform the analyses the samples were set at a working height of 8 mm and scanned for 180 seconds, enough time to reach a sufficient number of X-ray counts.

4.2.3 Focused ion beam

The Focused ion beam (FIB) is an instrument that adds to the SEM imaging capabilities, by allowing the removal or deposition of materials via ion sputtering, as shown in figure 4.9.

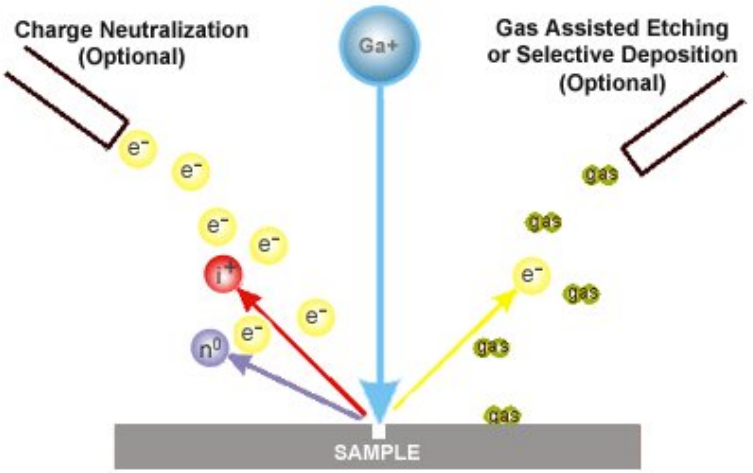

FIGURE 4.9: Principle of FIB, Wikimedia Commons, CC

A similar columnar vacuum chamber is used, where an ion source (gallium being very common) produces the ions, that then are accelerated to energies between 1 KeV and 50 KeV. Using the FIB for imaging is not suggested, because the ions hit the sample with more energy, damaging the area as it is analysed. This technique is instead used for depositing and removing material and for preparing samples for transmission electron microscopy (TEM). The ion beam bombards an area of the sample, creating a "trench":

by effectively slicing the sample its structure can be studied, which can be very useful in the study of thin films like in this work. It is not uncommon for FIB instruments to be fitted also with a SEM column and an EDAX instrument: this allows the positioning and focusing on the target area non destructively by using the SEM, and the analysis of the chemical composition of a section by using the EDAX. The disadvantage of using the FIB to study at a sample section is that the ion beam bombardment can not prevent the redeposition of material that has been ejected. This may lead to inaccurate quantitative readings by the EDAX, if the story of the sample is unknown. The instrument used to perform the FIB trenching was an FEI Helios NanoLab Dual beam®, fitted with an EDAX® EDS system. As with the SEM, the working height, energy of the beam and magnification were adjusted as per required by the sample. The FIB trenching was performed with a Ga ion beam with a range of energies between 1 pA and 65 nA.

4.2.4 Transmission electron microscopy

The Transmission electron microscope (TEM) is another microscopy technique that utilises electrons, but instead of studying the interactions between the beam and the surface of the sample, a TEM beam travels through the sample producing an image on a fluorescent screen placed after the beam - sample interaction. Figure 4.10 shows the main parts of a TEM.

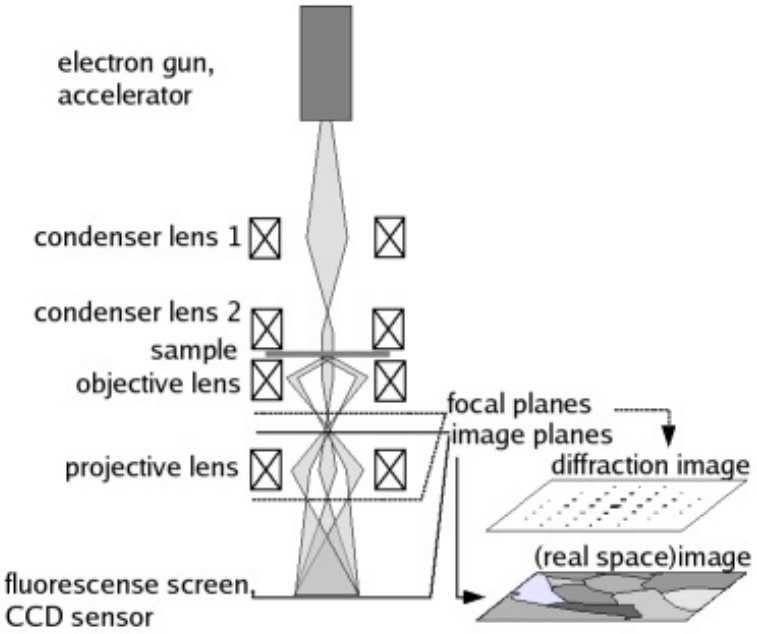

FIGURE 4.10: Transmission electron microscope scheme, Wikimedia Commons, CC

TEMs are capable of higher resolutions than any other microscopy instrument, allowing the resolution of atomic size features. This makes a TEM a very powerful instrument to perform studies on thin films and their substrates. A TEM is also used to learn useful information on the crystalline structure of the analysed samples, via the diffraction

image plane. The main issue with TEMs though is the sample preparation. The electron beam has to transmit through the sample to produce an image, which means that the sample has to be *electron transparent*: this is achieved by thinning the sample to a thickness of about 50 nanometers. The FIB is a useful tool to perform this preparation, since it can be used to trench both sides of a flat sample very precisely. The thickness of the sample directly affects the image contrast: a thick sample will not be electron transparent, and the image will look dark and difficult to resolve. An unevenly prepare sample may also affect the image: since the contrast is related to the atomic mass of the material crossed by the beam (heavier atoms will interact with the beam more, reducing the contrast in the image), thicker areas may look darker not because of their different chemical make up, but because the beam had to travel through a longer path. This may lead to misinterpretation of the resulting image. The instrument used for this work was a JEOL® 2100FCs S/TEM, probe aberration corrected fitted with a windowless EDAX® EDS. The calibration was performed before each sample investigation following an instrument specific procedure, that consists in the alignment of the electron beam by changing the settings of the electromagnetic lenses controlling it.

4.2.5 X-ray diffraction

X-ray diffraction (XRD) is a technique where the crystalline structure of a material is studied. X-rays are produced from a source and directed towards the sample. The interaction between the atoms and the incident beam at different angles causes the X-rays to diffract constructively at specific directions. Combining the intensity of the diffracted beam with the sample angle allows the determination of the crystalline structure.

4.2.5.1 Bragg's Law

The outcome of the interaction between a lattice of atoms of a materials and the incident X-ray beams is determined by *Bragg's law*:

$$2d \sin\theta = n\lambda \tag{4.3}$$

where d is the spacing between the atomic planes, θ is the incident angle, n is an integer and λ the wavelength of the incident beam. There is constructive interference when Bragg's law is satisfied; if not, the X-rays interfere with each other destructively, resulting in no signal at the detector.

This technique allows also to investigate the residual stress or strain in a material, since if the spacing between the planes changes, the diffraction angle changes accordingly, as shown in equation 4.4.

$$\theta = \arcsin\frac{n\lambda}{2d} \tag{4.4}$$

Figure 4.11 shows how Bragg's law applies to XRD.

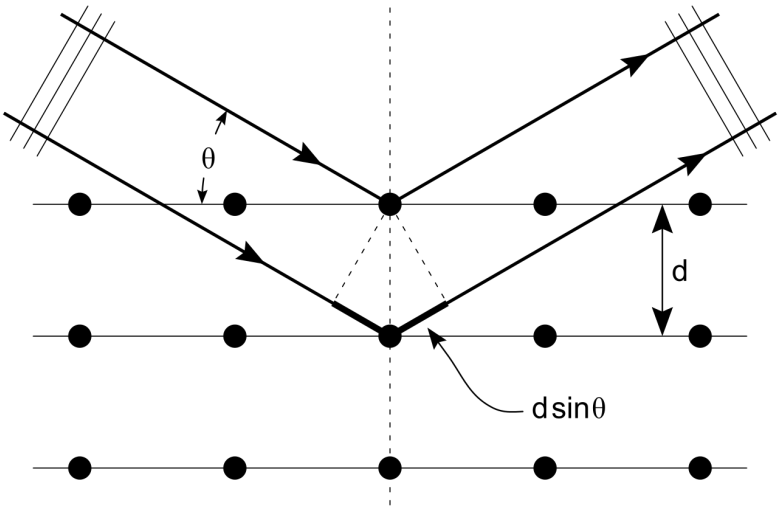

FIGURE 4.11: How Bragg's law applies to XRD, Wikimedia Commons, CC

By comparing the reference values of d with the sample measurements, it is possible to evaluate the amount of strain that the film is subjected to, by using equation 4.5.

$$\epsilon = \frac{d - d_0}{d} \tag{4.5}$$

For this work the instrument used was a Rigaku® Smartlab equipped with a Cu lamp (wavelength of 1.5406 $\mathring{A}$). The instrument settings were kept as machine default, with the exception of the sampling angle which was set at 0.01 degrees. The calibration of the height of the samples was automatically performed by the controlling software, adjusting the height of the sample to optimize the signal / noise ratio. According to the manual the estimated error related to the positioning of the sample amounts to a peak shift of ± 0.02 2θ, which produces the strain errors shown in table 4.1.

Plane	**Peak Shift (°)**	**d Spacing (Å)**	**Strain (%)**
{110}	± 0.02	± 0.0005	± 0.02
{200}	± 0.02	± 0.0002	± 0.01
{211}	± 0.02	± 0.0001	± 0.01

TABLE 4.1: Error values for peak position, d spacing and strain

4.2.6 X-ray photoelectron spectroscopy

X-ray photoelectron spectroscopy (XPS) is a technique used to investigate the very first few nm of a material surface. This is done by shining a monochromatic X-ray beam on the sample, which excites the material and cause the emission of electrons that are collected in an electron energy analyser and an electron detector [114], as shown in figure 4.12.

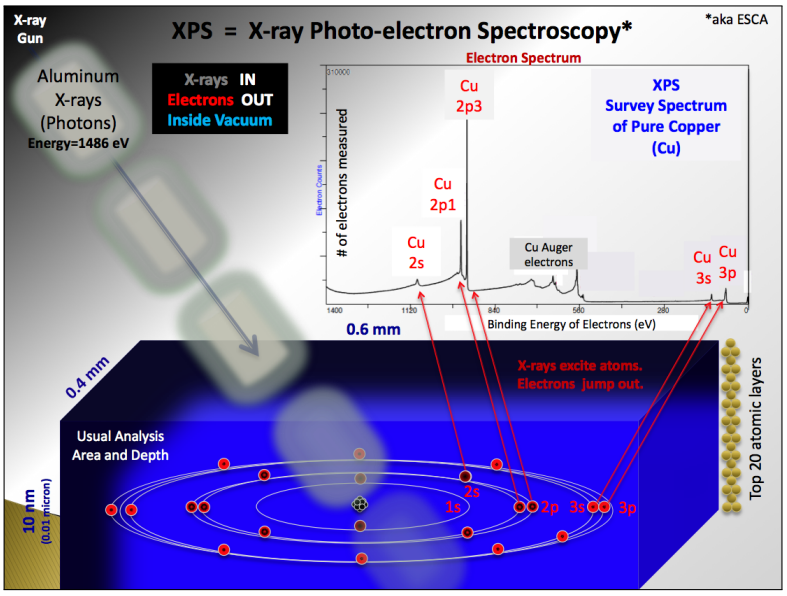

FIGURE 4.12: Principle of XPS, Wikimedia Commons, CC

The instrumentation measures the kinetic energy (eV) and the number of electrons leaving the sample surface (counts). Each element has a very specific emission profile, corresponding to the binding energies of the electrons to their atoms. By knowing the incident energy (most instruments use the 1486.6 eV Al Kα radiation) the binding energy can be calculated using the Rutherford equation (equation 4.6):

$$E_{binding} = E_{photon} - (E_{kinetic} + \phi) \tag{4.6}$$

where $E_{binding}$ is the binding energy, E_{photon} is the energy of the incident X-ray, $E_{kinetic}$ the measured energy of the emitted electron and ϕ the work function of the detector (all in eV). The resulting spectrum shows peaks corresponding to the binding energies of the electrons from different orbitals being emitted by atoms in the first $\approx$ 10 nm of the sample being studied. One of the advantages of this technique is its accuracy in resolving the elemental concentration of a material, allowing measurements of $\approx 0.1\%$ of its atomic composition. Moreover, due to the fact that electron energies change when atoms are bonded, it is possible to understand the chemical bonds of the surface of the sample. For this work the instrument used was a VG Scientific Escalab mk II XPS system using an Al X-ray anode.

4.2.7 Ellipsometry

Ellipsometry is an optical technique used to measure the properties of thin films[115]. By shining a light elliptically polarized on the sample under study the interactions between the film and the light will influence the amplitude (amplitude ratio Φ_a) and the phase (phase difference Δ_{ph}) of the beam, as shown in figure 4.13.

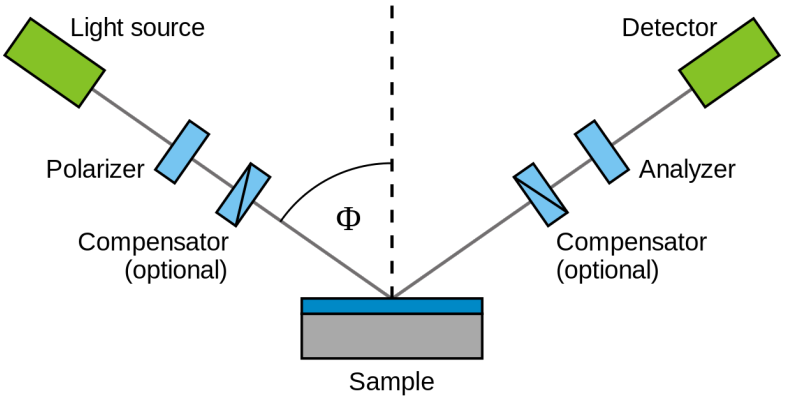

FIGURE 4.13: Principle of Ellipsometry, Wikimedia Commons, CC

These parameters will change even if the film thickness is smaller than one nanometre, making this technique very sensitive and useful for determining without destroying the sample its thickness. The obtained values of Φ_a and Δ_{ph} needs to be compared to a model, based either known film parameters or as close as possible. This implies that, since many factors can influence the material and its interaction with the light, care needs to be taken when choosing the right model for the interpretation of the results to avoid any mistakes. For this work a Rudolph Research Auto EL single wavelength (632.8 nm) ellipsometer was used.

Part III

Experimental part

Chapter 5

CVD, PECVD and ALD precursors

Chapter 5 introduces the chemical precursors commonly used to obtained Nb based materials through CVD - PECVD and ALD. An overlook on the chemical reactions is presented, with the compounds and processes chosen for this work explored in more detail.

5.1 What is a precursor?

A chemical compound that participates in a chemical reaction to produce another compound is called a *precursor*. Metal-containing precursors for chemical depositions can be found or synthesized in various state,from gaseous to relatively in-volatile solids. A suitable precursor should possess the following properties:

- *transportability*: the precursor should be capable of reaching the deposition chamber with relative ease.
- *controllability*: the quantity of volatile precursor should be directly controllable through variations of temperature or pressure.
- *stability*: the precursor should be capable of remaining stable at the temperatures required for the transport.
- *reactivity*: the precursor should, if in the right thermochemical conditions, promptly react in the deposition chamber leading to the desired deposition.

The selection of a precursor is led by the satisfaction of all these parameters: even if theoretically possible for all the elements of the periodic table, does not always translate into practically useful chemicals; the selection has to take in account not only the desired deposition but also parameters like substrates, deposition temperature, chamber pressure and material. Figure 5.1 shows the periodic table with in green the elements for which precursors have been synthesized highlighted in green.

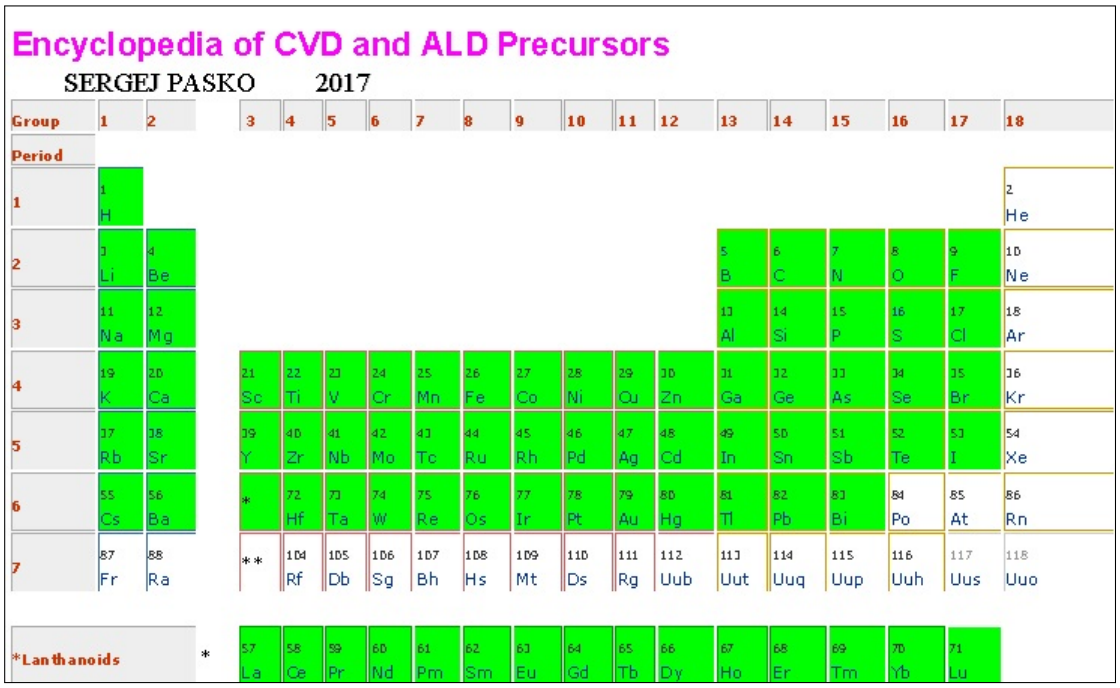

FIGURE 5.1: Periodic Table of Elements - For green marked CVD precursors available

Precursors can be generically grouped in two macro categories: *inorganic precursors* and *metallorganic precursors*. Although an universally accepted definition does not exist, inorganic precursors are characterized by the lack of carbon in their structure. Metallorganic precursors, on the other hand, are identified by the presence of carbon-hydrogen bonds. Table 5.1 shows some of the differences between the two macro groups, which can guide the precursor selection process.

Properties	**Inorganic precursors**	**(Metal) organic precursors**
Reactivity	Good	Very good
Volatility	Poor to Very good	Very good
Thermal Stability	Very good	Poor to good
Reaction temperature	Medium to High	Low
Cost	Low to High	High
Shelf life	Very long	Medium

TABLE 5.1: Differences between inorganic and organic precursors

5.2 Niobium inorganic precursors

The chemistry of niobium has been studied for a long time. It is known to form very stable compounds with nonmetals, which can then be used as precursors in CVD. Out of all these, the more commonly used compounds are the ones reported in table 5.2.

	Nb (V) Chloride	**Nb (V) Bromide**	**Nb (V) Iodide**
Formula	$NbCl_5$	$NbBr_5$	NbI_5
Molar Mass (g/mol)	270	492	737
Appearance	Yellow solid	Dark Red solid	Yellow solid
Density (g/cm^3)	2.7	4.4	5.3
Melting point (°C)	204	254	543
Boiling point (°C)	248	364	543

TABLE 5.2: Properties of most common Nb-based halogen compounds

From the table it can be noted that there's an increase in density, melting point and boiling point values with the increasing of the halogen atom molecular weight.

The balanced reaction for depositing niobium from these chemicals would be equation 5.1:

$$2Nb(halogen)_5 + 5H_2 \longrightarrow 2Nb + 10H(halogen) \tag{5.1}$$

where *halogen* is either chlorine, bromine or iodine. This mechanism implies the full reduction of the Nb oxidation state from +5 to 0. These compounds are all thermally stable, sufficiently volatile, controllable when heated and with a long shelf life, while their deposition temperature is high (above 500 °C). Care has to be paid when handling them: these precursors react with moisture according to the following equation 5.2:

$$2Nb(halogen)_5 + 5H_2O \longrightarrow 2NbO_5 + 10H(halogen) \tag{5.2}$$

A moisture free environment is therefore needed to store and handle these chemicals. This can be achieved by operating a N_2 filled glovebox.

5.2.1 Niobium pentachloride

$NbCl_5$ has been the chosen precursor for our studies.

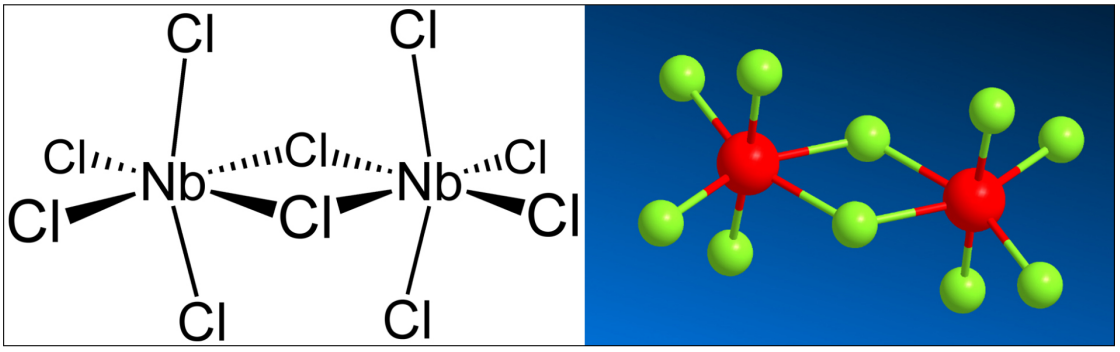

FIGURE 5.2: Niobium pentachloride molecule

This precursor, as shown in figure 5.2, was chosen because its:

- *availability*: the compound is largely used in the chemistry world, therefore easy to source.
- *cost*: due to the high production, the cost of it is lower compared to $NbBr_5$ and NbI_5.
- *suitability to the process*: the reaction temperature, even if high, can be exploited to deposit on copper substrates.

$NbCl_5$ (99% pure) was acquired from SigmaAldrich® (CAS number: 10026-12-7). A yellow crystalline solid when pure, it oxidizes in a white fluffy material allowing to visually verify if any contamination has occurred during its handling. A suitable container (from now on called a *bubbler*) had to be designed to use this precursor. The designed bubbler (figure 5.3) is composed by two separate parts: the lid part is a $3\ \frac{3}{8}$ inches CF flange with an inlet and outlet pipes of $\frac{1}{4}$ inch diameter welded through it terminating on air side with 2 Swagelok® Nupro metal valves. . The body is a $3\ \frac{3}{8}$ inches bored CF flange with 11 cm of stainless steel pipe welded and blanked off. A silver coated copper gasket is used when assembling the lid and body, held together by 8 M8 bolts and nuts.

FIGURE 5.3: Lid and body of designed bubbler

The precursor transfer is done in a MBRAUN® LABmaster glovebox, as shown in figure 5.4, where the levels of oxygen and water vapour are controlled and kept below 0.1 ppm at all times. The precursor is firstly weighted in a glass beaker on a digital scale, then the glass beaker is transferred in the body of the bubbler which then gets sealed.

FIGURE 5.4: Glovebox filling procedure

Once connected to the deposition system, heating is provided via glass fiber Hemiheating® heater tapes that are wrapped around the bubbler. The temperature is monitored by two thermocouples (one on the side of the bubbler, one on the lid) and controlled via a RKC® MA901 PID control, guaranteeing the uniform heating of the bubbler.

5.2.1.1 Bubbler flow simulation

The transport of the precursor is obtained by flowing purified BOC® 99.99999% Argon gas through the inlet of the bubbler. To maximize the carrying of the evaporated precursor by the carrier gas, the inlet pipe entry angle has been evaluated by using ANSYS Fluent. A more indepth discussion on the methodology used to simulate the gas flow is reported in Chapter 6.
Three scenarios were taken in account: inlet pipe coming straight down, inlet pipe turning at 45°, inlet pipe turning at 90°. The results are presented in figure 5.5. The pressure was set at 5 mbar (deposition pressure) and the temperature at 130°C (deposition temperature).

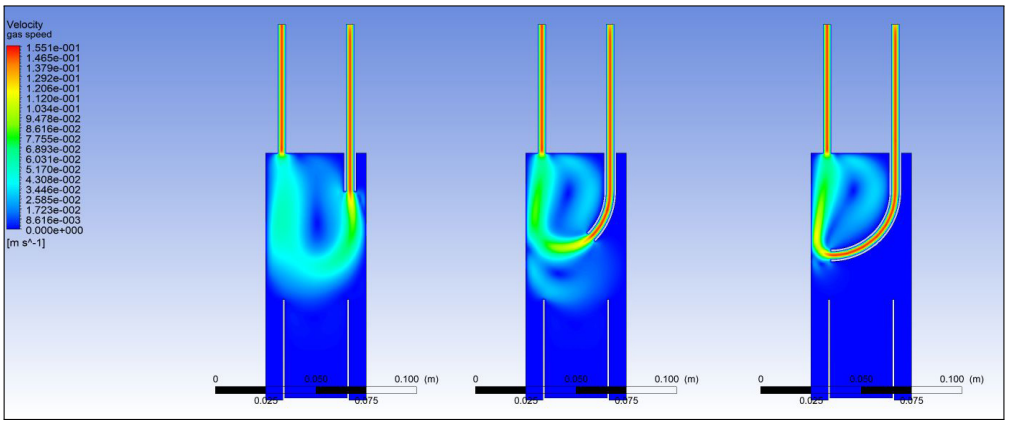

FIGURE 5.5: Simulation of Argon gas flow in the bubbler. The colours represent the gas velocity

From the simulation results, the inlet coming straight down allows the gas to come in and slow down above the beaker containing the precursor, to be then sucked away from the outlet without much turbulence, carrying evaporated precursor in the chamber. The inlet pipe turning at 45° instead allows the gas to slow down above the beaker but also to swirl above the beaker edges, which by creating more turbulence allows more precursor to be moved and therefore carried. The inlet pipe turning at 90° instead doesn't seem to allow any gas to circulate around the beaker. This may allow some precursor transport in the chamber only if the bubbler is saturated with volatile precursor. Although the improvements of the second scenario over the first may be minimal, the third scenario was discarded. The inlet pipe at 45° was chosen over the other two, to allow a good transport of precursor and a sufficient turbulence in the bubbler.

5.2.1.2 Vapour pressure analysis

Niobium pentachloride is a solid at room temperature with very little vapour pressure. This increases with temperature, as demonstrated by Sadoway and Flengas [116]. In their work, they measured the vapour pressure of $NbCl_5$ at different temperatures as reported in table 5.3.

Temperature (°C)	**Pressure (mmHg)**	**Pressure (mbar)**
153.80	17.1	22,798062
158.70	22.3	29.730806
163.00	26.5	35,33033
164,00	30.9	41,196498
175.50	57	75.99354
182.00	77.1	102.791262
187.20	99.1	132.122102
190.00	111.4	148.520708
191.20	116.2	154.920164
206.50	247.5	329.97195

TABLE 5.3: Temperature and vapour pressure of $NbCl_5$ measured by Sadoway and Flengas

The plotted data were used to extrapolate a fitting equation, equation 5.3:

$$Pressure = 0.0092 \times e^{(0.051 \times \text{Temperature})} \tag{5.3}$$

where the pressure is in mbar and the temperature in °C. The R^2 of the fitting curve is 0.9977. Figure 5.6 shows the data plotted overlayed with the fitting curve.

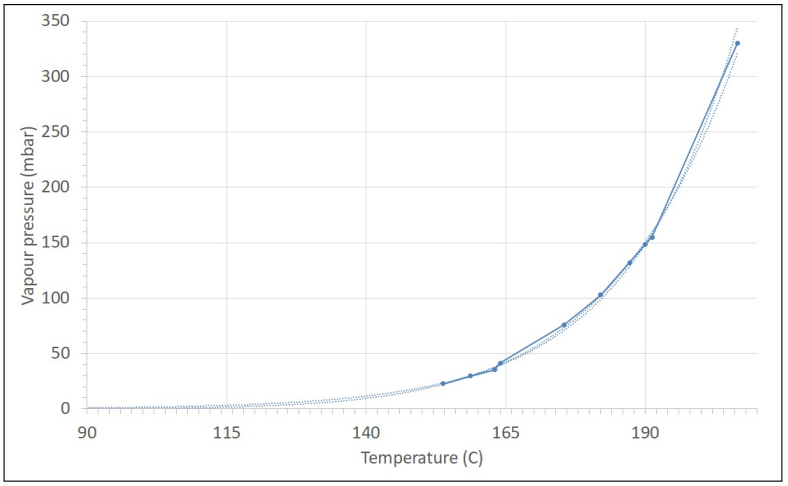

FIGURE 5.6: $NbCl_5$ vapour pressure vs temperature

The graph shows that the precursor starts to develop a vapour pressure once heated to about 100 °C, increasing exponentially. These values were chosen as a starting point to optimize the precursor deposition temperatures.

Temperature (°C)	**Duration (h)**	**Weight loss (grams)**	**Precursor use (g/h)**
100	4	0.125	0.03125
110	4	0.5	0.125
120	4	1	0.25
130	4	2	0.5
140	4	4	1
150	4	8	2

TABLE 5.4: $NbCl_5$ temperature vs weight loss and evaporation per hour

To measure the effective transport of precursor in the chamber, the precursor weight was monitored. Different temperature runs were carried, with 100 sccm Argon flowing through the bubbler. After each test run (4 hours of running time, to allow a significant quantity of precursor to be transported), the precursor was weighted using a precision scale and a glass beaker as holder and the weight change recorded. The weight changes at different temperatures are reported in table 5.4; these values were used to know the quantity of precursor left in the bubbler without having the need of inspecting it after every deposition, and to calculate the efficiency of the reaction chambers / deposition process.

5.3 Niobium metallorganic precursor

Metallorganic precursors are, as previously mentioned, compounds containing carbon - hydrogen bonds, even if this is not an absolute definition. In these complex molecules the metal to be deposited is weakly bonded or coordinated to the organic parts of the molecule. This means that the thermal energy needed to break these bonds and allow the deposition mechanisms is much lower than the thermal energy needed for inorganic precursors, but that also means that the precursors have to be treated more carefully or decomposition may happen in the bubbler (or before the chamber).

5.3.1 Tris(diethylamido)(tert-butylimido)niobium (V)

In our study, we chose to use one metallorganic precursor, *Tris(diethylamido)(tert-butylimido)niobium (V)*, as shown in figure 5.7.

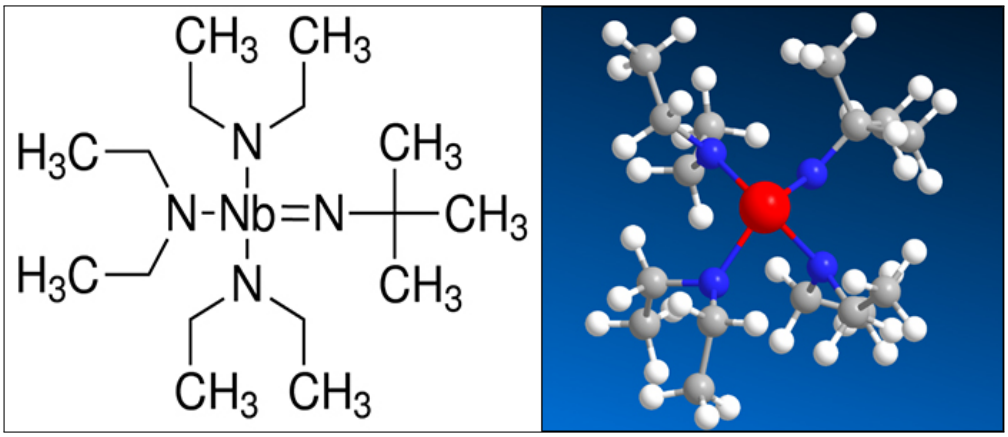

FIGURE 5.7: Molecule of Tris(diethylamido)(tert-butylimido)niobium (V)

This liquid compound has a niobium atom in the center, surrounded by three diethylamido groups and one tert-butylimido; it is worth to notice that the niobium is exclusively bonding with the nitrogen atoms, since the carbon atoms are already taken by the organic chains. The nature of this precursor renders it very reactive due to its weak bonds but also very sensitive to temperature, as it starts to decompose at 130 °C. The vapour pressure though, being a liquid, is sufficiently measurable at 80 °C. Thanks to its nitrogen content, reactivity and high vapour pressure at relatively low temperatures, as shown in figure 5.8, this precursor was chosen to perform atomic layer deposition (ALD) of niobium nitride, as presented in appendix A.

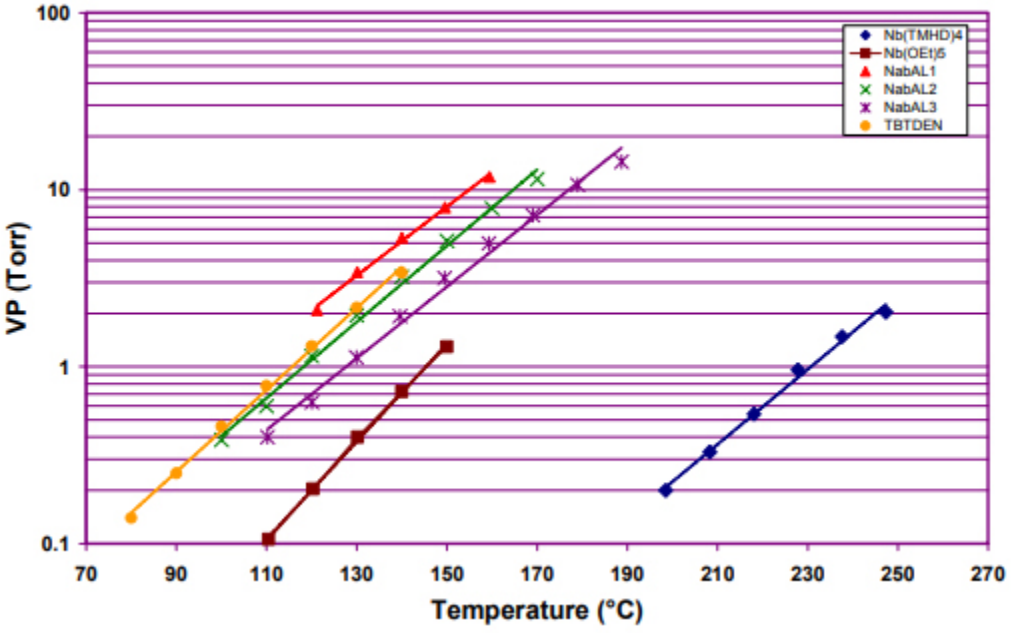

FIGURE 5.8: Vapour pressure for different metallorganic Nb precursors. Tris(diethylamido)(tert-butylimido)niobium is labelled as TBTDEN

5.4 Titanium inorganic precursor

Titanium tetrachloride, a titanium based halogen precursor, was selected as the third precursor to perform the deposition of niobium - titanium alloys. $TiCl_4$ (99,9% pure) was acquired from SigmaAldrich (CAS number:7550-45-0).

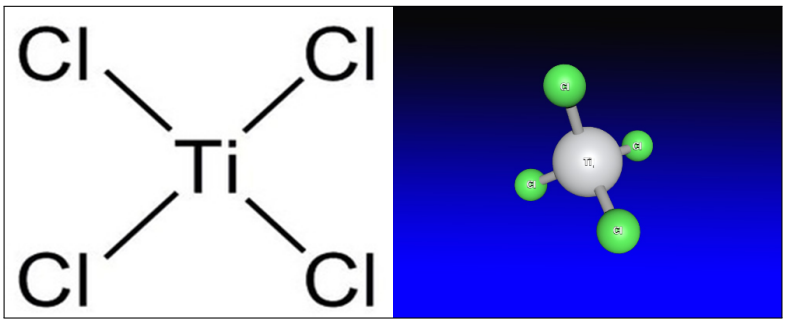

FIGURE 5.9: Titanium tetrachloride structure

$TiCl_4$, shown in figure 5.9. is chemically similar to $NbCl_5$: they are both bonded to the same halogen atom, chlorine, and therefore react through the same chemical route to deposition. In this case, the reaction is:

$$2TiCl_4 + 4H_2 \longrightarrow 2Ti + 8HCl \tag{5.4}$$

with a reduction of the oxidation state of titanium from 4+ to 0, similarly to the niobium reaction route. The advantage of this Ti precursor is its liquid state which makes its transport to the reaction chamber very easy, compared to the Nb precursor. The vapour pressure curve for this precursor is reported in figure 5.10. This was plotted using the Antoine equation for this compound (equation 5.5):

$$log_{10}(\text{Pressure in bar}) = 4.84969(\frac{1990.235}{\text{Temperature in }^{\circ}\text{K} + 2}) \tag{5.5}$$

Equation 5.5 is then rearranged in equation 5.6:

$$\text{Pressure in mbar} = 1000 * 10^{4.84969-(\frac{1990.235}{273.25+2+\text{Temperature in }^{\circ}\text{C}})} \tag{5.6}$$

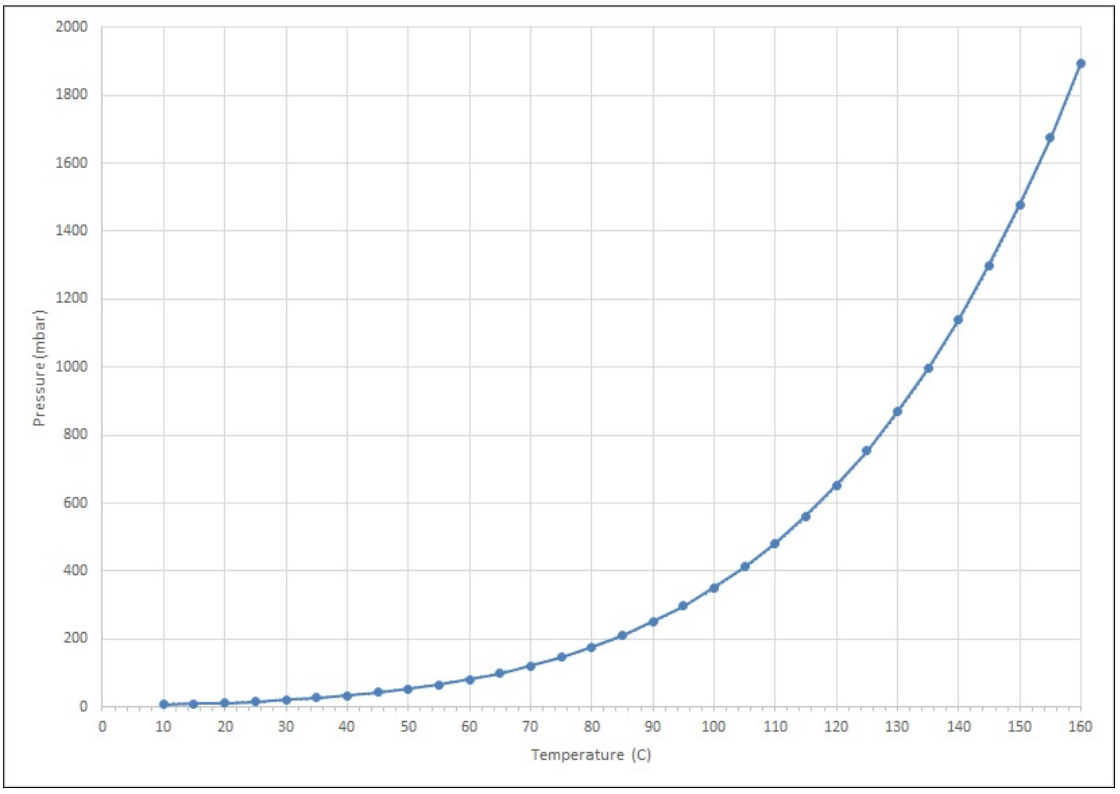

FIGURE 5.10: $TiCl_4$ vapour pressure vs temperature

It can be seen from figure 5.10 that the temperature needed to obtain a measurable vapour pressure is 100°C less than the what is needed $NbCl_5$. Therefore it was decided to use this precursor at room temperature, without any external heating.

Chapter 6

Development of a CVD reactor and PECVD reactor for SRF thin film deposition

In this chapter the different deposition chambers are discussed, with some considerations on the designs, pros and cons of each system.

6.1 Temperature and gas velocity simulations framework

6.1.1 Knudsen number, Reynolds number and gas continuum

Simulation programs have been improving constantly over the years, and are now capable of finding solutions for a wide array of real life situations. This does not mean though that anything can be simulated: especially when it comes to fluid dynamics, two parameters need to be evaluated before considering the use of softwares. These two parameters are the *Knudsen number* and the *Reynolds number*.

6.1.1.1 Knudsen Number

The Knudsen number (Kn) is an dimensionless parameter, given by the following equation (6.1) [117]:

$$\mathrm{Kn} = \frac{\lambda}{L} \tag{6.1}$$

where λ is the *Mean free path* of the molecules and L is a characteristic length. The mean free path is the average distance a molecule travels before colliding. This is calculated according to the following equation 6.2 [117]:

$$\lambda = \frac{RT}{\pi d^2 N_A P \sqrt{2}} \tag{6.2}$$

Where:

- R: ideal gas constant, 8.3144598(48) $\frac{J}{mol \times K}$
- T: temperature of the gas in kelvin
- d: diameter of the molecule in meters
- N_A: Avogadro's number, $6.022140857 \times 10^{23}$
- P: pressure in pascal

A fluid dynamics simulation requires a *continuous fluid* to be considered acceptable; if the fluid is not a continuous, the assumptions made by the software would not be physically accurate and the results would be unreliable or / and unrealistic. To evaluate this, the Knudsen number is used. If its value is below 1, as a general rule the fluid is considered continuous. In this work, using argon or hydrogen at 140 °C and 5 mbar of pressure, the mean free path changes from 0.05 to 0.01 mm. The smallest characteristic length is the diameter of the pipes, 4 mm. The Knudsen number ranges therefore from 0.01 to 0.0025, two orders of magnitude below the limit, implying that the simulations are operating in an acceptable regime.

6.1.1.2 Reynolds number

The Reynolds number (Re) is a dimensionless parameter used in fluid dynamics that identifies the type of flow in a particular situation. It is given by the following equation 6.3 [118]:

$$\mathrm{Re} = \frac{vL}{\nu} \tag{6.3}$$

where:

- v: velocity of the fluid relative to the object in m/s
- L: characteristic length in m
- ν: kinematic viscosity, ratio of dynamic viscosity and density of the fluid (m^2/s)

If the Reynolds number is below 2000, the fluid is flowing in laminar flow, so in parallel layers without disruption between the layers. If the Re is above 4000, the flow is turbulent, where the changes in pressure and flow speed are chaotic. Between these values, the flow is in a transient regime, meaning that it is difficult to predict the laminar or turbulent contributions.

Simulations can be done on both laminar and turbulent regimes, even though the turbulent cases require more computational power and more assumptions, making them less reliable.

In this work typical conditions are gases entering the chamber at 0.13 m/s with a kinematic viscosity of between 1 and 5×10^{-5} N*s/m^2. The Reynolds number then changes between 1200 and 200, identifying the flow as laminar. The software was therefore set to solve for laminar flows, based on the previous calculation.

6.1.2 ANSYS Fluent: a Computational fluid dynamics (CFD) software

A computational fluid dynamics (CFD) software was used to produce simulations of the temperature and gas velocity profiles. The chosen software was ANSYS Fluent Student, which provides a free to use student license, although with some limitations. The following equations are taken from the ANSYS Fluent Theoretical Manual [119], where they are discussed in more detail. The software works by solving equations for the conservation of *energy*, *momentum* and *mass* applied to the geometry and boundary conditions of the reactor under study. This is the equation for the conservation law for *energy* (6.4):

$$\frac{\partial}{\partial t}\rho(\hat{U}+\frac{1}{2}v^2) = -(\nabla\cdot\rho\nu(\hat{U}+\frac{1}{2}v^2)) - (\nabla\cdot q) + \rho(\nu\cdot g) - (\nabla\cdot pv) - (\nabla\cdot[\tau\cdot v]) \quad (6.4)$$

This equation includes two major terms commonly used in CFD, the internal energy associated with the random movements of the molecules and the kinetic energy associated with observable fluid motion, plus the energy of interaction between molecules. This energy conservation law states that the rate of gain of energy per unit volume $[\frac{\partial}{\partial t}\rho(\hat{U}+\frac{1}{2}v^2)]$ is equal to:

- $-(\nabla\cdot\rho\nu(\hat{U}+\frac{1}{2}v^2))$ = rate of energy input per unit volume by convection;
- $-(\nabla\cdot q)$ = rate of energy input per unit volume by conduction;
- $\rho(\nu\cdot g)$ = rate of work done on the fluid per unit volume by gravitational force;
- $-(\nabla\cdot pv)$ = rate of work done on the fluid per unit volume by pressure forces;
- $-(\nabla\cdot[\tau\cdot v]$ = rate of work done on the fluid per unit volume by viscous forces.

The software utilizes a finite volume method (FV) to convert the coupled partial differential equations in algebraic equations that can be then solved numerically. The studied volume is divided into a finite number of adjacent control volumes (CV) and the equation 6.4 is applied to each one of them. This way the solver integrates the equations over each CV, returning discrete equations that conserve each quantity per CV. As an example, the discretization of the equations for the steady state conservation for a scalar quantity ϕ is reported, proven by the following equation written for an arbitrary control volume V in integral form:

$$\oint \rho\phi\bar{v}\cdot d\bar{A} = \oint \Gamma_\phi\nabla\phi\cdot d\bar{A} + \int_V S_\phi dV \quad (6.5)$$

where:

- $\bar{A}$ = surface area vector
- Γ_ϕ = diffusion coefficient for ϕ

- ∇_ϕ = gradient for ϕ
- S_ϕ = source of ϕ per unit volume

Equation 6.5 is applied to each CV, or cell, in the computational domain under study. Figure 6.1 shows an example of a CV, a two dimensional triangular cell. Applying the discretization of 6.5 on any given cells gives:

$$\sum_{N faces} \rho_f \bar{v}_f \phi_f \cdot \bar{A}_f = \sum_{N faces} \Gamma_\phi (\nabla \phi)_n \cdot \bar{A}_f + S_\phi V \tag{6.6}$$

where:

- *N faces*: Number of faces enclosing cell
- ϕ_f: Value of ϕ convected through face f
- $\rho_f \bar{v}_f \phi_f \cdot \bar{A}_f$: Mass flux through the face f
- $\nabla\phi)_n$: Magnitude of $\nabla\phi$ normal to face f

The discrete values of the scalar ϕ are stored by default at the cell centers (c0 and c1 in figure 6.1, from [120]). Face values ϕ_f are though needed to calculate the convection terms in 6.6 and need to be interpolated from the cell center values. This is done by the software using an *upwind scheme*, where the face value ϕ_f for a cell is derived from the cell upstream, or upwind, relative to the direction of the normal velocity v_n.

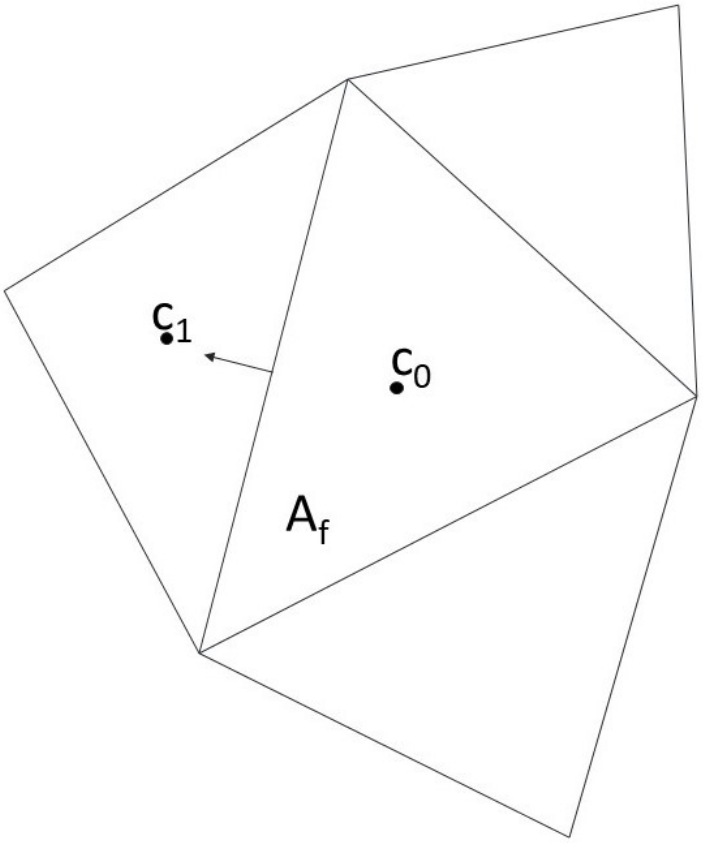

FIGURE 6.1: Example of control volume or cell

ANSYS Fluent was used to draw the models, generate the mesh (the CV structure that the software overlays on the model and uses to perform its calculations, as in figure 6.2) and run the simulations. For each simulation, a hybrid quadrangular - triangular mesh was employed, which is commonly used for CV methods; four boundary conditions were selected for each simulation:

- *Wall*: the walls of the reactor, set at a fixed temperature.
- *Inlet flow velocity*: the reactor inlets, and the speed at which the gases enter the chamber.
- *Heater - sample temperature*: the temperature measured at the sample.
- *Outlet pressure*: the reactor outlets and the pressure at which the chamber is.

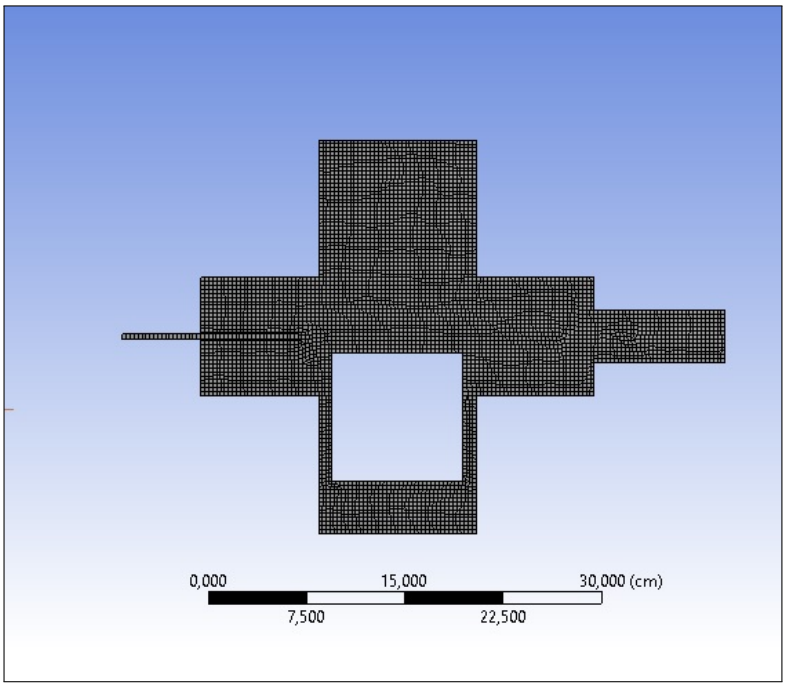

FIGURE 6.2: An example of meshing. In this case, the first iteration of the cvd deposition chamber

The equations were solved sequentially due to limited processing power available. As mentioned before, for each variable the software computes its value using values from the same cell and the neighbouring cells. The value at the centre of the cells was selected as default. The energy equation option was selected to simulate the profile and gradient of temperature around the heater area. Argon and Hydrogen were used as gases for most of the simulations and their parameters were taken from the Fluent database:

	Density (g/cm^3)	**Cp(erg /g-k)**	**κ (erg/cm-s-k)**	**Viscosity (poise)**
Hydrogen	8.189e-05	1.4283e+08	16720	8.411e-05
Argon	0.0016228	5206400	1580	0.0002125

TABLE 6.1: Table of physical properties from ANSYS Fluent database

The pressure of the reactor was set at the initialization of the calculations at 5 mbar, for reasons discussed in chapter 7, and the gravitational acceleration was set at -9.8 m/s^2 along the Y axis. The gases velocities were derived for the simulations from the volumetric values of 100 sccm for argon and 100 sccm for hydrogen using the following relation (eq. 6.7):

$$\text{Gas velocity in} \frac{m}{s} = \frac{\text{Volumetric rate in sccm}}{60 \times \text{Area of the inlet}} \tag{6.7}$$

4 mm I.D. pipes (1/4 inch O.D. thin walled) were used as inlets in all the reactors. Therefore, for 100 sccm the value of gas velocity at the inlet returns a speed of roughly 13.8 cm /s.

The outlet pressure of the chamber was set at 5 mbar, as previously mentioned, and the software adapts the outlet pressure and velocity after every iteration to maintain the conditions of continuous flow in the chamber. The temperature at the heater was set at 700 °C without any heat flux between the walls and the outside of the reactor.

Since the equations are non linear, it is important to control the variations in ϕ. This is done through the introduction of an *under-relaxation factor*, which acts as a dampener in the changes of, in this case, ϕ. Each iterated value of ϕ depends on ϕ_{old}, the old value, on $\Delta\phi$, the change in value, and α, the under relaxation factor (eq. 6.8):

$$\phi = \phi_{old} + \alpha\Delta\phi \tag{6.8}$$

The software has default values for the under relaxation parameters; these are meant to be modified only if the variations in the computed values swing greatly between iterations, leading to a non convergence. Since each simulation performed converged in a reasonable amount of time and iterations, the under relaxation values for pressure, density, momentum and energy were kept at their default values.

The results are discussed in this chapter, along with design considerations and some deposition results.

6.2 CVD reactor development

6.2.1 First iteration and first depositions

A 6 way cross piece was chosen as the first reactor. The 4 DN100CF flanges were connected to:

- Penning and Pirani gauge
- Bellow connected to pumping assembly
- Gas inlet
- Viewport

The viewport was removed to introduce and remove samples. The pumping array is made by a Pfeiffer TMH 260 C Fomblin turbomolecular pump, capable of pumping 260 l/s. The turbomolecular pump was originally backed by an Edwards XDS10 dry scroll pump, replaced subsequently by an Edwards EM 18 sealed rotary vane oil pump. The replacement was made necessary by the filter placed between the turbomolecular pump and the backing pump malfunctioning and damaging the pump. The outlet of the backing pump is connected to an COSSH extraction system, to prevent any reaction gases to escape into the lab. The gas lines, the chamber walls and the pumping bellows are all wrapped in heater tapes and kept at 10 °C above the bubbler temperature at all times. This is to reduce the quantity of precursor condensing in the pipes, leading

to clogs, and on the chamber walls. Figure 6.3 shows a schematic drawing of the first chamber arrangement. The green dots are valves.

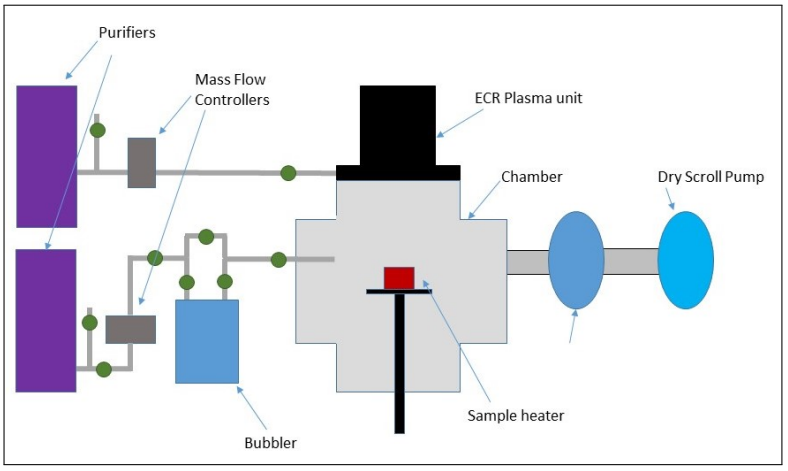

FIGURE 6.3: Schematic of the first iteration of the CVD deposition system

The top DN160CF flange had the ECR plasma unit connected to it. This was later removed for reasons discussed further on. The carrier gas line (argon) and the co-reagent gas line (hydrogen) were connected to two separate SAES getter purifiers to reduce the level of impurities potentially present in the cylinders. The carrier gas line was then connected through a mass flow controller, and then to the bubbler. A bypass line was installed above the bubbler. The line was then connected to the chamber gas inlet.

6.2.1.1 Heater assembly

The heater assembly comprised 7×24 W halogen light bulbs, all connected in series. The light bulbs are resting on a custom designed stainless steel plate, shown in figure 6.4, with a groove for a 46 mm in diameter and 0.5 mm in thickness stainless steel tube, that acts as sample support and heat shield at the same time. The array is connected through ceramic vacuum feed throughs to a Variable transformer (VARIAC), which provides the power. The full assembly is shown in figure 6.5, mounted on a vacuum flange with an additional heatshield.

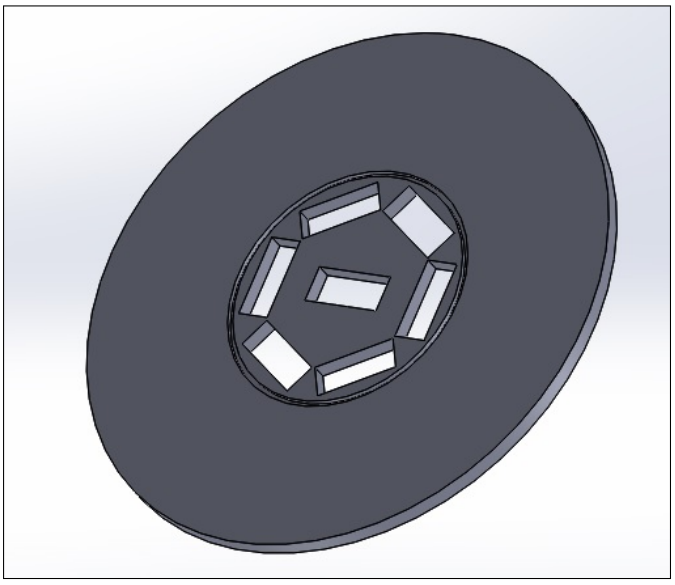

FIGURE 6.4: Light bulb support plate

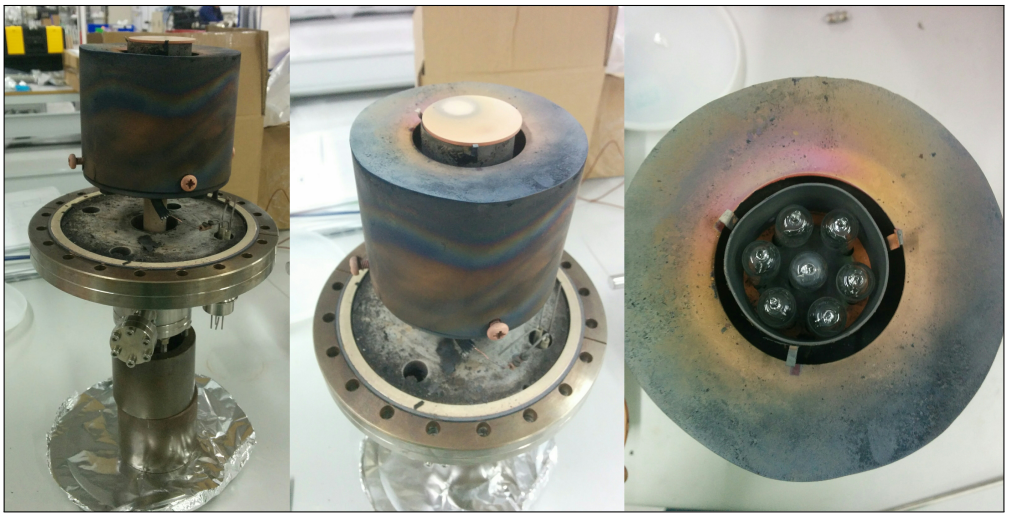

FIGURE 6.5: Light bulb heater and flange assembly

To perform metal depositions, it is paramount to isolate the electrical contacts from the reactive gases. If not, an electrically conductive film can grow and cause shorts to earth. For this to happen, though, the temperature needs to be high enough to trigger the chemical reactions. In order to prevent this, the heater assembly went through many iterations:

- *Light bulbs isolation*: the hottest part of the assembly can be found at the surface of the light bulbs. If then the gases seep through to it, the surface gets coated with a shiny layer of metal. This firstly translates in a drop in temperature on the sample, since the heat generated by the tungsten filament is not reaching the sample any more but is reflected back towards the inside of the light bulbs themselves. Figure 6.6 shows how the lightbulbs may end up coated during the

deposition. Secondly, this trapped heat increases the temperature of the light bulbs quartz walls, making them sag and deform at first, or worse making them crack and consequentially explode. Isolating the light bulbs completely though could prevent the sample from being directly exposed to them and not heating up sufficiently. The solution found was to make sure that the connection between the sample and the heat shield - support was very good by securing the sample to the plate through flexible strips.

- *Ceramic plate*: if the light bulbs got coated, the more common issue faced was a bridging between the live electrical contacts and the ground through the support plate. At first, the plate was replaced with an identical support machined out of MACOR ceramic. This, though, did not withstand the high temperatures and was therefore abandoned. The electrical contacts were then coated with a ceramic paste to prevent this from happening, but the rigidity of the solidified paste was too high and could not take the repeated strain of the heating and cooling cycles, cracking and falling off in the chamber.

- *Connections*: initially the light bulbs were connected in series with copper wire and barrel connectors: this, ideally, allowed quick replacement of the malfunctioning light bulbs. In practice, the difficulty of identifying which light bulb had failed meant that the complete array needed replacing at every failure. Moreover, the high temperatures reached by the heater assembly would soften the brass connectors, leading to disconnections and slippages of the connectors from the light bulbs pins. This was addressed by creating the connections by spot welding nickel strips to the light bulb pins.

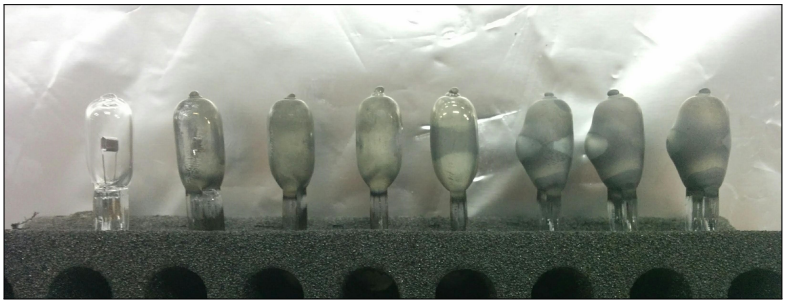

FIGURE 6.6: Progress of coating on the light bulbs. Left to right, light bulb not coated to light bulb fully coated and heavily deformed

6.2.1.2 First deposition attempts

The first six depositions were not successful.

For the first three attempts, a copper plate was placed above the heater and the samples were secured to it. By doing so, the heat provided was dissipated by the copper plate and insufficient to take the samples to the right deposition temperature.
The following three attempts were characterized by a pump failure after 15 minutes

of deposition (malfunctioning filter), one precursor condensation clog due to a failure of a heater tape between the bubbler and the chamber, and one leak that ruined the precursor in the bubbler before starting the deposition.

6.2.1.3 Copper match box

After the first deposition attempts did not prove successful nor satisfactory, the cause was attributed to the lack of precursor reaching the deposition area. To verify this theory, a *copper matchbox* was constructed. As shown in figures 6.7, 6.8 and 6.9, an oxygen free 0.5 mm thick copper plate was cut and bent into a match box shape.

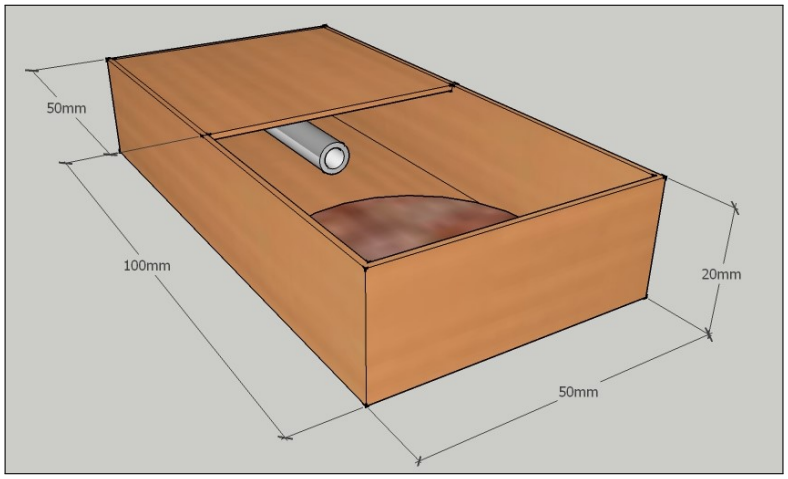

FIGURE 6.7: 3D drawing of the match box - sample side view

A round slot was cut on one side to slide and install the match box on the inlet pipe. Figure 6.7 shows the pipe and the sample relative positions.

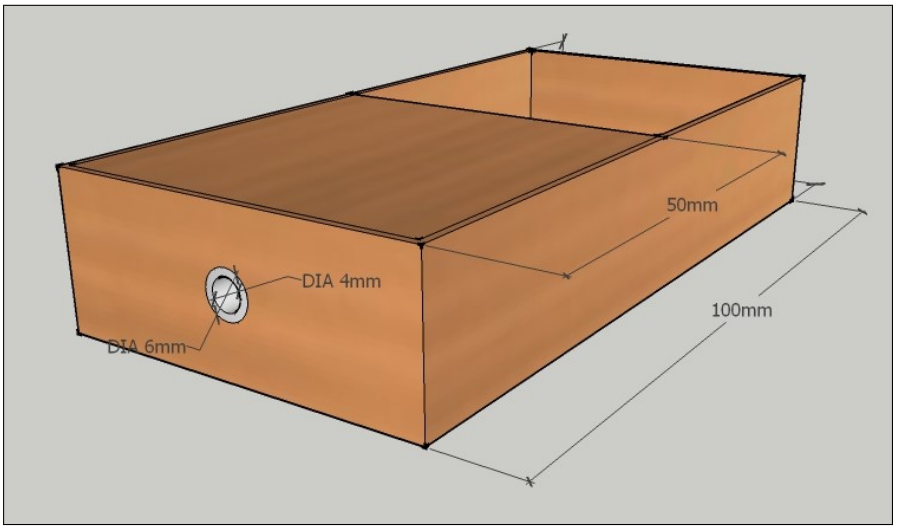

FIGURE 6.8: 3D drawing of the match box - inlet side view

The role of the match box was to contain the precursor introduced in the chamber in a volume as close as possible to the heater, preventing it from dispersing in the reactor

and condensing on the chamber walls. The substrate was placed as shown in figure 6.7. The deposition parameters are reported in table 6.2:

	Values
Temperature (°C)	500
Pressure (mbar)	5
Chamber temperature (°C)	120
Argon flow (sccm)	100
Hydrogen flow (sccm)	100
Precursor temperature (°C)	120
Deposition time (h)	4

TABLE 6.2: Match box deposition parameters

The first deposition result is shown in figure 6.9.

FIGURE 6.9: Match box opened. The grey part is Niobium

While the substrate showed no growth, the part of the match box between the heater and the substrate showed a silvery smooth coating. SEM and EDX analysis were performed on both the silver coating and the uncoated copper.

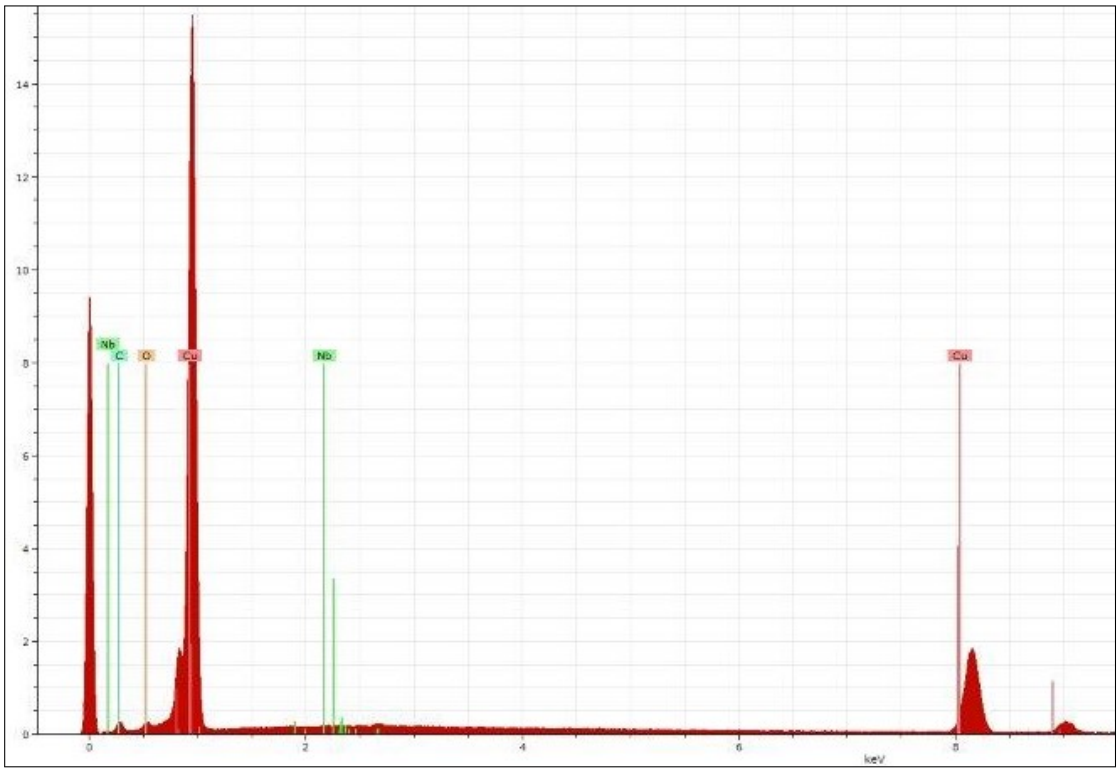

FIGURE 6.10: EDX of non coated part of match box

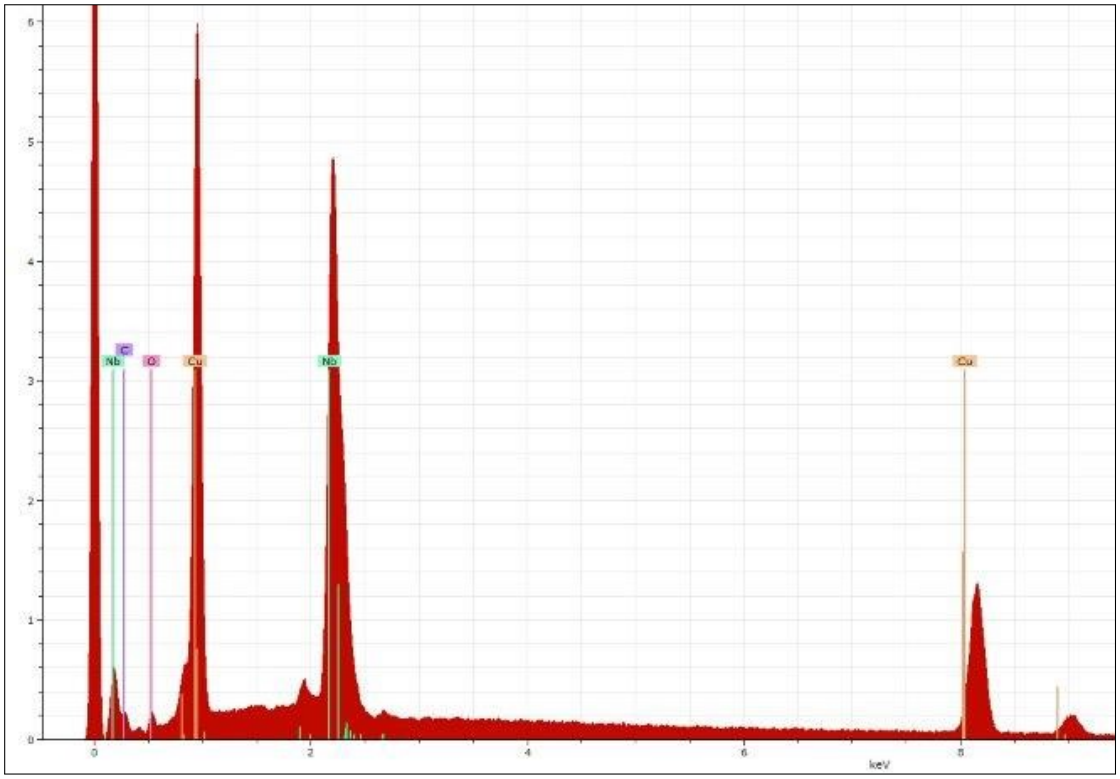

FIGURE 6.11: EDX of coated part of match box

		Uncoated part		Coated part	
Element	**AN**	**[wt.%]**	**[norm. at.%]**	**[wt.%]**	**[norm. at.%]**
Copper	29	42	79	27	40
Carbon	6	2	17	2	16
Oxygen	8	0	3	0	2
Niobium	41	0	0	41	41

TABLE 6.3: EDX elemental quantitative analysis for the uncoated and the coated part

Figure 6.10 presents the EDX scan from the uncoated area while figure 6.11 presents instead the EDX scan from the coated area. Table 6.3 reports the weight percentage and the normalized atomic percentage quantities for both the uncoated and coated part. In the uncoated part scan, the dominant peak corresponds to copper, which is what is expected. In the coated part scan the copper signal is still present, although in reduced intensity, while the niobium signal is now evident, nearly equal in intensity to the copper signal. The presence of the copper signal even in the niobium coated area is attributed to the EDX technique, as discussed in chapter 4, where the sampling volume depends on the energy of the incident electron beam. These measurement were taken with a 15 KeV beam, suggesting that the film thickness is low.

To verify this, the coated area was cut out of the match box, prepared with FIB and, using the high resolution SEM of the FIB instrument, images were taken.

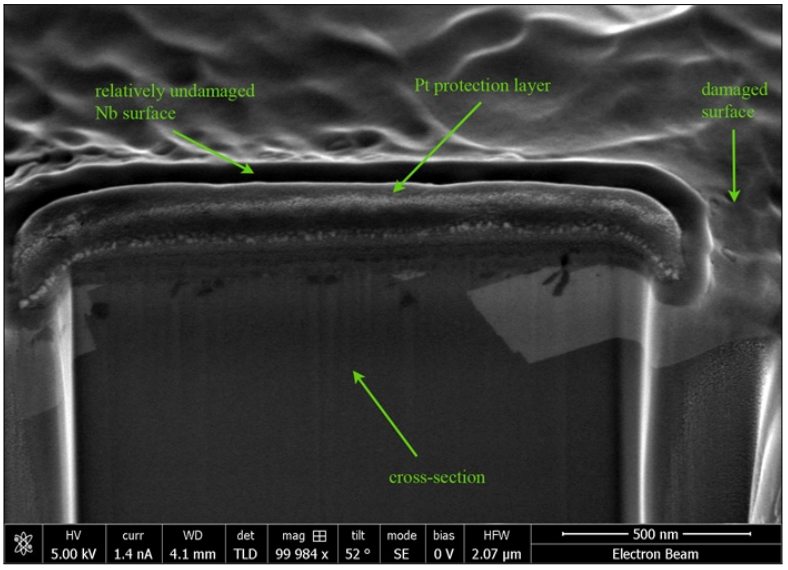

FIGURE 6.12: High resolution SEM image of match box coated area

Figure 6.12 and 6.13 show the SEM images taken on the sample. As predicted from the EDX measurements, the thickness of the film is low, estimated in roughly 70 nm.

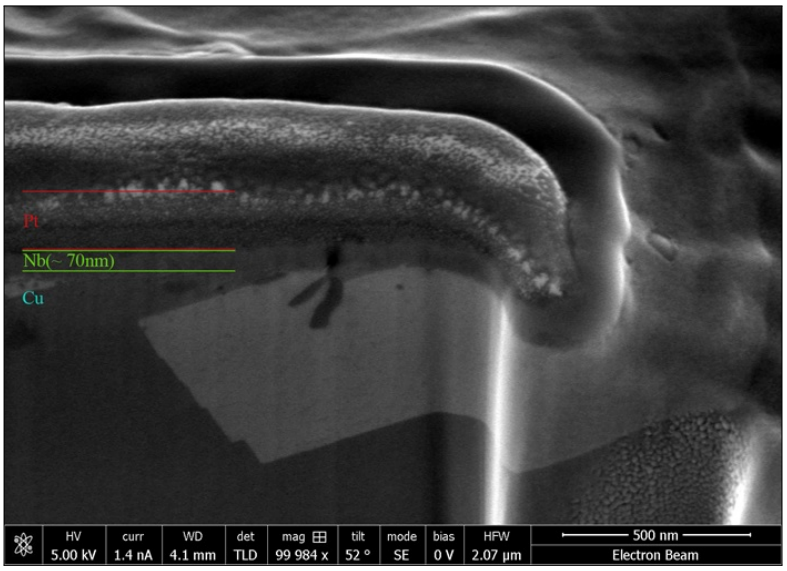

FIGURE 6.13: High resolution SEM image of match box coated area - zoomed on edge of sample

The FIB sample was then prepared for TEM imaging. Figure 6.14 shows the deposited film and the substrate.

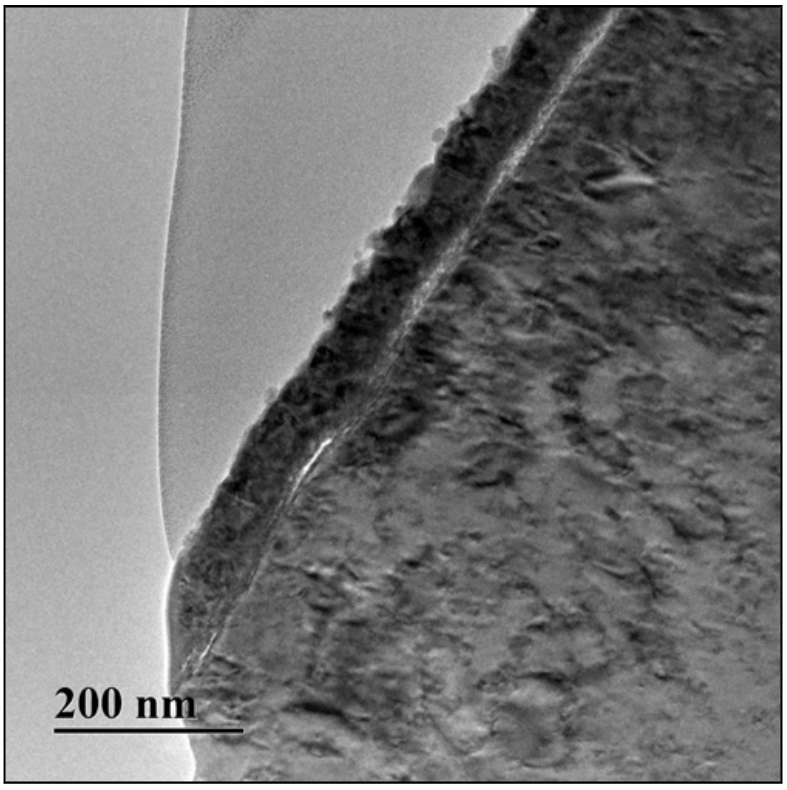

FIGURE 6.14: TEM image of the match box coated area sample

TEM is sensitive to the thickness of the sample and its atomic composition. By adjusting the image contrast, it is possible to resolve the different materials, as shown in 6.15.

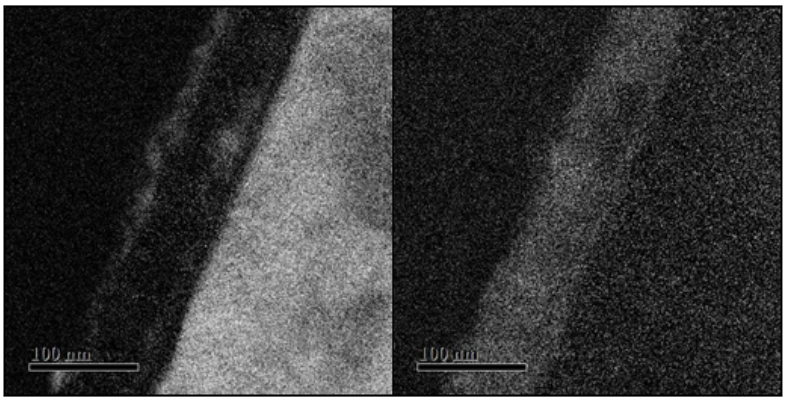

FIGURE 6.15: Contrast TEM image of the match box sample: the contrast was adjusted to show brigh or dark areas according to the molecular weight of the sample. On the left, the Cu is highlighted while on the right the Nb

This way, the niobium film, highlighted on the right, can be seen. By using an elemental mapping software, it was possible to determine the composition of the cross section of the film, as shown in figure 6.16.

This proves that the film is, as previously seen, 70 nm thick, and made of pure niobium.

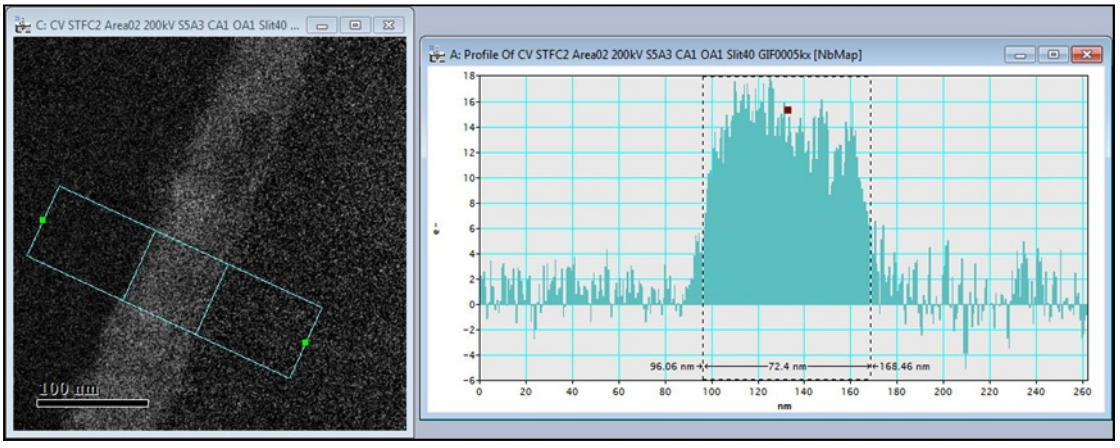

FIGURE 6.16: Elemental map of the deposited layer cross section

An estimate of the efficiency of this deposition was done using the $NbCl_5$ reduction rate. At 120 °C, the amount of precursor used over four hours of deposition with 100 sccm of Argon as carrier gas is 1 gram (0.25 g/h × 4). According to the chemistry of the reaction, if the reduction of niobium is complete 1 mol of $NbCl_5$ produces 1 mol of Nb. Knowing the molecular weight of $NbCl_5$ and Nb, 1 gram of $NbCl_5$ is equivalent to 0.003 mol, which in turn corrispond to 0.34 grams of metallic niobium. Having measured the deposited area and approximated it to a circle, it measures roughly 7 cm^2, and being 70 nm thick it has a volume of 4.9×10^{-5} cm^3. Knowing that the density of niobium is 8.57 g/cm^3, the estimated weight of the deposited layer is 4.2×10^{-4} g. This seems to indicate that the quantity of precursor that reacted to form a niobium film on

the copper match box is roughly 0.1 % of the precursor introduced in the chamber.

This estimate does not take in consideration any other reaction routes and assumes that the film is 100 %Nb. These are assumptions that may not be entirely true. If, for example, niobium oxide was part of the film, the density of it would be lower, and so the calculated efficiency. This value can therefore provide an indication of the deposition system performance, but its limitations have to be kept in mind when discussing it.

The use of the match box provided the first successful depositions, even though the film grown were too thin to perform any further studies. This lead to the following considerations:

- *Temperature*: deposition temperature is an important parameter for growth rate. The area directly over the heater was reaching the T necessary to trigger the reaction, but not the rest of the box.
- *Gas flow*: the use of the box did not provide an effective way to confine the gas flow. Rainbow patterns were found on the joint gaps, suggesting that the precursor was escaping from the corners of the box.
- *Manufacture*: different boxes were built to repeat the experiments but, being hand cut and hand folded, may have been slightly different from one another, reducing the level of repeatability of the experiments.

The match box was therefore abandoned.

6.2.2 Two pipes from the side and simulations

After the results obtained with the copper match box, it was decided to change the gas delivery arrangement (one pipe to the side of the sample and one from the side 20 cm above) to a different geometry. To improve the possibility of the precursor and the co-reagent reacting together, the co-reagent line was modified with the addition of a bypass entering the chamber parallel to the precursor delivery inlet.

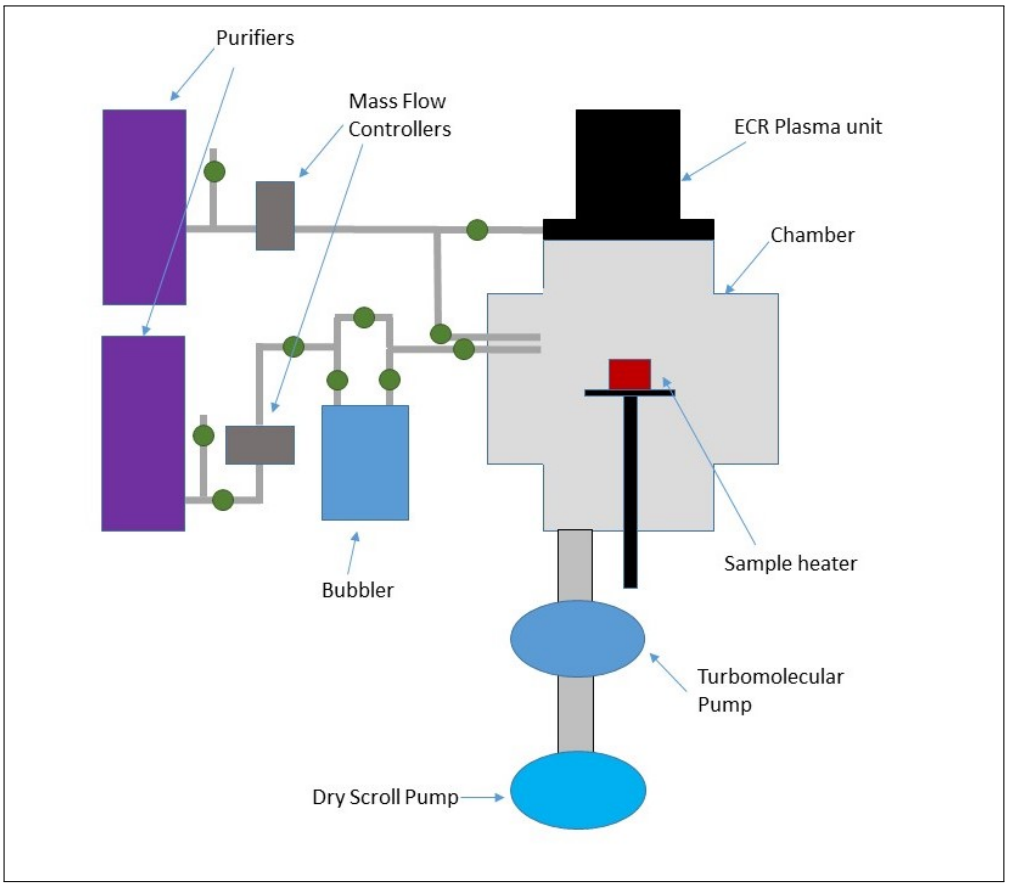

FIGURE 6.17: Second iteration of the first chamber: co-reagent bypass next to precursor inlet

In this new configuration, shown in figure 6.17, the hydrogen and the precursor inlets were terminated at the same distance from the sample, 4 cm, and were 5 mm apart. This lead to an improvement in growth rate, from 70 nm for 4 h to 500 nm over the same time, an efficiency of now 1.2 %. The deposition profile over the substrates did not improve. The samples look more deposited the closer to the gases inlets, with the surface further away poorly coated if coated at all. To identify the problem, simulations were performed, shown in figure 6.18 and 6.19.

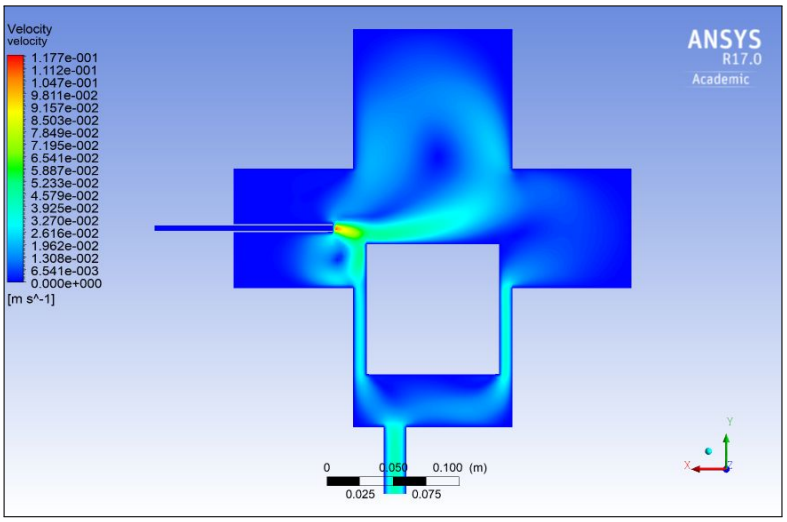

FIGURE 6.18: Argon velocity profile

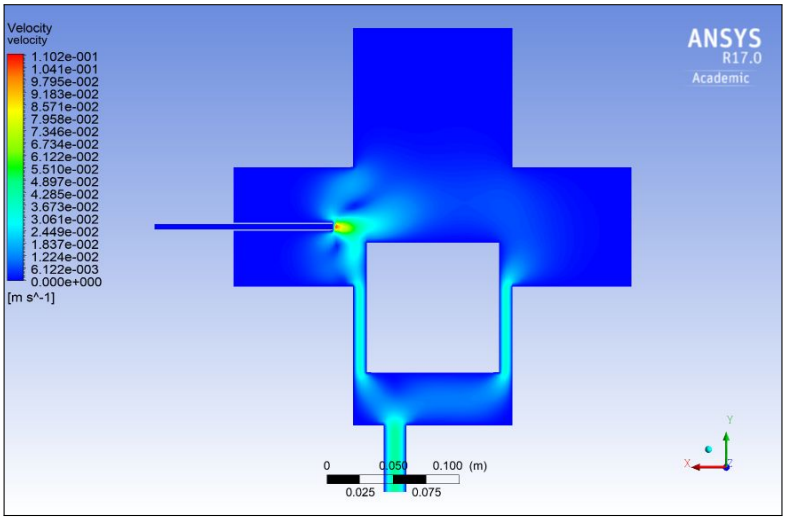

FIGURE 6.19: Hydrogen velocity profile

The results obtained from the simulations highlight the different paths that the argon and the hydrogen take once in the chamber. Argon seems to flow over the deposition area, to then "lift off" half way across the sample. Hydrogen instead seems to flow above the deposition area, not across it like argon. The reason for this was attributed to the effect of heat: the gas slows down before reaching the hot substrate and, when close to it, is warmed up, becomes lighter and rises away from the sample. This agrees with the experimental findings, attributing the limited growth away from the inlets to both gases (hydrogen more than argon, but both nonetheless) lifting off.

6.2.3 Small vertical chamber

To improve on the results obtained with the first chamber (6 way cross piece), a new design was assembled. The reasons behind the new design were:

- *Gas direction*: having inlets from the top of the chamber introducing the gases perpendicularly to the substrates would limit the lifting effect seen in the first chamber.
- *Volume*: reducing the volume of the chamber would mean less pumping volume and therefore quicker pumping times.
- *Surface*: a smaller chamber would mean less surface area, so less precursor lost to chamber condensation.
- *Symmetry*: the gas dynamics would be easier to control in a cylindrical chamber.
- *Simulation*: a smaller symmetrical shape would be less calculation intensive.

A 10 cm long tube with DN160CF flanges at both ends was chosen as deposition chamber. For practical reasons, the new chamber was connected to the existing precursor / co-reagent lines, leaving the possibility of using the previous and the new chamber, as shown in figure 6.20.

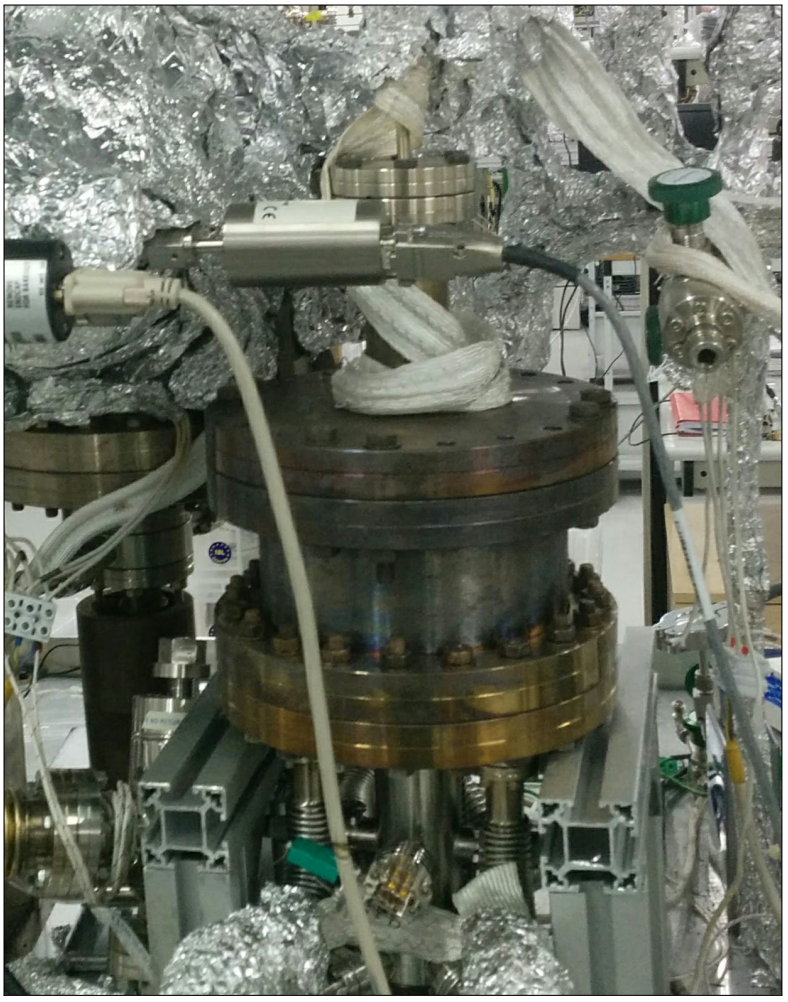

FIGURE 6.20: The new deposition chamber integrated into the previous deposition system

The heater assembly chosen, shown in figure 6.21, was a new iteration of the light bulbs heater: the electric contacts were kept as segregated as possible from the reaction gases by using a 10 cm O.D. tube to act as a physical barrier. Both end of the tube were flattened and polished, to guarantee a good adhesion with the support plate and the bottom flange.

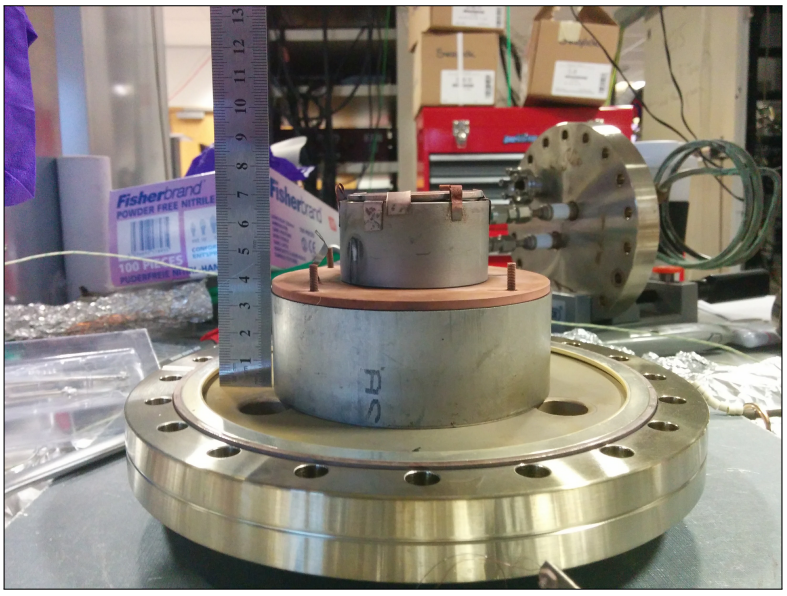

FIGURE 6.21: Heater assembly for the small chamber. The light bulb heater support is resting on a 10 cm O.D. tube that also provides isolation from the gases to the electrical contacts

6.2.3.1 Custom bottom flange and shower head top flange

Following one of the design principles for the new chamber, *symmetry*, a new DN160CF custom made flange was manufactured to harmonize the dynamics of the pumped gases. This flange has 3 DN16CF ports arranged in a triangular fashion, and one DN35CF-DN40CF port in the centre of the flange, shown in figure 6.22. The three ports are connected to three 1.5 meter long bellows, going to the pumping assembly. The pumping speed of the chamber can be adjusted by a operating a valve above the turbomolecular pump. The central port is dedicated to the electrical connections: a 15 cm long tube terminating in a blanked off DN35CF-DN40CF flange is connected to 2 DN16CF feedthroughs, connecting the two ends of the light bulb array to the Variac.

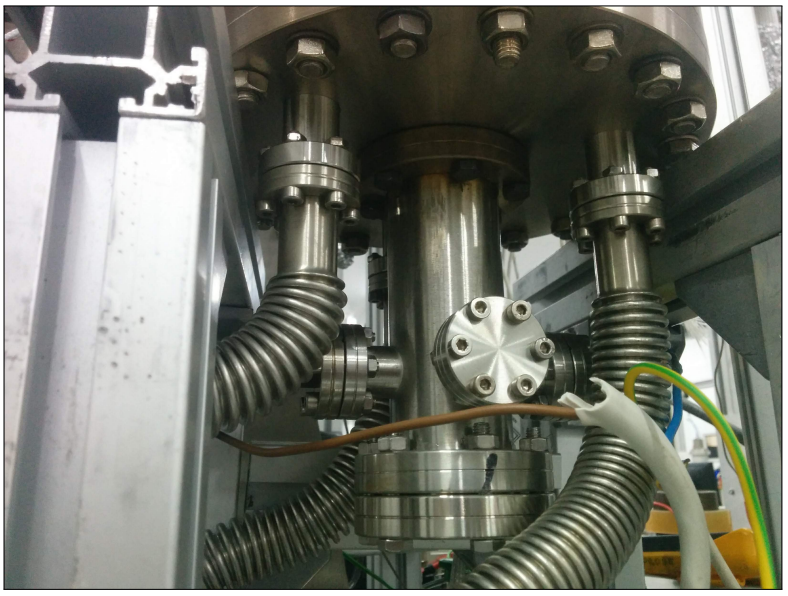

FIGURE 6.22: Custom made bottom flange, showing the 3 pumping ports and the heater electrical connections

6.2.3.2 Simulations and shower head

Simulations were performed on the little chamber. Figures 6.23 and 6.24 show the results for the gases velocity and temperature profile, with 100 sccm of Ar, 100 sccm of H_2, 5 mbar of pressure in the chamber and 140 °C wall temperature.

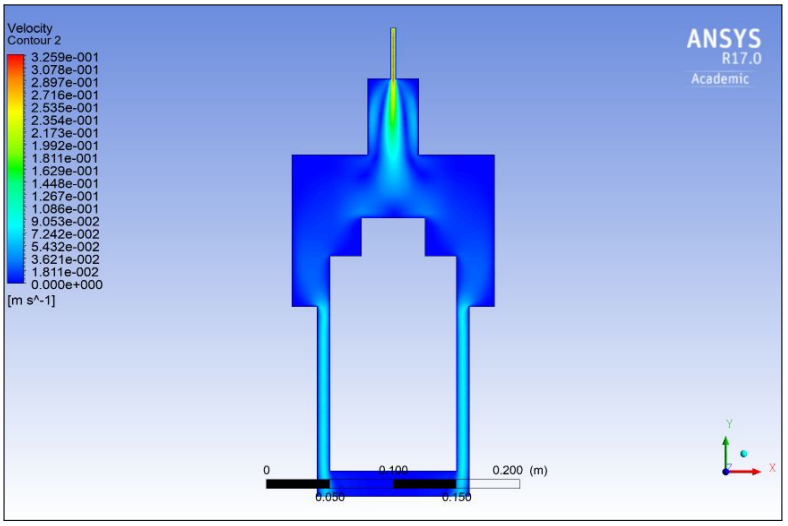

FIGURE 6.23: Gas velocity for small chamber with standard adaptor flange DN35CF-DN40CF to DN160CF at the top

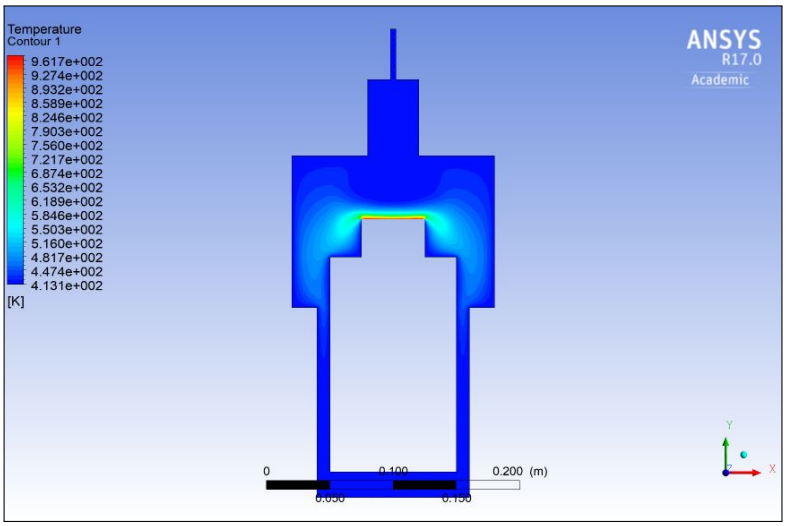

FIGURE 6.24: Temperature profile for small chamber with standard adaptor flange DN35CF-DN40CF to DN160CF at the top

From the simulations results, it can be seen that the gases speed profile forms a plume with the sample at its tip. This is unwanted, since the gases jet may create a local cold spot in the middle of the sample, compromising the deposition.

To mitigate this phenomenon, the top flange, a standard adaptor flange DN35CF-DN40CF to DN160CF, was modified and a shower head was manufactured. The shower head was made out of a 2 mm thick plate of stainless steel 316, with 1 mm holes drilled through in a regular perpendicular pattern; it was secured to the top flange through a metal ring and 4 M6 screws. Figure 6.25 shows the assembly, with the 10 cm O.D. shower head.

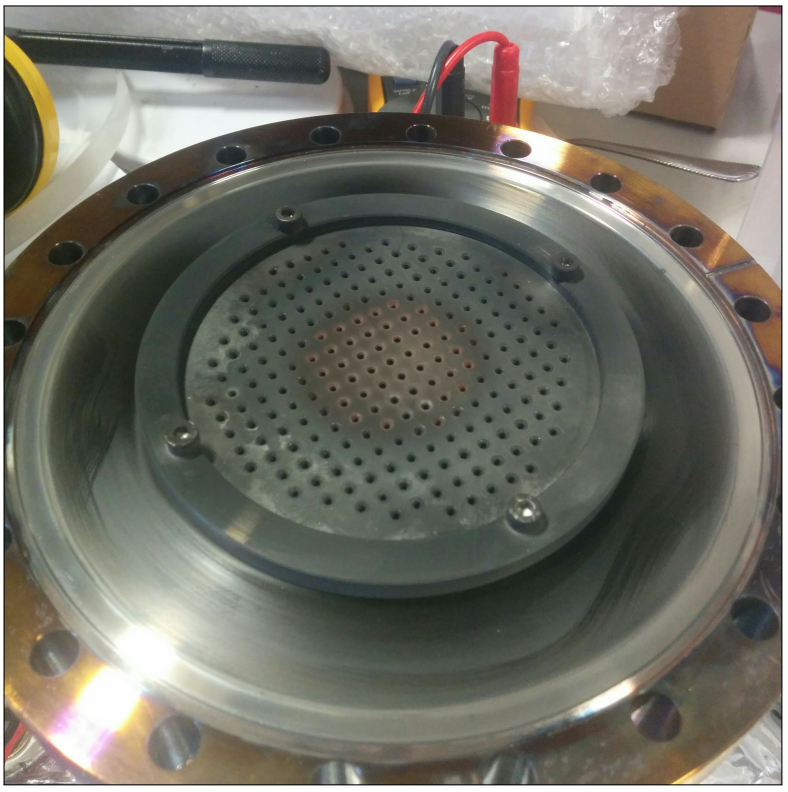

FIGURE 6.25: Flange with shower head installed

It is worth to notice that the shower head is much larger than the inlet tube diameter, which is 48 mm. This was dictated by the practicality and ease of machining.

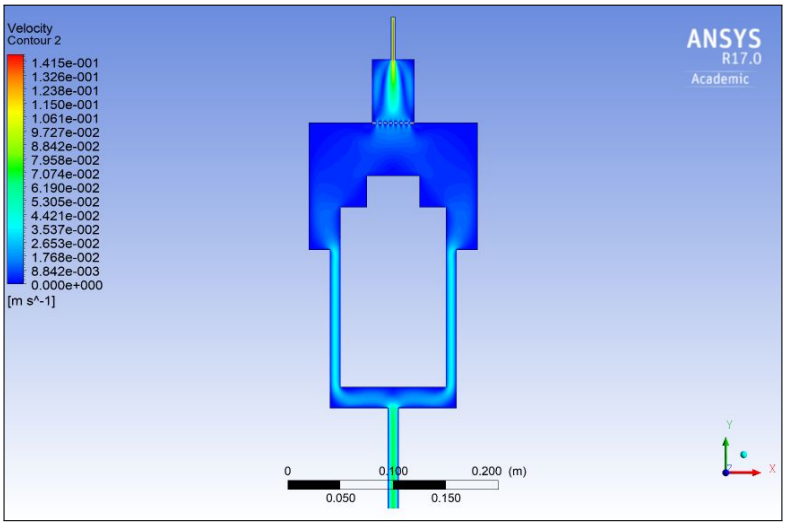

FIGURE 6.26: Gas velocity for small chamber with standard adaptor flange DN35CF-DN40CF to DN160CF at the top and shower head

Figures 6.26 and 6.27 show the simulation results for the shower head contribution: it can be noted that the speed of the gases is decreased considerably, nullifying the possibility of creating cold spots during the film growth.

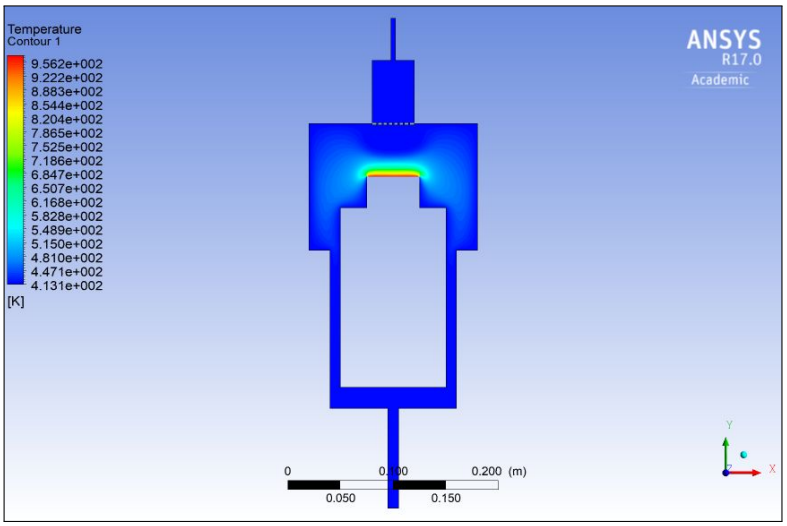

FIGURE 6.27: Temperature profile for small chamber with standard adaptor flange DN35CF-DN40CF to DN160CF and shower head

6.2.3.3 Heater meltdown

The first deposition was stopped by a short of the light bulb array. Once the chamber was opened, it was found that the substrate had melted, implying that the temperature on the substrate was of at least 1000 °C. This required a new heater support, heat shield and light bulbs. The cause for this are not clear, since the same heater design had been used before at the same values of voltage and current. It is possible that, due to all the components being new, the heat reflected by the chamber wall focused in the middle of the reactor, adding to the heat from the light bulbs. After the heater was replaced, though, this phenomenon did not repeat.

6.2.3.4 Deposition rate vs Fe content

Depositions were run using the same parameters as for the previous depositions in the large chamber. Having both the precursor / carrier gas and the co-reagent gas entering the chamber through the same inlet and then flowing homogeneously over the sample gave the expected results.

The samples looked uniformly coated, without any wave pattern (mark of precursor consumption or missing co-reagent) over the surface. The samples were SEM imaged, and figures 6.28 and 6.29 show the surface of a representative sample.

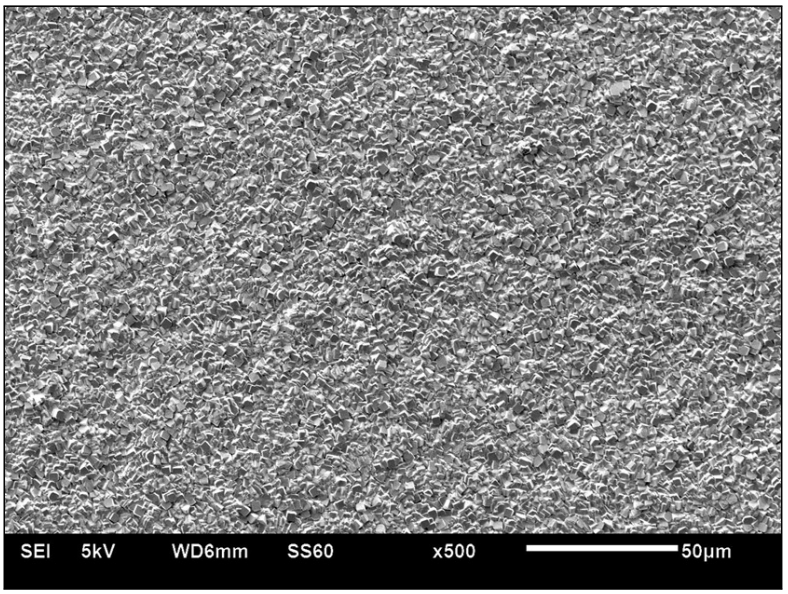

FIGURE 6.28: SEM image of surface of sample grown on small chamber with shower head

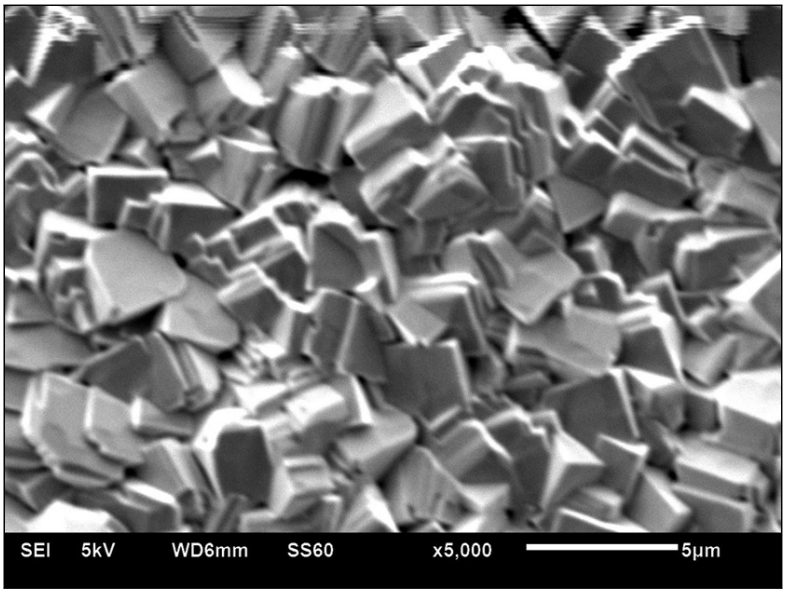

FIGURE 6.29: Magnification of SEM image 6.28

The SEM images show that the surface looks crystalline, with crystallites of ≈2.5 μm in size across. These results were different from any other growth obtained to this point, and the cause was attributed at first to the enhanced deposition rate thanks to the new chamber gas delivery system.

To verify this the samples were cross sectioned with FIB, as shown in figure 6.30.

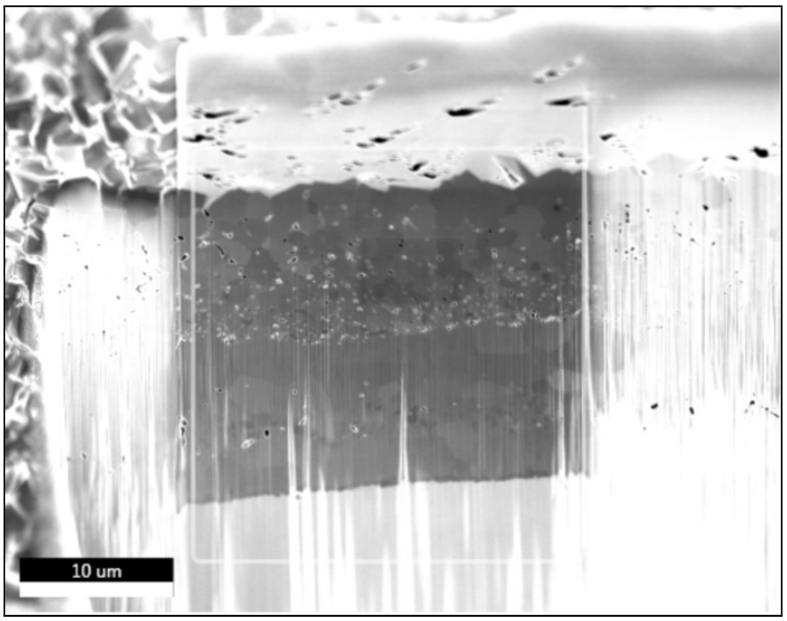

FIGURE 6.30: FIB cross section of sample on small chamber with shower head

The average thickness of the samples was 20 μm, which compared to the 70 nm of the very first deposition achieved on the copper match box is a major improvement: the efficiency, in this case, raises to nearly 50 %.

Figure 6.30 also shows two very distinct types of growth: for the first 10 μm of deposition the grains to grow compact and relatively large (5 - 10 μm across). The 10 μm closer to the surface of the film are instead characterized by voids and smaller grains (1 - 5 μm) that get slightly larger the closer to the surface. To understand the reason of this, EDX scans were also performed on the cross sections, and are presented in figure 6.31.

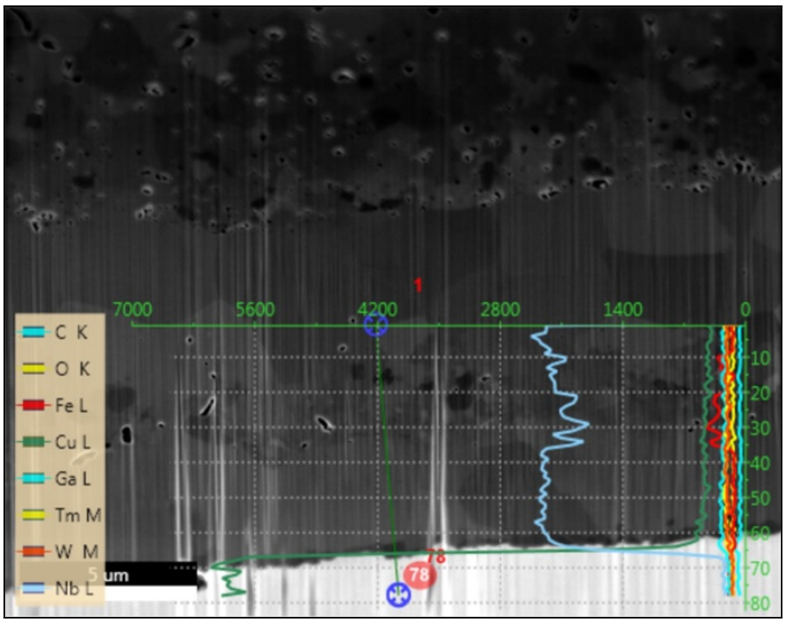

FIGURE 6.31: EDX scan of the cross section of figure 6.30

The elemental mapping shown in figure 6.31 was performed on the first 10 μm of deposition. The red line represents the concentration of iron, Fe, present in the sample. Fe is incredibly detrimental to SRF properties and even a small concentration in the film can negate any superconductivity. This had not been found on any other samples before, so further investigations were conducted to isolate the source the contamination. A more detailed scan of the area is shown in figure 6.32.

The presence of iron in the sample is shown by the EDX maps. From figure 6.30 and (figure 6.32) it can be seen that the concentration increase of Fe corresponds to the different film structure. The area of high Fe concentration shows dark spots, which could either be voids or Fe grains, surrounded by small grains of Nb. This is even more evident in the part of the film closer to the surface, where the contamination and consequent structure change seems severe.

This was found on all the samples grown with the shower head in the small chamber. Since the shower head was made of steel, it was therefore removed to rule out its contribution to the contamination. Since the Fe was concentrated in the middle to top part of the previously deposited films, the deposition time was also shortened from 4 hours to 2 to see if the deposition could be stopped before the Fe contamination started. Figure 6.33 shows a FIB cross section of a sample grown in the same conditions, but for 2 hours and without shower head.

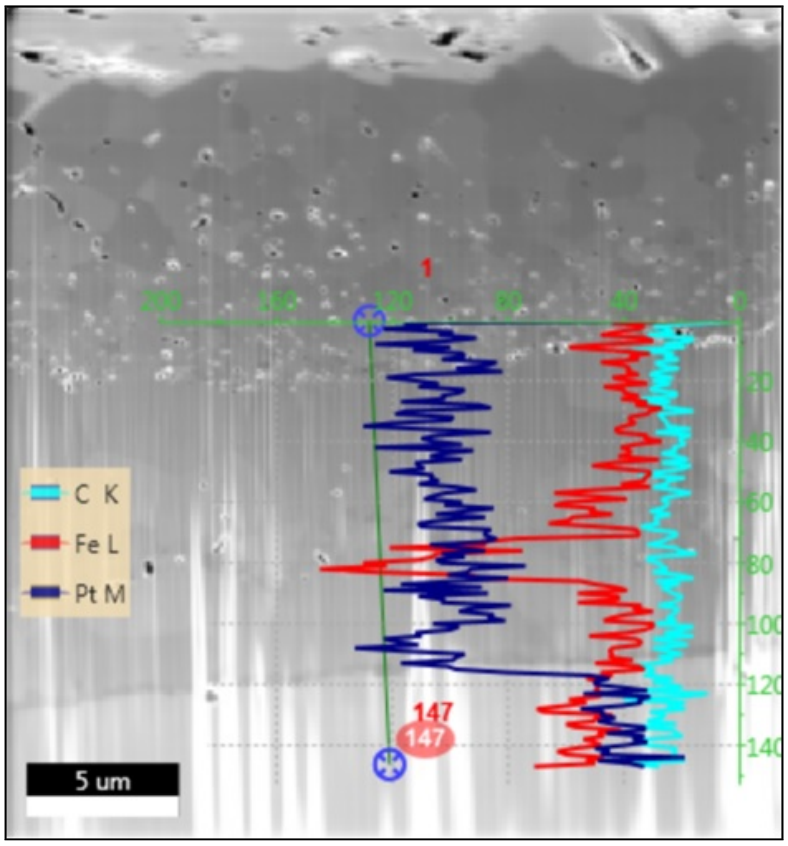

FIGURE 6.32: Detailed scan of area containing Fe

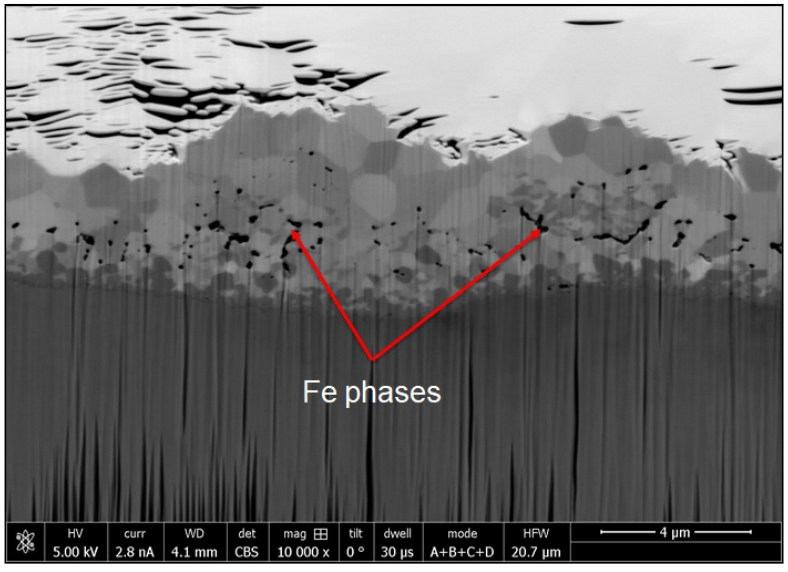

FIGURE 6.33: FIB cross section of sample grown for 2 h and without shower head

The darker areas in figure 6.33 are not voids but Fe contamination, and the growth structure is similar to the Fe contaminated area in figure 6.30, with small crystals irregularly distributed. In this case, though, the 2 μm of film closer to the surface show relatively large Nb grains and do not show any voids or dark spots, suggesting that the Fe did not contaminate the film in the final stages of the growth. Since Fe was

still present, removing the shower head reduced the amount of Fe included in the film, without neutralizing it.

The contamination distribution was not homogeneous in the samples deposited: if the Fe was present and dispersed in the entire samples thickness that would have suggested a problem with the precursor delivery, such Fe contamination in the bubbler. This way the Fe would have been incorporated with the Nb during the growth, being delivered at the same time.

Removing the shower head did affect the deposition by reducing the Fe concentration, but did not resolve the problem since contamination was found in the samples deposited with or without it.

The reason for this contamination was therefore attributed in part to the shower head, and in part to the top flange: due to the small volume of the chamber, the top flange during deposition reached 300 °C. It is known that hydrochloric acid attacks and sequestrate the cromium in the stainless steel, forming H_2 and $CrCl_2$. The higher the temperature and concentration of the HCl, the more severe the effect. In our conditions it is possible that this reaction compromises the steel leaving Fe exposed over the sample. Since the FIB images show dark spots randomly distributed in the films, it is possible that exposed μm sized Fe particulates were dislodged from the shower head or top flange by either the gas delivery or by small vibrations to then fall down or be carried by the gases to the growing film.

Since this phenomenon was attributed to the geometry of the chamber and too random to control, the reactor was so deemed unusable for Fe-free Nb depositions.

6.2.4 Larger vertical chamber

From the experience acquired from the small vertical chamber, a new reactor was sourced. An identical stainless steel tube was manufactured, with a length of 20 cm instead of 10 cm. The remaining parts (heater, top and bottom flanges) were kept the same, with the removal of the shower head. Figures 6.34 and 6.35 show the results of the simulations run on the chamber. Thanks to its symmetry, it was computationally easier and therefore possible to explore a 3D simulation.

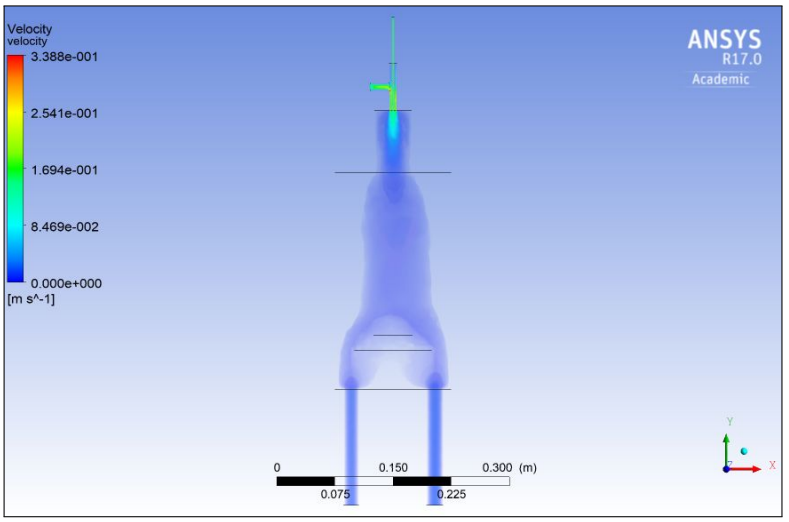

FIGURE 6.34: Gases velocity profile for the larger vertical chamber

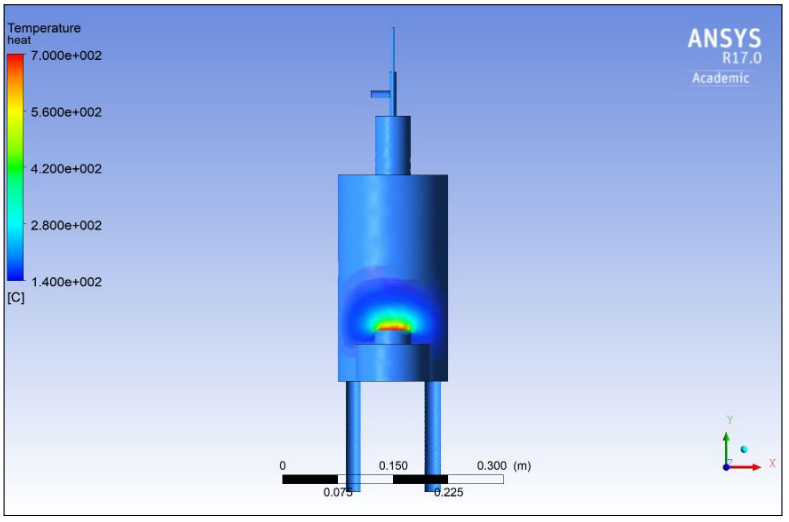

FIGURE 6.35: Temperature profile for the larger vertical chamber

It can be noted that the gases enter the chamber and slow down before reaching the substrate, preventing the gases jet from cooling the substrate and compromising the deposition. Niobium was successfully deposited in this chamber, and the results are presented in chapter 7. Niobium nitride and niobium titanium nitride depositions with ammonia gas as a co-reagent were also attempted, but some modifications had to be made to the top flange.

The first attempt of NbN did not produce any growth, but a solid deposit at the connection where the Ar + precursor and the NH_3 pipes meet. The temperature in that area was measured at 200 °C, sufficient to trigger the deposition reaction. A custom flange (identical to the one used at the bottom of the chamber) was installed at the top of the chamber, with the precursor entering from the centre and the co-reagent entering from one of the side ports, as shown in figure 6.36.

FIGURE 6.36: Custom flange installed at the top of the chamber: the precursor enters with carried by Ar through the middle pipe, while the co-reagent (hydrogen of ammonia) enter from the left port

The second attempt was partially successful: the sample did not show any growth but the chamber walls did. A dark grey deposit, possibly as Nb_4N_5, was evenly distributed from the top of the chamber down to the bottom (figure 6.37).

FIGURE 6.37: Images of the grey deposit after the NbN deposition

This suggests that the precursor was reacting with the NH_3 before reaching the surface of the substrate. A balance between the delivery of the precursor close to the sample but risking the surface cooling and far from the sample but having no precursor left was found by modifying the delivery system, as shown in figure 6.38 and figure 6.39.

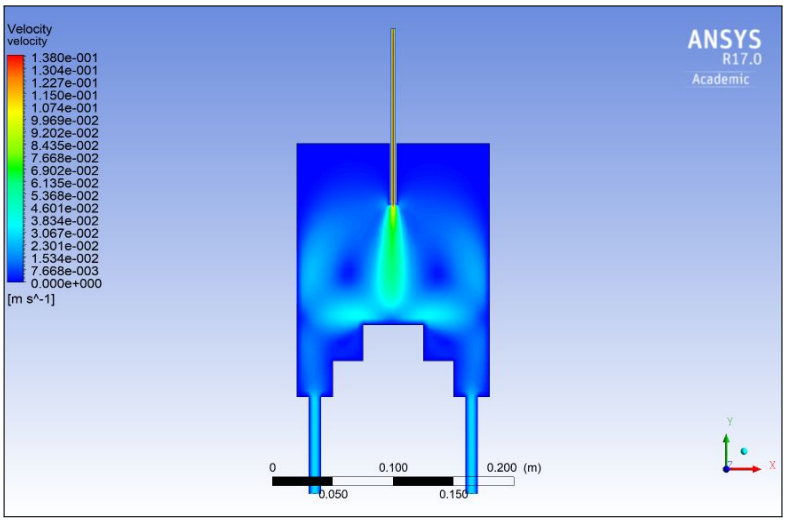

FIGURE 6.38: Gases velocity profile with the addition of the delivery pipe

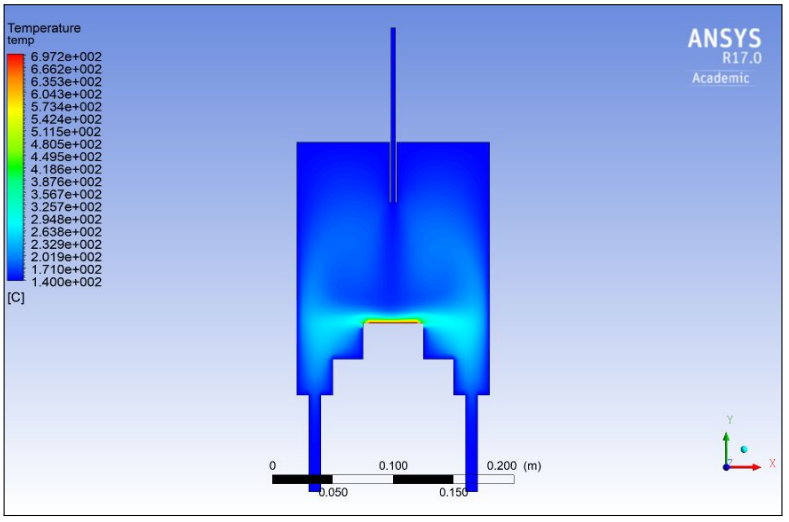

FIGURE 6.39: Temperature profile with the addition of the delivery pipe

The precursor pipe was extended inside the chamber, and different heights relative to the sample were tried. The results will be discussed in chapter 7.

6.3 Conclusion

The deposition systems have been iteratively improved, as seen on the increased deposition rate from the first chamber to the large vertical chamber. The use of fluid dynamics simulation has helped this process greatly and aided in the troubleshooting. The next step for the deposition chambers now is to evolve to 3D samples, to start a deposition program on simple cylindrical shapes, as a step in the cavity coating direction, even though this will certainly require some adjustments (heater redesign).

Chapter 7

Thin film for SRF deposited via CVD and PECVD

In this chapter the depositions obtained with the reactors described in chapter 6 are presented. The results and the practical feasibility of SRF coatings for particle accelerators are discussed.

7.1 Niobium depositions using $NbCl_5$

7.1.1 Substrate choice

One of the objectives of this work is to deposit niobium and niobium alloys by using CVD and assess their superconductive properties for potential accelerator applications. As discussed in the introduction, the rationale behind thin films on copper is to reduce the costs driven by the niobium, being an expensive material, and by its poor thermal conductance, that increases the cost of the cryogenic systems. To replicate the possible end goal, a copper cavity, the substrates chosen for the depositions were oxygen free copper disks, 5 cm in diameter by 2 mm in thickness. These disks are produced by K.J. Lesker out of oxygen free copper and were cleaned prior to deposition by ultrasonication in distilled water, then acetone (Sigma Aldrich, 99.5 % purity, CAS 67-64-1) then isopropanol (Sigma Aldrich, 99.5 % purity, CAS 67-63-0).

As discussed in 7.1.6, using Cu substrates becomes a hindrance when superconducting measurements are performed, due to the techniques available to us (RRR and SQUID). The complete destruction of the substrate is needed to explore the superconductive properties of the thin films.

Ideally, silicon would be a better substrate, since it does not interfere with the measurements. Silicon substrates were used but quickly abandoned: the films did not adhere to the substrate, regardless of the deposition conditions. The deposited films were flaky, and the film would break apart as soon as it was removed from the deposition chamber. This was attributed to the large difference in lattice parameters between Nb

and Si (0.3294 nm against 0.5431 nm), leading to a high mismatch between the film and the substrate.

An intermediate way was attempted: Cu disks were coated by Atomic layer deposition with 50 nm of MgO and Al_2O_3, in an attempt to insert an electrical insulating layer between the niobium films and the Cu substrate. The deposition outcomes did not differ from the silicon substrate ones, though, and this path was also abandoned.

It could be possible to reduce the stresses between the film and the substrate by heating and cooling down at a very slow rate (1 degree / minute), but with our heating system this was not possible or achievable.

The depositions presented from here onwards were all done on Cu substrates. The results shown have been obtained with the large vertical thermal CVD chamber discussed in section 6.2.4 unless specified, as for the PECVD chamber for the results presented in section 7.1.10 and with the 6 way cross piece chamber described in section 6.2.2 for the results presented in 7.2.1 and 7.2.2.

7.1.2 Deposition parameters study

7.1.2.1 Importance of precursor flow

As discussed in chapter 5 and 6, the precursor chosen for the deposition of pure Nb metal was $NbCl_5$. The main reason was cost, followed by availability. To guarantee the precursor flow to the reactor, the pipe lines had to be heated to a temperature higher than the temperature of the bubbler: if this is not the case, the precursor condenses on the cold spots, causing at best no deposition, while in the worst case scenario a solid occlusion, or clog. This can be generally fixed by heating up the lines, but when it is not sufficient the only solution is dismantling the suspected clogged line and clean it or replace it. Atmosphere leaks in the vacuum system are also detrimental to the precursor delivery, since through them moisture can enter the pipe lines and react with the precursor creating niobium oxychloride phases, also clogging the pipes. It was found that 10 °C above the precursor temperature are enough to prevent any condensation, as long as the lines are leak tight.

7.1.2.2 Pressure

The deposition pressure in CVD is one of the governing parameters that control the properties of the final film. Three different deposition pressure were tried, to see how this would affect the film growth. Sample temperature (700 °C), precursor temperature (130 °C), argon and hydrogen flow (100 sccm) were kept constant for the depositions. The pressure in the chamber was regulated via a valve on top of the pumping assembly.

Table 7.1 shows the results of this trial: the lowest pressure tried, 1 mbar, did not lead to any growth of the film that was measurable with the instruments at the time available (EDX): since its lower detection limit is $\approx$ 1000 ppm in weight of a given element, and knowing that at 15 KeV the sampling depth is roughly 1 μm, anything thicker than 10

Deposition Pressure (mbar)	Growth	Notes
1	No	/
5	Yes	Satisfactory
10	Yes	Flaky

TABLE 7.1: Different growth pressures and visible effect on the film

nm should produce a signal stronger than the background [121]. This was not the case for these samples. The cause was attributed to the higher pumping speed needed to achieve the lower pressure in the chamber, which may have extracted the precursor too quickly not leaving it enough time to react on the surface of the sample.

On the contrary, at the highest pressure chosen, 10 mbar, the growth on the substrate was very different. The film cracked and came off the substrate while the deposition was running (visible through a viewport on the side of the deposition chamber), so with both the film and the substrate very hot; a mismatch in expansion coefficients was therefore ruled out. The cause of this poor adhesion and delamination was attributed to a too high concentration of precursor in the chamber, with the film nucleating on the substrate to then grow normal to the surface instead of across it.

At a pressure of 5 mbar, the deposition was deemed satisfactory, with all the substrate covered and a well adherent film. Kapton tape was used to conduct a preliminary check of the adhesion of the films, covering the sample with 2 cm of tape, waiting for 30 seconds and then pulling it away. This was devised in house to have an indication of the adhesion of the films, since using a standard scotch test requires the scoring of the film with a blade, compromising the structure of the films and preventing any SRF test.

The pressure for all the depositions was so set at 5 millibar.

7.1.2.3 Temperature

The deposition temperature is another crucial parameter for CVD. The heat provides energy to the molecules taking part in the reaction, allowing the equilibrium to shift from the reagents to the products. Moreover, this translate in faster and more efficient reaction rates, which translates in faster growth rates. A high temperature, according to the reactions studied, may be necessary to remove some unwanted products trapped in the film [122].

For this work, three temperatures were studied: 500 °C, 600 °C and 700 °C. Lower temperatures were considered and attempted, but no Nb films were detected via EDX or SEM on the substrate. 700 °C was chosen as the limit for copper substrates. Copper melts at 1085 °C, but begins to soften at 750 °C.

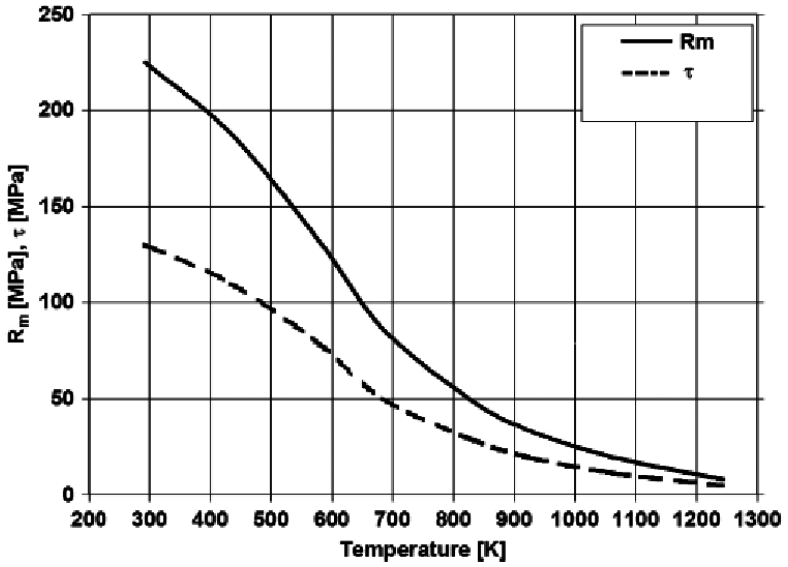

FIGURE 7.1: Dependence of copper tensile strength (Rm) and shear strength (τ) on temperature

Figure 7.1 [117] shows that already at 700 °C Cu mechanical properties are greatly diminished: going to a higher temperature may benefit the niobium growth, but (as discussed in section 6.2.3.3) it will compromise the substrate. Hence the temperature of 700 °C was chosen as highest deposition temperature.

7.1.3 SEM results

Being able to see the film grown on the substrate is not sufficient to assess the presence of a deposit on the substrate surface, which is why microscopy was performed. In this section the SEM results for the samples obtained at three different temperatures are reported.

7.1.3.1 500 °C

Figure 7.2 shows an SEM image taken on the surface of the sample obtained at 500 °C.

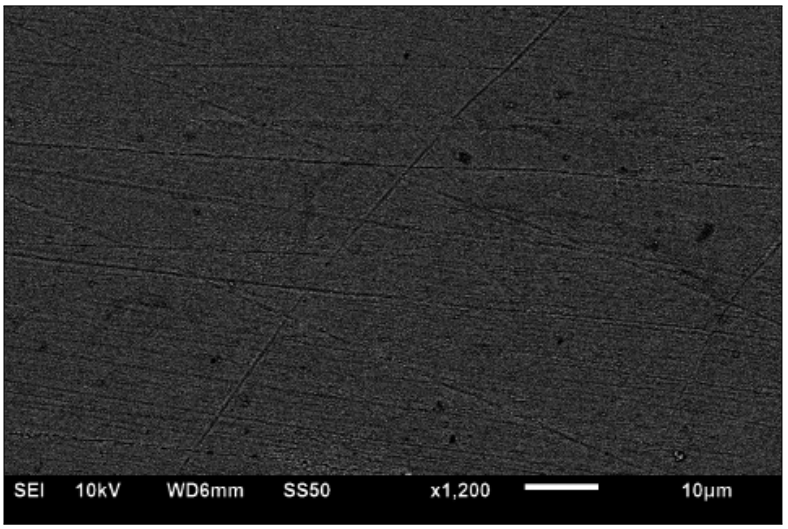

FIGURE 7.2: SEM image of sample obtained at 500 °C

The 500 °C depositions are characterized by a lack of features on the surface of the film, due to the very low film thickness. The cross section of the films, as previously shown in figures 6.12 and 6.13, together with the EDX scan (figure 6.11) proves that the film thickness is less than 100 nm. The sample shows straight lines going across the surface. These are scratches that were present on the substrates before the deposition and, since the thickness of the film is smaller than the scratches width, remained visible in the SEM images. The samples were washed thoroughly before each deposition process, but not polished, hence why the presence of scratches. These surface features disappeared in the samples obtained at higher temperature, thanks to thicker coatings filling the scratches in.

7.1.3.2 600 °C

Figures 7.3 and 7.4 were taken on a sample prepared at 600 °C. The surface of the film now looks very different: the scratch marks seen in figure 7.2 are not visible any more, probably coated over. The features look chaotic at low magnification, but as shown in figure 7.4 are organized at short range. This suggests that the film had enough energy to nucleate and grow in an ordered way, but not enough energy to relax and dissipate the differences in growth planes once different nucleation islands would get in contact.

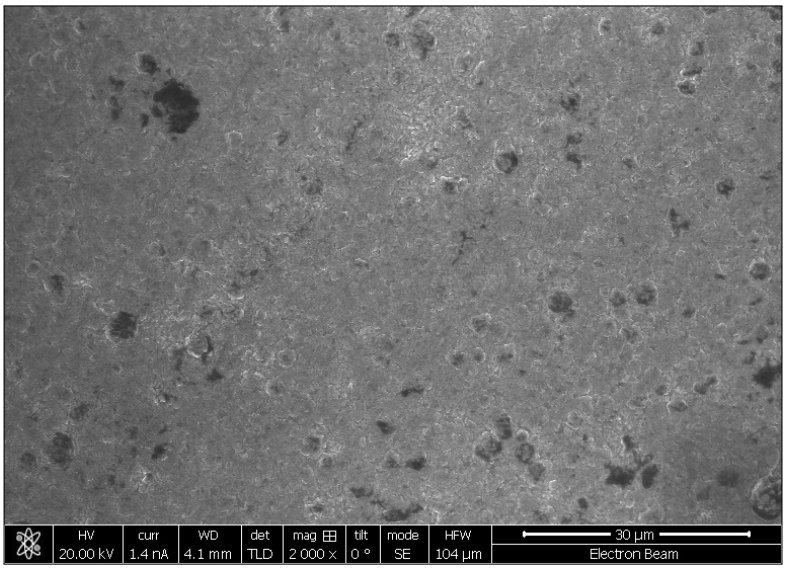

FIGURE 7.3: SEM image of sample obtained at 600 °C

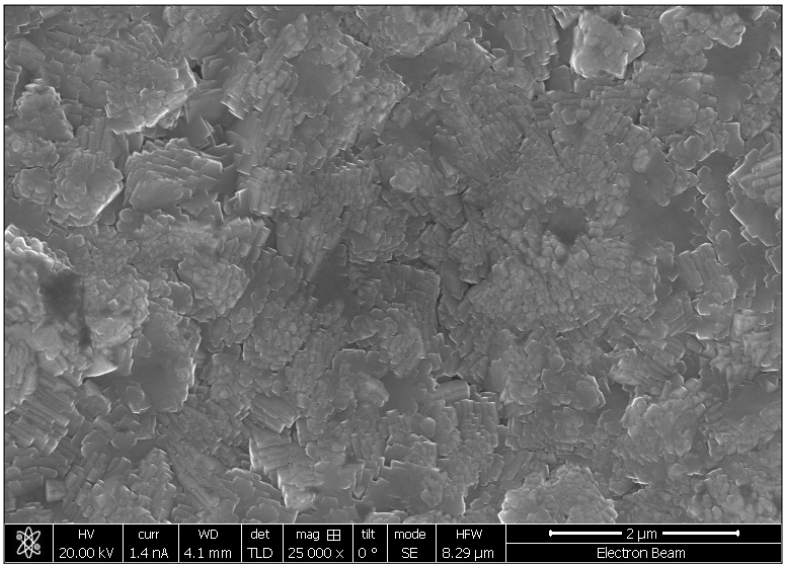

FIGURE 7.4: SEM image of sample obtained at 600 °C

The FIB cross section (figure 7.5)shows that the film is about 2 μm thick, more than 20 times the thickness of the samples prepared at 500 °C.

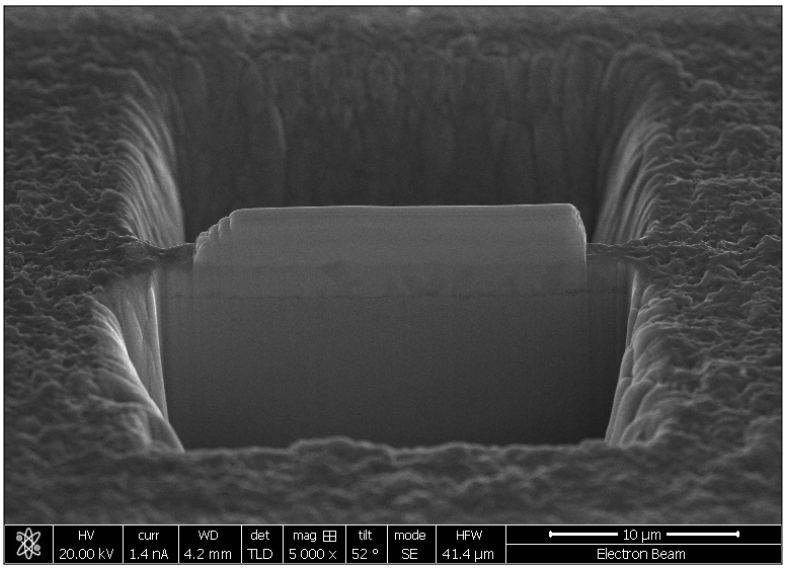

FIGURE 7.5: FIB cross section of sample obtained at 600 °C

7.1.3.3 700 °C

Figures 7.6 and 7.7 show the images taken on samples grown at 700 °C. The surface of the film now looks organized, with big crystals easily distinguishable at relatively low magnification.

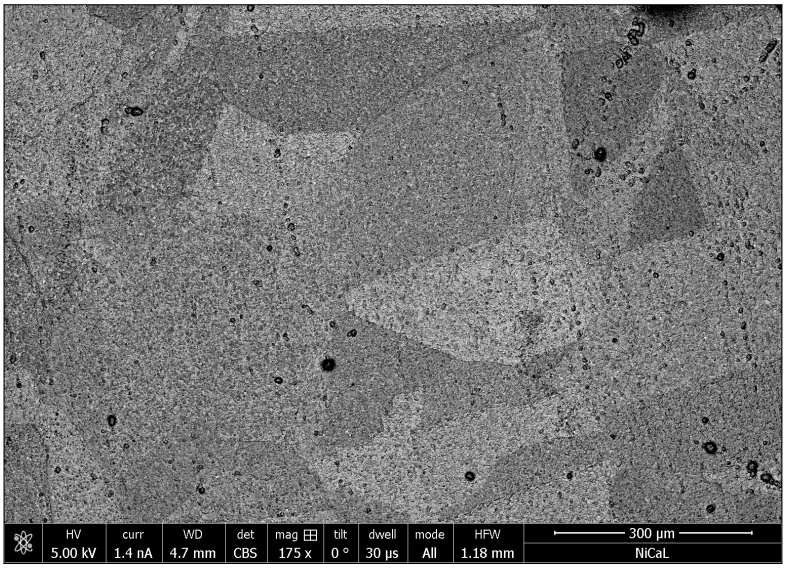

FIGURE 7.6: SEM image of sample obtained at 700 °C

The cross section shows that the film thickness now is of about 20 μm, 10 times thicker than the samples deposited at 600 °C. It can also be seen that the deposition is characterized by randomly arranged grains, neither columnar or equiaxial, smaller in size (less than 1 μm across) closer to the surface of the substrate and becoming increasingly larger (up to 10 μm across) the further away from it.

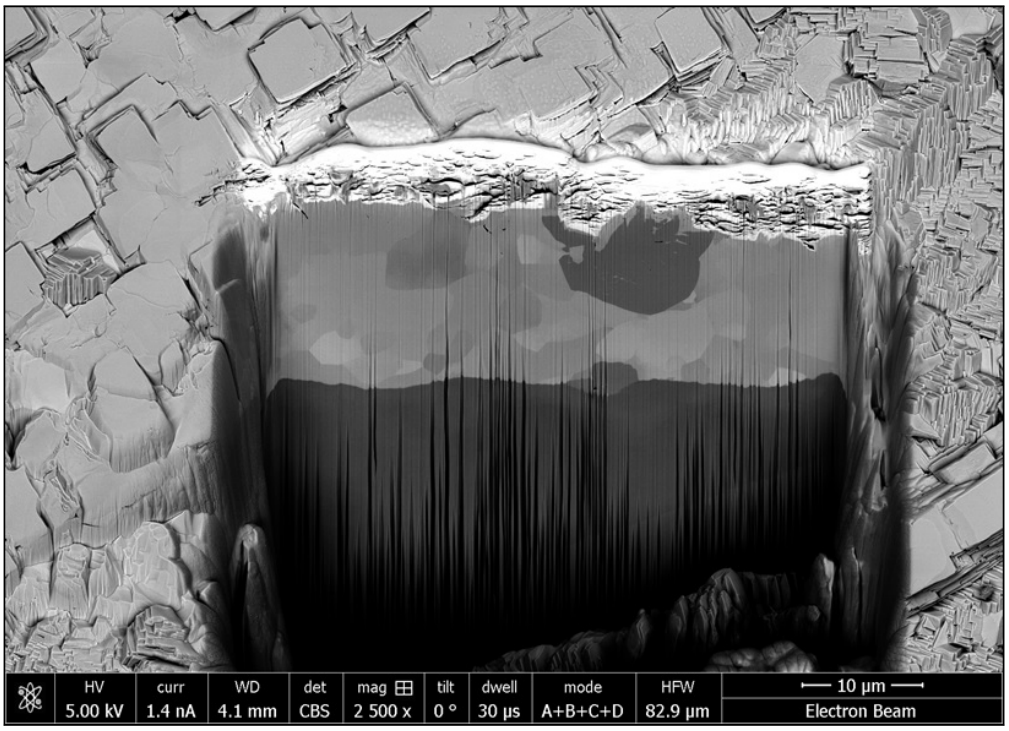

FIGURE 7.7: FIB cross section of sample obtained at 700 °C

Figure 7.8 shows how the three temperatures affect the surface of the depositions. As already discussed, the lower temperature deposition seems to create a film too thin to cover the substrate residual features. The samples deposited at 600 °C show a very different surface: the film grows in what seem to be a more organized structure, with crystallites a few hundred nm in size. A quasi random distribution of crystal orientation seems to be present: most crystallites aggregate in regularly arranged units for ≈ 1 μm, that are then randomly organized over 1 - 2 μm of distance. This also seems to create voids in the film, at least on the surface layers, where the larger crystals meet and do not coalesce. The depositions at 700 °C show an even more organized structure than the samples deposited at 600 °C: the crystals now look square, measure a few μm across, and the voids present in the lower temperature depositions have disappeared. The structure now looks tightly packed, in what seems like a planar arrangement of crystallites, which are less randomly oriented. Voids and crystal size are important parameters for SRF applications: the presence of small grains signifies a large number of grain boundaries, where impurities may aggregate. These areas can degrade the current transport properties of Nb, creating a weak superconducting region [123]. The presence of voids can increase the amount of secondary electron yield (SEY), a phenomenon through which an electron can hit the surface of the cavity and cause the emission of more than one electron, cascading the cavity into breakdown. Voids increase the surface area of the material, increasing the area exposed to the electrons and therefore the number of electrons statistically emitted after a collision. Both these parameters can be addressed once the cavity is being crafted: the grain size can be controlled by metallurgy or by manufacturing processes, while the surface voids can be reduced via polishing.

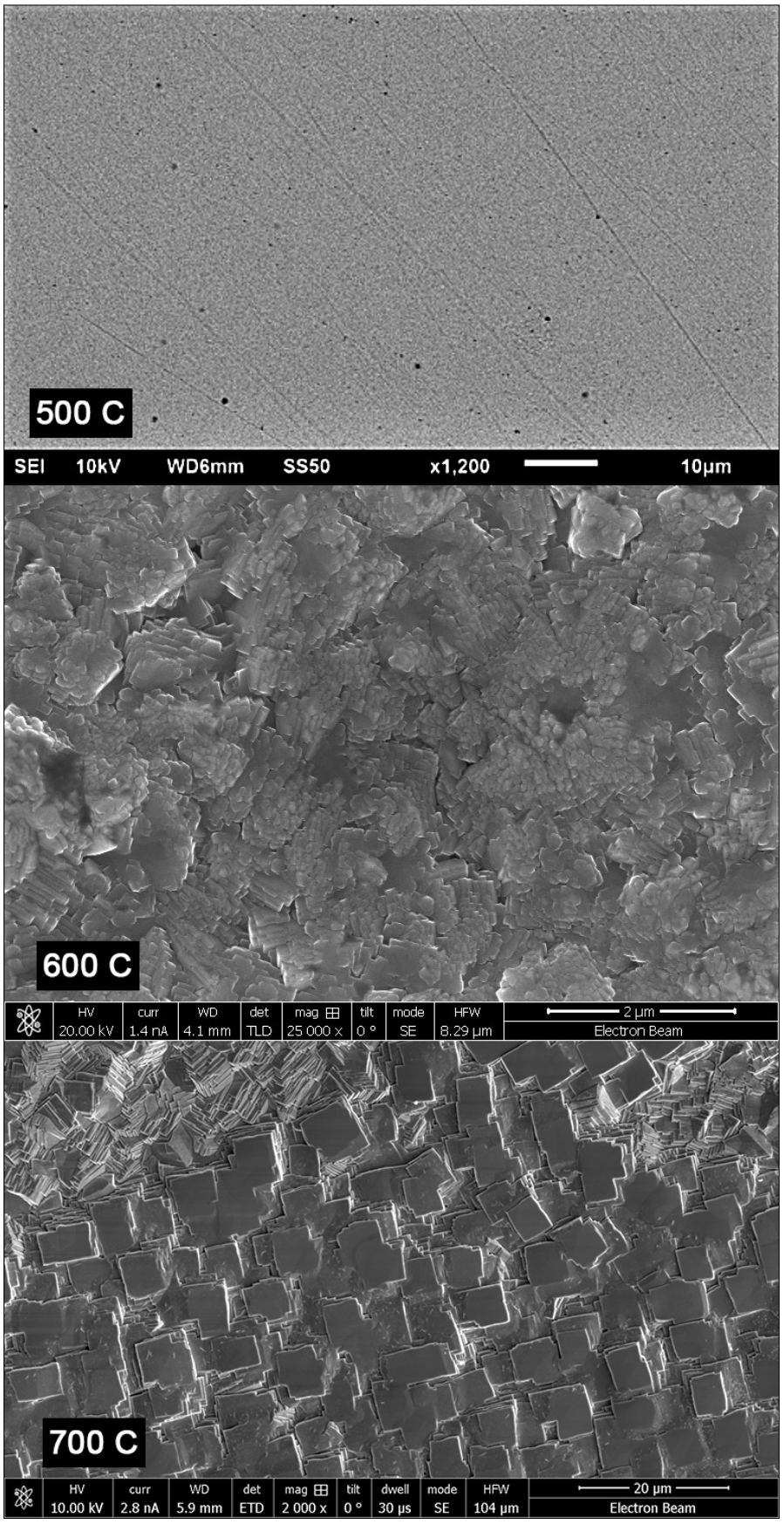

FIGURE 7.8: SEM images of the films obtained at different temperatures

7.1.4 TEM results

The SEM results together with the FIB cross sectioning were successful in helping determining the surface features and the thickness of the grown film. It was chosen to perform TEM investigations on some of the samples, to determine with a higher degree of confidence the thickness of the films and their structure. In this section the TEM results for the samples are reported.

7.1.4.1 500 °C

Figure 7.9 shows different magnifications of the sample grown at 500 °C.

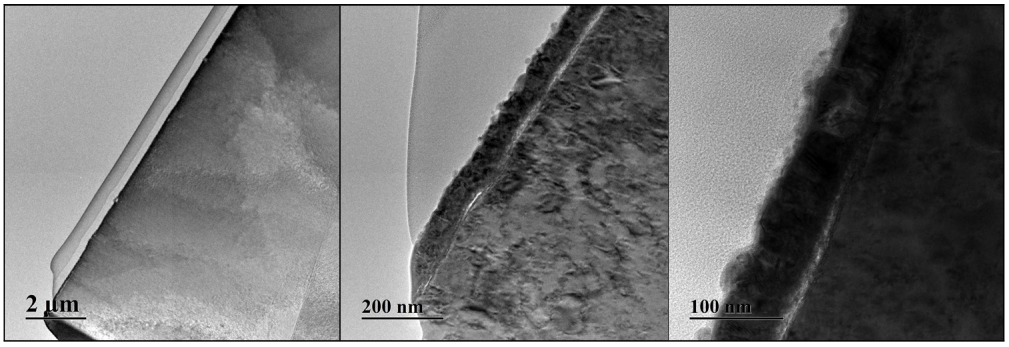

FIGURE 7.9: TEM images of sample grown at 500 °C

The figure shows that the film thickness is below 100 nm. It can be seen that there are no evident grains or crystals, being either too small to resolve or too randomly oriented. Selected Area Electron Diffracion (SAED) was therefore performed on different areas of the sample, to verify the crystallinity of the film. Figure 7.10 shows three different areas of the sample.

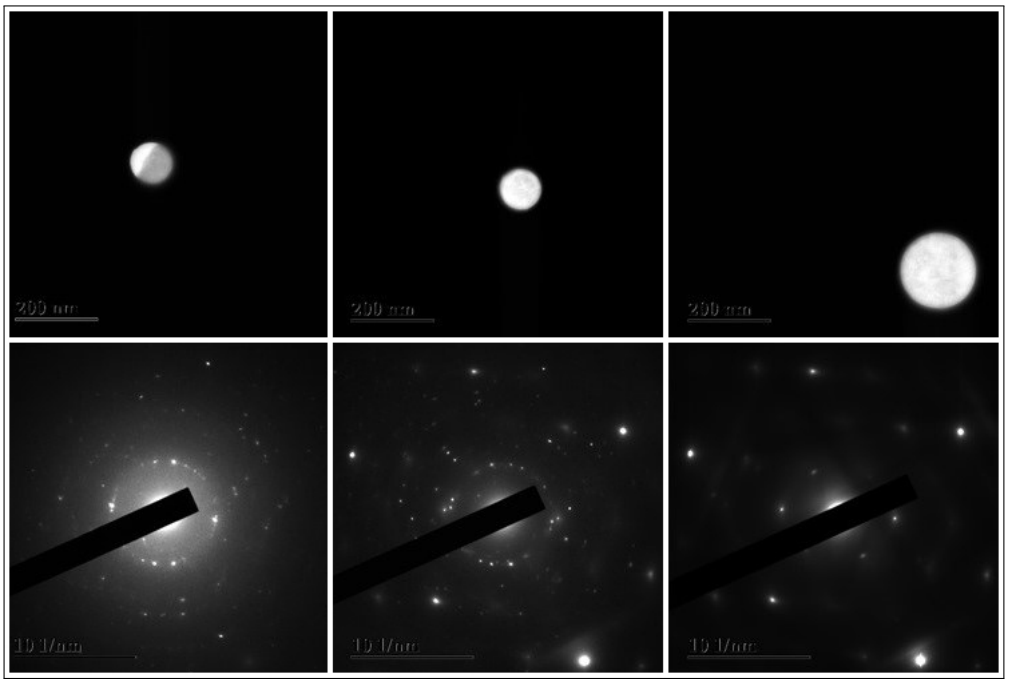

FIGURE 7.10: SAED of three areas of 7.9: left - platinum protective layer; middle - film; right - copper substrate

SAED is used to identify if a material is amorphous or crystalline. A crystalline sample will show few and well distinguished diffraction dots, corresponding to different crystal orientations. The more a material is amorphous the less defined the diffraction dots are, replaced instead by rings with the middle of the picture as their centre.

On the left, the area sampled is the platinum layer sputtered on top of the film during FIB sample preparation. As expected, the area is mostly amorphous, with a few orientations more prevalent than others (the white spots in the ring).

The right picture shows the copper substrate and, being this a bulk material, it has a clearly defined crystalline structure, noted by the few bright spots in the image.

The film is presented in the middle part of figure 7.10: due to its thickness, as already mentioned, it is difficult to clearly identify its nature since both patterns from the platinum and the copper can be seen overlapping in the SAED.

7.1.4.2 600 °C

TEM images were taken from the samples grown at 600 °C. Figures 7.11 and 7.12 show that the film is about 2 μm thick, as previously mentioned. The structure now is crystalline, with grains of about average 500 nm in size.

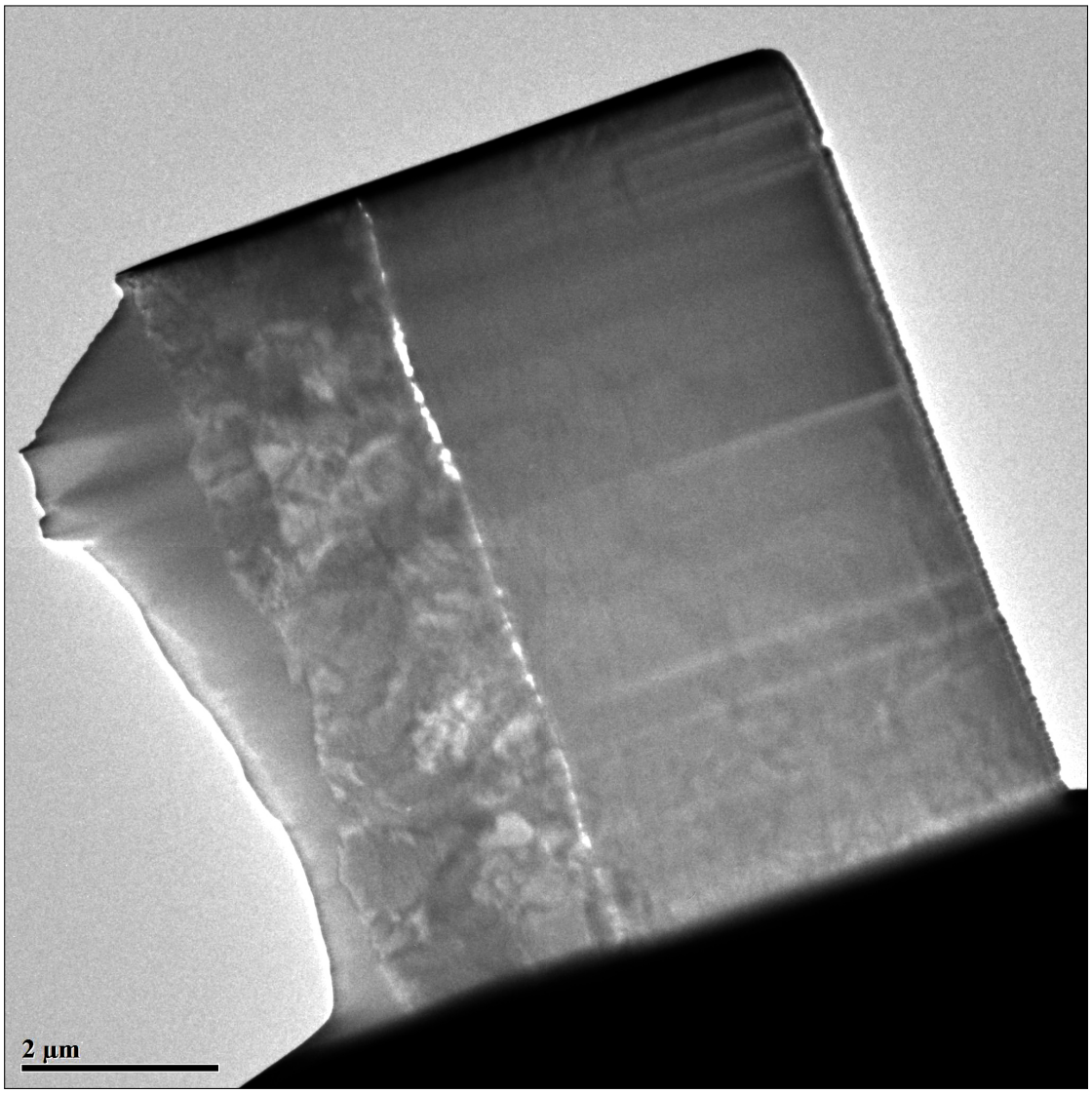

FIGURE 7.11: TEM images of sample grown at 600 °C

The deposition seems to start from small crystals close to the substrate surface, with sizes below 100 nm, to then continue in progressively larger grains, up to 1 μm in size. There is no particular grain arrangement, since they all seem to be randomly arranged. Another feature visible from the TEM image is the interface between the film and the substrate, where a very bright deposit is present. This could be attributed to even smaller grains, or to a slightly different chemical composition, as for example if the surface was oxidized. This was not, though, further explored.

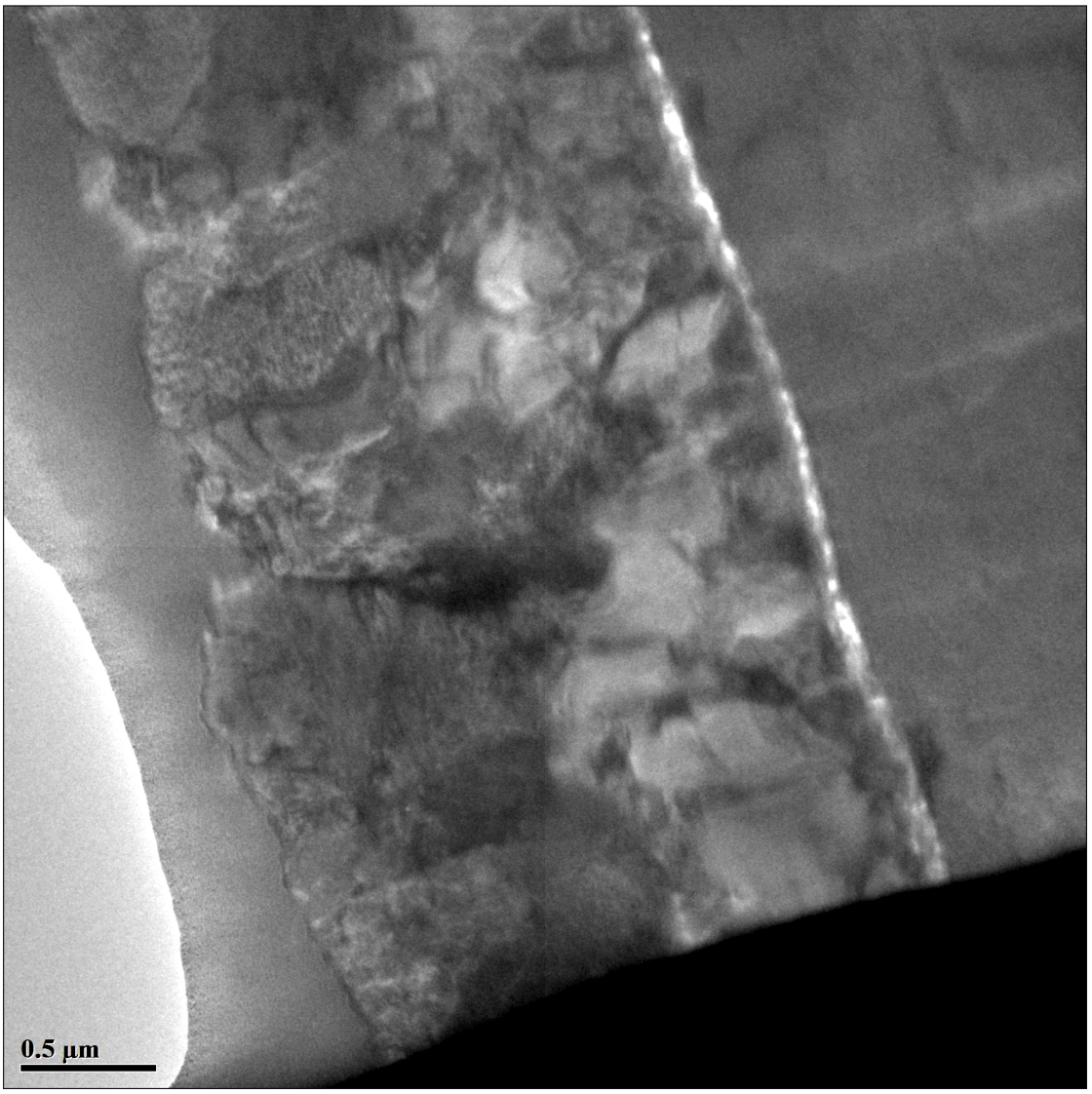

FIGURE 7.12: Magnification of the sample shown in figure 7.11

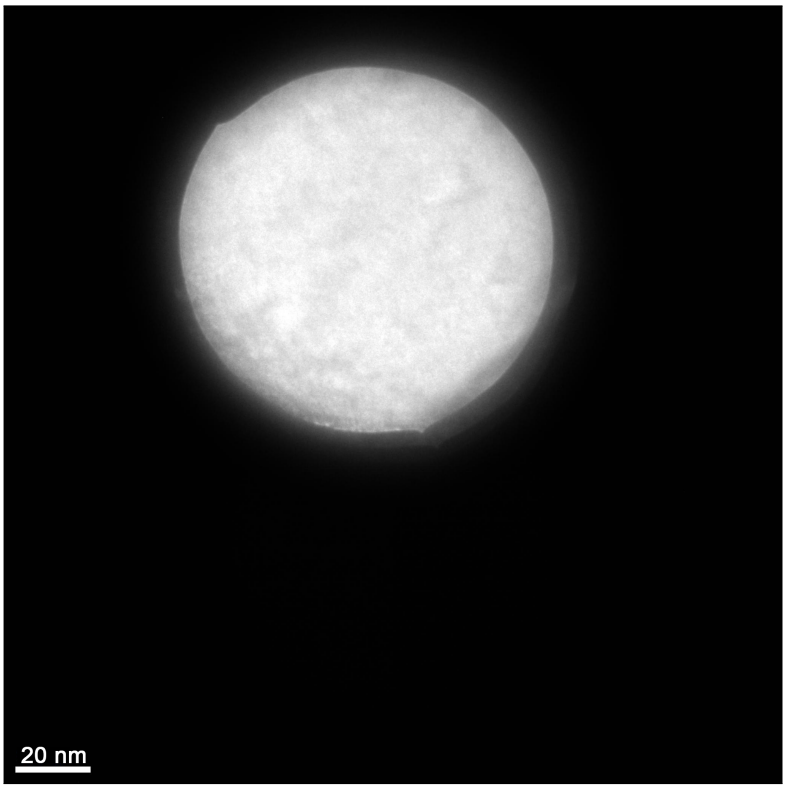

FIGURE 7.13: Area selected for SAED of sample shown in figure 7.11

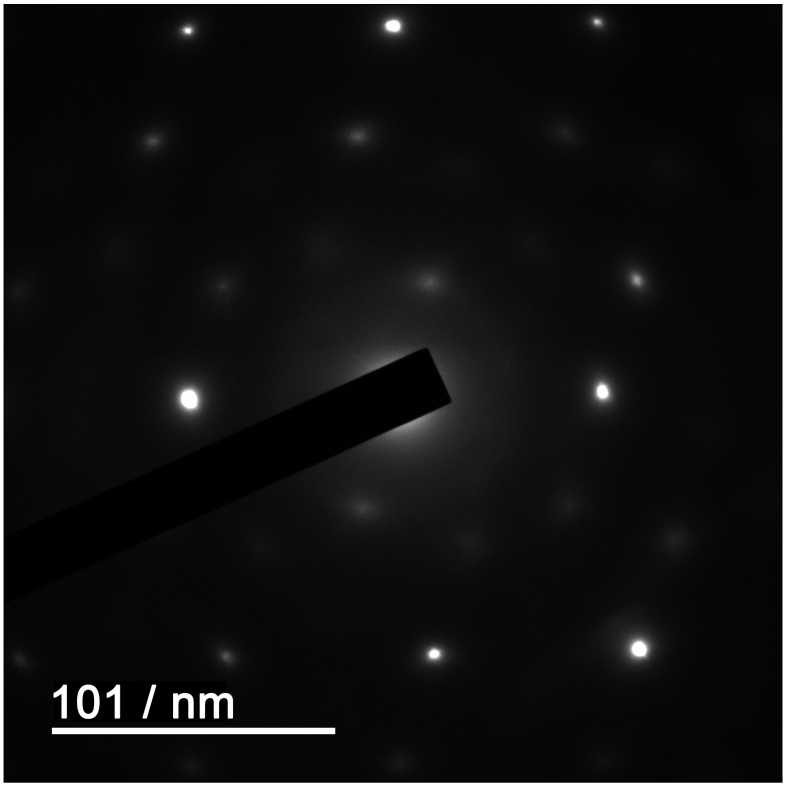

FIGURE 7.14: SAED result of sample shown in figure 7.11

The SAED shown in figure 7.14, taken from the area shown in figure 7.13, if compared to figure 7.10, looks remarkably different: while the film deposited at 500 °C shows a large number of dots arranged in a circular pattern, the 600 °C deposition shows a few dots, very well defined and bright. As mentioned before, the crystallinity of a material can be defined by how many diffraction spots are present in the pattern: the fewer spots, the more the crystallites are oriented along the same planes. In the case of figure 7.14, the small number of dots indicate that the majority of crystallites are oriented in the same direction. The size of the crystallites can also influence the diffraction pattern: randomly oriented large crystals would still be made of a larger number of atoms arranged all in the same lattice orientation than small crystallites. The consequent diffraction pattern would then show less dots than a random distribution of smaller crystallites due to less possible orientations of the few large crystallites being studied.

7.1.4.3 700 °C

As mentioned, the main reason of performing TEM imaging was to verify the films thickness and the presence of a crystalline structure. TEM investigations are though a lengthy process, from the preparation of the sample to the investigation itself. For these reasons, the TEM of the samples grown at 700 °C were not performed, since as shown in figure 7.7 the sample thickness and the crystalline structure are evident without any need for further investigations.

7.1.5 XRD results

The SEM and TEM investigation returned information on the structure of the films but, to identify the crystalline structure, microscopy can only provide a part of the information needed. This is why to investigate the crystalline phase of the deposited films, X-ray diffraction was performed. Figure 7.15 show the XRD reference pattern for niobium ([124]) compared with the spectra obtained from the samples deposited at different temperatures.

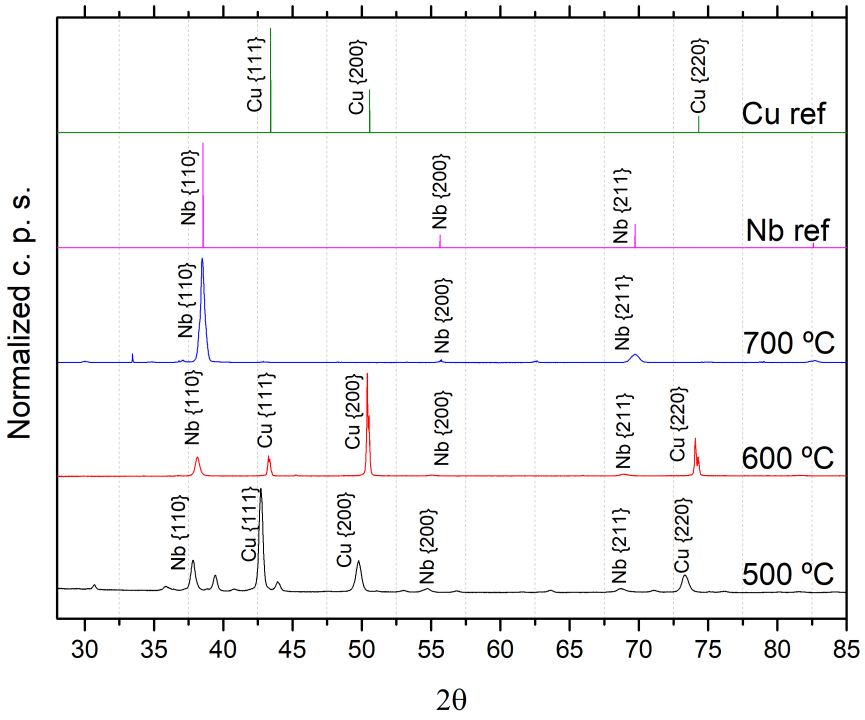

FIGURE 7.15: Niobium reference spectrum and spectra obtained from samples deposited at different temperature

The peak intensities were normalized to the most intense peak, which was the Cu {111} for the 500 °C samples, Cu {200} for the 600 °C samples and Nb {110} for the 700 °C samples. The relative intensities for the Nb peaks in the 700 °C plot seem to match the reference, with a predominant {110} orientation, followed by {211} and {200}. It is possible that the same is true for the lower temperature depositions, but the signals are to weak to affirm this with certainty.

7.1.5.1 500 °C

The thickness of the samples deposited at 500 °C presented a challenge for the XRD investigation: if the growth is thin, the x-ray beam will travel through the film and interact more with the substrate than with the film. To work around this, the XRD instrument has to be capable of performing *Grazing Incidence XRD* (GIXD). In GIXD the investigation is conducted at very low angles of incidence, to let the xray beam travel through as much film as possible, and the results are later adjusted. Not all instruments can do this: a different type of sample holder and stage that holds the xrd lamp have to be installed in the instrument and calibrated on the particular sample under study.

It can be noted from figure 7.15 that the copper peak at {111} is quite prominent, as well as the other crystal orientation of copper. Niobium is present, with the main {110} phase at 37.85 2θ. This indicates a shift from the niobium 110 reference peak at 38.53 2θ; a shift to lower angles can be attributed to compressive strain of the material.

This can be explained by the difference in linear temperature expansion coefficients [125] between copper (17 m / mK) and niobium (7 m / mK) and the very low thickness of the film: as the sample heats up to 500 °C, the 5 cm copper disk expands to 5.04 cm. After the deposition, the copper cools down shrinking to its original 5 cm diameter. This shrinkage though happens with the niobium film on the copper substrate. Niobium would shrink from 5.04 cm to 5.02 cm, due to its lower thermal expansion coefficient being smaller than copper. As the film is very thin, it does not have the mechanical strength to oppose this reduction, ending up compressed as seen in the XRD peak shift.

7.1.5.2 600 °C

Figure 7.15 shows the XRD of one of the samples grown at 600 °C. For these and the 700 °C deposition temperature samples it was not necessary to perform GIXD, but standard XRD. Compared to the spectrum of the deposition at 500 °C, the 600 °C film shows one niobium peak at 38.13 2θ, indicating that the stress in the film is lower than the samples deposited at lower temperature, but still present. The copper has also been affected by the temperature, with the {200} phase now more prominent than the {111}, indicating that at 600 °C the substrate is already starting to change and shift. The copper substrate used for the deposition at 500 °C shows the {111} peak at 42.72 2θ, where the reference shows the same orientation at 43.42 2θ. For the deposition at 600 °C, the {111} peak is at 43.27 2θ, only 0.15 2θ away from the reference. For the 700 °C deposition the peak was too weak to be identified, possibly due to the thickness of the film. Similarly to the 111 plane, the {200} peaks are respectively at 49.78 2θ for the 500 °C and 50.4 2θ for the 600 °C depositions, where the reference is at 50.57 2θ. This trend can be seen for the {220} plane, with 73.35 2θ for the 500 °C and 74.07 2θ for the 600 °C depositions, where the reference is at 74.32 2θ. For the samples deposited at 700 °C the copper signals were too weak to be clearly identified, as mentioned probably due to the thickness of the Nb film, so nothing conclusive can be said about it.

7.1.5.3 700 °C

The first thing that can be noted from the spectrum obtained from the 700 °C deposition is the absence of the copper peaks. The thickness of the film, about 20 μm, provides enough material for the XRD beam shielding the substrate.

The second thing is the matching between the reference and the deposited sample. As per reference, the niobium {111} peak is at 38.54 2θ which is separated by 0.06 2θ from the sample Nb {111} peak at 38.48 2θ. The deposited film is still stressed, but less so than the samples deposited at lower temperature, suggesting that the thickness of the film is absorbing the substrate compression better than the thinner films.

7.1.5.4 Nb and Cu strain ($\epsilon\%$)

The strain were calculated for the Nb and Cu peaks using equation 4.5. The results are showed in figure 7.16 and figure 7.17. The error bars are present in the Nb and Cu figures, but may not be easily visible especially in the Cu data due to the error being small compared to the magnitude of the strain.

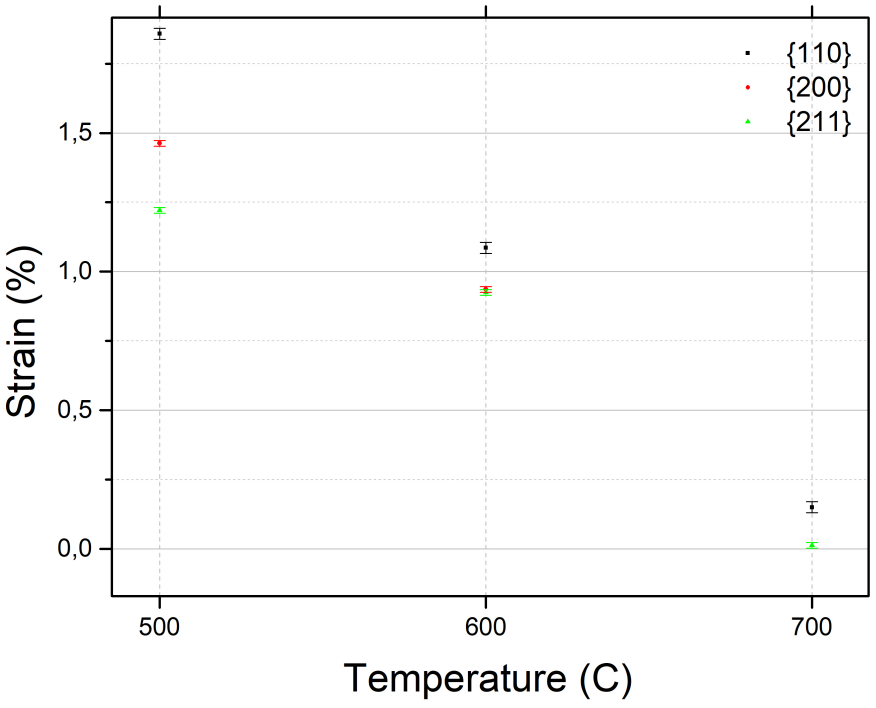

FIGURE 7.16: Strain % values for the three Nb planes analysed obtained from the Nb samples at different temperatures

The Nb results shows that the strain is relatively high for all the planes in the sample deposited at 500 °C, decreasing for the deposition at 600 °C and nearly disappearing for the films obtained at 700 °C. These results suggest that the increase in temperature leads to a less strained film. The increased thickness leads to increased mechanical resistance, which seems to reduce the effects of the substrate thermal expansion on the film structure.

The strain for each measurable Cu peak were calculated and are reported in figure 7.17.

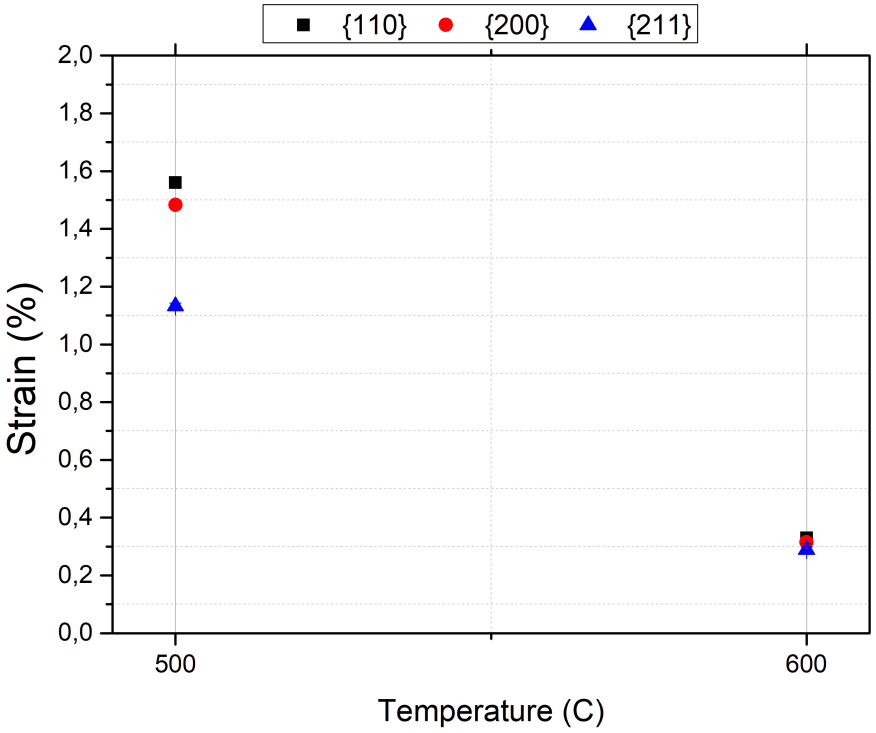

FIGURE 7.17: Strain % values for the three Cu planes analysed obtained from the Nb samples at different temperatures

These results suggest that the substrates are strained but as the temperature increases, the strain is reduced considerably. It is possible that at 600°C, even if at the edge of the softening range, the microstructure of the substrate changes. Since the substrates history and processing is uncertain, it can only be assumed that during their production the substrates are subjected to a treatment (pressing, cooling, cutting) that forces the crystallites to assume a preferred orientation. Once heated to 600 °C, the residual stresses present in the material begin to be relaxed, leading to a change in the orientation of the crystallites from the {111} phase to the {200} phase.

7.1.5.5 Crystallite size

From the XRD results, an estimate of the size of the crystallites can be derived by using the Scherrer equation [126].

Deposition Temperature (°C)	**Peak Position (2θ)**	**FWHM (2θ)**	**Wavelength ($\AA$)**	**Crystallite size (nm)**
500	37.82	0.47	1.5406	18.65
600	38.13	0.38	1.5406	23.09
700	38.48	0.30	1.5406	29.31

TABLE 7.2: Calculation of the crystallite size with the Sherrer equation

Table 7.2 shows the results obtained from the XRD results. The crystallite sizes are a loose estimate, and not matching the SEM and the TEM results. This can be attributed to the nature of the Sherrer's equation, since the it assumes an uniform distribution of small crystals, as it was originally devised for XRD of powders. Other techniques can be used to determine the size of the crystals, like Electron back scattering diffraction (EBSD, [127]).

7.1.6 RRR results

One of the aim of this work is to prove that accelerator grade niobium can be deposited on copper with chemical deposition techniques. Depositing niobium that is not superconductive would not be useful for a cavity, and to verify this the sample Residual resistivity ratio was measured.

The RRR of a film gives an indication of its performance once placed in a RF field. For niobium, the highest the value the better the performance, since this implies a very low resistivity at very low temperatures. To perform the analysis, as explained in chapter 4, the samples were covered with kapton tape and immersed in 100 ml of 1:1 solution of water and nitric acid until full dissolution of the copper substrate. This was necessary because of the electrical conductivity between the film and the substrate: by applying the 4 point probe on the film, the measurement would be done on the resistivity of the copper as well, which has RRR values between 50 and 700 [128].

The method did not always work. The thickness of the samples grown at 500 °C proved to be insufficient for this technique: once etched away, the film would be too delicate to resist any sort of manipulation - even stabilized on the kapton. This would translate in a poor electrical contact between the film and the four point probe, returning an open circuit signal between the two +I and -I pins.

To investigate this issue, high resolution SEM was performed on the film after the transfer to the kapton tape.

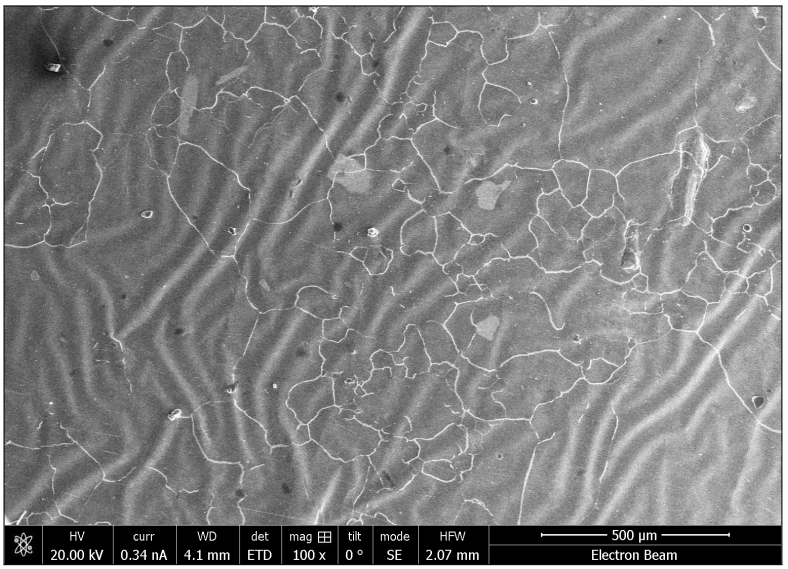

FIGURE 7.18: High resolution SEM picture of film grown at 500 °C once removed from copper substrate

Figure 7.18 shows two main features: the kapton tape was corrugated and the film was fragmented. The corrugation of the kapton was probably due to the way it was applied to the samples: the tape was applied to one edge of the sample and slowly lowered onto it, carefully applying pressure. This may have introduced some stretch in the tape, that released when the substrate was etched away creating ripples tens of microns in size, and not noticeable by naked eye. The film fragmentation was attributed to the same effect. The lack of thickness of the material made it inherently fragile and with very low mechanical properties, so when the kapton relaxed it pulled the film with it, creating cracks and valleys. Figures 7.19 and 7.20 show the cracks in the film at a higher magnification.

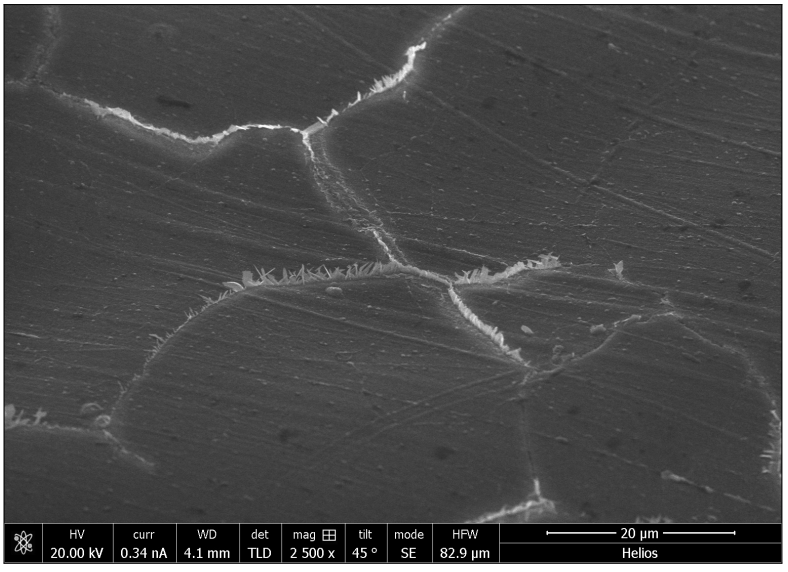

FIGURE 7.19: High resolution SEM picture of film grown at 500 °C once removed from copper substrate

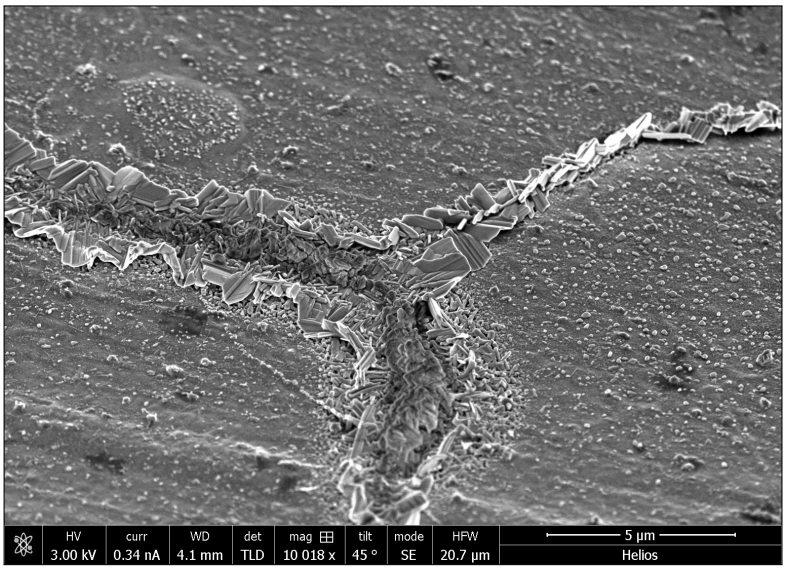

FIGURE 7.20: High resolution SEM picture of film grown at 500 °C once removed from copper substrate

This was the reason for the open circuit between the probe current pins: the microscopic fragmentation of the film united to a lack of thickness made it impossible for the current to travel through the film, making the measurements impossible to perform.

This issue did not present itself when testing the samples grown at 600 °C and 700 °C, thanks to the thickness of the films being considerably larger and the film capable of bending with the kapton without fracturing.

The RRR for the samples deposited at 600 °C was measured, as it is shown in figure 7.21.

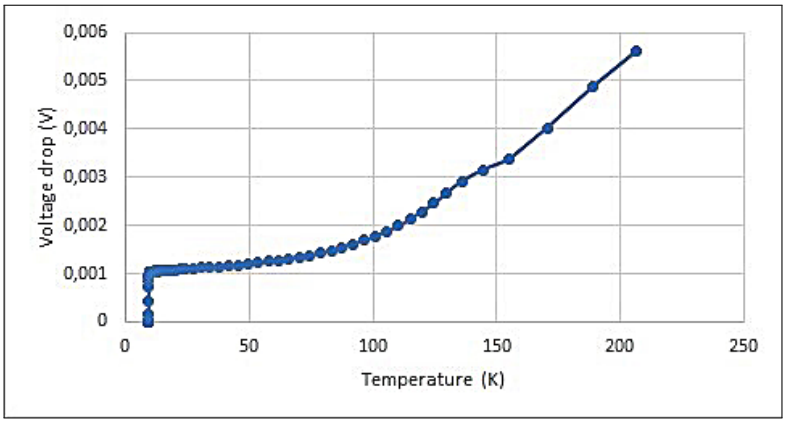

FIGURE 7.21: Voltage drop curve versus temperature of sample deposited at 600°C

The voltage drop at room temperature was measured at 10 mV, and, from the voltage drop at 10 °K, the RRR was calculated for this sample at 10.

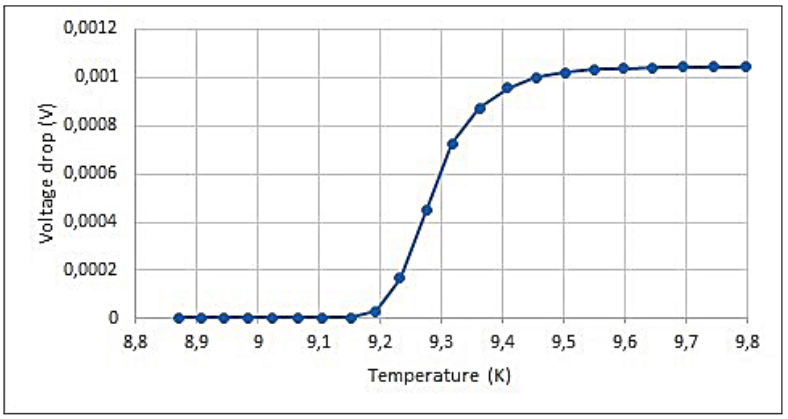

FIGURE 7.22: Magnification of T_c point for sample deposited at 600°C

In figure 7.22 the magnification of the voltage drop curve is reported; the transition from conducting to superconducting sets in at 9.4 °K, with a full superconductive state reached by 9.15 °K.

The RRR for the samples deposited at 700 °C was measured, as it is shown in figure 7.23.

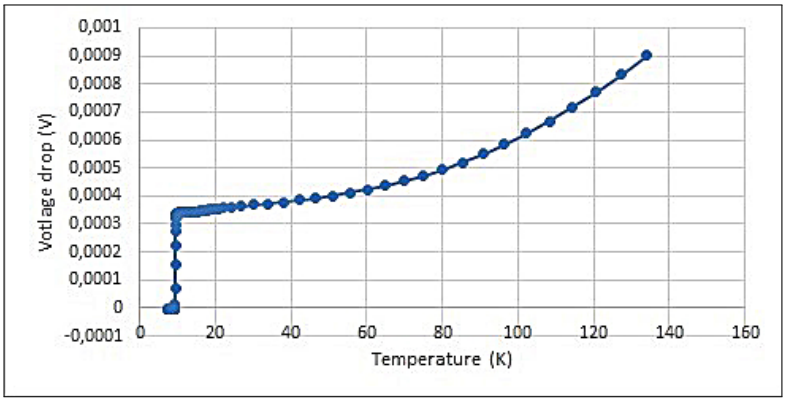

FIGURE 7.23: Voltage drop curve versus temperature of sample deposited at 700°C

The voltage drop measured for this sample at room temperature was also around 10 mV, but with a lower voltage drop at 10 °K compared to the samples grown at 600 °C, the RRR was measured at 31.

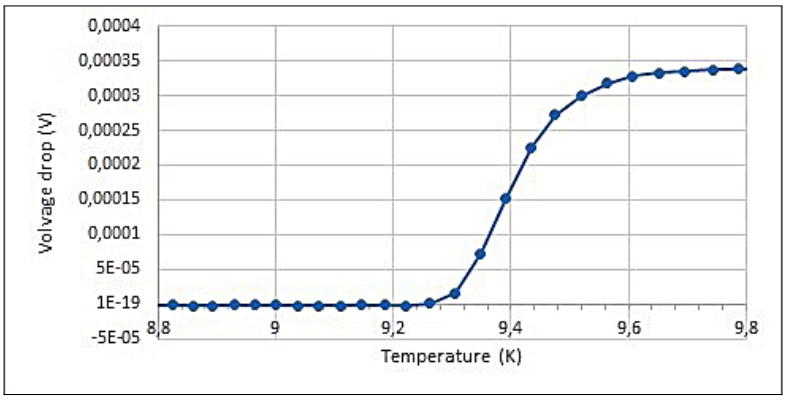

FIGURE 7.24: Magnification of T_c point for sample deposited at 700°C

Figure 7.24 shows the transition temperature point for the the sample deposited at 700 °C. The superconductive transition sets in at 9.6 K, reaching a fully superconductive state by 9.3 K.

The comparison between the transition temperatures of the two types of samples is shown in figure 7.25.

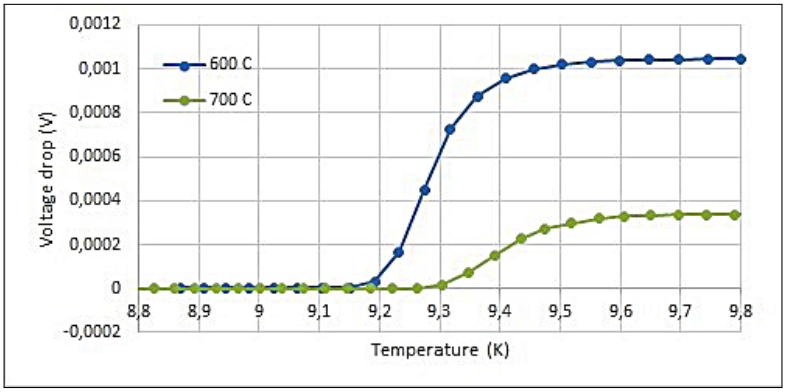

FIGURE 7.25: Comparison between the transition temperatures for the samples grown at 600 °C and 700 °C

At first glance, it can be seen that the two curves are, in T, very similar. The superconductive transition seems to set in at a slightly lower temperature for the 600 °C than the 700 °C samples. This was ruled out from being an instrumental inaccuracy, since the temperature sensors used (Cernox temperature sensors from Lakeshore ®) were placed behind the sample and can guarantee at 10 °K an accuracy of ± 10 mK [129]. To guarantee the temperature uniformity the samples were mounted on an thermally insulated holder and surrounded by 30 mbar of He gas, which would thermalize by convection the sample with the cryo cooler. The resistance of the films at low temperatures differs though, with the thinner film having a higher resistance. This discrepancy was attributed to the lower crystalline order, as shown in figure 7.11 compared to figure 7.7. The larger grains of the samples grown at higher temperature are more similar to the niobium bulk, therefore behaving like it [130].

7.1.7 SQUID results

Once assessed the T_c, the next important parameter for a superconductive film is the value of H_{c1}. The SQUID magnetometer is, as described in chapter 4, used to measure when this value is reached and magnetic field starts entering the superconductive film. It was chosen to perform SQUID magnetometry only on the samples grown at 700 °C, since the more promising as discussed so far.

Figure 7.26 shows the full hysteresis of one of the samples grown at 700 °C.

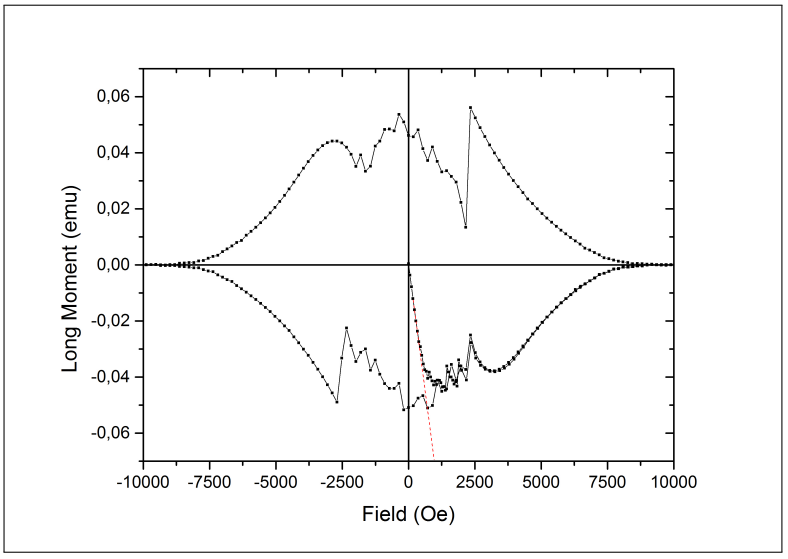

FIGURE 7.26: SQUID magnetometry of sample grown at 700 °C

The value of H_{c1} is about 25 % of the value of bulk niobium at 4 °K [131, 132], measured at 350 Oe for this sample, while H_{c2} is found at 8000 Oe. There is flux pinning between 1200 and 2500 Oe, suggesting the presence of defects (grain boundaries / dislocations) in the film. These defects are contributing in lowering the field of first penetration, since the field can enter the superconductor through grain boundaries [133–136] at lower fields than the bulk material.

7.1.8 Local magnetometry measurement

As discussed in chapter 4, SQUID magnetometry may not be ideal for measuring thin films, due to difficult alignment of the sample and the magnets. The local magnetometry measurement is more reliable, since there is no need for alignment, and does not require the destruction of the sample substrate. This instrumentation is at CEA-Saclay, and only one sample was measured to date.

This experiment provide H_{c1} (or H_p in presence of surface defects) as well as some information on the pinning behavior. Figure 7.27 provides H_{c1} sample vs T^2 for the sample grown at 700 °C. The T_c of the film is very close to the expected value for bulk Nb but the H_{c1} of the film is lower: 70 mT instead of 180 mT for bulk Nb, as shown in figure 7.27.

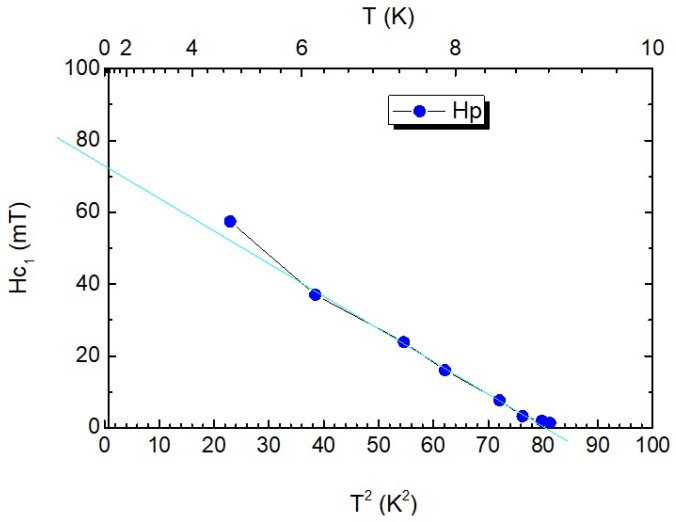

FIGURE 7.27: H_{c1} of sample deposited at 700 °C vs T^2. The intercept of the curve with abscissas gives T_c while the intercept with ordinates provides an estimation of H_{c1} at 0 K. The T_c of the film is very close to the expected value for bulk Nb but the H_{c1} of the film is lower: 70 mT instead of 180 mT for bulk Nb

The comparison of the signal at 24 mT with a signal at 25 mT in bulk Nb shows that at this field the FWHM of the Bell shape is ≈ 5 times wider for the deposition than for bulk Nb indicating the presence of a larger density of pinning defects. In bulk Niobium, bundles of dislocations are known to decrease H_{c1} and are suspected to be the main pinning defect. Indeed, with a ξ of 40 nm the grain boundaries in the bulk material will not affect much the superconducting electrons. It is possible that the remaining stress in the film is contributing in lowering the value of H_{c1}, by creating dislocations that would act as pinning centres. It is worth to note that the value of H_{c1} measured with the SQUID magnetometer is 1/2 the value of the local magnetometry reading: since the SQUID measurement was obtained after the removal of the film from the substrate, the kapton tension could have increased the stress in the film lowering H_{c1} even more. This would explain why, for the same deposition conditions, the value of H_{c1} is higher for the non dissolved substrate.

7.1.9 Conclusion on Nb on Cu depositions

The depositions of Nb with thermal CVD have been presented. The results show a trend in growth rate that is proportional to the deposition temperature. The quality of the film measured evaluated with the RRR show that the high temperature film has the same T_c of pure bulk Nb, although the field of first penetration is significantly lower than the bulk equivalent.

These results, presented in table 7.3, suggest that, of the available deposition temperatures, at least 700 °C are necessary to achieve a niobium deposit with good superconducting properties. By depositing at higher temperatures, as done by [41], it would be possible to obtain a better quality film and, therefore, potentially higher RRR and

Deposition temperature (°C)	**Film thickness (μm)**	**RRR**	**T_c (°K)**	**H_{c1}**	**H_{c2}**
500	0.1	non measurable	non measurable	/	/
600	2	4-10	8.9 - 9.2	/	/
700	20	27-31	9.2 - 9.3	350	8000

TABLE 7.3: Thermal CVD niobium results

higher H_{c1}. To do so, though, a different substrate is required, capable of withstanding temperatures higher of 950 °C. To improve the heteroepitaxial growth, this material would need a similar lattice parameter to niobium and, to be able to be used in an accelerator, a similar thermal conductance to copper.

Two materials that could be used to take this work forward could be tungsten and molybdenum; their properties are compared to Nb in table 7.4.

Material	**Lattice parameter (Angstrom)**	**Melting temperature (°C)**	**Thermal conductivity (W / m K)**
Niobium	3.294	2477	52
Copper	3.597	1085	386
Tungsten	3.1648	3422	163
Molybdenum	3.1470	2623	140

TABLE 7.4: Physical properties of Nb,Cu,W and Mo

Both W and Mo have very similar lattice parameters, with the same difference between Nb and Cu. The thermal conductivity is certainly lower than Cu, but three times better than niobium [125].

7.1.10 Niobium depositions via PECVD

The deposition of Niobium via PECVD was attempted in the first chamber using as a plasma generator the ECR unit. This way the energy needed by the reaction is provided partially through the plasma, achieving a lower deposition temperature or a higher quality film at higher temperature. A few runs were performed and it was found that at temperatures lower than 500 °C the film would not grow. Moreover, the films grown with plasma and a higher temperature had no different properties than the ones grown via thermal CVD. It was determined that due mainly to the distance of the substrate from the plasma and the particular design of the ECR unit, the plasma had no effect on the film growth.

The depositions were attempted again in the new ECR chamber, the reactor purposely designed to position the sample much closer to the ECR plasma dome. Samples at 500 °C were grown with and without plasma. The films grown without the plasma

looked as expected, grey and metallic shiny. The substrate surface was not fully coated (about 25 % of the surface).

The samples grown with plasma looked very different. First of all, as shown in figure 7.28, the surface looked dark blue.

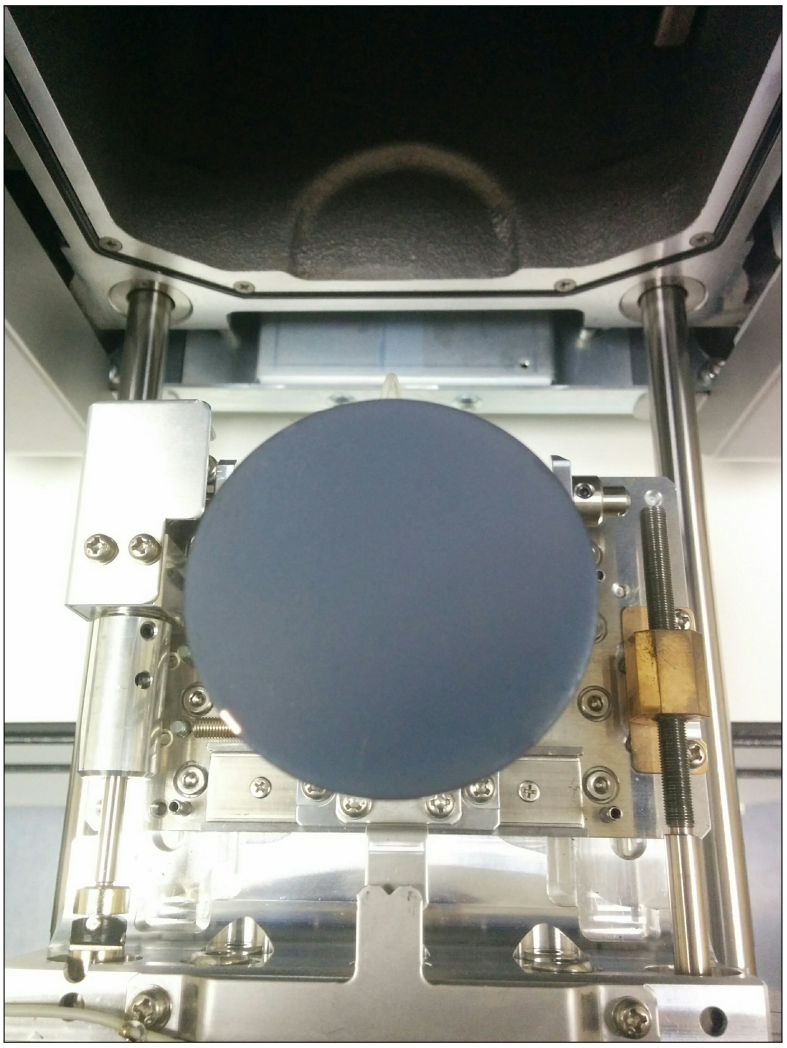

FIGURE 7.28: Picture of Nb sample grown with plasma in new ECR chamber

As previously experienced, the dark colouration is a sign of heavy oxidation of the film, normally due to a leak in the chamber. To support this hypothesis, figure 7.29 shows the SEM image of the surface of the sample: the film shows an open structure, highly porous and irregular.

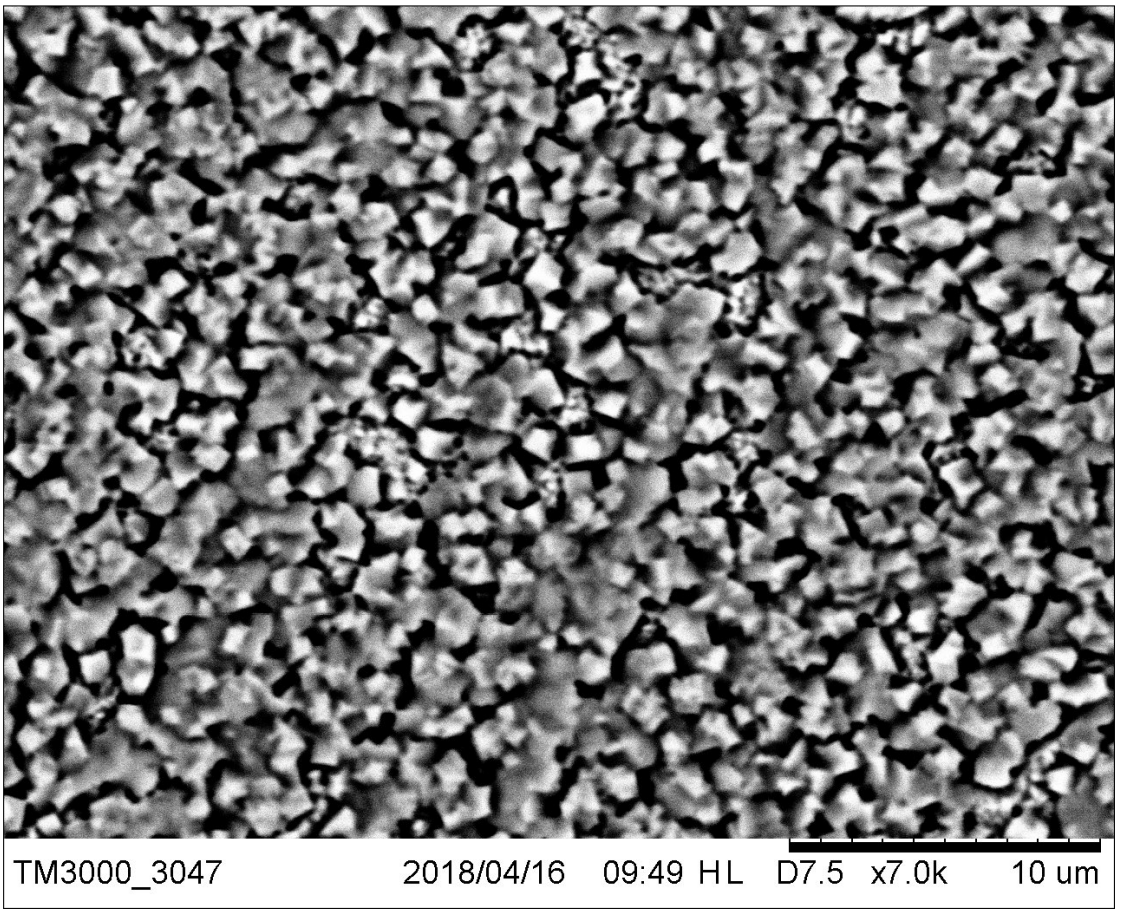

FIGURE 7.29: SEM image of sample shown in figure7.28

As the EDX confirmed, the oxygen content of the film was above atomic 50%.

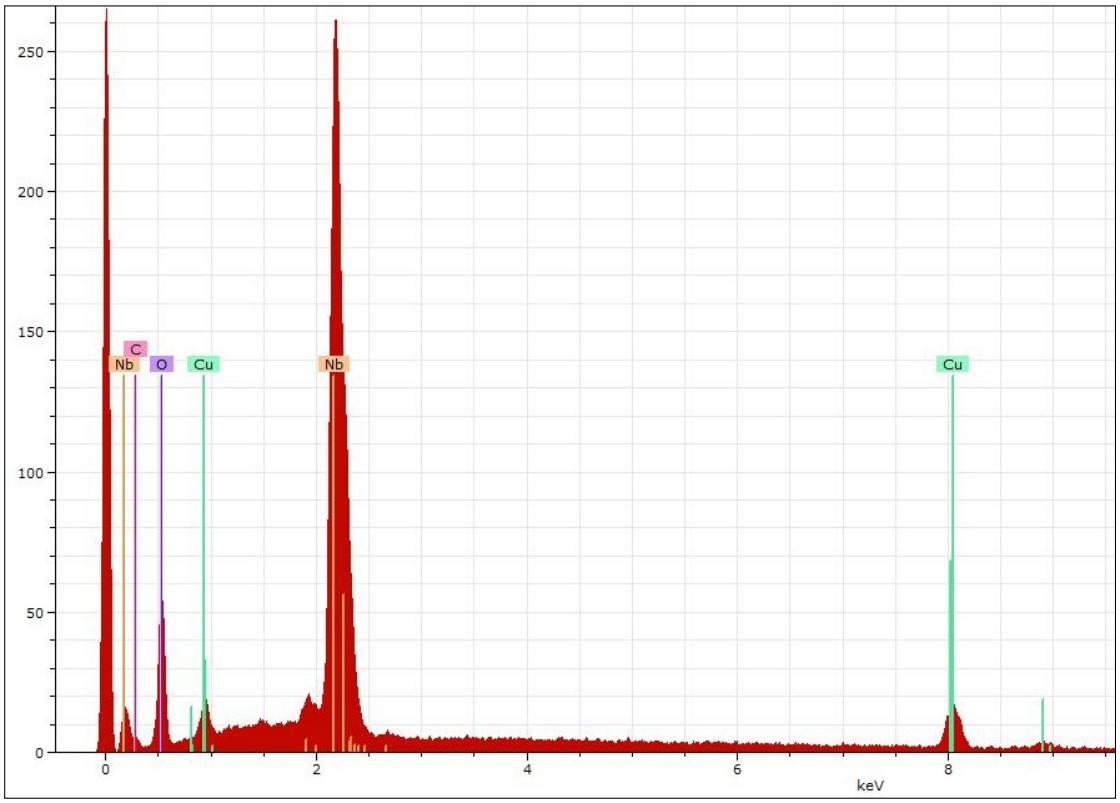

FIGURE 7.30: EDX of sample shown in figure 7.29

This certainly implied a leak in the system. After having changed all the metal gaskets, o-rings and rubber seals a few times, the leak was identified in a crucial adaptor flange that connected the ECR to the chamber. The helium leak rate through it was below 10^{-7} mbar l / s, but it was enough to allow oxygen through and into the film during the deposition. Since the item was one of a kind, it was sent to repair but has not returned yet, effectively stopping the depositions. The reason why this leak had not been identified was that it was a leak in the weld, so nothing could be done about it.
The new ECR chamber showed that the plasma is effective, incrementing the reaction rate to the point of creating a thick deposit in a short time, as the copper signal cannot be seen in the EDX graph (figure 7.30). As a future plan, once the part is repaired, it would be worth exploring different plasma powers and substrate temperatures, and see how these relate to the superconductive properties.

7.2 Niobium Nitride

As mentioned in chapter 1, Niobium nitride has a higher T_c (16.8 °K) than niobium [137], a lower H_{c1} [138] but a higher H_{c2} [139]. All these factors make it an interesting contender for SRF uses. Of all the possible deposition routes that lead to NbN, two were chosen:

$$2NbCl_5 + 5H_2 + N_2\text{Plasma} = NbN + HCl \tag{7.1}$$

$$NbCl_5 + NH_3 + H_2 = NbN + HCl \tag{7.2}$$

Equation 7.1 describes the use of N_2 ECR plasma as a source of nitrogen atoms added to the standard $NbCl_5$ + H_2 reduction already tried successfully. The other equation, 7.2, replaces H_2 as the reducing agent with NH_3 gas, much more reactive.

7.2.1 NbN deposition in first chamber with ECR plasma

The first deposition attempt was performed in the first chamber with the ECR plasma unit. The chemical route is shown in equation 7.3:

$$2NbCl_5 + 5H_2 + N_2\text{Plasma} = NbN + HCl \tag{7.3}$$

According to Uyama, [140] by mixing nitrogen and hydrogen in a plasma ammonia gas would form. By choosing a ratio of N_2 : H_2 equal to 1:3, the gases entering the ECR plasma would create reactive ammonia, that would then travel to the sample to react with the Nb precursor.

The same deposition parameters were used for this process, with the addition of nitrogen gas flowing in the ECR plasma unit. The plasma power was set at 250 W.

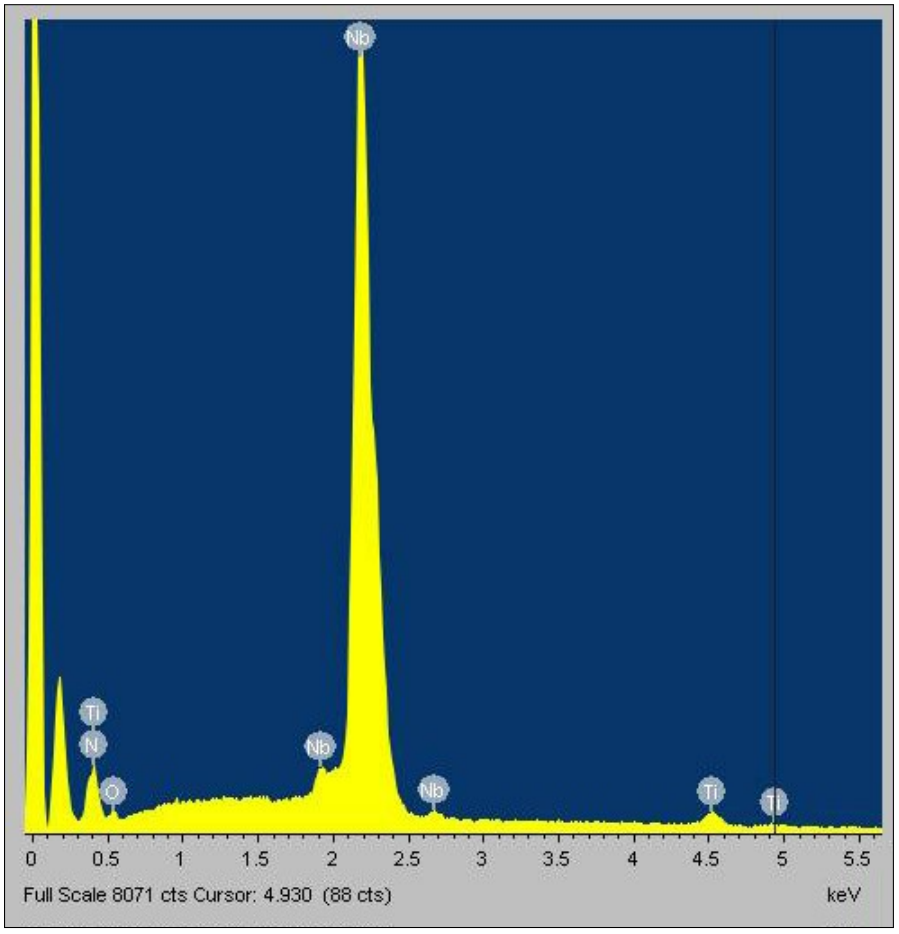

FIGURE 7.31: EDX scan of NbN sample deposited with ECR first chamber

Figure 7.31 shows the EDX scan of the NbN sample. The Nb and N peaks are present and were evaluated both at atomic 46 % of the film. The remaining 8 % is divided between 4 % of oxygen and 2 % of titanium. The titanium was explained from the a small quantity of $TiCl_4$ precursor trapped in the bubbler line, since the deposition before this one was a Ti based one. The oxygen could have been trapped by the deposited Ti as TiO_2 once the sample was exposed to air, due to their presence in the right ratio.

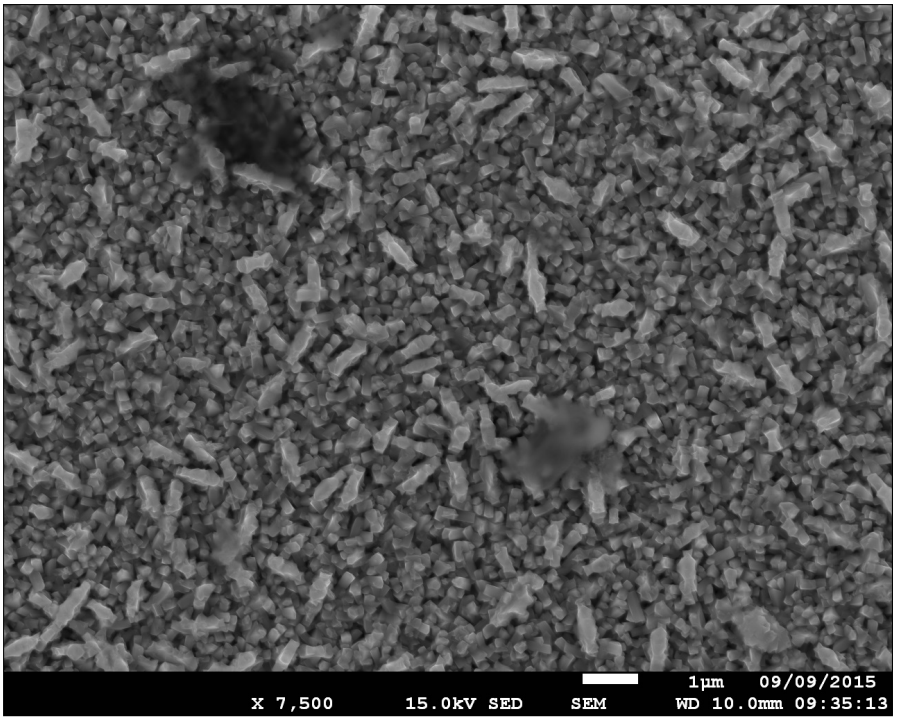

FIGURE 7.32: SEM image of NbN sample deposited with ECR first chamber

From the SEM picture in figures 7.32 and 7.33 it is clear that the surface of the film is crystalline, characterized by stick-like features about 1 μm long. The surface of the film also looks porous, open.

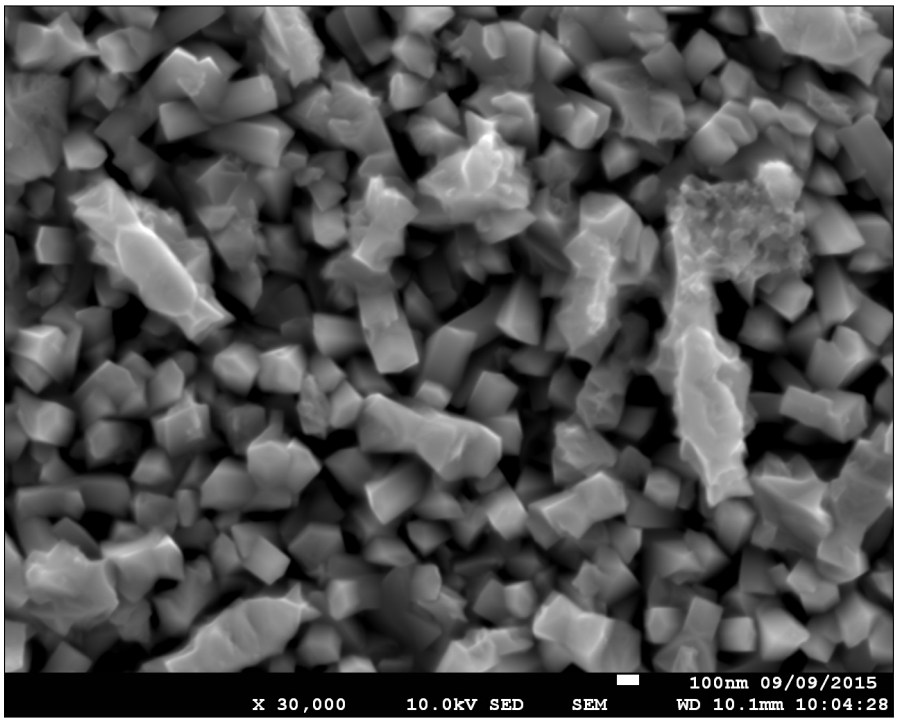

FIGURE 7.33: Magnification of 7.32

XRD analysis was therefore performed on this sample, shown is figure 7.34.

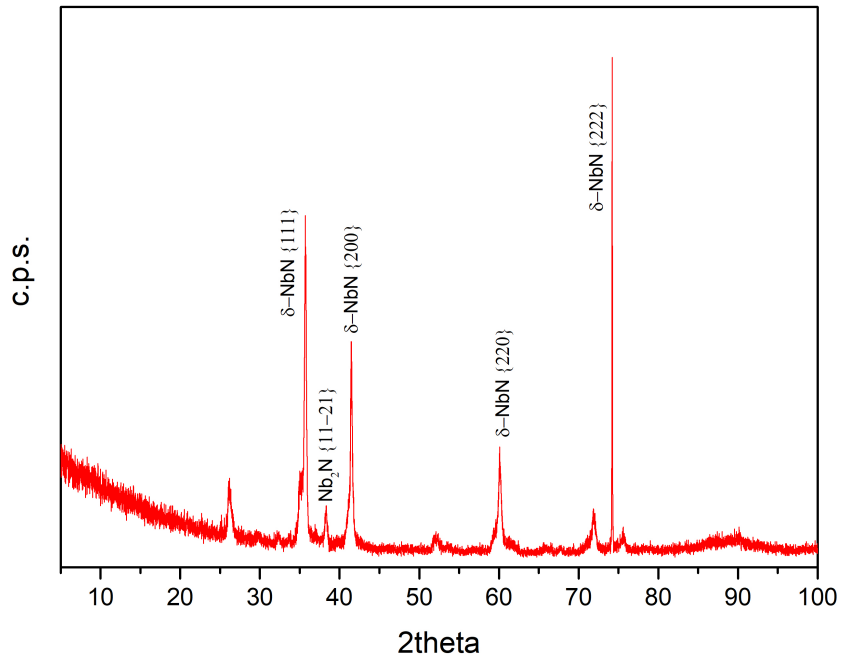

FIGURE 7.34: XRD of NbN sample obtained with ECR plasma

As seen in the work of [122], [141], the sample matches the δ-NbN phase, with a majority of crystals oriented along the {222} plane, followed by the {111} and the {200} orientations.

To perform SRF measurements the copper substrate had to be etched away with nitric acid, as previously explained. It was found that the nitrides of niobium, unlike pure niobium, can be dissolved by nitric acid and, after the etching was completed, the film disappeared completely from the kapton substrate.

The second deposition was characterized by the plasma dome breaking, as explained in section B.1.1.3. This promising deposition technique had to be therefore abandoned, due to the lack of instrumentation available.

7.2.2 NbN with NH_3 in first chamber with thermal CVD

After verifying the feasibility of NbN deposition on copper, but stopped by the lack of plasma, a different reaction route was explored. Instead of creating the ammonia gas in the plasma chamber, ammonia gas was supplied directly with the hydrogen to the reaction chamber. This required some modifications to the deposition lines, with a new corrosion resistant mass flow controller to handle the ammonia gas flow.

The reaction mechanism is shown in equation 7.4.

$$NbCl_5 + NH_3 + H_2 = NbN + HCl \tag{7.4}$$

The deposition conditions were kept as before, with the addition of ammonia flowing in the chamber at 100 sccm. The first deposition appeared matte, not shiny, and SEM was performed, showed in figures 7.35 and 7.36.

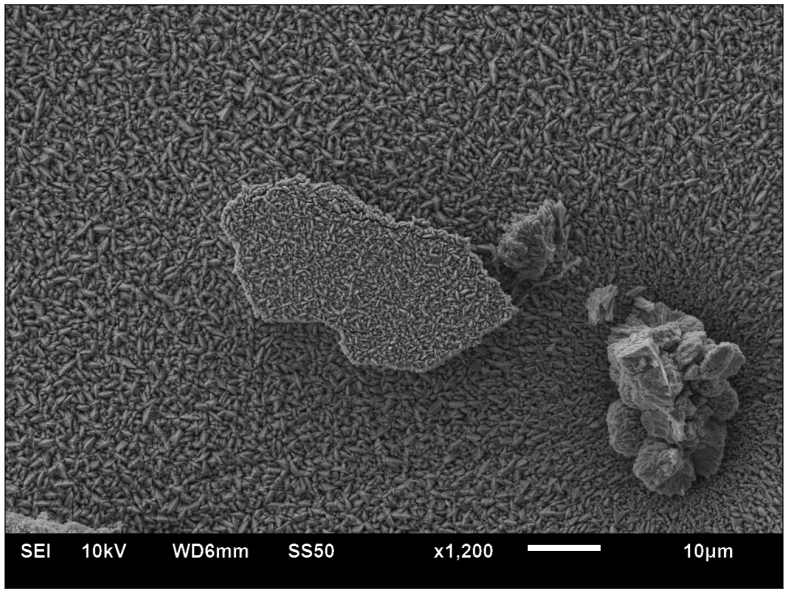

FIGURE 7.35: NbN film deposited in the first chamber with Nb precursor and ammonia gas

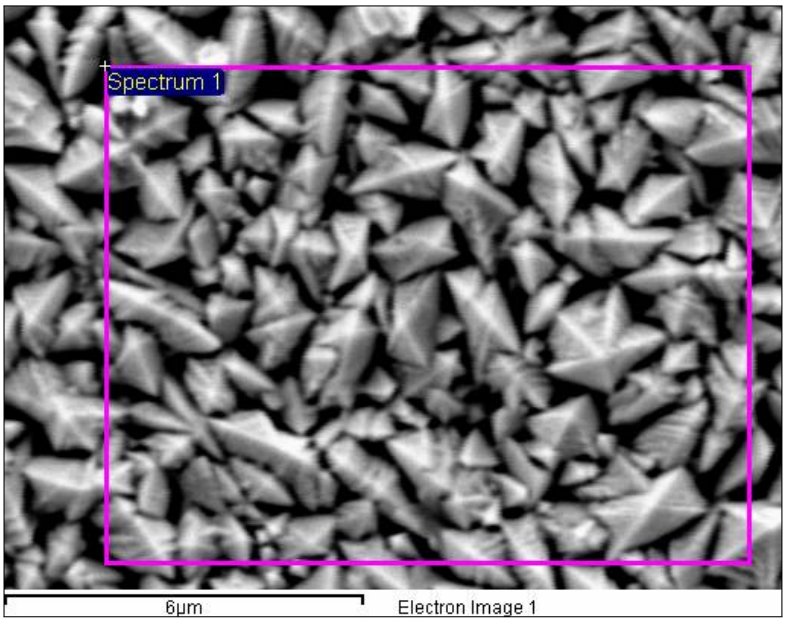

FIGURE 7.36: EDX sampling area from sample shown in figure 7.35

The surface features look different from the structures seen for pure Nb or for the NbN grown with the ECR. Compared to figure 7.32, the crystals seem sharper and more tightly packed, leaving a less open structure.

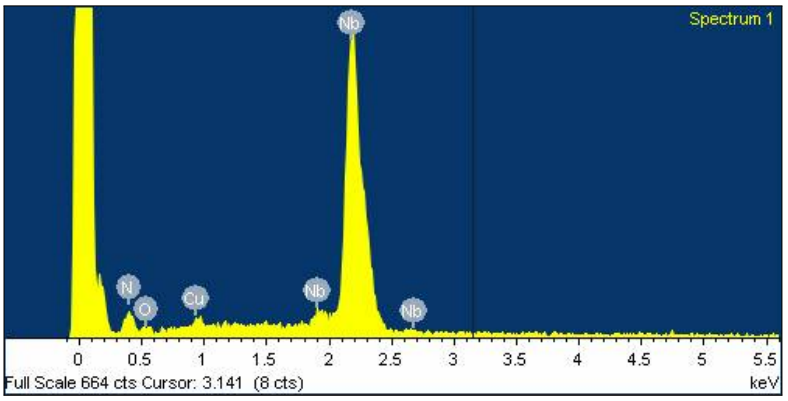

FIGURE 7.37: EDX of NbN shown in 7.36

An EDX was therefore performed, shown in figure 7.37; the atomic percentage of Nb and N in the film was measured at 46 % for both, suggesting a very close stoichiometric ratio. The remaining 8 % belonged to oxygen (6.5 %) and copper (1.5 %).

The sample was cross sectioned, to measure the thickness of the layer. From figure 7.38 it can be seen that the layer is approximatively 500 nm thick, which is less than what was expected, based on the pure niobium depositions.

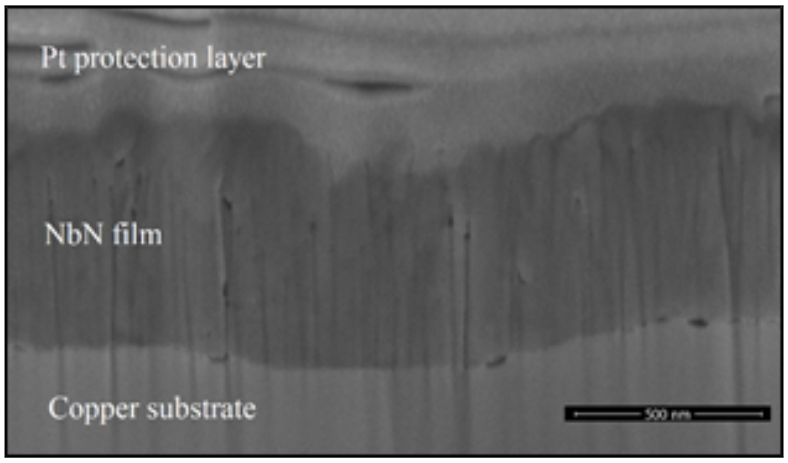

FIGURE 7.38: Cross section of NbN sample obtained with ammonia

From the cross section in this case it was difficult to discern any crystalline structure, therefore XRD was performed to verify the structure of the material.

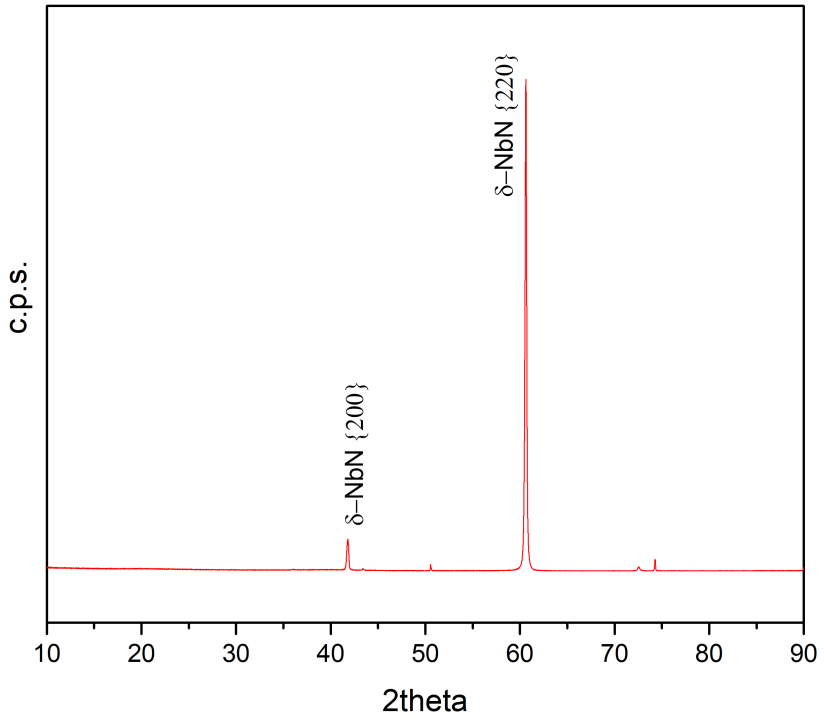

FIGURE 7.39: XRD on sample obtained with ammonia in first chamber

The deposit, as shown in figure 7.39, is crystalline, but with a different phase distribution compared to the ECR deposited samples. In this case there seems to be less phases present in the material, with a strong predominance of {220} over {200}.

The lack of growth rate was attributed to the non optimal geometry of the first chamber, as previously discussed in chapter 6. To grow thicker samples, the large vertical chamber was then used.

7.2.3 NbN in large vertical chamber

The large vertical chamber is the system that has the highest growth rate per hour, thanks to the optimization of the gas dynamics and heater. After the first deposition, where the inside of the chamber were coated with a dark grey deposit, as shown in chapter 6, a new delivery system had to be devised. The precursor inlet was prolonged into the chamber until 2 cm away from it, to make sure that the precursor would reach the substrate before reaching the sides of the chamber and react there.

After a few calibrating depositions, where the length of the pipe was shortened by 2 cm from the original design due to the precursor jet cooling down the sample, the NbN deposition program resumed by replicating the same parameters used in the other chambers (temperature, pressure and precursor temperature), with mixed results.

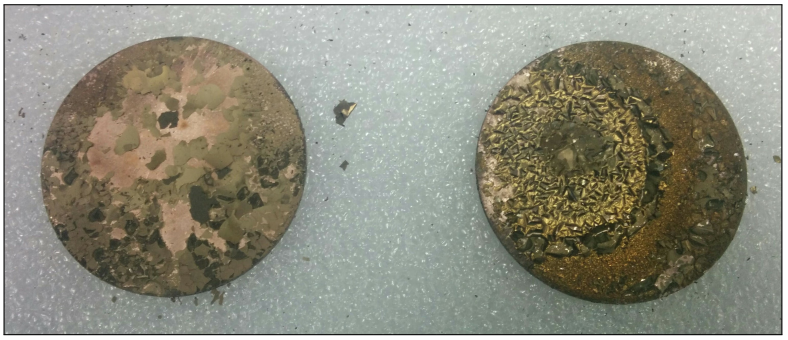

FIGURE 7.40: NbN samples deposited with different precursor temperatures: 130 °C (left) and 120 °C (right)

The first deposition after the modifications to the gas delivery turned out very flaky, with the film falling off the substrate. The same flow rates were kept for the second deposition, not to compromise the fluid dynamics of the chamber, but the precursor temperature was reduced from 130 °C (left) to 120 °C. As mentioned in table 5.4, by acting on the precursor temperature it is possible to increase or decrease the amount of chemical compound reaching the chamber. A too high growth rate may be due an excess of reacting precursor, so by lowering the bubbler temperature the growth rate should also decrease. The deposit still came off, but not as much as the previous example. Both these samples are shown in figure 7.40. By reducing the temperature of the precursor even further, down to 110 °C, the film did not de-laminate from the substrate any more. The surface did not look fully coated, probably due to very little precursor (0.25 grams over 2 hours) actually reaching the chamber, shown in figure 7.41.

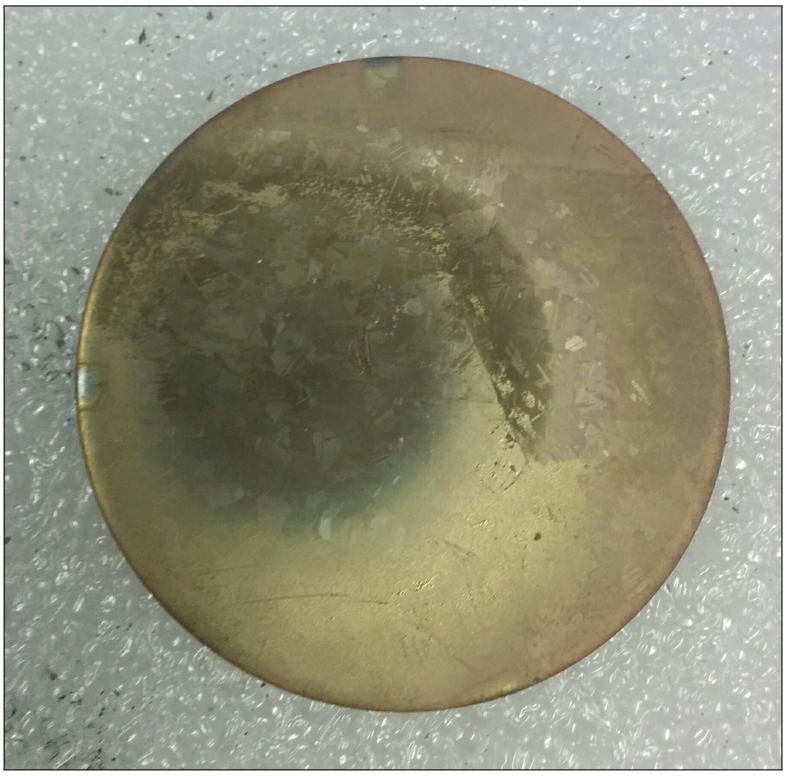

FIGURE 7.41: NbN sample deposited with precursor at 110 °C

XRD was performed on the coated area of the sample, with the results reported in figure 7.42.

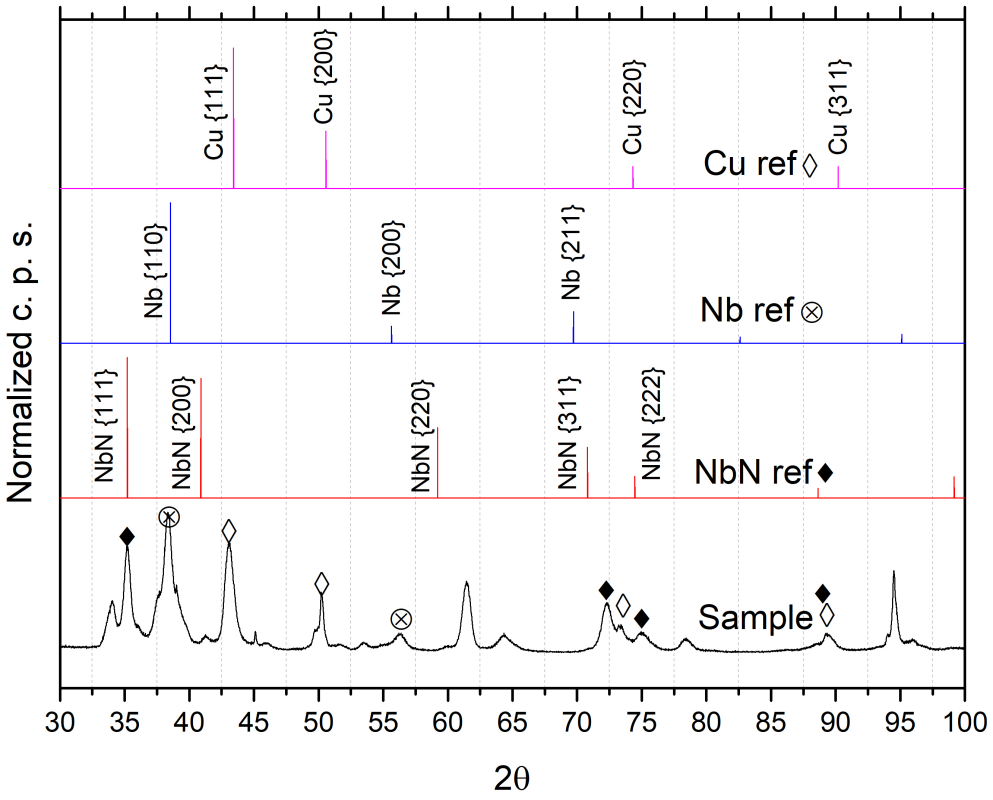

FIGURE 7.42: XRD of sample deposited with precursor at 110 °C

The plot shows the sample in black compared with the Nb, NbN and Cu XRD reference plots. The references used were the body centred cubic Im-3m {04-001-0381} for the Nb, the face centred cubic Fm-3m {04-009-2090} for the Cu and the face centred cubic Fm-3m {03-065-9399} for the NbN. As it can be seen, the sample is characterized by a mixture of crystalline orientations: the NbN {111} (35.23 2θ of the sample compared to the 35.26 2θ reference) and NbN 222 (73.48 2θ of the sample compared to the 74.46 2θ) orientations are present, with possibly the NbN {311} plane although shifted to the right quite considerably (1.6 2θ). The peak at 61.43 2θ, according to the work by Goto et al. [142], can be attributed to the NbN {103} orientation. The pure Nb {110} plane can be seen at 38.28 2θ in the sample (38.54 2θ for the reference), with the {200} orientation at 56.32 2θ (55.64 2θ for the reference). This suggests that there could be some pure Nb crystals present in the film with a {110} preferred orientation, as seen in the reference and in the previous pure Nb samples. Copper planes are also present, matching the {111} and the {200} orientations. This can be attributed to the film being very thin, as seen before, and the x-rays travelling through the deposition to the substrate causing its diffraction pattern to appear in the sample plot. Excluding the copper signals, the presence of both NbN and Nb diffraction planes suggests that the film is not made of a single material, but a combination of the two. The dark area of the sample was found

to be directly under the gas outlet, even though far enough to reduce the gas jet cooling of the surface.

The strain for the Nb and NbN peaks was calculated, and is reported in 7.5.

	Nb {110}	**Nb {200}**	**NbN {111}**	**NbN {311}**	**NbN {222}**
Strain	0.52	1.01	0.13	1.76	0.67
Error	± 0.02	± 0.02	± 0.02	± 0.02	± 0.02

TABLE 7.5: Strain present in NbN sample for the Nb and NbN planes

The crystallite size for the NbN was estimated at 17 nm, while for the Nb the crystallite size is 7 nm.

Time constraints prevented this program from proceeding further, but the results achieved in the large vertical chamber show a solid starting point to perform NbN depositions thicker than the ones obtained in the first chamber.

7.3 Titanium

The deposition of pure titanium metal from $TiCl_4$ was performed before attempting the deposition of NbTiN from both $NbCl_5$ and $TiCl_4$. This was done mainly to verify that the newly installed second bubbler and delivery line were functioning properly. Titanium was deposited using the same deposition parameters for Nb, with the exception of the precursor bubbler temperature: this was kept at room temperature since the $TiCl_4$,being liquid, develops a good vapour pressure without needing any heating.

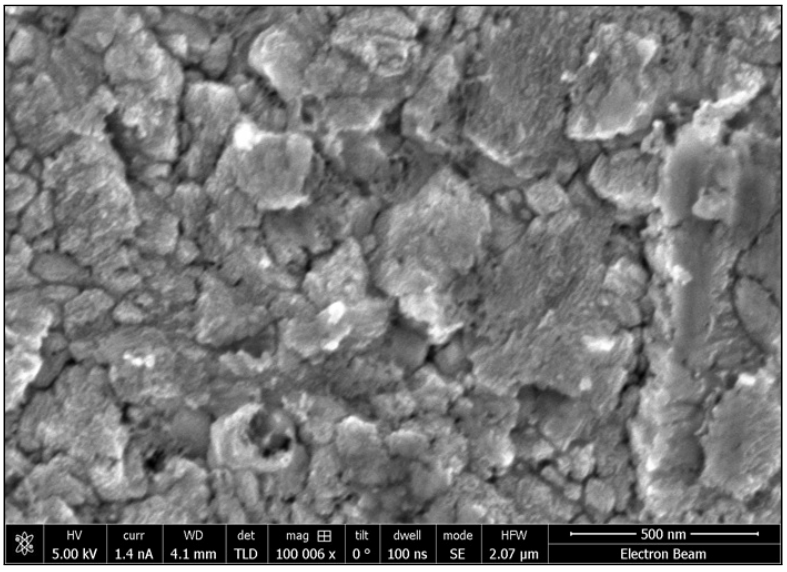

FIGURE 7.43: SEM image of surface of Ti film on Cu

After the deposition, the sample had a dark blue metallic coating on it. Figure 7.43 shows the SEM image of the surface of the film, that looks rough and not very regular. A cross section was performed, shown in figure 7.44. Here the surface of the film looks

irregular and shows what seem to be a disordered arrangement of grains. This suggests that the film is crystalline, at least at short range, since the size of the features visible in figure 7.44 varies from below 50 nm to 400 - 500 nm. This lack of order at long range could be caused by a too low deposition temperature, providing enough energy for the deposition reactions to happen but not enough to allow the crystals to coalesce and reorganize in a more regular structure. The film does not seem to coat the substrate well, as evident from the gaps between the Ti and the Cu.

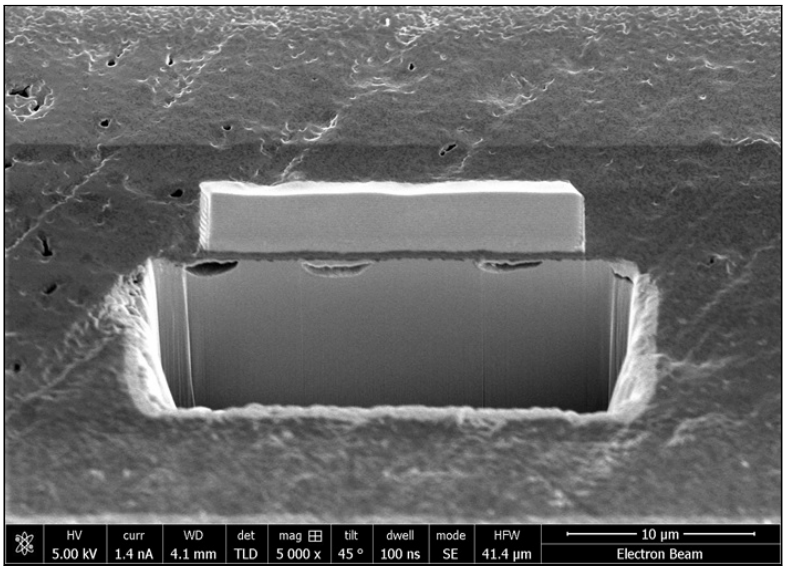

FIGURE 7.44: Cross section of Ti deposition on Cu

The film thickness was measured, as shown in figure7.45.

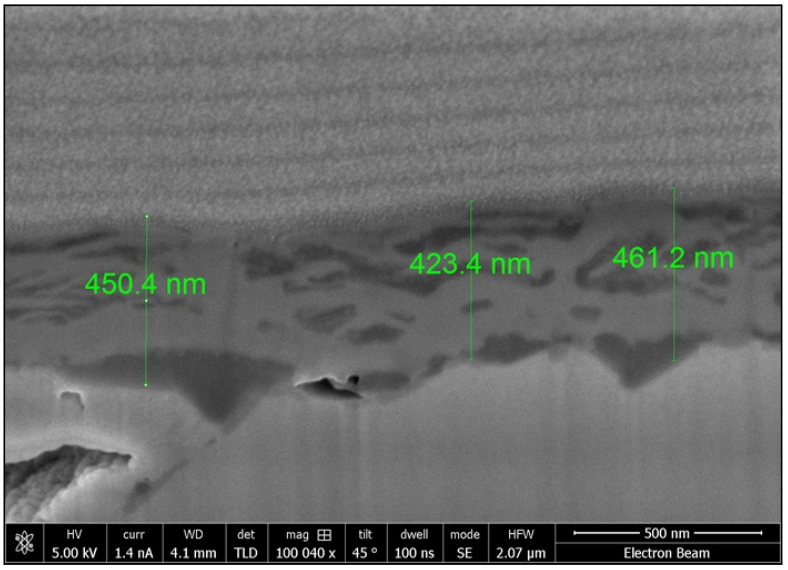

FIGURE 7.45: Magnification of 7.44

The measurement show that the thickness of the film is 450 ± 20 nm. Since the purpose of this test was to verify the feasibility of a Ti coating, and these images proved the required information, no further investigation was performed.

7.4 Niobium Titanium Nitride

Another niobium based material candidate for SRF applications is Niobium Titanium Nitride (NbTiN)[143]: with a T_c of 17 °K it would require a cooling infrastructure considerably smaller and less expensive.

To deposit NbTiN, the following reaction route shown in equation (7.5) was chosen:

$$NbCl_5 + NH_3 + 3H_2 + TiCl_4 = NbTiN + 9HCl \tag{7.5}$$

The deposition conditions were kept as per previous depositions, with the addition of TiCl_4 carried in the chamber by argon flowing through the TiCl_4 bubbler at 25 / 50 / 100 sccm. The results presented here are from the sample deposited with 50 sccm of Ar flowing through the Ti precursor bubbler , that gave the best results.

Figure 7.46 shows the cross section of the deposited film. The surface is rough, with nucleation bubbles randomly distributed at every 5 microns.

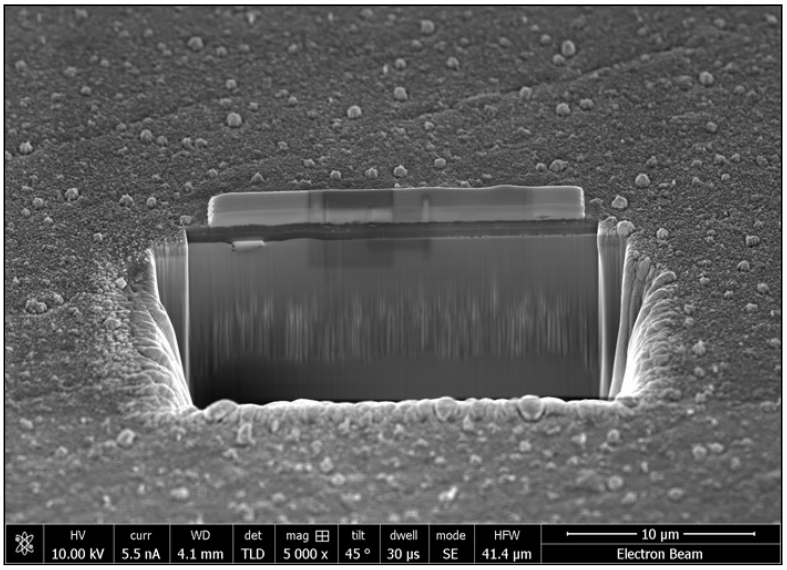

FIGURE 7.46: Measurement of NbTiN sample thickness

The film can be seen clearly in figure 7.47: the measurements show that the deposit is about 800 nm thick, since these samples were obtained in the first chamber (as discussed in chapter 6) and so the deposition rate had not been yet optimized.

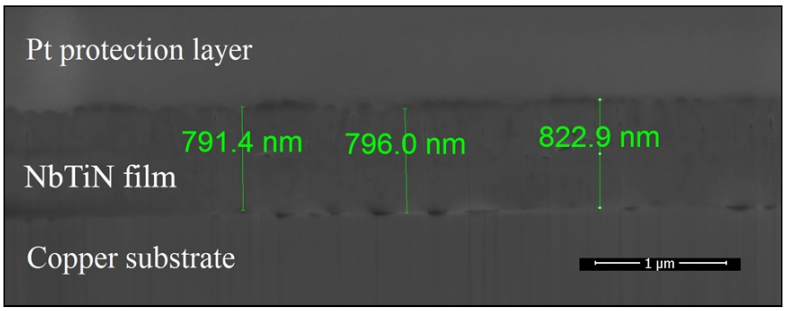

FIGURE 7.47: Cross section of NbTiN sample

The EDX shows the presence of Ti and Nb, as well as of Cu, O and N, shown in figure 7.48. In all the three depositions attempted, the quantity of Ti remained stable at atomic 13 %, with Nb at atomic 23 - 25 % and N oscillating between atomic 29 - 34 %. The remaining atomic % was oxygen, which was explained after finding a leak in the deposition chamber.

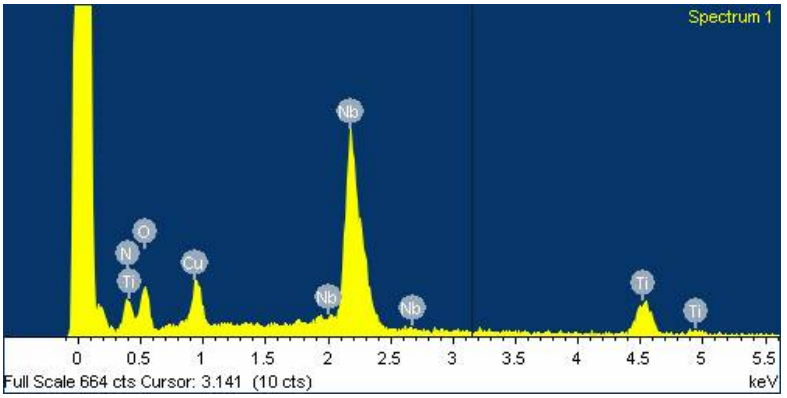

FIGURE 7.48: EDX of NbTiN sample

XRD was performed on one of the samples, and the result is shown in figure 7.49. As the image shows three crystalline orientations of $NbTiN_2$ are present belonging to the face centred cubic Fm-3m space group (reference {01-077-2990}), with the largest peak at 42.47 2θ attributed to the 200 orientation.

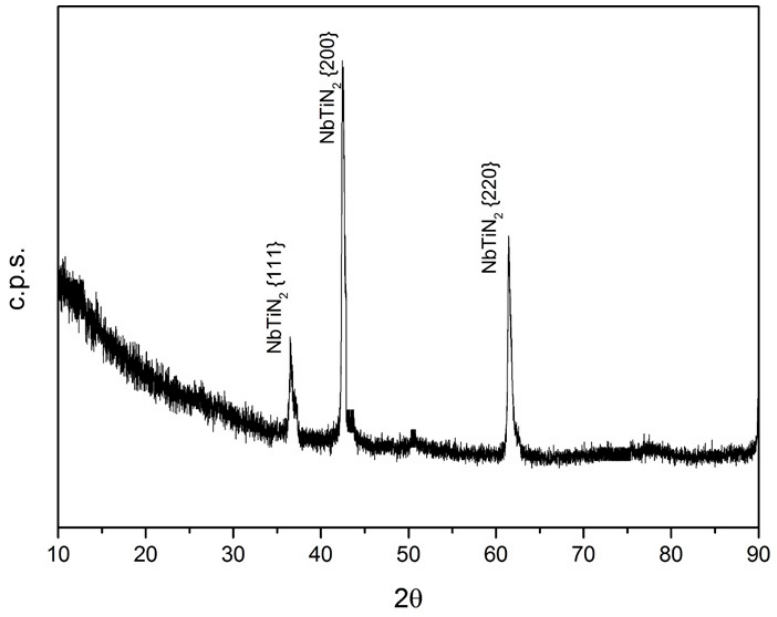

FIGURE 7.49: XRD of NbTiN sample

The peak shifts and the calculated strain are reported in table 7.6.

	$NbTiN_2$ {111}	**$NbTiN_2$ {200}**	**$NbTiN_2$ {221}**
Ref Peak Position (2θ)	35.91	41.7	60.45
Sample Peak Position (2θ)	36.53	42.39	61.41
Shift (2θ)	-0.62	-0.69	-0.96
Strain (%)	1.64	1.55	1.41
Error	± 0.02	± 0.02	± 0.02

TABLE 7.6: Peak shift and strain calculated for $NbTiN_2$ sample

All the peaks show a shift to the right (hence the negative values) compared to the peaks from the reference spectrum [144]. This suggests that the film is under compression stress, with a strain of more than 1 % for each plane. As seen for the thin films previously reported, this could be due to the copper substrate contracting during cooldown and compressing the film.

As for NbN, the impossibility of removing the film without destroying it made any SRF measurement non feasible. Further depositions in the large vertical reactor could have improved on the existing results, but the lack of time prevented us from performing any further experiments.

7.5 Conclusions

The deposition of SRF compatible niobium on copper via CVD has been proven, with novel SRF measurements conducted on it. The results show a material with T_c matching the bulk niobium, a good crystalline structure and a thickness that can reach tens

of microns while still performing. The field of first penetration is not as high as bulk niobium, which may prevent this material to be of use in high gradient - high field SRF applications.

The advantage for low field cavities is though undeniable, especially if the cavity geometry is particularly complex: a copper cavity could be easily and cheaply machined in the shape required, as for crab cavities, and successively coated with the process described.

Particular care has to be used in the substrate temperature handling: a slow cool down may prevent any stress in the films, potentially also reducing the stress in the niobium deposit.

Niobium nitride has been successfully deposited in the first chamber with and without plasma, and in the large vertical chamber. The plasma deposition showed an interesting structure, which would have been explored further if the instrument did not fail. The results of the depositions with ammonia show a niobium nitride film with a crystalline structure and chemical composition very close to the references. Further studies are needed to confirm the superconductivity performance of these materials, using techniques that may not require the lift off of the film from the substrate.

Niobium Titanium nitride was deposited, with mixed results: the films contained Nb, Ti and N, with Nb and N more abundant than Ti. The samples superconductive properties have not been tested yet and, as for the NbN, until a different non conductive substrate will be used performing these tests will be difficult. The first depositions look certainly promising, suggesting that the parameter space of the precursor gas pressures and temperatures can be adjusted to achieve the right stoichiometry in the film.

Chapter 8

Conclusions and future outlook

8.1 Summary and conclusions

Niobium cavities are a fundamental part of modern superconducting particle accelerators, and reaching the theoretical limits of the material will push the research of alternative ways to improve the existing technology. Depositing niobium on substrates with a better thermal conductivity is one of these research pathways, and it is what this work has succeded to achieve. Novel insight on the superconducting properties of niobium deposited on copper with chemical vapour deposition has been shown, proving that the technique can produce good quality thin films displaying good superconducting properties. This work has shown the journey undertaken to achieve these results. In chapter 6 different chamber designs have been shown and discussed, with the help of gas flow simulations to aid the understanding of the deposition results. The importance of a properly designed system has been highlighted, influencing factors like growth rate and quality of the growths. The use of the chlorine based precursors has been found detrimental for the stainless steel reactors ([145]), as the repeated cycles of hot HCl gas exposure followed by air / moisture heightened the corrosion speed of the chamber, leading to inclusions of Fe precipitates in the films. Different iodide or bromide based precursors may not prove as damaging to the chambers, since the lack of HCl in the reaction products.

Chapter 7 shows the successful depositions of niobium and niobium alloys on copper substrates, with the superconductive properties measured for the niobium samples. The temperature of the deposition has proven crucial for the chosen reaction path: 500 °C are sufficient to produce a deposit on the substrate, but with no good enough properties. The best results were obtained with the substrate at 700 °C, which was the highest temperature achievable on Cu before its softening point. It is possible that a higher temperature would improve the films properties, but a different substrate would be required. It has been shown that CVD can be used to produced good quality niobium, with T_c matching the bulk material although with lower field of first penetration. The H_{c1} value of the best samples was 70 mT, which even if still far from the bulk material

value it still translates in roughly 10 MV/m acceleration gradient, that can be suitable for a large number of applications (low gradients are needed in the early stages of a LINAC, where these coatings could be used). The NbN and NbTiN depositions also seem to match the reference materials, at least regarding their crystallographic structure and morphology. A different substrate would be needed to perform superconductivity measurements, due to the conductivity of copper, or a different film lift off technique, due to the films solubility in nitric acid. PECVD depositions were also attempted but, due to a number of unforeseeable reasons, it was not possible to explore this path as much as it was originally planned.

Atomic layer deposition of niobium nitride using the same chlorine based Nb precursor and a Nb metallorganic precursor were attempted with mixed results, presented in Appendix 8: the film growth was proven, although the samples exhibited a high level of oxygen, reason attributed to the history of the reactor. Suggestions for a new type of UHV ALD reactor have been presented, with the exploration of a reactor design and a low cost - easy to use control system.

8.2 Recommendations for further work

Future experiments could explore the following avenues:

- *Subtrates*: as mentioned in chapter 7, the major limiting factor of the CVD niobium is the substrate chosen. Copper starts to become unstable right at the inset of the temperature required for the $NbCl_5$ reduction to happen via thermal CVD. It would be interesting to study the effect of the depositions at higher temperatures (700 °C to 1100 °C) and their superconductive qualities. Different materials could be used as substrate to perform proof of concept level investigations, as for example tungsten or molybdenum, thanks to their high melting temperature combined with a lattice parameter very close to the of of Nb. This would allow to reach higher deposition temperatures and to create films with less residual stress. The challenging part would be to manufacture the cavity out of these materials, but that could be an engineering challenge worth the SRF gain.

- *Cavity coating*: since the depositions on copper have been successful, it would be interesting to proceed with the deposition on a mock up copper cavity. To do so, the cavity could be introduced in a vacuum furnace, to avoid any oxygen contamination from the outside, and both end of the cavity could be connected to the deposition system - one inlet and one pumping port. The cavity could then be tested in a real accelerator test bench and its performance could be evaluated.

- *Reverse cavity coating*: since high temperatures are required to deposit on Cu, an inverse approach could be attempted: a graphite cavity could be machined and used as RF susceptor inside a CVD deposition chamber. The high melting point of graphite would allow to reach temperatures above 1000 °C, ideal for

the Nb deposition. After a few mm of Nb growth the graphite would be etched away, leaving a bulk like Nb cavity of the desired shape. This approach has been attempted already by Ultramet with encouraging results, but more can be done.

- *Plasma assisted deposition*: time constraints prevented us to pursue this research path any further, but the possibility of using plasma to reduce the deposition temperature is enticing. This would allow to use substrates like copper but achieving Nb thin films with better properties than the ones obtained in this work.

- *CVD - ALD of multilayered systems*: as discussed by [103, 146], a multilayer superconductor - insulator - superconductor structure may be able to enhance the H_{c1} of bulk niobium, by adding a few tens of nanometers of electrical insulator on top of bulk Nb, coated then with another thin layer of superconductor. This is achieved by exploiting the increased parallel H_{c1} in films with thickness smaller than the London penetration depth [147]. For a 20 nm NbN film, the theoretical value for parallel H_{c1} is 4.2 °T, which would significantly boost the cavity performance in RF TM_{010} mode, where the field flows parallel to the cavity surface. The Nb would be effectively screened by the combined effect of the thin superconductors and the insulators (that impede vortex movement and penetration in the cavity), with an increase of H that would be proportional to the number of S-I layers deposited on top of the Nb bulk. While CVD may not allow to easily control the thickness of these complex systems, ALD will enable to deposit materials of the desired composition and size. This may not be trivial, though, since as shown in appendix A the choice of precursor, deposition conditions and reactor state need to be controlled extremely well to avoid any contamination in the film. By using CVD, bulk-like niobium could be grown on copper, then coated using ALD for the layer thickness precision, then coated again with CVD of NbN or NbTiN. This would require a bespoke hybrid CVD / ALD system, but it could provide deep insight into understanding this phenomenon.

Chemical based deposition techniques have not received much attention in the accelerator world. The need for cost saving, together with a need for more complex cavity designs, has opened up a door for these applications. There is still a considerable amount of research to be done, since a few issues discussed in this work still require some understanding, and this work hopes to provide some insight into the capabilities and flexibility of these techniques. It is the writer's pride to see the value of this work already been highlighted during the International Particle Accelerator Conference '17 in Busan, Korea, where some results were part of a plenary presentation given by a researcher from Cornell university, USA[45]. Hopefully, this research will be continued, to lead to a better understanding and application of chemical vapour depositions for SRF and accelerators.

Appendix A

Atomic Layer Deposition of Niobium Nitride from different precursors and reactor considerations

Appendix A introduces early results obtained via Plasma Enhanced Atomic Layer deposition: the attempts to deposit Niobium Nitride from the precursors discussed in Chapter 5, the results obtained with a commercial reactor and some considerations. A UHV reactor design is proposed to address the shortcomings of the commercial reactor.

A.1 Atomic Layer deposition (ALD)

Chemical vapour deposition (CVD), as mentioned in chapter 3 and seen in chapter 7, permits the deposition of films a few microns thick in less than an hour, at the expense of precise thickness control. On the contrary Atomic layer deposition (ALD), even if considerably slower than CVD, can be used for situations where the thickness of the deposited layer needs to be controllable with a resolution down to the nanometer.

A.2 Potential for ALD in SRF applications

Recent works by Gurevitch [148] and Kubo [149, 150] on superconductor insulator superconductor systems have highlighted the need for a very high degree of control over the thickness of the layers that will make up these materials. Keeping in mind that the final goal would be to coat a copper cavity, if this control can be achieved with Physical Vapour Deposition (PVD) and the use of High Power impulse magnetron sputtering (HiPims), it would still prove challenging to coat a complex shape such as a cavity. While CVD can provide quality films deposited over large surface areas with high geometric ratios (such as elliptical cavities or crab cavities) in short time frames (few microns of thickness of pure Nb per hour of deposition), controlling such thickness to the nanometer scale could prove very difficult. ALD can provide the degree of control needed to allow

the deposition of complex structures such as Superconductor Insulator Superconductor with very precise thickness control. The key is the precursors selection: the inappropriate combination of precursors and deposition parameters may cause contamination or non uniform deposition. The precursors presented in chapter 5 were used in a commercial ALD system, to verify their compatibility with the ALD process.

A.3 Experimental setup

The experiments presented were conducted on an Oxford Instruments OpAL® plasma enhanced atomic layer deposition facility (PEALD), shown in figure A.1. The instrument allows the use of five different precursor containers and four separate coreagent gases. The chamber contains a heater plates capable of reaching 450 °C; the reactive gases can be fed in the top part the reactor where a RF plasma can be generated and pulsed according to the desired deposition parameters.

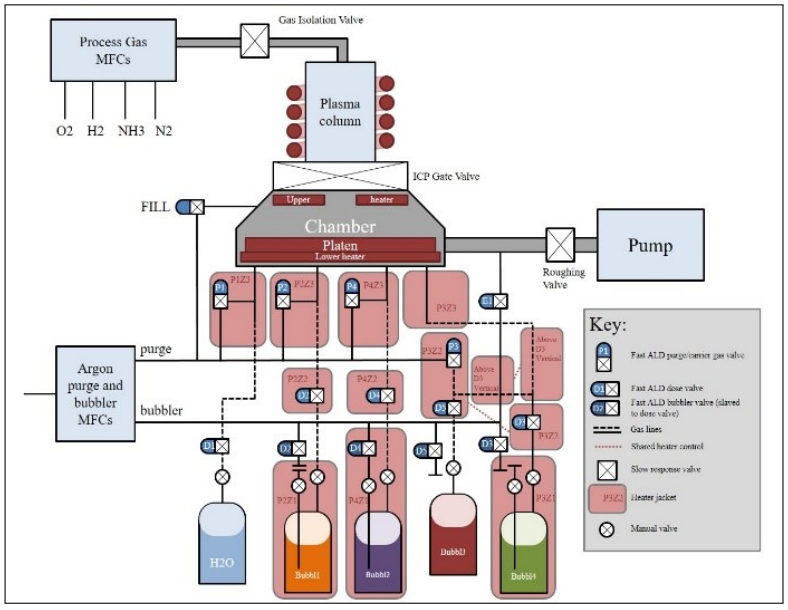

FIGURE A.1: PEALD commercial reactor schematic

The thickness of the films obtained was measured by ellipsometry: a light of a known polarization is shone on the surface of the coated samples and the changes in polarization correlate to the thickness of the films.

A.3.1 NbN from chlorinated precursor depositions

Niobium pentachloride has been explored first as a precursor for the deposition of niobium nitride films because of previous experience, presented in Chapter 7. The $NbCl_5$ was contained in a commercial stainless steel two legged bubbler connected to the deposition facility and kept under argon atmosphere. The bubbler was purged before the deposition to reach the system base pressure to avoid any sudden change in pressure during the deposition which could have hindered the uniformity of the growth. Different

precursor temperatures were tested, but no growth was seen below 115 °C, which was then selected as the growth temperature for this batch of samples. Nitrogen gas plasma was used as the source of nitrogen, mixed with hydrogen gas to provide the reduction of $NbCl_5$. The gases were introduced in the plasma generation area above the chamber with a ratio of N_2 H_2 of 5:1. Silicon (100) samples were used as substrates, since coated copper could not be measured with the available ellipsometer. The temperature of the substrate and number of cycles were varied as deposition parameters, as shown in table A.1.

A.3.2 NbN from metallorganic precursor depositions

Tris(diethylamido)(tert-butylimido)niobium was used as a precursor for the deposition of niobium nitride films. The temperature of the substrate was kept constant during the depositions at 300 °C, as suggested in literature ([151]). As with the $NbCl_5$ depositions, the bubbler was purged before the depositions to avoid pressure excessive spikes once started. The temperature of the bubbler and the doses were varied during the experiments. Silicon (100) and glass (microscope slides) were used as substrates.

A.4 Results and Discussion

A.4.1 NbN from chlorinated precursor depositions

Table A.1 shows the growth parameters and results for the experiments conducted using the chlorinated precursor. One cycle was as follows: the argon gas was set at 100 sccm for 5 s, followed by a $NbCl_5$ pulse of 2 s, then purged for 5 s. The Ar was then set to 0, while the N_2 to 50 sccm and the H_2 to 10 sccm for 4 s. The plasma was therefore ignited at 300 W for 3 s. The N_2 and H_2 were then reduced to 0 sccm while the Ar was set to 100 sccm for 5 s to close the cycle.

Sample	**Growth Temp (°C)**	**Cycles**	**Thickness (nm)**	**Growth rate (nm / cycle)**
1	300	100	3.67	0.037
2	350	100	3.73	0.037
3	350	500	11.8	0.024
4	350	100	3.86	0.039
5	400	1000	28.76	0.029
6	400	200	7.58	0.038
7	450	100	2.36	0.024
8	450	700	20.1	0.029

TABLE A.1: Depositions from $NbCl_5$

The results show an average growth rate of 0.03 nm per cycle, which is lower than the reported one of 0.06 nm per cycle. This could be attributed to a low quantity

of precursor being bled into the deposition chamber, but system limitations prevented us from raising this any further. According to literature, the higher the deposition temperature the less contaminants would be left behind in the film, especially chlorine coming from the reduction of the Nb. To verify the amount of contaminants, the samples deposited at the highest temperatures achievable in this deposition system were analysed with XPS X-Ray photo-electron spectroscopy, as shown in figure A.2. Samples 5, 6 and 8 were therefore investigated. Sample 5 was labelled 400 °C cold while sample 6 400 °C hot because the former was extracted from the chamber when at 80 °C, while the latter was taken out of the system while the heating plate was still hot. Sample 7 was similarly to sample 5 extracted once the system had cooled to 80 °C, hence why 450 °C cold. The lower temperature of extraction should limit the oxidation of the films once exposed to air. From the XPS results, all the samples exhibited N 1s peak at around 397 eV, which shows that nitrogen is present in the film. In the 200 eV 210 eV range all the samples show a peak at 206.8 eV, indicating Nb_2O_5. The broadening towards 209.4 eV is also indicative of Nb_2O_5. For 450 °C Cold, the shoulder at 204.4 eV suggests shifting towards NbN though there is clearly a mixture of the oxide film as well. Cl presence would be prominent around 198 eV 200 eV, where a small wide peak can be noted. The effect on the cooling temperature seems to be of little impact on the composition of the films, since all of them show the presence of the oxide phase. These results are explained by the nature of the reactor: the system had been used previously for depositions of oxide materials for semiconductors, contributing therefore a considerable presence of oxygen. The reactor used is an open-load system: this means that when the samples are introduced in the deposition area, the entire inner surface adsorbs oxygen. This either reacts with the precursors during the deposition or is included in the film, leading to the results presented. As suggested by Fang [152, 153], this contamination can be controlled by including the reactor chamber inside an oxygen free volume, like a glove box, followed by a 1 hour long hydrogen plasma cleaning of the reactor, making sure that the chamber leak rate would never go above the 10^{-3} mbar per minute. By implementing these solutions it is possible to avoid oxygen contamination. This, together with the fact that temperature required to achieve the complete reduction of $NbCl_5$ (above 500 °C) is not achievable in this system, shows that this deposition system may not produce satisfying result if used with Cl based precursors.

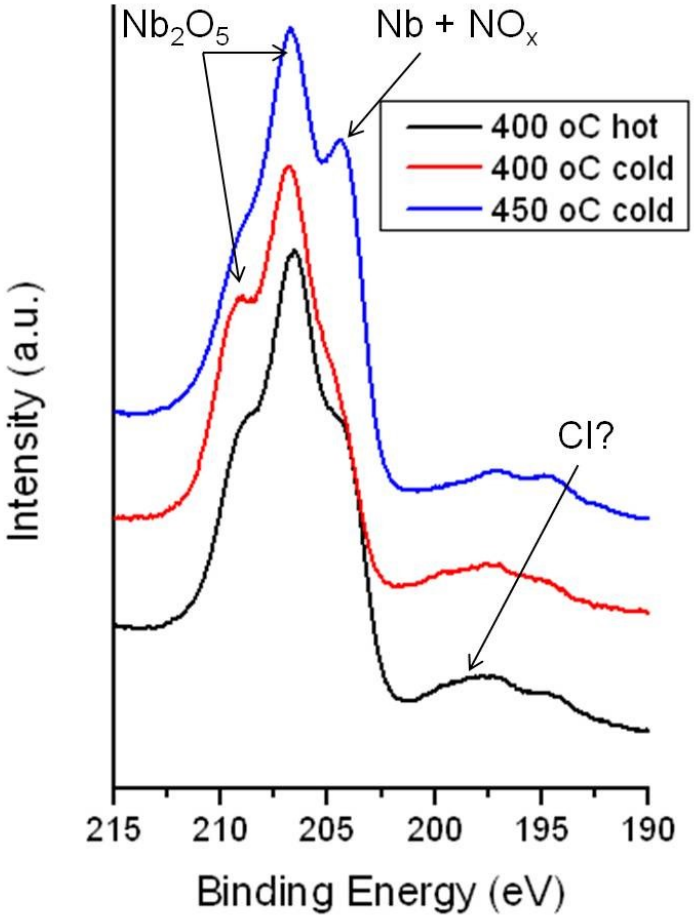

FIGURE A.2: XPS analysis of depositions from $NbCl_5$

A.4.2 NbN from metal organic precursor depositions

Once verified that the inorganic precursor was not suited to the system available, a metal organic precursor was chosen. Tris(diethylamido)(tert-butylimido)niobium (Nb - TBTDEN) has been previously used to deposit NbN, since its liquid form should allow a better transfer from the bubbler to the chamber and, since its an organic compound, it should react at lower temperatures than its inorganic counterpart. The precursor has a few drawbacks after all: its considerably more expensive than the inorganic precursor (a factor 100), and, being organic, it may decompose if heated too much. The bubbler temperature was therefore set at 70 °C for the first deposition and increased by 10 °C for each following run.

Table A.2 shows the growth parameters for the metal organic precursor growth attempts. The precursor is contained in a single leg bubbler, which means that there is no way to push the precursor out of the bubbler by using a carrier gas. The vapour pressure of the precursor has to be high enough to allow the precursor to reach the chamber, and this seems to be achieved only above 105 °C. The use of plasma generated purely by N_2 also seems to be insufficient to allow the reaction with the precursor, which is why H_2 was added in the plasma. This has led to an increase in the deposition rate to 0.04 nm

Precursor T (°C)	**Cycles**	**N_2 flow (sccm)**	**H_2 flow (sccm)**	**Growth (nm)**
70	50	60	-	0.3
80	50	60	-	0.3
90	50	60	-	0.3
100	50	60	-	2
105	50	60	-	3
110	50	60	-	4.7
110	400	60	-	12
110	400	60	10	17

TABLE A.2: Deposition from Nb-TBTDEN

per cycle. Figure A.3 shows the thickness distribution of the deposited film over the silicon substrate. The thickness changes from 8 nm to 17 nm across the sample, suggesting that the positioning of the substrate inside the deposition chamber has a great impact over the growth results.

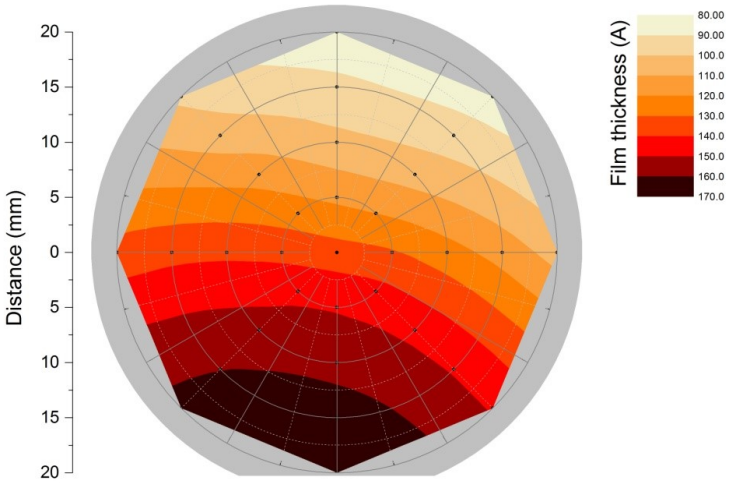

FIGURE A.3: Si substrate thickness distribution

XPS analysys was performed on the sample, as shown in figure A.4. The peak at ≈397 eV can be attributed to the N 1s peak, which shows that nitrogen is present in the film. The peak at 207.5 eV could be Nb_2O_5, but according to [154] it could be the oxide layer on top of a NbN film. This could only be confirmed by a peak for NbN at 203.1 eV but it was made difficult to resolve due to the broadening of the peak at 207.5 eV. The peaks at ≈ 284 eV is attribute to surface carbon, probably coming from handling the sample from the deposition chamber to the XPS instrument. The peaks between 360 eV and 380 eV can be attributed to the Nb in Nb_2O_5, while the peak at 397 eV is the N present in the NbN. The peak at 530.20 eV could be attributed to the oxygen present in the Nb_2O_5, or to a thin layer of oxide on the surface of the film. Due to the lack of data in the energy range above 800 eV it was not possible to resolve the peak at 740 eV.

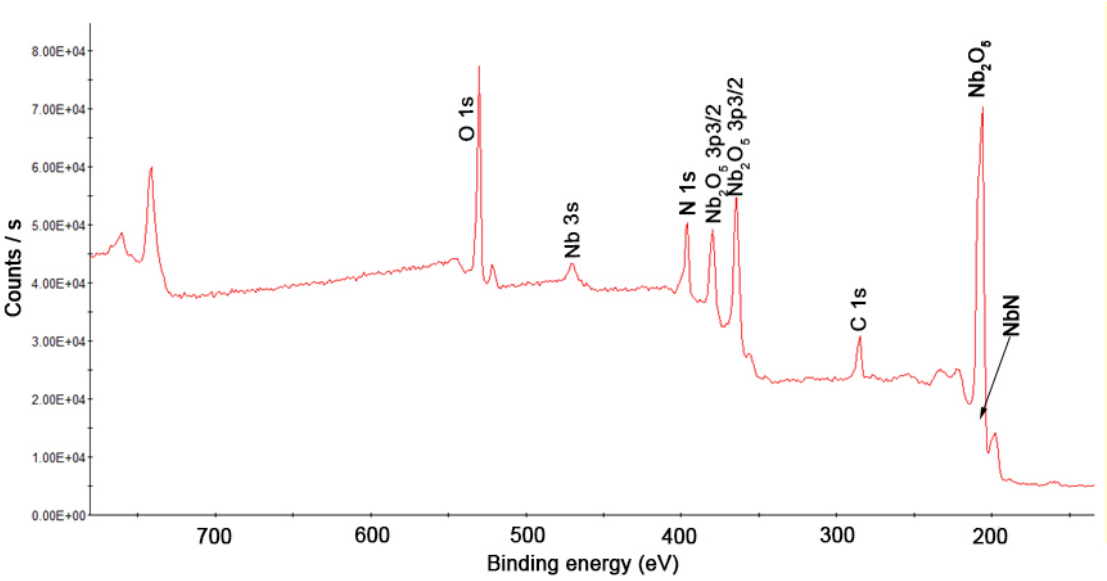

FIGURE A.4: XPS analysis of depositions from (Nb-TBTDEN)

The growth rate is still low, suggesting that the deposition parameters could be improved. This was not possible in the time frame we had at our disposal to utilize the instrument.

A.5 New ALD system development

A.5.1 Chamber flow simulation

The opAL PEALD facility has proven useful to explore the two precursors at our disposal. From the experiments it has been shown that, for the samples obtained from both precursors, oxygen contamination is constantly present and, due to the nature of the instrument and the limited access to it, it was not possible to conduct any further work on it.

A replica of the large vertical chamber descripted in chapter 6 was proposed as an ALD chamber, to improve on the issues aforementioned: by using a leak tight UHV chamber with a base pressure of 10^{-8} mbar the oxygen contamination would be reduced to negligible levels. By using a heater capable of reaching 600 °C the chlorine contamination would also disappear, allowing the use of the $NbCl_5$ precursor. As previously described, the dimensions of the chamber, the gases flow rates and the deposition pressure guarantee a laminar continuous flow, as shown in figure A.5.

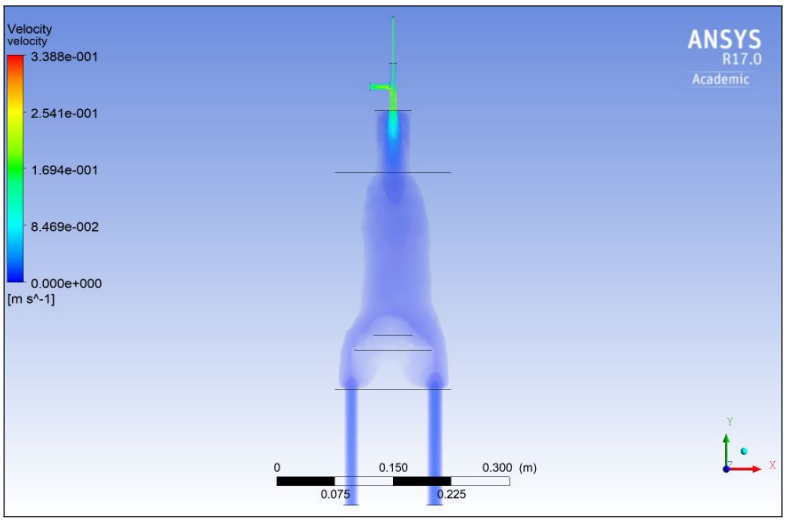

FIGURE A.5: Fluent gas flow simulation of new chamber

A.5.2 Arduino Control system

ALD valves are capable of switching between closed and open in intervals as little as one millisecond. To achieve such speed, the valves are pneumatically activated but electrically triggered. A high pressure compressed air line feeds into the valves, maintaining them in their resting state (closed or open according to how they are connected to the line). An electromagnet, connected to an external +24V power supply, changes the state of the valve when the voltage changes.

In a commercial system, the valves are connected to a *Programmable Logic Controller* (PLC) unit that, interfaced with control programs like the *Labview* suite, reads the state of the valves and controls them.

Setting up a PLC unit is not in the scope of this work nor at the moment part of the knowledge or experience of the writer; commissioning it to an external company could be possible, but the high cost may render a commercial reactor more financially justifiable.

For this work, a cheaper solution that relies on an *Arduino microcontroller* is presented.

A.5.2.1 What is an Arduino?

An Arduino is a low cost programmable microcontroller, shown in figure A.6, operating on a C / C++ language. Since its inception in 2003, a wide array of models has become available on the market, based on different microcontrollers and architectures.

The Arduino board is designed with ease of connection as primary goal, providing a number of inputs and outputs, digital or analog, that can be operated by an ad-hoc written code.

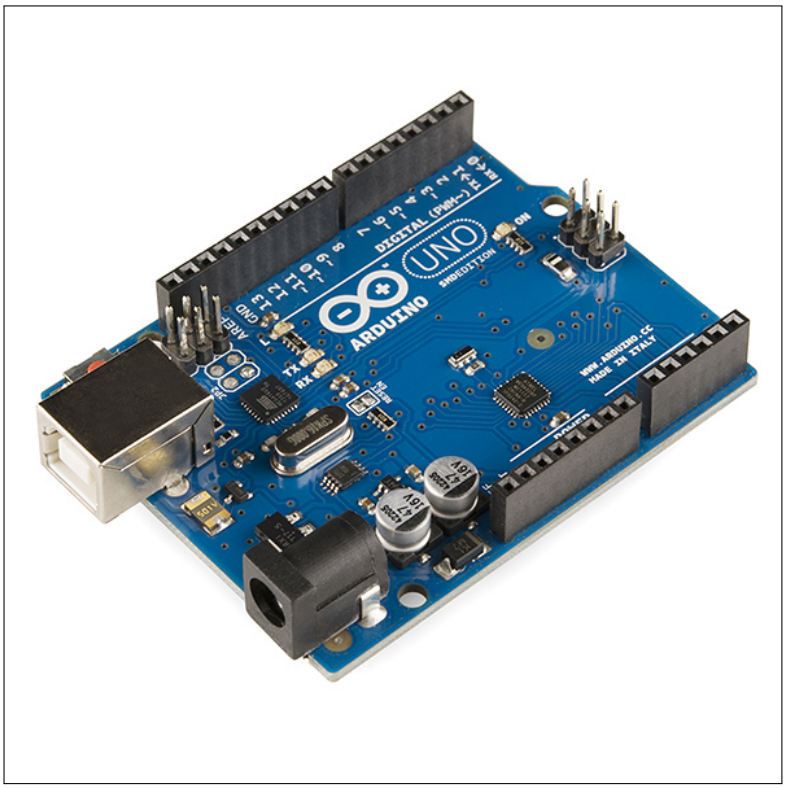

FIGURE A.6: Arduino Uno board

An Arduino Uno was chosen as prototype for the control system, which is fitted with 14 digital input / output ports and 6 analog inputs. It can be connected via an USB-B to any computer and programmed via an open source software downloadable from "https://www.arduino.cc".

A.5.2.2 Time accuracy

ALD does not only require fast switching valves but also accuracy between cycles: if the time interval between different valves switching changes, the effect can be more or less precursor or gas introduced in the chamber, creating irregular cycles and compromising the high control over the growth layers. The Arduino Uno uses a ceramic resonator at 16 MHz that the hardware / software utilizes when asked to perform timed operations, like in this case switching valves at certain intervals. Ceramic resonators are reliable only if they are kept at a constant temperature: a small oscillation and the resonating frequency changes, and therefore the time readings. This level of accuracy is not acceptable for ALD, but it is not an unsolvable problem. Thanks to its popularity, Arduinos benefit from a large community of users, and over the years a large number of accessories (called *shields*) have been designed and produced. For this time accuracy need, a *DS3231* shield is the solution, as shown in figure A.7 [155].
This item belongs to the family of *Real Time Clocks*, which are nothing but very precise quartz based clocks; these days, most electronic devices have at least one of them embedded.

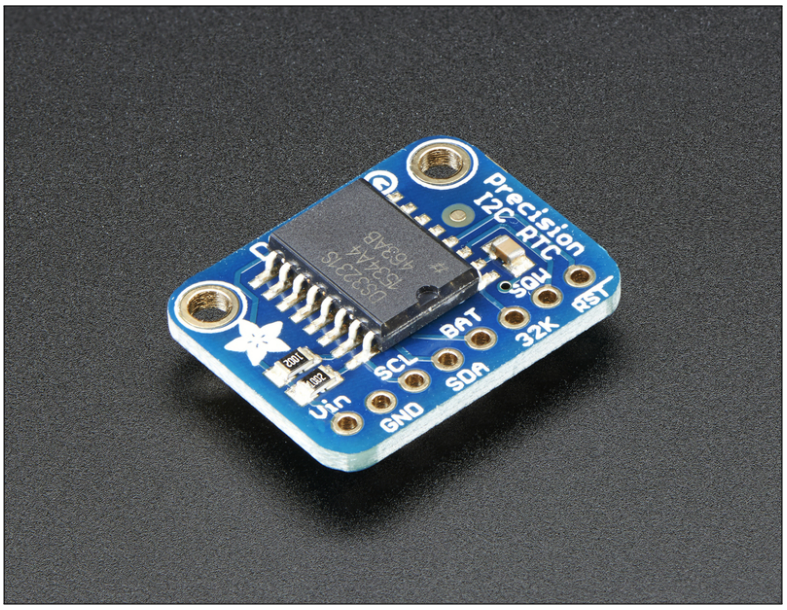

FIGURE A.7: Real Time Clock DS3231

The advantage of this particular unit is that the crystal is embedded in the chip and with it a thermometer measures the changes in environment temperature. The variations are therefore measured and accounted for, making this unit capable of losing less than 5 seconds over 1 month of continuous operation. As a reference, a quartz digital watch loses on average 15 seconds a month. The unit is easily connected to the Arduino and used then as a time keeper.

A.5.2.3 Switching circuit

The Arduino board is powered by a 9 V, either a 9 V battery or a transformer. A transformer is certainly the better option since a battery may not last until the end of a long deposition process. The output connections are capable of providing a $\pm$ 5 V signal. As previously mentioned, the ALD valves electromagnet require a signal of +24 V, so the Arduino on its own can not provide enough voltage to control them. Alternatively, a 24 V power supply could have been connected to a relay, and operated by the Arduino output signals; this option was explored, but the cost of such fast switching relays was deemed too high.

A solid state alternative was then found: transistors are, in a way, relays. Therefore a controlling circuit was designed, as shown in figure A.8; this simple arrangement is composed by a resistance, a transistor and a diode.

- *TIP122 transistor*: chosen because of its capability of handling voltages up to 100V, it was connected according to the diagram in figure A.8. The emitter terminal was connected to ground. The collector terminal was connected to the +24 V power supply and the ALD valve electromagnet.

- *1 kΩ resistor*: the base terminal, the controlling part of the transistor, was connected to the Arduino output pin, but with a resistor inserted in series. The TIP122 is not triggered by voltage but by the right current flowing to the base terminal. A 1 kΩ resistor was used to limit the current flowing from the Arduino output.

- *1N4002 diode*: connected in parallel with the electromagnet, it was placed to protect the transistor. If a device with a coil (like the ALD valve electromagnets) is powered and then stopped, a reverse voltage spike up to several hundreds of V travels back through the circuit, even if only for a few microseconds, and it can burn the transistor. A diode inserted in parallel acts as a voltage rectifier, allowing the voltage to flow in one direction but not in the opposite.

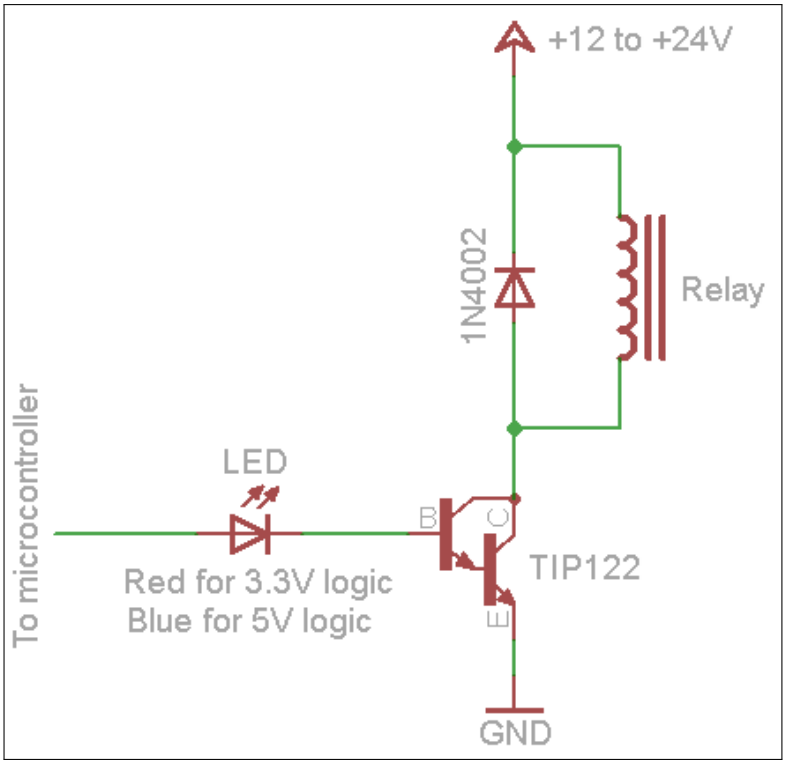

FIGURE A.8: Example of switching circuit diagram

4 ALD valves were acquired to perform the tests. The circuit was designed and machined in house with 4 separate channels available, shown in figures A.9 and A.10.

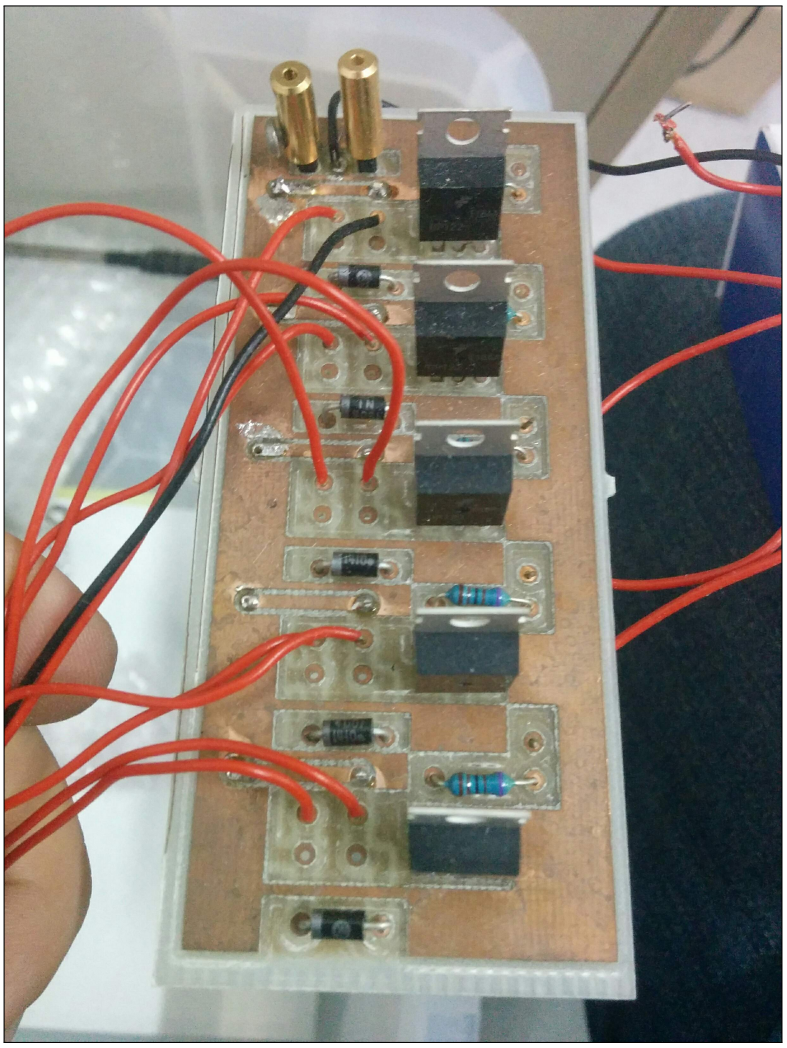

FIGURE A.9: Switching circuit board / top side

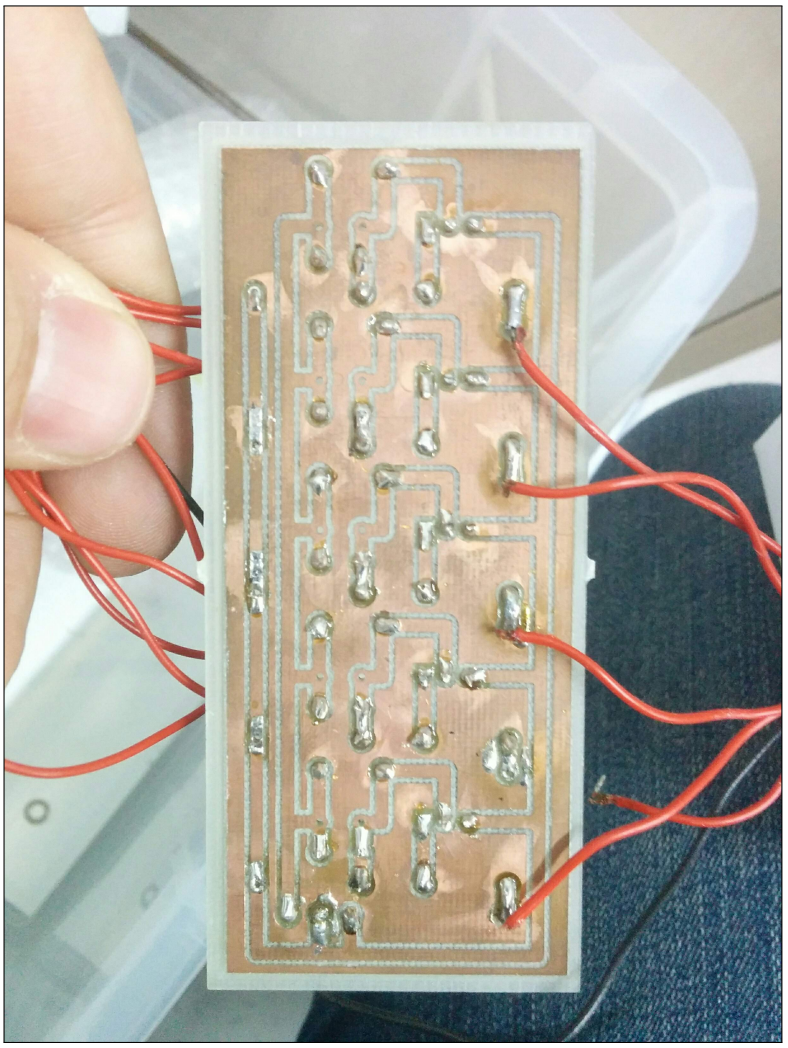

FIGURE A.10: Switching circuit board / bottom side

A.5.2.4 Code

The Arduino requires programming to be able to function. As previously stated, the language used is a version of C /C++ that is very easy to learn and implement. As an example, the following code was written to operate 4 valves / channels:

```
1
2 int reading = 0;                    // define pins for temp
    sensor
3 int sensorPin = A0;
4 int valvebub = 1;                   // define 4 valves connected
    to digital pins
5 int valvepur = 2;
6 int valvehyd = 3;
7 int pwrplasm = 4;
8
9 void setup(){
```

```
10   pinMode(valvebub, OUTPUT);       // sets the digital pins as
      output. Every pin outputs +5V
11   pinMode(valvepur, OUTPUT);
12   pinMode(valvehyd, OUTPUT);
13   pinMode(pwrplasm, OUTPUT);
14 }
15
16 void loop(){
17   delay(5000);                        //wait 5 sec before
      starting the cycle
18   reading = analogRead(sensorPin);
19   int celsius = reading / 2;
20   if (celsius < 250) {
21     deposit ();
22   } else {
23     delay (500);}
24 }
25 void deposit () {
26   int i;
27   for (int i=0; i<=100; i++){
28     digitalWrite(valvebub, HIGH);     // sets the bubbler valve
       on
29     delay(500);                       // waits for 500
      milliseconds
30     digitalWrite(valvebub, LOW);      // sets the bubbler valve
       off
31     delay(1000);                      // waits for a second
32     digitalWrite(valvepur, HIGH);     // sets the purge valve
      on
33     delay(3000);                      // waits for 3 seconds
34     digitalWrite(valvepur, LOW);      // sets the purge valve
      off
35     delay(1000);                      // waits for a second
36     digitalWrite(valvehyd, HIGH);     // sets the hydrogen
      valve on
37     delay(5000);                      // waits for 5 seconds
38     digitalWrite(pwrplasm, HIGH);     // sets the plasma on
39     delay(3000);                      // waits for 3 seconds
40     digitalWrite(pwrplasm, LOW);      // sets the plasma off
41     digitalWrite(valvehyd, LOW);      // sets the hydrogen
      valve off
```

```
42      delay(1000);                        // waits for a second
43      digitalWrite(valvepur, HIGH);       // sets the purge valve
        on
44      delay(5000);                        // waits for 5 seconds
45      digitalWrite(valvepur, LOW);        // sets the purge valve
        off
46      delay (500);
47    }
48 }
```

The main advantage of writing a code is that the level of customization is relatively unlimited. The main disadvantage, compared to a full Labview interface, is in the slightly steeper learning curve required to operate the Arduino.

A.5.2.5 Verification

The Arduino + circuit was tested without the valves by connecting the terminals to an oscilloscope. The electrical signal would switch down to 1 millisecond, which was considered very satisfactory.

Once connected to the ALD valves (not flowing any gas through them), it was possible to verify that the system works down to 10 ms switching intervals: the verification was done by listening to noise that the compressed air actuator would make when switching.

A.6 Conclusions

The use of the commercially available opAL plasma enhanced atomic layer deposition system has not allowed the deposition of pure NbN from the halogen or the MOCVD Nb precursors. The causes of this were mainly attributed to the history of the reactor itself, having being mostly used for the deposition of oxides. The heater plate was also not considered sufficient to fully remove the Cl residue from the deposited films. On these results, a new reactor and its control system has been studied, with promising early results.

Appendix B

Development of PECVD reactor

Appendix B presents the work done on the development of the PECVD reactors. This was not included in the main part of the thesis because the results obtained with it were too preliminary and non conclusive, if though promising. Hereby are reported the engineering considerations, the simulations, the first experiments and the conclusions obtained.

B.1 Plasma enhanced CVD reactor development

B.1.1 ECR unit on first chamber

To perform plasma enhanced chemical vapour deposition (PECVD), an RF source and a resonator are required. For our work, an Astex microwave ECR plasma unit was installed on the top flange of the first chamber (6 way cross, figureB.1). This unit is capable of outputting up to 2000 W of RF power at 2.45 GHz; ECR plasma is denser than 13.65 MHz plasma and used to produce larger numbers of charged ions.

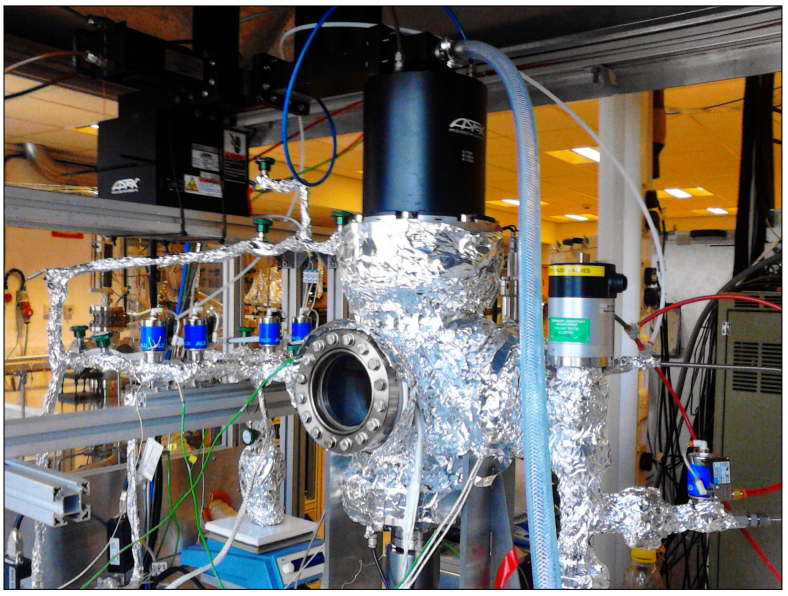

FIGURE B.1: ECR plasma unit installed on the first deposition chamber

To perform the $NbCl_5$ reduction from H_2, a high quantity of energy is require. In CVD, this energy is provided thermally, while in PECVD part of the energy budget is delivered through the creation of ionized species in the plasma, as described in chapter 3. The advantage of this technique is to be able to obtain the same film properties but at lower deposition temperature, releasing the high temperature constraint and widening the range of suitable substrates.

B.1.1.1 PECVD Nb

The ECR plasma was used to deposit at first Nb samples. Figure B.2 one sample coated by using the following parameters:

	Values
Temperature (C)	700
Pressure (mbar)	5
Chamber temperature (C)	140
Argon flow (sccm)	100
Hydrogen flow (sccm)	100
Precursor temperature (T)	130
Deposition time (h)	4
Plasma power (W)	500

TABLE B.1: Nb deposition parameters using ECR plasma on first chamber

FIGURE B.2: Sample of Nb on Cu deposited with ECR plasma

The sample shows incomplete coverage: this uncoated area does not appear in other samples deposited via thermal CVD in the same conditions, and it was attributed to an obstacle between the precursor outlet and the sample.

The copper also seems recrystallized, the reason why will be discussed in chapter 7.

SEM imaging was done on the sample (figure B.3): the surface looks glassy and amorphous, without the sharp features previously seen on samples grown via thermal CVD.

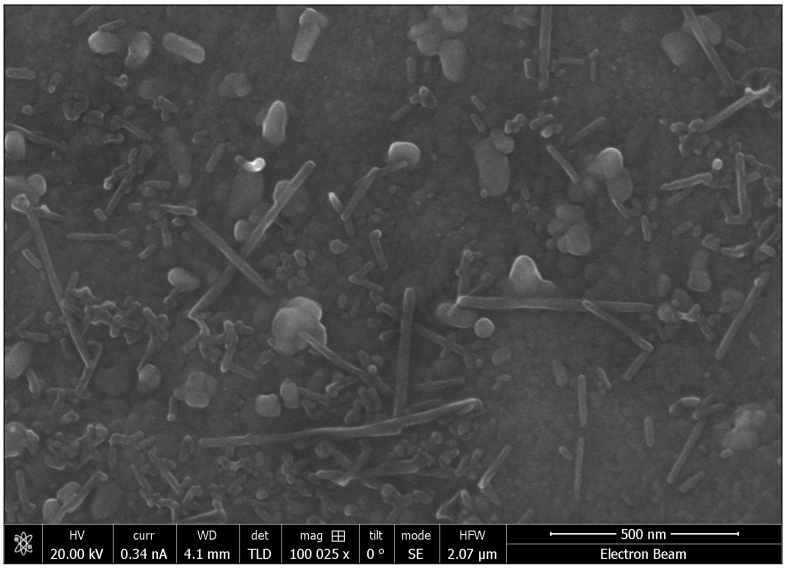

FIGURE B.3: SEM image of Nb on Cu deposited with ECR plasma

The sample was then cross sectioned with FIB, as shown in figure B.4. The deposit looks amorphous, and roughly 200 nm thick.

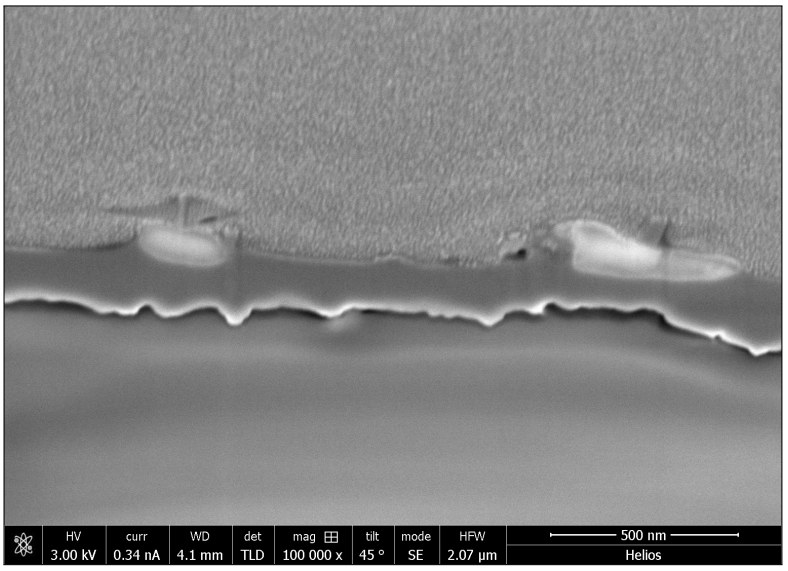

FIGURE B.4: Cross section of Nb on Cu sample grown with ECR plasma

The same growth conditions used for previous CVD growths with the addition of the ECR plasma reduced the growth rate by 50 %, halving it. The film was characterized further, and the results were reported in chapter 7.

B.1.1.2 PECVD NbN

Niobium nitride, as discussed in chapter 1, has a higher T_c than Nb, so it would be desirable to be able to coat Cu cavities with this material to reduce the cooling infrastructure costs. A Nitrogen line / mass flow controller were added to the chamber; the deposition parameters used are reported in table B.2.

	Values
Temperature (°C)	700
Pressure (mbar)	5
Chamber temperature (°C)	140
Argon flow (sccm)	100
Hydrogen flow (sccm)	100
Nitrogen flow (sccm)	35
Precursor temperature (°C)	130
Deposition time (h)	4
Plasma power (W)	500

TABLE B.2: NbN deposition parameters using ECR plasma on first chamber

According to Uyama[140] NH_3 is formed by adding N_2 and H_2 in ratio 1:3 in the plasma via the following equationB.1:

$$NH + H_2 \longrightarrow NH_3 \tag{B.1}$$

The plasma discharge produces the NH radicals by the reaction of nitrogen molecular ions, N_2^+ with hydrogen molecules, H_2, or hydrogen atoms H.

Ammonia reacts with $NbCl_5$ following the reaction route shown in equation B.2:

$$NbCl_5 + H_2 + NH_3 \longrightarrow NbN + 5HCl \tag{B.2}$$

The sample was partially coated with a light bronze film, compatible with the colour of NbN (not silver but bronze). The sample was then SEM imaged, and figure B.5 shows that the growth structure is very different from the Nb samples deposited with thermal CVD, as shown in chapter B.6.

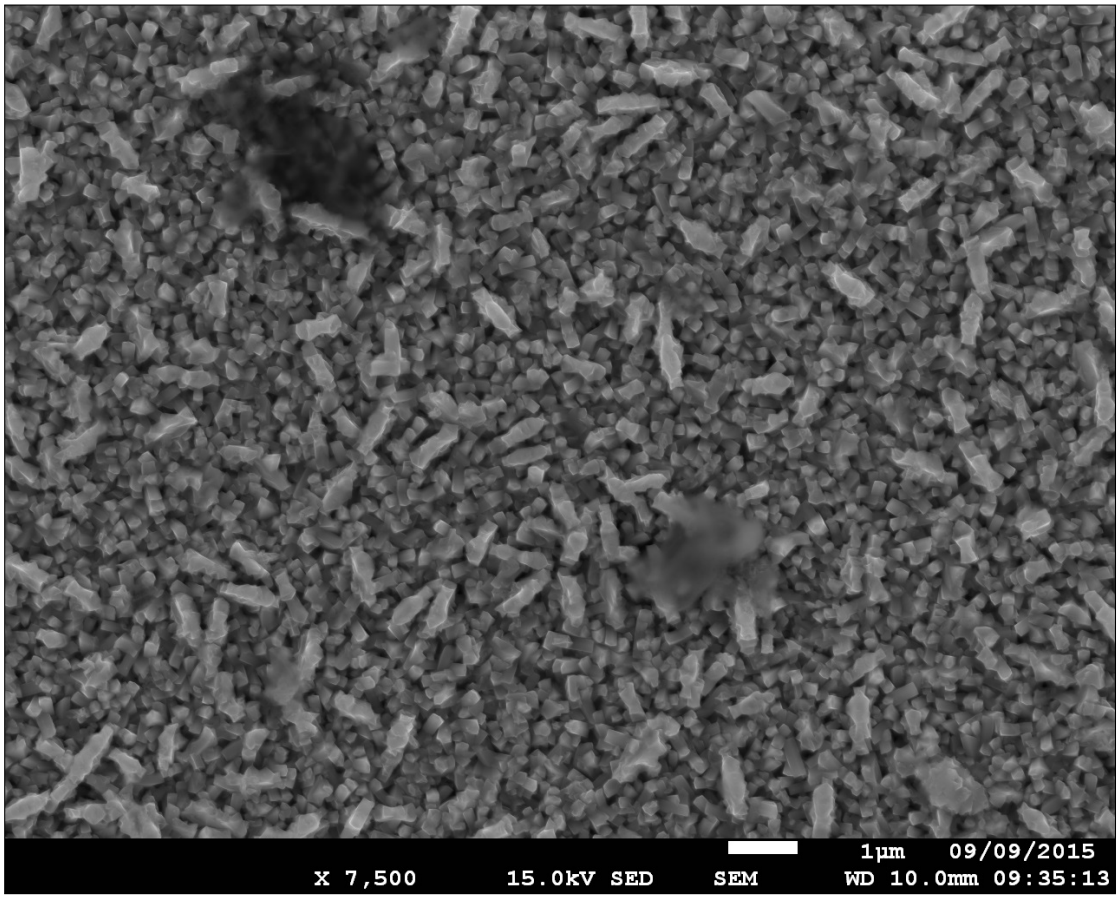

FIGURE B.5: SEM image of NbN growth

Figure B.6 shows the surface of the deposition of Nb obtained at 700 °C on the top, while showing the surface of the deposition of NbN on the bottom. The Nb deposit is characterized by a closely packed structure, with sharp layered features visible in the micrograph. Compared to it, the NbN surface seems to be more open, with "stick" like features randomly arranged and oriented.

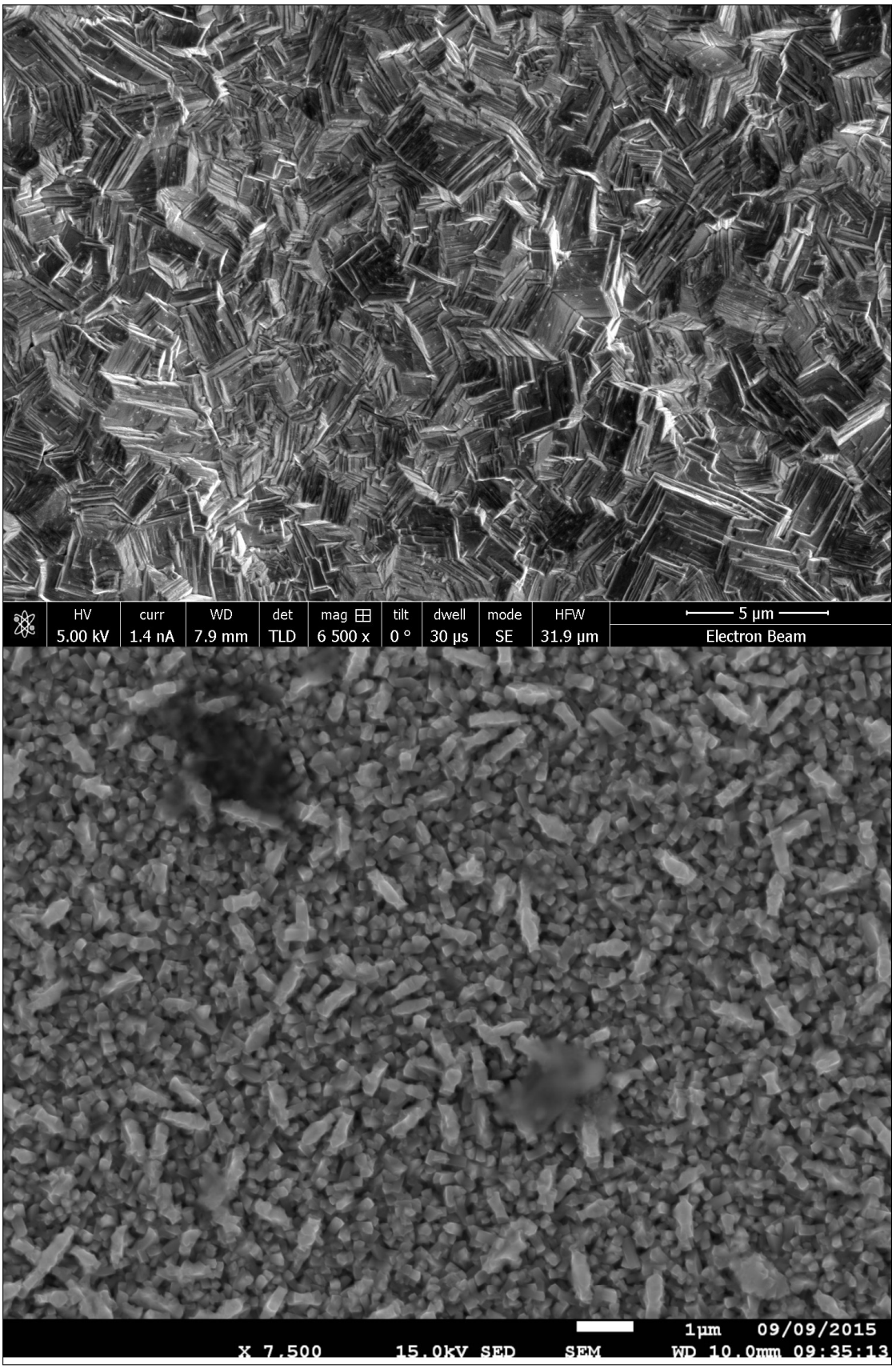

FIGURE B.6: SEM image of Nb (top) and NbN (bottom) deposition. The images were taken with two different SEM (JEOL 6610 and FIB Helios), as explained in chapter 4

The EDX results showed the presence of Nb and N, in a ration of 0.91:1 (table B.3).

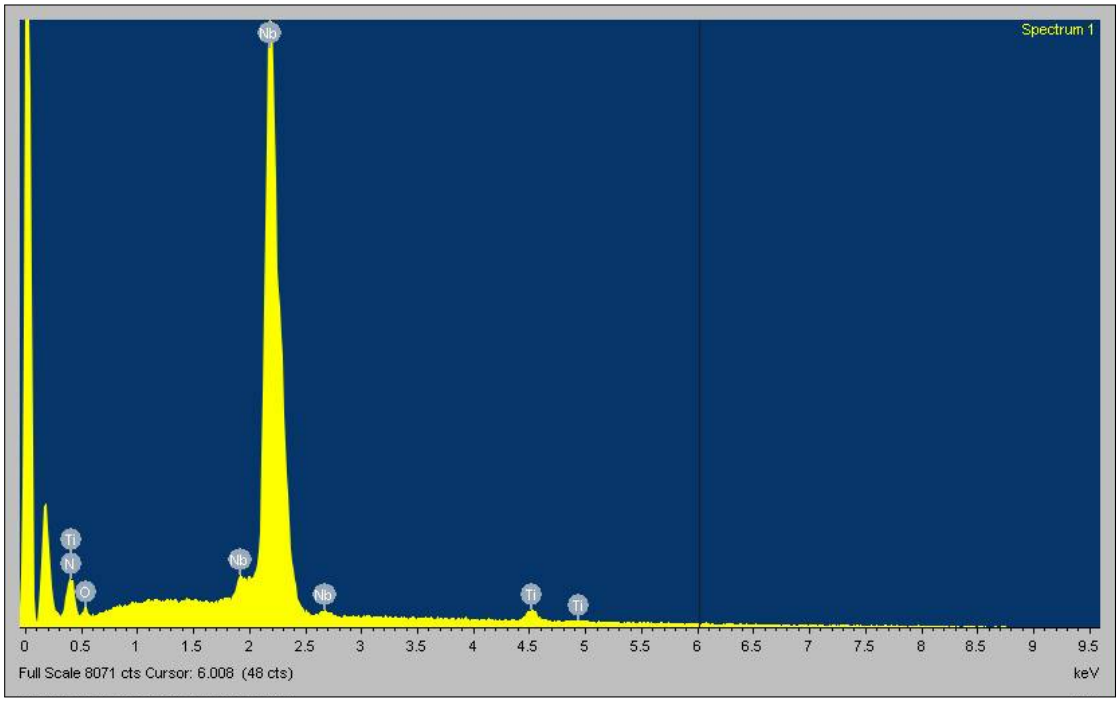

FIGURE B.7: EDX results of NbN deposition with ECR unit

Titanium was also found in the sample, due to some residue left in the gas line from the previous deposition, where titanium was deposited on a Cu substrate.

Element	**Weight%**	**Atomic%**
N	13	48
O	2	5
Ti	2	3
Nb	82	44

TABLE B.3: EDX results of NbN sample obtained with ECR

The sample was then cross sectioned, to investigate the thickness of the material.

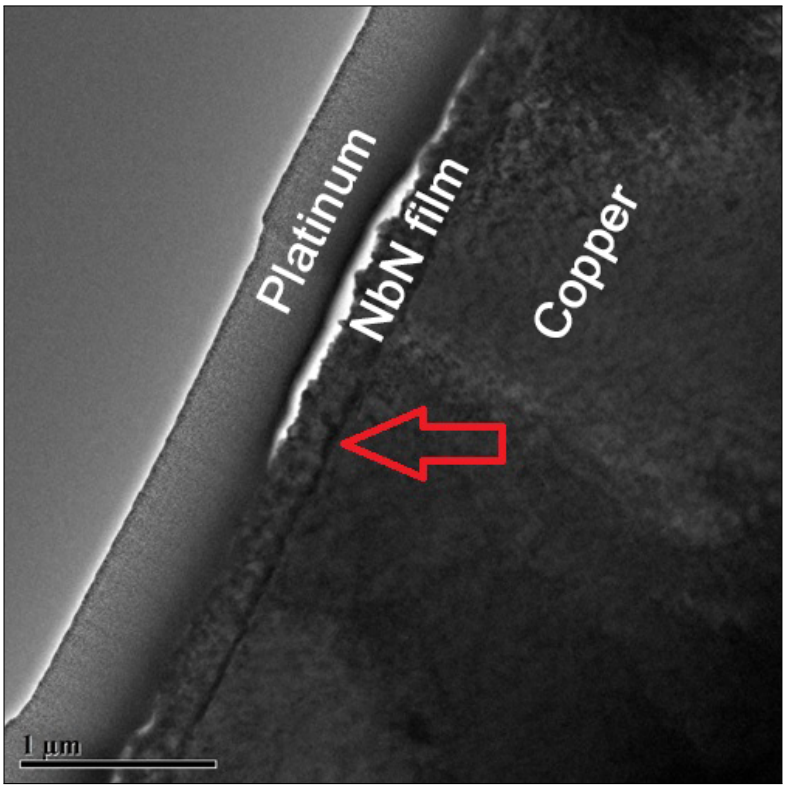

FIGURE B.8: NbN cross section - the red arrow indicates the film

Figure B.8 shows that the film, indicated by the red arrow, is roughly 200 nm thick, which agrees with the previous Nb ECR growth rate. The lack of features suggests that the deposited NbN layer may be characterized by very small crystals less than 100 nm in size. A darker layer seems to be present at the interface between the Cu substrate and the film: a different structure may exist in this region of the sample but it was not investigated any further. The layer visible above the NbN is platinum, coming from the FIB sample preparation.

B.1.1.3 Plasma dome rupture

During the cool down of the second NbN deposition attempt, the light bulbs ruptured, projecting the sample vertically into the quartz plasma dome, which shattered. The sample was also irrecoverable. Being the ECR unit manufactured in 1993 and having the manufacturer gone out of business in the mid-90's, a replacement part was not available off the shelf. It was commissioned to a quartz glass blowing artisan from the US, which took time to produce a suitable replacement. After this event, the ECR unit was removed from the first chamber. Later on, it was installed on the new PECVD chamber discussed in section B.1.3.

B.1.2 Capacitive RF plasma inside the chamber

With the ECR plasma offline, the research was steered towards 13.56 MHz RF plasma. The main reason was the availability of an 300 W RF power supply that was so used to

perform the experiments.

B.1.2.1 Coil design

The power supply is connected to a matching unit, a variable circuit capable of changing parameters to reduce the amount of reflected power redirected from the plasma to the power supply itself.

Even so, matching units can only function in a range of frequencies: therefore the structure should possess at least a resonant frequency as close as possible to the 13.56 MHz. As a designing starting point, the parameters for the RF coil were limited by the size of the chamber, the distance between the top flange and the heater, the diameter of the heater. Within these constraints, using the calculator found on "http://hamwaves.com/antennas/inductance.html", the following parameters were selected (table B.4):

Height of the coil	5 cm
Diameter of the coil	10 cm
Diameter of the tubing	6.2 mm
Number of turns	3

TABLE B.4: RF coil parameters

A 1/4 inch O.D. copper tube was used to make the coil. Once installed on the DN160CF flange, it was connected to a network analyser to measure the resonance frequency, which was found at 88 MhZ, not too far from the 90 MHz given by the calculation. This was deemed acceptable since it was in range of the matching unit. Water cooling was applied to prevent any damage to the coil itself during operation.

B.1.2.2 Deposition results

Four depositions were performed with this configuration. Deposition time, temperature, precursor temperature, gases flow and pressure in the chamber were kept constant, while the plasma power was set at 25/50/75/100 W. In all four cases, the substrate were covered, but not homogeneously. The introduction of the coil added turbulences that modified the flowing of the gases over the substrates.

B.1.2.3 Corrosion and deposition

The use of this RF coil was stopped after a few depositions, due to some unwanted chemical reactions. Copper does not react with the products of the Nb reduction (i.e. hydrochloric acid), but copper oxide does, according to the chemical route in equation B.3 [156]:

$$CuO + 2HCl \longrightarrow CuCl_2 + H_2O \tag{B.3}$$

The CuO layer is attached by the hydrochloric acid through a redox reaction, leaving on the surface of the coil $CuCl_2$. This is a brown hygroscopic solid that readily absorbs water to change in $CuCl_2 \times 2H_2O$, its azure dihydrate form, as it can be seen in figure B.9. Since the chamber is not provided with a load-lock system, there was no way to prevent water from entering the chamber and reacting with the $CuCl_2$, which had then to be mechanically removed. After doing so, the copper tube was inevitably thinner, leading to a shift in the resonant frequency, to the point of being outside the range of the matching unit and requiring a coil replacement.

FIGURE B.9: Copper coil after four depositions. The colour of copper chloride deposit can be seen

A metallic coating also started to appear on the vacuum side of the feedthroughs, even if far away from the hot reaction area. The deposited samples were analysed but the results obtained were not conclusive regarding the plasma contribution to the reaction.

Even though potentially viable for other deposition, the amount of corrosion seen on the copper coil was clearly due to the chemicals used. It was therefore deemed not suitable for the deposition of pure Nb, and so abandoned.

B.1.3 ECR unit on second chamber

B.1.3.1 Custom chamber

A new chamber was manufactured to perform PECVD depositions. The chamber is comprised by a 25 cm long pipe with two DN160CF flanges at the ends, with a 8 cm long intersection terminating in a DN100CF flange, shown in figure B.10.

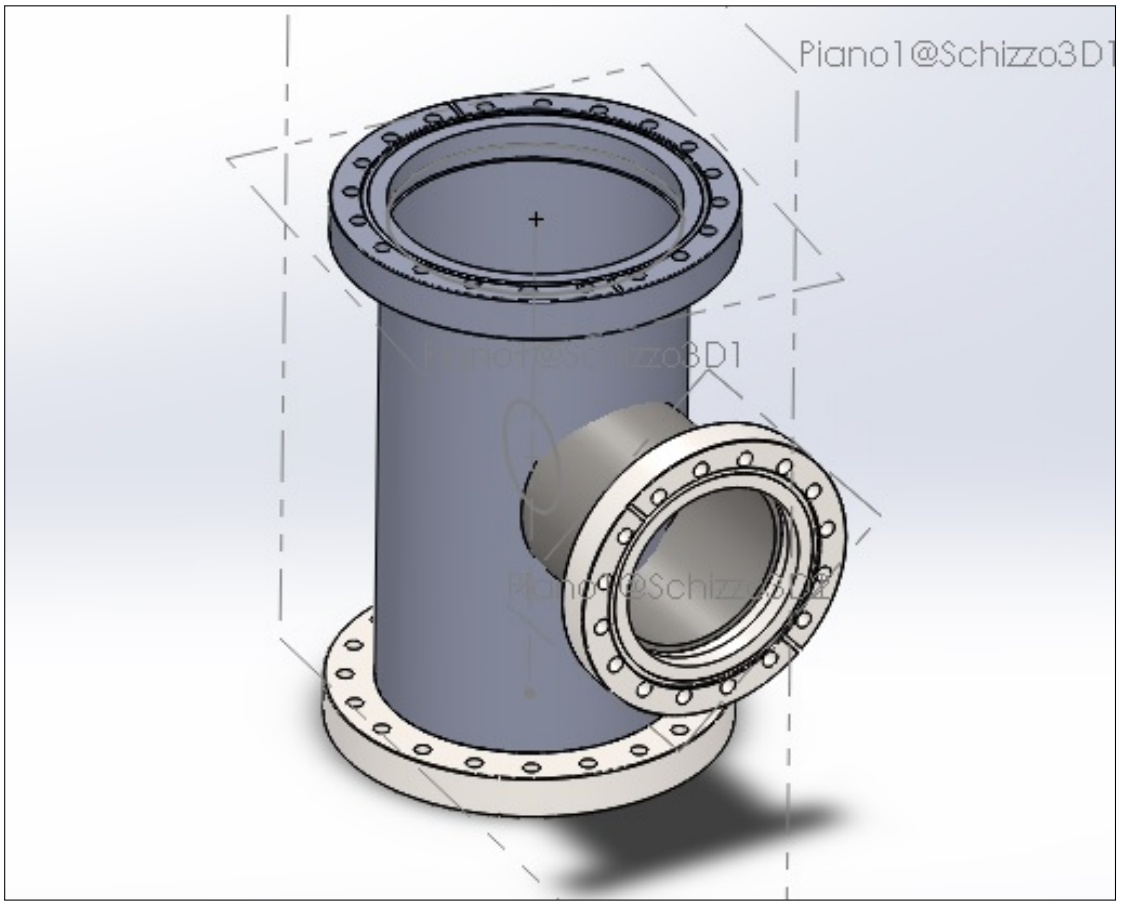

FIGURE B.10: 3D model of the PECVD chamber

The top of the chamber was connected through a custom made adaptor flange to the ECR plasma unit discussed in section B.1.1.

The bottom of the chamber was connected to a custom made flange with three DN16FC pumping ports, to evenly distribute the pumping of the chamber and to simplify the gas dynamics; a special fitting discussed below was welded in the middle of the bottom flange.

A viewport was connected to the DN100CF flange, and it is the port through which the samples are introduced and removed from the chamber. The viewport was covered

with aluminium foil during the PECVD process to stop any RF leakage from escaping the vessel, since untreated glass is transparent to RF.

B.1.3.2 Corrosion resistant sealed heater

As previously described, the light bulb based heater is capable of bringing the sample to very high temperature, but its performance has proven unstable and at times detrimental. Various ideas were explored whilst looking for a valid replacement. The main parameters considered were heating power followed by durability. The new heater would have to be capable of reaching at least 800 °C, while providing constant and stable heat with repeatable performance between experiments. The chosen heater is presented in figure B.11 and B.12. The design is from Heatwave Labs and comprises a tungsten filament suspended in a Inconel jacket, all mounted on a stainless steel 316 cylinder. The electrical connections are on the air side of the assembly, isolated from the chamber and the deposition processes, to prevent the contamination and shorting issues experienced with the light bulb heater. The filament itself is contained in its own vacuum, also isolated from the chamber, to prolong the life of the filament itself. A new power supply (30 V-40 A) was needed to operate this heater, since the Variac is not capable of producing a high enough current required by the new part.

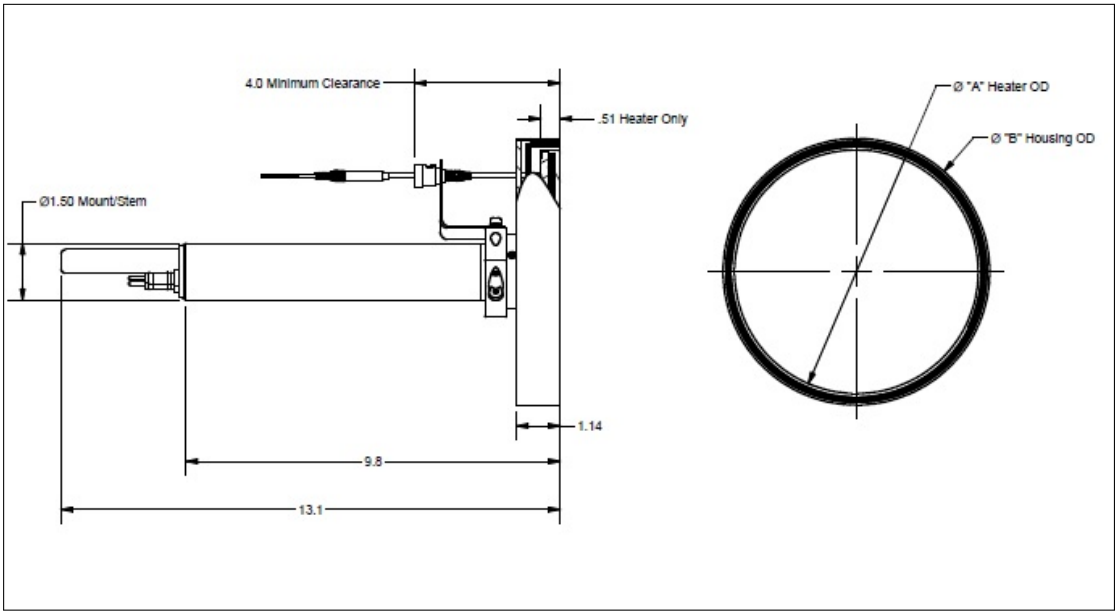

FIGURE B.11: Sealed heater technical drawing

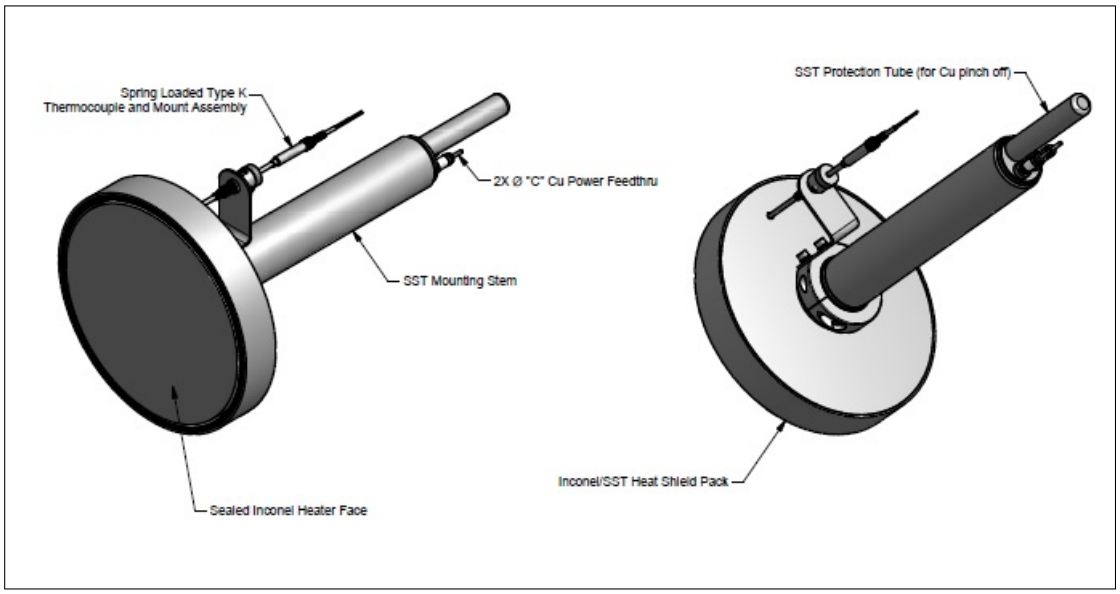

FIGURE B.12: Sealed heater 3D model

A sealed K type thermocouple was mechanically pushed against the bottom of the heater plate, to measure the temperature of the plate. Sufficient time was given to the samples to ensure temperature uniformity. The heater stem is a smooth electropolished 1.5 inches wide cylinder, which required a special bracket to be mounted. This bracket had to be modified to fit the chamber design and vacuum welded on the custom DN160CF bottom flange (figure B.13). The vacuum seal is guaranteed by two Kalrez rings, capable of withstanding temperatures slightly higher than 300 °C.

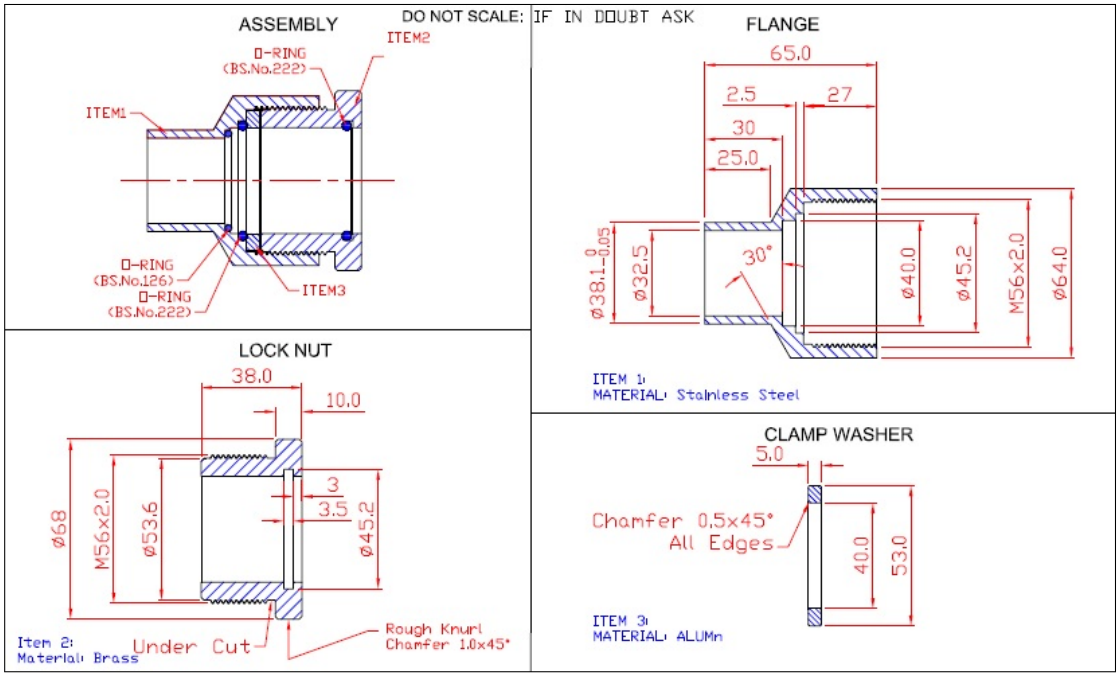

FIGURE B.13: Drawing for modified mounting bracket

FIGURE B.14: Sealed heater with custom flange and bracket assembly

The full assembly is shown in figure B.14. Once installed, the heater did not reach the temperatures that were specified in the technical data. Moreover, after 10 runs, the filament broke and rendered the heater useless. The unit has been shipped away for repairs, but as of today it has not been returned yet.

B.1.3.3 Flat Filament heater replacement for PECVD rig

The broken sealed heater was replaced by a custom flat filament heater. A coated filament was bent and embedded in a 10 cm in diamater MACOR plate. Two separate heater plates were manufactured, one covering an area of 5 cm in diameter and the other of 10 cm in diameter, to allow the heating of 5 cm and 10 cm wide round substrates.

To avoid major changes to the chamber pumping system and design, a 1.5 inches electro polished tube was used as support for the heater assembly, to use the same custom flange already manufactured.

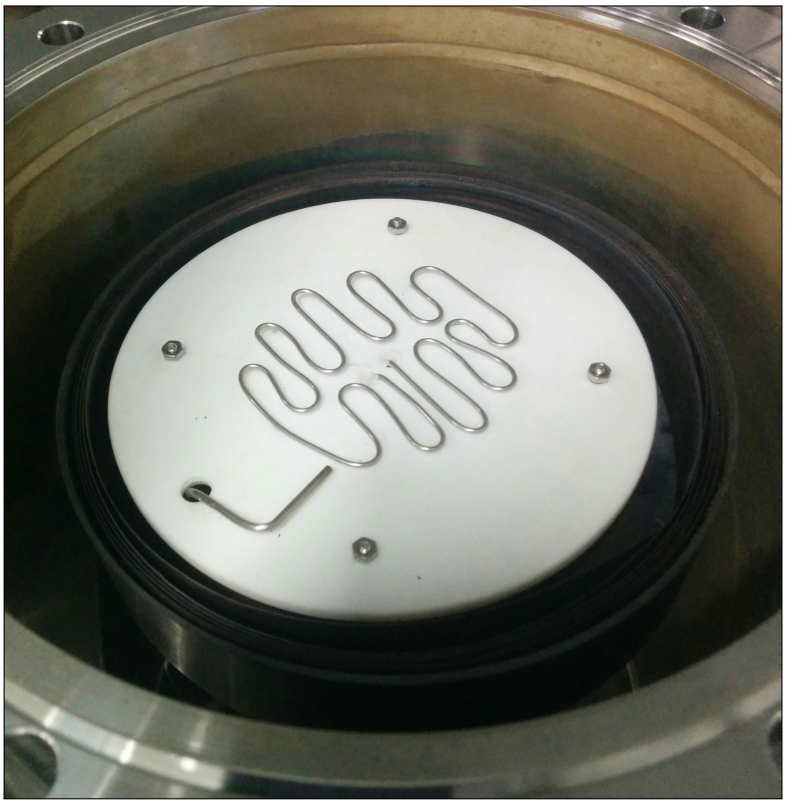

FIGURE B.15: Flat filament heater installed

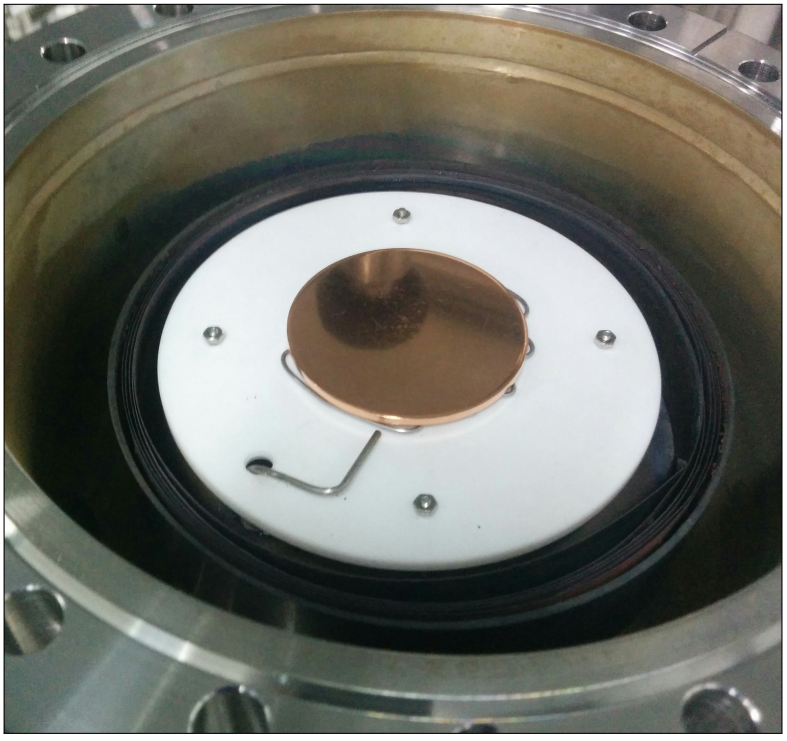

FIGURE B.16: Flat filament heater with sample covering it

A DN16 CF flange was vacuum welded to one end of the tube, where a DN16 CF flange with two ceramic - copper feedthroughs was installed to leave the electrical

connections on air side. The Inconel / tungsten heatshield from the sealed heater was connected to the other end of the tube, where the ceramic heater plate, as shown in figures B.15 and B.16, was rested on a 4 inch O.D. stainless steel tube. Two ceramic beaded 1 mm thick copper wires were used to connect the filament to the feedthroughs. This new assembly replicated the sealed heater design concept of keeping away the reaction gases from the electrical parts, to limit if not prevent any conductive coating deposition on the insulated parts and leak or short current to ground, requiring constant disassembling, cleaning and replacing of the filaments.

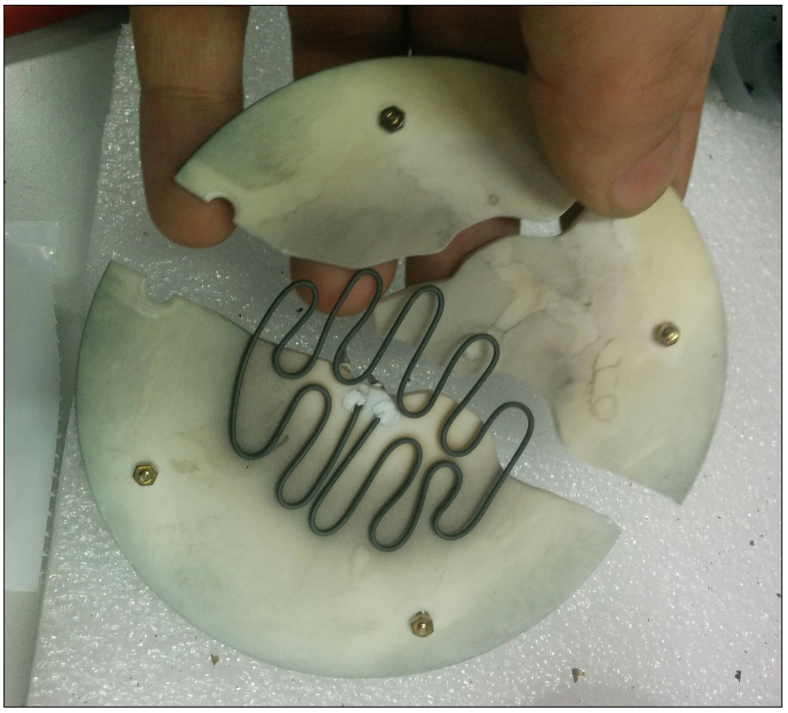

FIGURE B.17: 5 cm heater after first run

During the first calibration run, the MACOR plate cracked while the filament was at 700 °C, as shown in figure B.17. The mechanical shock broke the incandescent filament, rendering this assembly unusable.

The plate was replaced with the larger one, as shown in figure B.18, to resume the deposition program.

A few calibration runs were performed, to assess the heater performance, and it was found that:

- *Larger uncovered area*: only 25 % of the heater filament was now covered by the substrate. This lead to more heat irradiation, and an increase in temperature of the chamber walls (from 80 °C to 100 °C).

- *MACOR strength*: the ceramic chosen for the heater assemblies could not withstand high temperatures. It was chosen because of its availability, ease of machining and relative low cost. According to its specifications, MACOR continuous operating temperature is 800 °C. This disagrees with our finding, since the plates

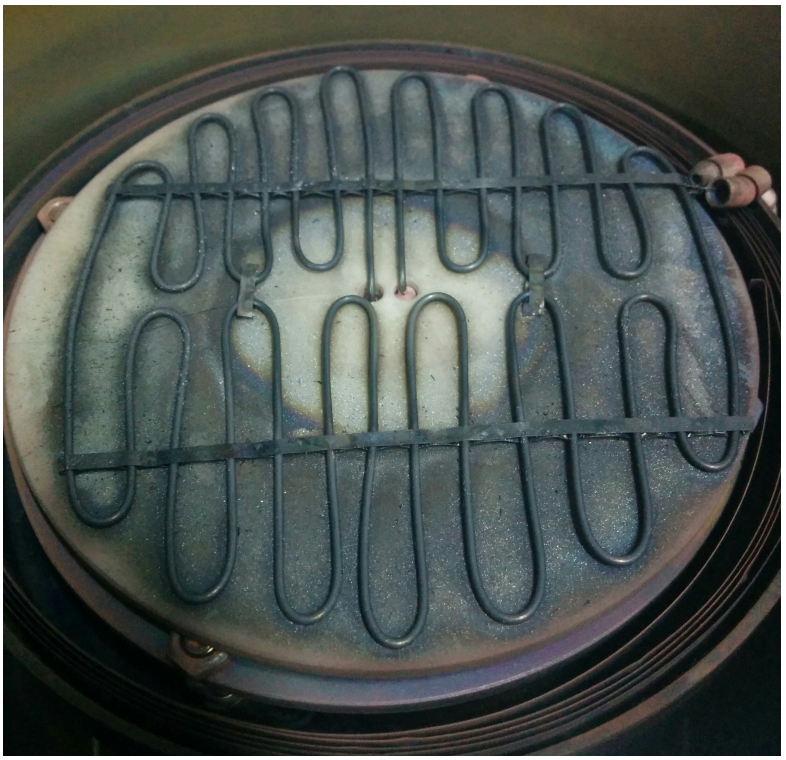

FIGURE B.18: 10 cm heater installed in the chamber. The white area lays in the shadow of the substrate, hence why is not coated

cracked in both cases at 700 °C. It is worth to notice that the cracks are aligned with the machined holes: this suggests that any machining of the plate introduces stress points in the material. The larger assembly, also cracked, but did not stop working: the hot filament did not receive a shock thanks to the spot welded support strips that increased the rigidity of the filament serpentine.

- *Poor contact*: the heat transfer between the filament and the substrate was poor: at full power, the filament temperature was measured at 800 °C, while the substrate was at 400 °C. This sizeable difference was attributed to the few contact points between the filament and the substrate. To improve it, the substrate could have been mechanically fastened on the heater plate, but the impossibility of machining the ceramic any further prevented this approach.

The flat heaters do provide thermal stability, control and reliability. The poor heat transfer to the substrate is though very detrimental to the design, being a primary factor in the choice of heaters. After these considerations the flat filament heater were abandoned, in favour of the light bulb based heater design.

B.1.3.4 Custom blast shield

The flat filament heaters were replaced with a newly machined light bulb heater plate, shown in figure B.19.

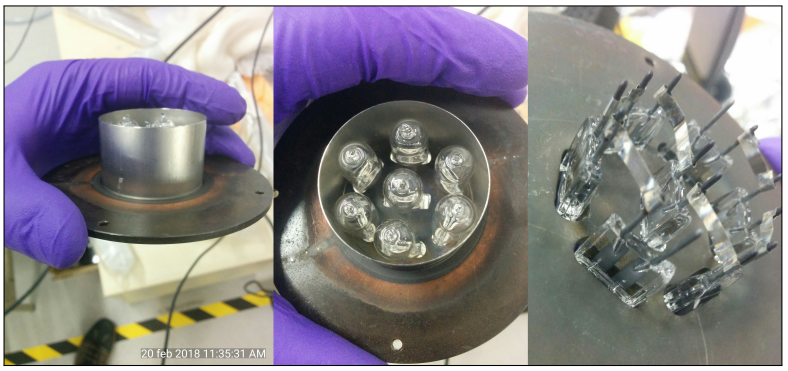

FIGURE B.19: Light bulb plate and bulbs connection array

Returning to the light bulb heater presented the same problem that had previously compromised the project, or the breaking of the ECR plasma quartz dome. This forced the introduction of a custom blast shield, shown in figures B.20 and B.21, to stop the sample from being projected upwards and hitting the dome in case of a catastrophic light bulb failure. This shield was fashioned out of a DN100CF 6 inches O.D. blanking flange (3 mm thick): a 48 mm hole was milled through the centre, 2 mm smaller in diameter than the 50 mm copper samples used as substrate.

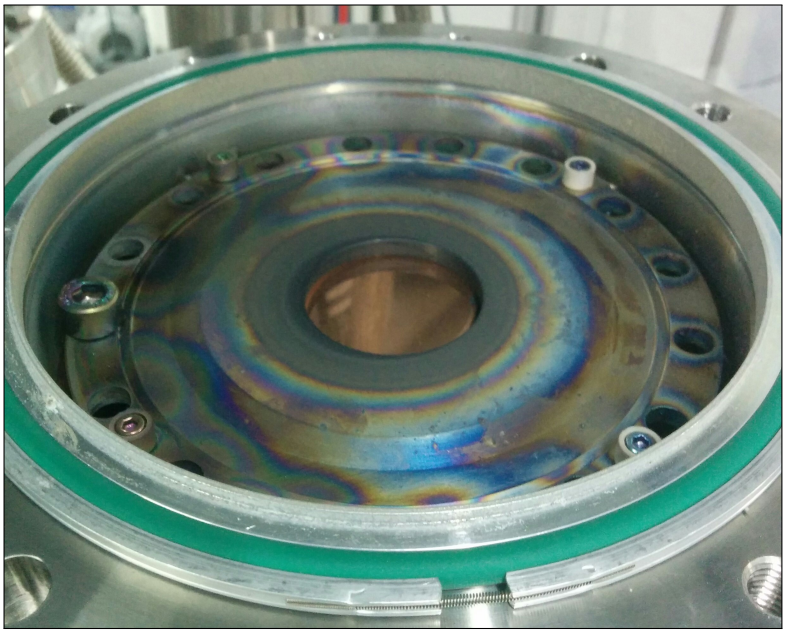

FIGURE B.20: Blast shield with copper substrate showing through the hole. The sample is not as close to the shield during the deposition

The shield was mounted on ceramic supports to isolate it from the ground. This was done to allow the possibility of measuring the amount of current produced from the plasma and, if not sufficient, to be able to apply a bias and therefore extract and direct ions from the plasma towards the substrate underneath.

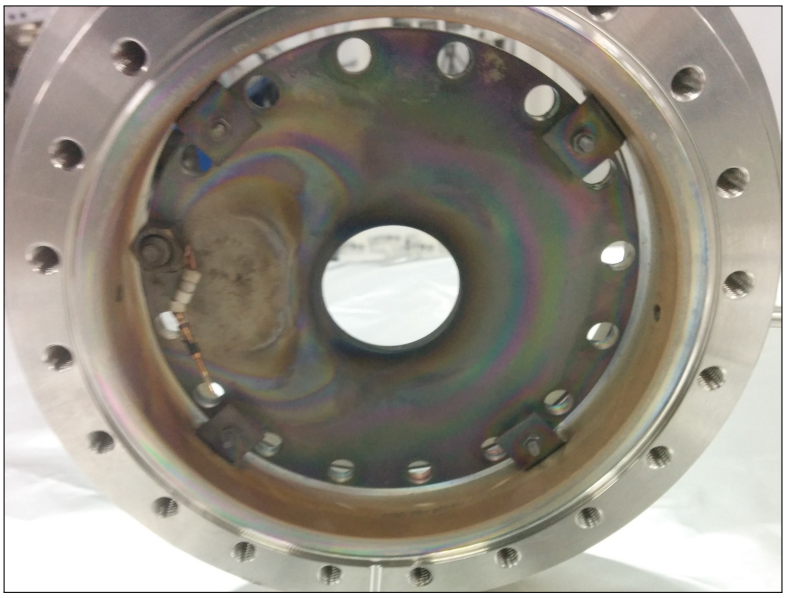

FIGURE B.21: Blast shield seen from underneath. The beaded copper wire on the left is connected to a feedthrough that allows either the grounding of the plate or the biasing of it

B.1.3.5 Flow simulation

Simulations were performed (figures B.22 and B.23) on the deposition chamber by using the same settings as previous simulations.

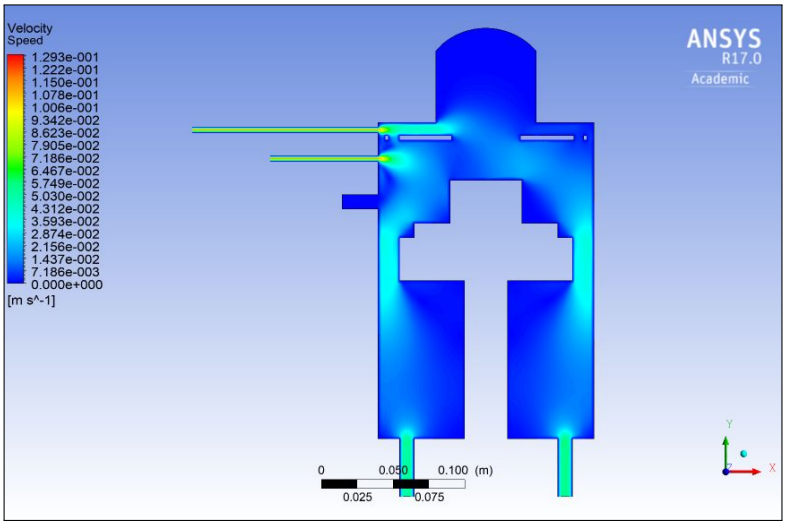

FIGURE B.22: Simulation of the gases speed entering the ECR deposition chamber

It was possible to optimize the height of the sample in the chamber in order to maximise the exposure to the precursor: this was done by running gas flow simulations with the same gas inlet and outlet parameters, but by modifying the height of the sample stage. A too low setting resulted in the gases flowing too high above the substrate, while having the sample stage too high resulted in the inlet gas flow being disrupted by the

substrate itself, creating turbulent patterns. Figures B.22 and B.23 show the best result obtained from the simulation runs, which was the final chosen geometry.

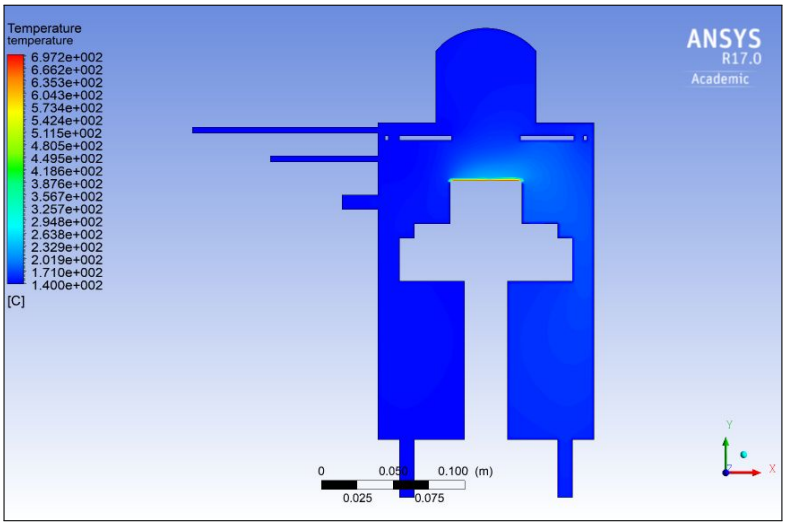

FIGURE B.23: Simulation of the temperature profile for the ECR deposition chamber

References

[1] M. Stanley (Milton Stanley) Livingston and 1910 Blewett, John P. (John Paul). *Particle accelerators*. New York : McGraw-Hill, 1962. Includes bibliography.

[2] Ernest Rutherford. The scattering of α and β particles by matter and the structure of the atom. *Philosophical Magazine*, 92(4):379–398, 2012.

[3] Rolf Wideröe. Über ein neues prinzip zur herstellung hoher spannungen. *Archiv für Elektrotechnik*, 21(4):387–406, 1928.

[4] Ernest O Lawrence and M Stanley Livingston. The production of high speed light ions without the use of high voltages. *Physical Review*, 40(1):19, 1932.

[5] Ernest O Lawrence. Method and apparatus for the acceleration of ions, February 20 1934. US Patent 1,948,384.

[6] Radio-craft, 1947. URL `http://www.americanradiohistory.com/Archive-Radio-Craft/1940s/Radio-Craft-1947-Jun.pdf`.

[7] CERN. Large hadron collider homepage. URL `https://home.cern/topics/large-hadron-collider`.

[8] VI Veksler. A new method of particle accelleration. In *Dokl. Akad. Nauk SSSR*, volume 44, pages 393–396, 1944.

[9] J David Jackson and WKH Panofsky. Edwin mattison mcmillan 19071991. a biographical memoir, 1996.

[10] Alexander Wu Chao, Karl Hubert Mess, Maury Tigner, and Frank Zimmermann. *Handbook of accelerator physics and engineering*. World Scientific, 1999.

[11] Fermilab. The tevatron accelerator, 2014. URL `https://www.fnal.gov/pub/tevatron/tevatron-accelerator.html`.

[12] Gustaf Ising. Prinzip einer methode zur herstellung von kanalstrahlen hoher voltzahl. *Ark. Mat. Astron. Fys.*, 18:1–4, 1924.

[13] Robert W Hamm, Kenneth R Crandall, and James M Potter. Proton-beam therapy linac, January 17 1995. US Patent 5,382,914.

[14] F Carminati, C Roche, Juan Antonio Rubio, Carlo Rubbia, Jean Pierre Charles Revol, and Robert Klapisch. An energy amplifier for cleaner and inexhaustible nuclear energy production driven by a particle beam accelerator. Technical report, P00019698, 1993.

[15] William P Griffith and Peter JT Morris. Charles hatchett frs (1765-1847), chemist and discoverer of niobium. *Notes and Records*, 57(3):299–316, 2003.

[16] Geoff Rayner-Canham and Zheng Zheng. Naming elements after scientists: an account of a controversy. *Foundations of Chemistry*, 10(1):13–18, 2008.

[17] M Peiniger and H Piel. A superconducting nb3sn coated multicell accelerating cavity. *IEEE Transactions on Nuclear Science*, 32(5):3610–3612, 1985.

[18] Mattia Checchin, Anna Grassellino, Martina Martinello, Sam Posen, Alexander Romanenko, and John Zasadzinski. Ultimate gradient limitation in niobium superconducting accelerating cavities. Technical report, Fermi National Accelerator Laboratory (FNAL), Batavia, IL (United States), 2016.

[19] K Saito et al. Critical field limitation of the niobium superconducting rf cavity. In *Proceedings of the 10th International Conference on RF Superconductivity, Tsukuba, Japan*, 2001.

[20] Anne-Marie Valente-Feliciano. Superconducting rf materials other than bulk niobium: a review. *Superconductor Science and Technology*, 29(11):113002, 2016.

[21] Sam Posen and Daniel Leslie Hall. Nb3sn superconducting radiofrequency cavities: fabrication, results, properties, and prospects. *Superconductor Science and Technology*, 30(3):033004, 2017.

[22] Daniel Leslie Hall, John Julian Kaufman, Matthias Liepe, Ryan Douglas Porter, James Sears, et al. First results from new single-cell nb3sn cavities coated at cornell university. *Proceedings of IPAC 2017*, 2017.

[23] M Peiniger, M Hein, and N Klein. Work on nb 3 sn cavities at wuppertal. Technical report, 1988.

[24] Dan Gonnella, Ralf Eichhorn, Fumio Furuta, Mingqui Ge, Daniel Hall, Vivian Ho, Georg Hoffstaetter, Matthias Liepe, Tim O'Connell, Sam Posen, et al. Nitrogen-doped 9-cell cavity performance in a test cryomodule for lcls-ii. *Journal of Applied Physics*, 117(2):023908, 2015.

[25] A Grassellino, A Romanenko, D Sergatskov, O Melnychuk, Y Trenikhina, A Crawford, A Rowe, M Wong, T Khabiboulline, and F Barkov. Nitrogen and argon doping of niobium for superconducting radio frequency cavities: a pathway to highly

efficient accelerating structures. *Superconductor Science and Technology*, 26(10): 102001, 2013.

[26] R Vaglio. Alternative superconducting materials for rf cavity applications. *Part. Accel.*, 61:127–136, 1998.

[27] Anne-Marie Valente-Feliciano. *Development of SRF monolayer/multilayer thin film materials to increase the performance of SRF accelerating structures beyond bulk Nb*. PhD thesis, 2014. URL `http://www.theses.fr/2014PA112254`. Thse de doctorat dirige par Antoine, Claire et Delayen, Jean Physique Paris 11 2014.

[28] DE Oates, Alfredo C Anderson, CC Chin, JS Derov, G Dresselhaus, and MS Dresselhaus. Surface-impedance measurements of superconducting nbn films. *Physical Review B*, 43(10):7655, 1991.

[29] S Isagawa. rf superconducting properties of reactively sputtered nbn. *Journal of Applied Physics*, 52(2):921–927, 1981.

[30] Alban Sublet, Walter Venturini Delsolaro, Mathieu Therasse, Thibaut Richard, Guillaume Rosaz, Sarah Aull, Pei Zhang, Barbora Bártová, Sergio Calatroni, and Mauro Taborelli. Developments on srf coatings at cern. 2015.

[31] Alexej Grudiev, Gilles Favre, Thibaut Richard, Ofelia Capatina, Carlo Zanoni, Alban Sublet, Federico Carra, Rama Calaga, Leonel Ferreira, Sergio Calatroni, et al. Design of a compact superconducting crab-cavity for lhc using nb-on-cu-coating technique. 2015.

[32] JR Gavaler, DW Deis, JK Hulm, and CK Jones. Superconducting properties of niobium-titanium-nitride thin films. *Applied Physics Letters*, 15(10):329–331, 1969.

[33] YP Purandare, AP Ehiasarian, and P Eh Hovsepian. Deposition of nanoscale multilayer crn/nbn physical vapor deposition coatings by high power impulse magnetron sputtering. *Journal of Vacuum Science & Technology A: Vacuum, Surfaces, and Films*, 26(2):288–296, 2008.

[34] B Leone, BD Jackson, JR Gao, and TM Klapwijk. Geometric heat trapping in niobium superconductor–insulator–superconductor mixers due to niobium titanium nitride leads. *Applied Physics Letters*, 76(6):780–782, 2000.

[35] VA. Price of nb per metric ton, 2018. URL `https://www.metalary.com/niobium-price/`.

[36] Robert Kephart, Nihan Sipahi, Philippe Piot, Stephen Milton, Brian Chase, Anna Grassellino, Oleg Pronitchev, Sergei Nagaitsev, Swapan Chattopadhyay, Vyacheslav Yakovlev, et al. Srf, compact accelerators for industry & society. 2015.

[37] Tai-Chang Chiang. Superconductivity in thin films. *Science*, 306(5703):1900–1901, 2004.

[38] D Gerstenberg and PM Hall. Superconducting thin films of niobium, tantalum, tantalum nitride, tantalum carbide, and niobium nitride. *Journal of The Electrochemical Society*, 111(8):936–942, 1964.

[39] Barbora Bártová, Duncan Alexander, Sergio Calatroni, Alban Sublet, Arthur Aebersold, Marco Cantoni, and Mauro Taborelli. Characterization of nb coating in hie-isolde qwr superconducting accelerating cavities by means of sem-fib and tem. Technical report, 2015.

[40] James Mitchell, Adam Tutte, Eric Montesinos, Robert Apsimon, Alick Macpherson, Graeme Burt, and Rama Calaga. Lhc crab cavity coupler test boxes. 2016.

[41] S Audisio, H Hamed, and D Hertz. Deposition and study of niobium coating on iron and copper substrates from reduction of nbcl5 by hydrogen or vapors of zinc. *Le Journal de Physique IV*, 5(C5):C5–1087, 1995.

[42] VM Arrieta and Shawn R McNeal. High-purity niobium superconducting radio frequency cavities. *Final Report (ULTRA-TR-06-4205), Grant DE-FG02-05ER84175, Ultramet for US Department of Energy, Washington, DC*, 2006.

[43] Victor A Arrieta, Shawn R McNeal, et al. Economical manufacture of seamless high-purity niobium. *Final Report (ULTRA-TR-10-4935), Grant DESC0002721, Ultramet for US Department of Energy, Washington, DC*, 2010.

[44] DL Hall, DA Gonnella, M Liepe, VA Arrieta, and SR McNeal. Quality factor measurements of the ultramet 3 ghz cavity constructed using chemical vapour deposition. 2013.

[45] Ryan Porter, Victor Arrieta, Daniel Hall, Matthias Liepe, James Maniscalco, Shawn McNeal, and Brian Williams. High-performance thin-film niobium produced via chemical vapor deposition (cvd). In *18th Int. Conf. on RF Superconductivity (SRF'17), Lanzhou, China, July 17-21, 2017*, pages 674–680. JACOW, Geneva, Switzerland, 2018.

[46] Th Proslier, Y Ha, J Zasadzinski, G Ciovati, P Kneissel, C Reece, R Rimmer, A Gurevich, L Cooley, G Wu, et al. Atomic layer deposition for srf cavities. Technical report, Fermi National Accelerator Laboratory (FNAL), Batavia, IL, 2009.

[47] Jim Norem, Nick Becker, Alexander Gurevich, Gianluigi Ciovati, Jeffrey Klug, Thomas Proslier, Maxim Kharitonov, Michael Pellin, and John Zasadzinski. Developing rf structures using atomic layer deposition. 2011.

[48] Jim Norem, Robert Rimmer, Charles Reece, Jeffrey Elam, Michael Pellin, Yang Ha, Lance Cooley, Thomas Proslier, Alexander Gurevich, Peter Kneisel, et al. Atomic layer deposition for srf cavities. Technical report, 2009.

[49] C Antoine and France CEA. Atomic layer deposition for srf cavities.

[50] Werner Buckel. *Superconductivity. Fundamentals and applications. 3. rev.* 1984.

[51] Heike Kamerlingh Onnes, Albert Perrier, and E Oosterhuis. Further experiments with liquid helium. h. on the electrical resistance of pure metals etc. vii. the potential difference necessary for the electric current through mercury below 4.19k. In *KNAW, Proceedings*, volume 15, pages 1406–1430, 1913.

[52] Walther Meissner and Robert Ochsenfeld. Ein neuer effekt bei eintritt der supraleitfähigkeit. *Naturwissenschaften*, 21(44):787–788, 1933.

[53] Fritz London and Heinz London. The electromagnetic equations of the supraconductor. *Proc. R. Soc. Lond. A*, 149(866):71–88, 1935.

[54] Charles Kittel, Paul McEuen, and Paul McEuen. *Introduction to solid state physics*, volume 8. Wiley New York, 1996.

[55] J. Bardeen, L. N. Cooper, and J. R. Schrieffer. Theory of superconductivity. *Phys. Rev.*, 108:1175–1204, Dec 1957. doi: 10.1103/PhysRev.108.1175. URL `https://link.aps.org/doi/10.1103/PhysRev.108.1175`.

[56] Leon N Cooper. Bound electron pairs in a degenerate fermi gas. *Physical Review*, 104(4):1189, 1956.

[57] Michael Tinkham. *Introduction to superconductivity*. Courier Corporation, 1996.

[58] Vitaly L Ginzburg. On superconductivity and superfluidity (what i have and have not managed to do), as well as on the physical minimumat the beginning of the 21st century. *ChemPhysChem*, 5(7):930–945, 2004.

[59] John Bardeen, Leon N Cooper, and J Robert Schrieffer. Microscopic theory of superconductivity. *Physical Review*, 106(1):162, 1957.

[60] Matthias Hein. *High-temperature-superconductor thin films at microwave frequencies*, volume 155. Springer Science & Business Media, 1999.

[61] JL Harden and V Arp. The lower critical field in the ginzburg-landau theory of superconductivity. *Cryogenics (England)*, 3, 1963.

[62] J Matricon and D Saint-James. Superheating fields in superconductors. *Phys. Lett., A*, 24, 1967.

[63] Mark K Transtrum, Gianluigi Catelani, and James P Sethna. Superheating field of superconductors within ginzburg-landau theory. *Physical Review B*, 83(9):094505, 2011.

[64] Michael Tinkham. *Introduction to superconductivity*. Courier Corporation, 2004.

[65] Hasan Padamsee. The science and technology of superconducting cavities for accelerators. *Superconductor science and technology*, 14(4):R28, 2001.

[66] Klaus Wille. *The physics of particle accelerators: an introduction*. Clarendon Press, 2000.

[67] Thomas P Wangler. *RF Linear accelerators*. John Wiley & Sons, 2008.

[68] Hasan Padamsee. *RF superconductivity: science, technology, and applications*. John Wiley & Sons, 2009.

[69] Hugh O Pierson. *Handbook of chemical vapor deposition: principles, technology and applications*. William Andrew, 1999.

[70] Anthony C Jones and Michael L Hitchman. *Chemical vapour deposition: precursors, processes and applications*. Royal society of chemistry, 2009.

[71] J Schlichting. Chemical vapor deposition of silicon carbide. *Powder Metallurgy International*, 12(4):196–200, 1980.

[72] Trung T Doan and Gurtej S Sandhu. Chemical vapor deposition technique for depositing titanium silicide on semiconductor wafers, January 11 1994. US Patent 5,278,100.

[73] Ki Kang Kim, Allen Hsu, Xiaoting Jia, Soo Min Kim, Yumeng Shi, Mario Hofmann, Daniel Nezich, Joaquin F Rodriguez-Nieva, Mildred Dresselhaus, Tomas Palacios, et al. Synthesis of monolayer hexagonal boron nitride on cu foil using chemical vapor deposition. *Nano letters*, 12(1):161–166, 2011.

[74] Alberto Maria Merlo. The contribution of surface engineering to the product performance in the automotive industry. *Surface and Coatings Technology*, 174: 21–26, 2003.

[75] Stephan Rupprecht, Alexandra Bloch, Stefan Rosiwal, Friedrich W Neukam, and Joerg Wiltfang. Examination of the bones-metal interface of titanium implants coated by the microwave plasma chemical vapor deposition method. *International Journal of Oral & Maxillofacial Implants*, 17(6), 2002.

[76] John R Abelson. Ultra-conformal cvd at low temperatures: The role of site blocking and the use of growth inhibitors. *ECS Transactions*, 33(2):307–319, 2010.

[77] Hiroshi Horie, M Imai, A Itoh, and Y Arimoto. Novel high aspect ratio aluminum plug for logic/dram lsis using polysilicon-aluminum substitute (pas). In *Electron Devices Meeting, 1996. IEDM'96., International*, pages 946–948. IEEE, 1996.

[78] K Grüter, M Deschler, H Jürgensen, R Beccard, and P Balk. Deposition of high quality gaas films at fast rates in the lp-cvd system. *Journal of Crystal Growth*, 94(3):607–612, 1989.

[79] S-Tong Lee, Zhangda Lin, and Xin Jiang. Cvd diamond films: nucleation and growth. *Materials Science and Engineering: R: Reports*, 25(4):123–154, 1999.

[80] Alfonso Reina, Xiaoting Jia, John Ho, Daniel Nezich, Hyungbin Son, Vladimir Bulovic, Mildred S Dresselhaus, and Jing Kong. Large area, few-layer graphene films on arbitrary substrates by chemical vapor deposition. *Nano letters*, 9(1): 30–35, 2008.

[81] Ya-Li Li, Ian A Kinloch, and Alan H Windle. Direct spinning of carbon nanotube fibers from chemical vapor deposition synthesis. *Science*, 304(5668):276–278, 2004.

[82] Timothy J Leedham, Anthony C Jones, Michael J Crosbie, Dennis J Williams, Peter J Wright, and Penelope A Lane. Chemical vapor deposition precursors, May 7 2002. US Patent 6,383,669.

[83] Paul O'Brien, Nigel L Pickett, and David J Otway. Developments in cvd delivery systems: A chemist's perspective on the chemical and physical interactions between precursors. *Chemical Vapor Deposition*, 8(6):237–249, 2002.

[84] Frank R Faller and Albert Hurrle. High-temperature cvd for crystalline-silicon thin-film solar cells. *IEEE Transactions on electron devices*, 46(10):2048–2054, 1999.

[85] Renaud Fix, Roy G Gordon, and David M Hoffman. Chemical vapor deposition of vanadium, niobium, and tantalum nitride thin films. *Chemistry of materials*, 5 (5):614–619, 1993.

[86] D Hazra, N Tsavdaris, S Jebari, Alexander Grimm, F Blanchet, F Mercier, E Blanquet, C Chapelier, and M Hofheinz. Superconducting properties of very high quality nbn thin films grown by high temperature chemical vapor deposition. *Superconductor Science and Technology*, 29(10):105011, 2016.

[87] Roy G Gordon, Seán Barry, Randy NR Broomhall-Dillard, Valerie A Wagner, and Ying Wang. Volatile liquid precursors for the chemical vapor deposition (cvd) of thin films containing tungsten. *MRS Online Proceedings Library Archive*, 612, 2000.

[88] Hyungsoo Choi, Sungho Park, and Tae Hyung Kim. Novel nickel precursors for chemical vapor deposition. *Chemistry of materials*, 15(20):3735–3738, 2003.

[89] Peter Atkins, Julio De Paula, and James Keeler. *Atkins' physical chemistry*. Oxford university press, 2018.

[90] Robert J Kee, Michael E Coltrin, and Peter Glarborg. *Chemically reacting flow: theory and practice*. John Wiley & Sons, 2005.

[91] WAP Claassen and J Bloem. The nucleation of cvd silicon on sio2 and si3 n 4 substrates i. the system at high temperatures. *Journal of the Electrochemical Society*, 127(1):194–202, 1980.

[92] R. Lowden D. Stinton, T. Bessman. Advanced advanced ceramics by chemical vapor deposition techniques. *Cer. Bul.*, 1988.

[93] JC Rostaing, F Coeuret, B Drevillon, R Etemadi, C Godet, J Huc, JY Parey, and VA Yakovlev. Silicon-based, protective transparent multilayer coatings deposited at high rate on optical polymers by dual-mode mw/rf pecvd. *Thin Solid Films*, 236(1-2):58–63, 1993.

[94] G Lucovsky, DV Tsu, RA Rudder, RJ Markunas, JL Vossen, and W Kern. Thin film processes ii. *Academic, Boston*, pages 565–619, 1991.

[95] SE Alexandrov. Remote pecvd: a route to controllable plasma deposition. *Le Journal de Physique IV*, 5(C5):C5–567, 1995.

[96] Dennis W Hess and David B Graves. *Plasma-Enhanced Etching and Deposition, Microelectronics Processing: Chemical Engineering Aspects*. American Chemical Society, Washington DC, 1989.

[97] John R Hollahan, Alexis T Bell, et al. Techniques and applications of plasma chemistry. 1974.

[98] HD Weakliem. Semiconductors and semimetals, vol. 21, hydrogenated amorphous silicon, part a, ed. ji pankove, 1984.

[99] Waldemar Singer, Alexey Ermakov, and Xenia Singer. Rrr-measurement techniques on high purity niobium. *TTC report*, 2, 2010.

[100] Gianluigi Ciovati, Joshua Spradlin, Pashupati Dhakal, Peter Kneisel, and Ganapati Rao Myneni. Rf performance of ingot niobium cavities of medium-low purity. 2015.

[101] S Candia and L Civale. Angular dependence of the magnetization of isotropic superconductors: which is the vortex direction? *Superconductor Science and Technology*, 12(4):192, 1999.

[102] AA Zhukov, GK Perkins, Yu V Bugoslavsky, and AD Caplin. Geometrical locking of the irreversible magnetic moment to the normal of a thin-plate superconductor. *Physical Review B*, 56(5):2809, 1997.

[103] CZ Antoine, S Berry, S Bouat, JF Jacquot, JC Villegier, G Lamura, and A Gurevich. Characterization of superconducting nanometric multilayer samples for superconducting rf applications: First evidence of magnetic screening effect. *Physical Review Special Topics-Accelerators and Beams*, 13(12):121001, 2010.

[104] G Lamura, M Aurino, A Andreone, and J-C Villégier. First critical field measurements of superconducting films by third harmonic analysis. *Journal of Applied Physics*, 106(5):053903, 2009.

[105] M Aurino, E Di Gennaro, F Di Iorio, A Gauzzi, G Lamura, and A Andreone. Discrete model analysis of the critical current-density measurements in superconducting thin films by a single-coil inductive method. *Journal of applied physics*, 98(12):123901, 2005.

[106] Muhammad Aburas, Claire Antoine, and Aurelien Four. Local magnetometer: First critical field measurement of multilayer superconductors. In *18th Int. Conf. on RF Superconductivity (SRF'17), Lanzhou, China, July 17-21, 2017*, pages 830–834. JACOW, Geneva, Switzerland, 2018.

[107] Yi Xie. *Development of superconducting RF sample host cavities and study of pit-induced cavity quench.* PhD thesis, 2013.

[108] JT Maniscalco, DL Hall, M Liepe, RD Porter, V Arrieta, S McNeal, and Brian Williams. Cornell sample host cavity: Recent results. In *8th Int. Particle Accelerator Conf.(IPAC'17), Copenhagen, Denmark, 14â 19 May, 2017*, pages 1142–1144. JACOW, Geneva, Switzerland, 2017.

[109] Jiquan Guo, Sami Tantawi, David Martin, and Charles Yoneda. Cryogenic rf material testing with a high-q copper cavity. In *AIP Conference Proceedings*, volume 1299, pages 330–335. AIP, 2010.

[110] E Brigant, E Haebel, and E Mahner. The quadrupole resonator, design considerations and layout of a new instrument for the rf characterization of superconducting surface samples. Technical report, 1998.

[111] R Kleindienst, O Kugeler, and J Knobloch. Development of an optimized quadrupole resonator at hzb. *Proceedings SRF 2013*, 2013.

[112] BP Xiao, CE Reece, HL Phillips, RL Geng, H Wang, F Marhauser, and MJ Kelley. Note: Radio frequency surface impedance characterization system for superconducting samples at 7.5 ghz. *Review of Scientific Instruments*, 82(5):056104, 2011.

[113] Ray F Egerton et al. *Physical principles of electron microscopy.* Springer, 2005.

[114] K Siegbahn and K Edvarson. β-ray spectroscopy in the precision range of 1: 105. *Nuclear Physics*, 1(3):137–159, 1956.

[115] Alexandre Rothen. The ellipsometer, an apparatus to measure thicknesses of thin surface films. *Review of Scientific Instruments*, 16(2):26–30, 1945.

[116] Donald R Sadoway and SN Flengas. Vapour pressures of solid and liquid nbcl5 and tacl5. *Canadian Journal of Chemistry*, 54(11):1692–1699, 1976.

[117] A Posmyk, J Myalski, and B Hekner. Composite coatings with ceramic matrix including nanomaterials as solid lubricants for oil-less automotive applications. *Archives of Metallurgy and Materials*, 61(2):1039–1043, 2016.

[118] Constantine Pozrikidis. *Fluid dynamics: theory, computation, and numerical simulation*. Springer, 2016.

[119] ANSYS Fluent et al. Theory guide. *Ansys Inc*, 2017.

[120] Inc. ANSYS. *ANSYS Academic Fluent Manual*. Release 17.

[121] Joseph I Goldstein, Dale E Newbury, Joseph R Michael, Nicholas WM Ritchie, John Henry J Scott, and David C Joy. *Scanning electron microscopy and X-ray microanalysis*. Springer, 2017.

[122] Frédéric Mercier, Stéphane Coindeau, Sabine Lay, Alexandre Crisci, Matthieu Benz, Thierry Encinas, Raphaël Boichot, Arnaud Mantoux, Carmen Jimenez, François Weiss, et al. Niobium nitride thin films deposited by high temperature chemical vapor deposition. *Surface and Coatings Technology*, 260:126–132, 2014.

[123] JH Durrell, CB Eom, A Gurevich, EE Hellstrom, C Tarantini, A Yamamoto, and DC Larbalestier. The behavior of grain boundaries in the fe-based superconductors. *Reports on Progress in Physics*, 74(12):124511, 2011.

[124] T Satish Kumar, S Rajesh Kumar, M Lakshmipathi Rao, and TL Prakash. Preparation of niobium metal powder by two-stage magnesium vapor reduction of niobium pentoxide. *Journal of Metallurgy*, 2013, 2013.

[125] Engineering ToolBox. Thermal conductivity of metals, 2003. URL `https://www.engineeringtoolbox.com/thermal-conductivity-metals-d_858.html`.

[126] AL Patterson. The scherrer formula for x-ray particle size determination. *Physical review*, 56(10):978, 1939.

[127] Olaf Engler and Valerie Randle. *Introduction to texture analysis: macrotexture, microtexture, and orientation mapping*. CRC press, 2009.

[128] F Fickett. Oxygen-free copper at 4 k: resistance and magnetoresistance. *IEEE Transactions on magnetics*, 19(3):228–231, 1983.

[129] Lakeshore. Cernox sensors specifications, 2018. URL `https://www.lakeshore.com/products/Cryogenic-Temperature-Sensors/Cernox/Models/Pages/Specifications.aspx`.

[130] J Halbritter. Granular superconductors and their intrinsic and extrinsic surface impedance. *Journal of superconductivity*, 8(6):691–703, 1995.

[131] DK Finnemore, TF Stromberg, and CA Swenson. Superconducting properties of high-purity niobium. *Physical Review*, 149(1):231, 1966.

[132] SB Roy, GR Myneni, and VC Sahni. On the reliable determination of the magnetic field for first flux-line penetration in technical niobium material. *Superconductor Science and Technology*, 21(6):065002, 2008.

[133] A Andreone, C Aruta, M Iavarone, F Palomba, ML Russo, M Salluzzo, R Vaglio, A Cassinese, MA Hein, T Kaiser, et al. Microwave properties of re–ni2b2c (re= y, er) superconducting thin films. *Physica C: Superconductivity*, 319(3-4):141–149, 1999.

[134] J Halbritter. A review of weak/strong links and junctions in high-tc superconductors as a transition to a mott insulator. *Superconductor Science and Technology*, 16(10):R47, 2003.

[135] J Halbritter. Transport in superconducting niobium films for radio frequency applications. *Journal of Applied Physics*, 97(8):083904, 2005.

[136] Roberto Russo. Quality measurement of niobium thin films for nb/cu superconducting rf cavities. *Measurement Science and Technology*, 18(8):2299, 2007.

[137] YM Shy, LE Toth, and R Somasundaram. Superconducting properties, electrical resistivities, and structure of nbn thin films. *Journal of Applied Physics*, 44(12): 5539–5545, 1973.

[138] MP Mathur, DW Deis, and JR Gavaler. Lower critical field measurements in nbn bulk and thin films. *Journal of Applied Physics*, 43(7):3158–3161, 1972.

[139] M Ashkin and JR Gavaler. The upper critical field of nbn film. *Journal of Applied Physics*, 49(4):2449–2451, 1978.

[140] Haruo Uyama and Osamu Matsumoto. Synthesis of ammonia in high-frequency discharges. ii. synthesis of ammonia in a microwave discharge under various conditions. *Plasma Chemistry and Plasma Processing*, 9(3):421–432, 1989.

[141] Y Ufuktepe, AH Farha, SI Kimura, T Hajiri, K Imura, MA Mamun, Faruk Karadag, AA Elmustafa, and HE Elsayed-Ali. Superconducting niobium nitride thin films by reactive pulsed laser deposition. *Thin Solid Films*, 545:601–607, 2013.

[142] Y Gotoh, M Nagao, T Ura, H Tsuji, and J Ishikawa. Ion beam assisted deposition of niobium nitride thin films for vacuum microelectronics devices. *Nuclear Instruments and Methods in Physics Research Section B: Beam Interactions with Materials and Atoms*, 148(1-4):925–929, 1999.

[143] P Fabbricatore, G Gemme, R Musenich, R Parodi, M Viviani, B Zhang, and V Buscaglia. Niobium and niobium-titanium nitrides for rf applications. *IEEE transactions on applied superconductivity*, 3(1):1761–1764, 1993.

[144] YT Yemane, MJ Sowa, J Zhang, L Ju, EW Deguns, NC Strandwitz, FB Prinz, and J Provine. Superconducting niobium titanium nitride thin films deposited by plasma-enhanced atomic layer deposition. *Superconductor Science and Technology*, 30(9):095010, 2017.

[145] Ehteram A Noor and Aisha H Al-Moubaraki. Corrosion behavior of mild steel in hydrochloric acid solutions. *Int. J. Electrochem. Sci*, 3(1):806–818, 2008.

[146] Alex Gurevich. Maximum screening fields of superconducting multilayer structures. *AIP Advances*, 5(1):017112, 2015.

[147] AA Abrikosov. On the lower critical field of thin layers of superconductors of the second group. *Soviet Physics JETP*, 19:988–991, 1964.

[148] A Gurevich. Enhancement of rf breakdown field of superconductors by multilayer coating. *Applied Physics Letters*, 88(1):012511, 2006.

[149] Takayuki Kubo. Multilayer coating for higher accelerating fields in superconducting radio-frequency cavities: a review of theoretical aspects. *Superconductor Science and Technology*, 30(2):023001, 2016.

[150] Takayuki Kubo, Yoshihisa Iwashita, and Takayuki Saeki. Radio-frequency electromagnetic field and vortex penetration in multilayered superconductors. *Applied Physics Letters*, 104(3):032603, 2014.

[151] Mario Ziegler, Ludwig Fritzsch, Julia Day, Sven Linzen, Solveig Anders, Julia Toussaint, and Hans-Georg Meyer. Superconducting niobium nitride thin films deposited by metal organic plasma-enhanced atomic layer deposition. *Superconductor Science and Technology*, 26(2):025008, 2012.

[152] Ziwen Fang, Helen C Aspinall, Rajesh Odedra, and Richard J Potter. Atomic layer deposition of tan and ta3n5 using pentakis (dimethylamino) tantalum and either ammonia or monomethylhydrazine. *Journal of Crystal Growth*, 331(1):33–39, 2011.

[153] Ziwen Fang, Paul A Williams, Rajesh Odedra, Hyeongtag Jeon, and Richard J Potter. Gadolinium nitride films deposited using a peald based process. *Journal of Crystal Growth*, 338(1):111–117, 2012.

[154] A Darlinski and J Halbritter. Angle-resolved xps studies of oxides at nbn, nbc, and nb surfaces. *Surface and interface analysis*, 10(5):223–237, 1987.

[155] Adafruit. Arduino ds3231 shield, 2018. URL `https://learn.adafruit.com/adafruit-ds3231-precision-rtc-breakout/overview`.

[156] Peter Atkins and Tina Overton. *Shriver and Atkins' inorganic chemistry*. Oxford University Press, USA, 2010.